

B7C FILE COPY

WRDC-TR-89-4133

AD-A226 627



RESEARCH AND DEVELOPMENT FOR
IMPROVED TOUGHNESS ALUMINIDES

B.J. Marquardt
G.K. Scarr
J.C. Chesnutt
C.G. Rhodes
H.L. Fraser

DTIC
SELECTED
SEP 14 1990
S D Cg D

GE Aircraft Engines
One Neumann Way
Cincinnati, Ohio 45215-6301

11 June 1990

Final Report for Period November 1985 - March 1989

Approved for public release; distribution unlimited.

MATERIALS LABORATORY
WRIGHT RESEARCH AND DEVELOPMENT CENTER
AIR FORCE SYSTEMS COMMAND
WRIGHT-PATTERSON AIR FORCE BASE, OHIO 45433-6533

90 09 13 099

NOTICES

When Government drawings, specifications or other data are used for any purpose other than in connection with a definitely related Government procurement operation, the United States Government thereby incurs no responsibility nor any obligation whatsoever, and the fact that the Government may have formulated, furnished or in any way supplied the said drawings, specifications or other data, is not to be regarded by implication or otherwise as in any manner licensing the holder or any other person or corporation or conveying any rights or permission to manufacture, use or sell any patented invention that may in any way be related thereto.

This report is releasable to the National Technical Information Service (NTIS). At NTIS, it will be available to the general public, including foreign nations.

This technical report has been reviewed and is approved for publication.

William R Kerr
WILLIAM R. KERR
Project Engineer
Processing and High Temperature
Materials Branch
Metals and Ceramics Division

Norman M. Geyer
NORMAN M. GEYER
Acting Chief
Processing and High Temperature
Materials Branch
Metals and Ceramics Division

FOR THE COMMANDER

Norman M. Tallan
NORMAN M. TALLAN, Director
Metals and Ceramics Division
Materials Laboratory

If your address has changed, if you wish to be removed from our mailing list, or if the addressee is no longer employed by your organization please notify WRDC/MLLM, WPAFB, OH 45433-6533 to help us maintain a current mailing list.

Copies of this report should not be returned unless return is required by security considerations, contractual obligations or notice on a specific document.

REPORT DOCUMENTATION PAGE

1a. REPORT SECURITY CLASSIFICATION Unclassified		1b. RESTRICTIVE MARKINGS										
2a. SECURITY CLASSIFICATION AUTHORITY		3. DISTRIBUTION/AVAILABILITY OF REPORT Approved for public release; distribution unlimited.										
2b. DECLASSIFICATION/DOWNGRADING SCHEDULE												
4. PERFORMING ORGANIZATION REPORT NUMBER(S)		5. MONITORING ORGANIZATION REPORT NUMBER(S) WRDC-TR-89-4133										
6a. NAME OF PERFORMING ORGANIZATION GE Aircraft Engines	6b. OFFICE SYMBOL (If applicable)	7a. NAME OF MONITORING ORGANIZATION Materials Laboratory WRDC, AFSC										
6c. ADDRESS (City, State, and ZIP Code) One Neumann Way Cincinnati, Ohio 45215-6301		7b. ADDRESS (City, State, and ZIP Code) WRDC/MLLM Wright-Patterson AFB, Ohio 45433-6533										
8a. NAME OF FUNDING/SPONSORING ORGANIZATION	8b OFFICE SYMBOL (If applicable)	9. PROCUREMENT INSTRUMENT IDENTIFICATION NUMBER F33615-85-C-5167										
8c. ADDRESS (City, State, and ZIP Code)		10. SOURCE OF FUNDING NUMBERS <table border="1"> <tr> <th>PROGRAM ELEMENT NO.</th> <th>PROJECT NO.</th> <th>TASK NO.</th> <th>WORK UNIT ACCESSION NO.</th> </tr> <tr> <td>62102F</td> <td>2420</td> <td>01</td> <td>70</td> </tr> </table>		PROGRAM ELEMENT NO.	PROJECT NO.	TASK NO.	WORK UNIT ACCESSION NO.	62102F	2420	01	70	
PROGRAM ELEMENT NO.	PROJECT NO.	TASK NO.	WORK UNIT ACCESSION NO.									
62102F	2420	01	70									
11. TITLE (Include Security Classification) Research and Development for Improved Toughness Aluminides												
12. PERSONAL AUTHOR(S) B.J. Marquardt, G.K. Scarr, J.C. Chesnutt, C.G. Rhodes and H.L. Fraser												
13a. TYPE OF REPORT Final	13b. TIME COVERED FROM 1 Nov 85 TO 30 Mar 89	14. DATE OF REPORT (Year, Month, Day) 11 June 1990	15. PAGE COUNT 180									
16. SUPPLEMENTARY NOTATION												
17. COSATI CODES <table border="1"> <tr> <th>FIELD</th> <th>GROUP</th> <th>SUB-GROUP</th> </tr> <tr> <td></td> <td></td> <td></td> </tr> <tr> <td></td> <td></td> <td></td> </tr> </table>		FIELD	GROUP	SUB-GROUP							18. SUBJECT TERMS (Continue on reverse if necessary and identify by block number) Titanium alloys, alpha-2, fracture toughness, micro-structure, processing, properties. (55)	
FIELD	GROUP	SUB-GROUP										
19. ABSTRACT (Continue on reverse if necessary and identify by block number) The objective of this program was to study and identify the basic mechanisms which can improve the toughness of alloys based on the intermetallic compound Ti ₃ Al. The improved properties offered by these alloys will increase their potential for application in rotating components and critical static parts in advanced aircraft engines. The program was conducted in two separate phases which addressed iterative alloy/processing studies as well as alloy scale up concerns. In the first phase of the program, the effects of solid solution alloying, tough second phase, and dispersoid additions were evaluated in parallel tasks. Subsequently, alloys were designed to make use of additive and/or synergistic effects by combining the various alloying and processing concepts. In the second phase of the program, three of the more promising compositions were selected for scale up and further microstructural and property evaluations. <i>Keywords</i>												
20. DISTRIBUTION/AVAILABILITY OF ABSTRACT <input checked="" type="checkbox"/> UNCLASSIFIED/UNLIMITED <input type="checkbox"/> SAME AS RPT. <input type="checkbox"/> DTIC USERS		21. ABSTRACT SECURITY CLASSIFICATION Unclassified										
22a. NAME OF RESPONSIBLE INDIVIDUAL William R. Kerr		22b. TELEPHONE (Include Area Code) 513-255-9834	22c. OFFICE SYMBOL WRDC/MLLM									

FOREWORD

This Final Report covers the work performed by the General Electric Company under Air Force Contract F33615-85-C-5167 for the time period from 1 November 1985 through 31 March 1989. The objective of this program was to study and identify the basic mechanisms which can improve the toughness of alloys based on the intermetallic compound Ti₃Al.

W.R. Kerr of the Processing & High Temperature Materials Branch, Metals and Ceramics Division, WRDC/MLLM, Wright-Patterson Air Force Base, Ohio, 45433-6533 was the technical contract monitor.

The program was conducted by the Engineering Materials Technology Laboratories (EMTL) at GE Aircraft Engines (GEAE) in Evendale, Ohio. J.C. Chesnutt was the program manager, and B.J. Marquardt was the principal investigator.

The analytical electron microscopy studies reported herein were conducted by G.K. Scarr of GEAE, C.G. Rhodes of the Rockwell International Science Center and H.L. Fraser of the Ohio State University. The authors wish to thank E.Z. Lanman for fractographic analysis conducted throughout the course of this program. In addition, the experimental assistance of R.L. Grant and the Laboratory Technical Services of EMTL is gratefully acknowledged, and the assistance of J.M. Overberg in producing the manuscript is highly appreciated.



Accesion For	
NTIS CRA&I	<input checked="" type="checkbox"/>
DTIC TAB	<input type="checkbox"/>
Unannounced	<input type="checkbox"/>
Justification _____	
By _____	
Distribution / _____	
Availability Codes	
Dist	Available or Special
A-1	

TABLE OF CONTENTS

	<u>Page</u>
1.0 INTRODUCTION	1
2.0 TECHNICAL PLAN	2
2.1 Objective and Scope	2
2.2 Program Plan	3
2.2.1 Phase I - Alloy Exploration and Preliminary Evaluation	4
2.2.2 Phase II - Alloy Scale-Up	5
3.0 RESEARCH AND DEVELOPMENT	6
3.1 Phase I: Alloy Exploration	6
3.1.1 Task 1 - Solid Solution Alloys	6
3.1.1.1 Processing and Heat Treatment	6
3.1.1.2 Mechanical Testing	14
3.1.1.3 Analysis of Deformation Structures	20
3.1.1.4 Alternate Microstructures	40
3.1.1.5 Task 1 - Summary	43
3.1.2 Task 2 - Tough Second Phase Alloys	44
3.1.2.1 Processing and Heat Treatment	44
3.1.2.2 Mechanical Testing	50
3.1.2.3 Analysis of Deformation Structures	55
3.1.2.4 Alternate Microstructures	68
3.1.2.5 Task 2 - Summary	71
3.1.3 Task 3 - Dispersoid Containing Alloys	72
3.1.3.1 Consolidation and Extrusion	72
3.1.3.2 Characterization of Extruded Powders	74
3.1.3.3 Mechanical Testing	82
3.1.3.4 Analysis of Deformation Structures	85
3.1.3.5 Task 3 - Summary	90
3.1.4 Task 4 - Combination Alloys	97
3.1.4.1 Processing and Heat Treatment	97
3.1.4.2 Mechanical Testing	97
3.1.4.3 Alternate Microstructures	108
3.1.4.4 Task 4 - Summary	112
3.2 Phase II - Alloy Scale-up	113
4.0 CONCLUSIONS	161
5.0 REFERENCES	163

LIST OF FIGURES

Figure No.	Title	Page
2-1	Flow diagram of overall program	3
3-1	As-extruded microstructures of (a) Ti-22Al-5Nb-3Ga-2Ta (IT-9), (b) Ti-25Al-5Nb-1Mo (IT-5) and (c) Ti-20Al-5Nb-5Sn (IT-3).	10
3-2	Optical micrographs of (a) Ti-20Al-5Nb-5Ga (IT-1) heat treated at 1135°C (2075°F), (b) Ti-25Al-5Nb-5Ga (IT-2) heat treated at 1177°C (2150°F) and (c) Ti-20Al-5Nb-5Sn (IT-3) heat treated at 1315°C (2400°F).	11
3-3	Optical micrographs of (a) Ti-20Al-5Nb-2.5Ga-2.5Sn (IT-4) heat treated at 1205°C (2200°F), (b) Ti-25Al-5Nb-1Mo (IT-5) heat treated at 1135°F (2075°F) and (c) Ti-25Al-5Nb-1Cr (IT-6) heat treated at 1135°C (2075°F).	12
3-4	Optical micrographs of (a) Ti-25Al-5Nb-10Zr (IT-7) heat treated at 1070°C (1960°F), (b) Ti-22Al-5Nb-3Ga-1Mo (IT-8) heat treated at 1121°C (2050°F) and (c) Ti-22Al-5Nb-3Ga-2Ta (IT-9) heat treated at 1165°C (2125°F).	13
3-5	Fracture surfaces of bend test specimens of (a) Ti-20Al-5Nb-5Ga (IT-1) (23.3 MPa \sqrt{m} (21.2 ksi \sqrt{in})), (b) Ti-25Al-5Nb-5Ga (IT-2) (12.1 MPa \sqrt{m} (11.0 ksi \sqrt{in})), (c) Ti-22Al-5Nb-3Ga-1Mo (IT-8) (24.6 MPa \sqrt{m} (22.4 ksi \sqrt{in})).	16
3-6	Fracture surfaces of Ti-25Al-5Nb-1Mo (IT-5) bend test specimens with fracture toughness values of (a) 20.3 MPa \sqrt{m} (18.5 ksi \sqrt{in}) and (b) 8.5 MPa \sqrt{m} (7.7 ksi \sqrt{in}).	17
3-7	Schematic diagram of specimen preparation procedure.	21
3-8	TEM micrographs of a dislocations and basal plane faults in a Ti-19.5Al-5Nb-5Ta-3Sn (IT-15) specimen deformed at room temperature.	25
3-9	TEM micrographs of a slip in a Ti-25Al-4Nb-2Ta-2V-1Mo (IT-11) specimen deformed at room temperature.	26
3-10	TEM micrographs of a dislocations on basal and prism planes in a Ti-25Al-4Nb-2Ta-2V-1Mo (IT-11) specimen deformed at room temperature.	27
3-11	(a) TEM micrograph of Ti-25Al-5Nb-1Cr (IT-6) illustrating thin, discontinuous beta phase, (b) TEM micrograph of Ti-25Al-5Nb-5Ga (IT-2) demonstrating continuous alpha-2 phase separating alpha-2 Widmanstatten plates.	29

LIST OF FIGURES (Continued)

Figure No.	Title	Page
3-12	(a) TEM micrograph illustrating $c+a/2$ slip in an alpha-2 grain oriented with the c axis 6° from the stress axis in Ti-20Al-5Nb-2.5Ga-2.5Sn (IT-4) tested at RT. (b) TEM micrograph showing $c+a/2$ slip in an alpha-2 grain in Ti-25Al-5Nb-1Mo (IT-5) tested at RT.	31
3-13	(a) TEM micrograph showing $c+a/2$ slip in an alpha-2 grain oriented with the c axis 16° from the stress axis in Ti-25Al-5Nb-10Zr (IT-7) tested at RT. (b) TEM micrograph illustrating $c+a/2$ slip in an alpha-2 grain oriented with the c axis 10° from stress axis in Ti-22Al-5Nb-3Ga-1Mo (IT-8) tested at RT.	32
3-14	(a) TEM micrograph illustrating $c+a/2$ slip in an alpha-2 grain oriented with the c axis 13° from the stress axis in a Ti-25Al-5Nb-1Mo (IT-5) specimen tested at 300°C (572°F). (b) TEM micrograph showing $c+a/2$ slip in an alpha-2 grain oriented with the c axis 12° from the stress axis in Ti-20Al-5Nb-5Sn (IT-3) tested at 300°C (572°F).	33
3-15	(a) TEM micrograph showing $c+a/2$ slip in an alpha-2 grain oriented with the c axis 15° from the stress axis in an Ti-25Al-5Nb-1Mo (IT-5) specimen tested at 500°C (932°F). (b) TEM micrograph illustrating $c+a/2$ slip in an alpha-2 grain oriented with the c axis 10° from the stress axis in Ti-22Al-5Nb-3Ga-1Mo (IT-8) tested at 500°C (932°F).	34
3-16	(a) TEM micrograph illustrating $c+a/2$ slip in an alpha-2 grain oriented with the c axis 6° from the stress axis in Ti-25Al-5Nb-1Cr (IT-6) tested at 500°C (932°F). (b) TEM micrograph showing $c+a/2$ slip in an alpha-2 grain oriented with the c axis 31° from the stress axis in Ti-25Al-5Nb-10Zr (IT-7) tested at 500°C (932°F).	35
3-17	Transmission electron micrographs of dislocations in an Ti-22Al-5Nb-3Ga-1Mo (IT-8) compression specimen tested at room temperature. The compression axis is horizontal to the figures where (a) $g = \bar{2}20\bar{1}$ and (b) $g = \bar{2}42\bar{2}$.	38
3-18	Transmission electron micrographs of dislocations in Ti-22Al-5Nb-3Ga-1Mo (IT-8) after compression testing at 500°C (930°F). The compression axis is horizontal to the figures where (a) $g = \bar{2}20\bar{1}$ and (b) $g = \bar{2}0\bar{2}2$.	39
3-19	Microstructures of beta solution treated material of (a) Ti-25Al-5Nb-1Mo (IT-5) and (b) Ti-22Al-5Nb-3Ga-1Mo (IT-8) and duplex microstructures produced by heat treatment within the alpha-2 plus beta phase field of (c) IT-5 and (d) IT-8.	41
3-20	As-extruded microstructures of (a) Ti-22.5Al-4Nb-2Ta-2V-1Mo (IT-10), (b) Ti-25Al-4Nb-2Ta-2V-1Mo (IT-11), (c) Ti-22.5Al-6Nb-2Ta-2Cr (IT-12) and (d) Ti-22.5Al-5Nb-5Ta-3Zr (IT-14).	47

LIST OF FIGURES
(Continued)

Figure No.	Title	Page
3-21	Optical micrographs of (a) Ti-22.5Al-4Nb-2Ta-2V-1Mo (IT-10) heat treated at 1095°C (2000°F), (b) Ti-25Al-4Nb-2Ta-2V-1Mo (IT-11) heat-treated at 1135°C (2075°F) and (c) Ti-22.5Al-6Nb-2Ta-2Cr (IT-12) heat-treated at 1095°C (2000°F).	48
3-22	Optical micrographs of (a) Ti-22.7Al-3Nb-3Ta-3V (IT-13) heat treated at 1095°C (2000°F), (b) Ti-22.5Al-5Nb-5Ta-3Zr (IT-14) heat-treated at 1095°F (2000°F), (c) Ti-19.5Al-5Nb-5Ta-3Sn (IT-15) heat-treated at 1175°C (2150°F) and (d) Ti-19.5Al-10Nb-3Ga (IT-16) heat treated at 1070°C (1960°F).	49
3-23	Fractographic analysis revealing overall surface roughness of fracture toughness specimens of (a) Ti-22.5Al-6Nb-2Ta-2Cr (IT-12) and (b) Ti-25Al-4Nb-2Ta-2V-1Mo (IT-11).	54
3-24	TEM micrographs of $c+a/2$ dislocations in a Ti-25Al-4Nb-2Ta-2V-1Mo (IT-11) specimen which was deformed at room temperature.	56
3-25	TEM micrographs of $c+a/2$ dislocations in a Ti-22.5Al-6Nb-2Ta-2Cr (IT-12) specimen which was deformed at room temperature.	57
3-26	TEM micrographs of $c+a/2$ and a dislocations in a Ti-22.5Al-5Nb-5Ta-3Zr (IT-14) specimen which was deformed at room temperature.	58
3-27	TEM micrographs of $c+a/2$ and a dislocations in a Ti-19.5Al-10Nb-3Ga (IT-16) specimen which was deformed at room temperature.	59
3-28	TEM micrographs of $c+a/2$ and a dislocations plus APB's in an Ti-22.5Al-4Nb-2Ta-2V-1Mo (IT-10) specimen which was deformed at 300°C (570°F).	61
3-29	TEM micrographs of $c+a/2$ and a dislocations in a Ti-22.5Al-6Nb-2Ta-2Cr (IT-12) specimen which was deformed at 300°C (570°F).	62
3-30	TEM micrographs of $c+a/2$ dislocations in a Ti-22.7Al-3Nb-3Ta-3V (IT-13) specimen which was deformed at 300°C (570°F).	63
3-31	TEM micrographs of $c+a/2$ and a dislocations in a Ti-22.7Al-3Nb-3Ta-3V (IT-13) specimen which was deformed at 500°C (930°F).	65
3-32	TEM micrographs of inhomogenous slip distribution in a Ti-19.5Al-10Nb-3Ga (IT-16) specimen which was deformed at 500°C (930°F).	66
3-33	TEM micrographs of a slip transfer across an alpha-2/beta interface in a Ti-22.5Al-6Nb-2Ta-2Cr (IT-12) specimen which was deformed at 300°C (570°F).	67

LIST OF FIGURES
(Continued)

Figure No.	Title	Page
3-34	Microstructures of beta solution treated material of (a) Ti-22.5Al-6Nb-2Ta-2Cr (IT-12) and (b) Ti-22.7Al-3Nb-3Ta-3V (IT-13), and duplex microstructures produced by heat treatment within the alpha-2 plus beta phase field of (c) IT-12 and (d) IT-13.	69
3-35	Bright-field electron micrographs of as-extruded Ti-24Al-11Nb-1.5%Er (IT-17) illustrating coarsened dispersoids and heavy deformation after (a) direct extrusion and (b) compaction plus extrusion.	75
3-36	Bright-field electron micrographs of as-extruded Ti-25Al-5Nb-1.5%Er (IT-18) showing coarse dispersoids after (a) direct extrusion and (b) compaction plus extrusion.	76
3-37	Bright-field electron micrographs of as-extruded Ti-25Al-5Nb-3.0%Er (IT-19) illustrating coarse dispersoids and recrystallized grains after (a) direct extrusion and (b) compaction plus extrusion.	77
3-38	Bright-field electron micrographs of as-extruded Ti-25Al-5Nb-5Ga-1.5%Er (IT-20) showing recovered and recrystallized grains with large dispersoids after (a) direct extrusion and (b) compaction plus extrusion.	79
3-39	Bright-field electron micrographs of as-extruded Ti-25Al-5Nb-5Ta-1.5%Er (IT-21) illustrating heavy deformation, coarse dispersoids, and beta phase after (a) direct extrusion and (b) compaction plus extrusion.	80
3-40	Bright-field electron micrographs of as-extruded Ti-25Al-5Nb-5Ta (IT-22) showing heavy deformation and beta phase after (a) direct extrusion and (b) compaction plus extrusion.	81
3-41	Weak-beam dark-field electron micrograph of the dislocation microstructure of Ti-25Al-5Nb-5Ga-1.5%Er (IT-20) after RT compression testing.	86
3-42	Weak-beam dark-field electron micrograph of $c+a/2$ dislocations in Ti-25Al-5Nb-5Ga-1.5%Er (IT-20) after RT compression testing.	87
3-43	Weak-beam dark-field electron micrograph of Ti-25Al-5Nb-5Ga-1.5%Er (IT-20) after RT compression testing with $g = 02\bar{2}1$ and the beam direction close to [1210].	88
3-44	Weak-beam dark-field electron micrograph of Ti-25Al-5Nb-5Ga-1.5%Er (IT-20) after RT compression testing with $g = \bar{2}02\bar{1}$ and the beam direction close to [1102].	89

LIST OF FIGURES (Continued)

Figure No.	Title	Page
3-45	Weak-beam dark-field electron micrograph of the dislocation microstructure in Ti-25Al-5Nb-5Ta (IT-22) after RT compression testing.	91
3-46	Weak-beam dark-field electron micrograph of $c+a/2$ dislocations in Ti-25Al-5Nb-5Ta (IT-22) after RT compression testing.	92
3-47	Weak-beam dark-field electron micrograph of Ti-25Al-5Nb-5Ta (IT-22) after RT compression testing with $g = 2\bar{0}21$ and the beam direction close to $[1\bar{2}10]$.	93
3-48	Weak-beam dark-field electron micrograph of the dislocation debris observed in the bands of c -component dislocations in Ti-25Al-5Nb-5Ta (IT-22) after RT compression testing. The beam direction is close to $[1\bar{2}10]$ and $g = \bar{2}021$.	94
3-49	Weak-beam dark-field electron micrograph of the dislocation microstructure in Ti-25Al-5Nb-5Ga-1.5%Er (IT-20) following compression testing 500°C (932°F) with the beam direction close to $[1\bar{2}10]$ and $g = 2\bar{0}21$.	95
3-50	Weak-beam dark-field electron micrograph of $c+a/2$ dislocations in Ti-25Al-5Nb-5Ga-1.5%Er (IT-20) after compression testing at 500°C (932°F). The beam direction is close to $[1\bar{2}10]$ and $g = 0002$.	96
3-51	Optical micrographs of (a) Ti-25Al-6Nb-3V-3Ta (IT-23) and (b) Ti-25Al-8Nb-3V-3Ta (IT-24) after heat-treatment at 1120°C (2050°F).	99
3-52	Optical micrographs of (a) Ti-25Al-6Nb-2V-2Ta-2Mo (IT-25) after heat-treatment at 1120°C (2050°F) and (b) Ti-25Al-8Nb-2V-2Ta-2Mo (IT-26) after heat-treatment at 1105°C (2025°F).	100
3-53	Optical micrographs of (a) Ti-23Al-6Nb-3V-3Ta-2Sn (IT-27) after heat-treatment at 1160°C (2125°F) and (b) Ti-25Al-5Nb-5Ta-2Mo (IT-28) after heat-treatment at 1120°C (2050°F).	101
3-54	Optical micrographs of (a) Ti-25Al-6Nb-2Ta-2Cr (IT-29) after heat-treatment at 1105°C (2025°F) and (b) Ti-23Al-6Nb-2Ta-2Mo-2Cr (IT-30) after heat-treatment at 1065°C (1950°F).	102
3-55	Larson-Miller plot for the time to 0.2% creep of Ti-24Al-11Nb and the Task 4 alloys.	106
3-56	Microstructure of Ti-25Al-8Nb-3V-3Ta (IT-24) after (a) beta solution heat-treatment and (b) heat-treatment in the alpha-2 plus beta phase field.	109

LIST OF FIGURES (Continued)

Figure No.	Title	Page
3-57	Microstructure of Ti-23Al-6Nb-2Ta-2Mo-2Cr (IT-30) after heat-treatment in the alpha-2 plus beta phase field followed by cooling rates of (a) 40°C (75°F) per minute and (b) 20°C (35°F) per minute.	110
3-58	Backscatter electron micrographs showing (a) inhomogenous microstructure of Ti-24.5Al-6Nb-2Mo-2Ta-2V (IT-A) and (b) homogeneous microstructure of Ti-23.5Al-2Nb-2Mo-2Ta-2Cr (IT-C).	115
3-59	Optical metallography following final heat-treatment of (a) Ti-24.5Al-6Nb-2Mo-2Ta-2V (IT-A), (b) Ti-24.5Al-8Nb-2Mo-2Ta (IT-B) and (c) Ti-23.5Al-2Nb-2Mo-2Ta-2Cr (IT-C).	116
3-60	Ductility of Phase II alloys before and after a 100 hour thermal exposure at 705°C (1300°F) as determined by (a) elongation and (b) reduction of area.	122
3-61	Macrophotos of tensile specimens of the alloy Ti-24.5Al-8Nb-2Mo-2Ta (IT-B) tested at (a) room temperature, (b) 205°C (400°F), (c) 425°C (800°F), (d) 540°C (1000°F), (e) 650°C (1200°F) and (f) 760°C (1400°F).	123
3-62	TEM micrographs of Ti-24.5Al-6Nb-2Mo-2Ta-2V (IT-A) showing the (a) microstructure after salt quench and (b) thinning of beta ribs after a 100 hour thermal exposure at 705°C (1300°F).	124
3-63	Bright-field TEM micrographs of Ti-24.5Al-8Nb-2Mo-2Ta (IT-B) showing (a) Widmanstatten alpha-2 plates with thin beta ribs and precipitation within alpha-2 and (b) precipitation of alpha-2 within the beta phase.	125
3-64	Bright-field TEM micrograph of alpha-2 sideplate colony at a prior-beta boundary of the alloy Ti-24.4Al-8Nb-2Mo-2Ta (IT-B). (a) Low magnification and (b) higher magnification with specimen tilted so that alpha-2/beta interfaces are parallel to the beam.	127
3-65	Bright-field TEM micrograph of Ti-24.5Al-8Nb-2Mo-2Ta (IT-B) after heat-treatment plus a 1300°F/100 hour exposure that has narrowed the beta ribs and produced regular dislocation arrays at the boundaries.	128
3-66	Bright-field TEM micrograph of Ti-23.5Al-2Nb-2Mo-2Ta-2Cr (IT-C) showing (a) general view of a colony which reveals a tendency to facet when tilted as in (b).	129
3-67	Smooth bar tensile properties of Ti-24.5Al-6Nb-2Mo-2Ta-2V (IT-A) before and after thermal exposure and notched bar tensile properties without thermal exposure.	130

LIST OF FIGURES
(Continued)

Figure No.	Title	Page
3-68	Extrapolation process used for determination of the constant in the Larson-Miller equation.	132
3-69	Larson-Miller curve for the time to 0.2% creep of Ti-24.5Al-6Nb-2Mo-2Ta-2V (IT-A) determined from test results over the temperature range of 540 to 760°C (1000 to 1400°F).	133
3-70	Microprobe analysis of oxygen rich layer on creep specimens of (a) Ti-24.5Al-6Nb-2Mo-2Ta-2V (IT-A) tested at 760°C (1400°F) for 194 hours and (b) Ti-24.5Al-8Nb-2Mo-2V (IT-B) tested at 650°C (1200°F) for 350 hours.	135
3-71	Bright-field TEM micrograph from 1000°F creep specimen of Ti-23.5Al-2Nb-2Mo-2Ta-2Cr (IT-C) showing (a) mottled appearance of alpha-2 colony with mostly clear beta ribs; (b) and (c) higher magnification views showing various morphologies of alpha-2 laths which precipitate during creep in the wider beta regions at colony boundaries.	137
3-72	Bright-field TEM micrographs from primary alpha-2 region in same specimen as Figure 3-71 showing a network of dislocations which were identified as having $\langle a \rangle$ Burgers vectors by $g \cdot b$ experiments such as (b) - (d). The individual segments are mostly in screw orientations.	139
3-73	Bright-field TEM micrographs from 760°C (1400°F) creep specimen of Ti-23.5Al-2Nb-2Mo-2Ta-2Cr (IT-C) showing (a) precipitate & dislocation-free beta region with (b) regular arrays of dislocations at the alpha-2/beta interfaces.	140
3-73	(Continued) Weak-beam dark-field TEM micrograph from 760°C (1400°F) creep specimen of Ti-23.5Al-2Nb-2Mo-2Ta-2Cr (IT-C) showing (c) possible decomposition at dislocations in alpha-2 phase.	141
3-74	Bright-field TEM micrographs of specimen in Figure 3-73 showing (a) faulting/twinning that is (b) sometimes wholly contained within an alpha-2 lath.	142
3-74	(Continued) Tilting the specimen as in (c) yields a selected-area electron diffraction pattern (d) which shows an orthorhombic distortion in the (0001) zone with 'twins' lying on {1010} habit planes.	143
3-75	(a) Bright-field TEM micrograph of specimen in Figure 3-73 showing a region with coarsened precipitates within the alpha-2 phase which light up in the dark-field micrograph (b) imaged with the (110) beta diffraction vector.	144

LIST OF FIGURES
(Continued)

Figure No.	Title	Page
3-76	Larson-Miller curve for the rupture life of Ti-24.5Al-6Nb-2Mo-2Ta-2V (IT-A) determined from test results over the temperature range of 540 to 760°C (1000 to 1400°F).	147
3-77	Stress/rupture specimens of (a) Ti-24.5Al-6Nb-2Mo-2Ta-2V (IT-A), (b) Ti-24.5Al-8Nb-2Mo-2Ta (IT-B), and (c) Ti-23.5Al-2Nb-2Mo-2Ta-2Cr (IT-C) tested in air at 760°C (1400°F) and an initial stress of 310 MPa (45 ksi).	148
3-78	Surface cracking of Ti-24.5Al-8Nb-2Mo-2Ta (IT-B) stress/rupture specimens tested at (a) 650°C (1200°F) for 127 hours and (b) 760°C (1400°F) for 47 hours.	149
3-79	Equivalent energy fracture toughness of scale-up alloys plotted as a function of test temperature.	151
3-80	LCF results for Ti-24.5Al-6Nb-2Mo-2Ta-2V (IT-A) and Ti-24.5Al-8Nb-2Mo-2Ta (IT-B).	155
3-81	LCF results for the alloy Ti-23.5Al-2Nb-2Mo-2Ta-2Cr (IT-C).	156
3-82	SEM micrographs of specimen BX25 showing (a) fracture initiation site and (b) microstructure immediately below the initiation site when revealed by plateau electropolish and etch techniques.	157
3-83	SEM micrographs of specimen BX27 showing (a) fracture initiation site and (b) microstructure immediately below the initiation site when revealed by plateau electropolish and etch techniques.	158
3-84	SEM micrographs of specimen B5 showing fracture initiation site after testing at 427°C (800°F) and a strain range of 1.5 percent.	159

LIST OF TABLES

Table No.	Title	Page
2-1	Mechanical Testing Program for Phase II	5
3-1	Compositions of Task 1 Alloys	7
3-2	Extrusion and Beta Transus Temperatures for Task 1 Alloys	9
3-3	Tensile Properties of Task 1 Alloys	18
3-4	Room Temperature Fracture Toughness of Task 1 Alloys	19
3-5	Alpha Slip Systems and Geometrically Equivalent Alpha-2 Indices	23
3-6	Phase Compositions of Ti-25Al-5Nb-5Ga (IT-2)	28
3-7	Tensile Properties for Microstructural Study of Task 1 Alloys	42
3-8	Fracture Toughness Test Results for the Microstructural Study of Task 1 Alloys	42
3-9	Compositions of Task 2 Alloys	45
3-10	Extrusion and Beta Transus Temperatures for Task 2 Alloys	46
3-11	Tensile Properties of Task 2 Alloys	51
3-12	Room Temperature Fracture Toughness of Task 2 Alloys	53
3-13	Tensile Properties for Microstructural Study of Task 2 Alloys	70
3-14	Fracture Toughness Test Results for the Microstructural Study of Task 2 Alloys	70
3-15	Compositions of Task 3 Alloys, weight %, aim/(actual)	73
3-16	Tensile Strength of Task 3 Alloys	82
3-17	0.2% Compressive Yield Strength of Task 3 Alloys	83
3-18	Room Temperature Fracture Toughness of Task 3 Alloys	84
3-19	Compositions of Task 4 Alloys	98
3-20	Task 4 Tensile Properties	103
3-21	Task 1 Tensile Properties as a Function of Specimen Configuration	104
3-22	Task 4 Creep Properties	105
3-23	Task 4 Stress/Rupture Properties	107

LIST OF TABLES

Table No.	Title	Page
3-24	Task 4 Room Temperature Fracture Toughness Properties	107
3-25	Tensile Properties for the Microstructural Study of Task 4 Alloys	108
3-26	Creep Test Results for the Microstructural Study of Task 4 Alloys after Testing at 650°C (1200°F)/172 MPa (25 ksi)	111
3-27	Fracture Toughness Test Results for the Microstructural Study of Task 4 Alloys	112
3-28	Phase II Alloy Compositions	113
3-29	Tensile Properties of Alloys IT-A and IT-B	117
3-30	Tensile Properties of Alloy IT-C	118
3-31	Notched Tensile Properties of Phase II Alloys	119
3-32	Post Thermal Exposure Tensile Properties of Phase II Alloys	120
3-33	Creep Properties of Phase II Alloys	131
3-34	Depth of Oxygen Rich Layer on Phase II Creep Specimens	136
3-35	Creep Parameters of Specimens Evaluated by AEM	136
3-36	Stress/Rupture Properties of Phase II Alloys	146
3-37	Fracture Toughness Data for Phase II Alloys	150
3-38	LCF Results from Phase II Testing	153
3-39	LCF Results from Phase II Testing of Alloy IT-C	154

1.0 INTRODUCTION

Advanced material and process technologies are needed to improve the thrust-to-weight ratio, increase performance, and extend the life of advanced aircraft gas turbine engines. Titanium aluminides, particularly Ti_3Al derivatives, are advanced lightweight materials which offer a 110 to 170°C (200 to 300°F) temperature advantage over commercial high temperature titanium alloys at comparable densities. These titanium aluminides are also competitive in strength at 40 percent lower density than some superalloys, but their use is currently restricted by their inherently low toughness. Improvements in the toughness of these materials should increase component life and extend applications to rotating components.

During the past several years, GE Aircraft Engines (GEAE) has conducted several internally funded programs to evaluate Ti-24Al-11Nb (Ti-14Al-21Nb in weight percent) as an engineering material. The primary objective of this effort was to gain metallurgical and design experience relative to the fabrication, application, properties, and general metallurgy of this alloy system. Combustor and exhaust components for advanced engines have been fabricated and successfully engine tested.

Feasibility studies of methods to improve the low temperature toughness of Ti_3Al alloys using special alloying, processing, and heat treatment have been conducted at GEAE. The results of these efforts have been encouraging and indicate that improvements in toughness are feasible.

This contract was preceded by an extensive research and development effort, much of it sponsored by the Air Force. Most of the previous work has been addressed in a recent review article [1]. The early success of several research and development programs inspired further work and helped to identify additional approaches for alloy improvements.

This program used an approach for improving the toughness of alpha-2 alloys through an evaluation of and understanding of the toughness controlling mechanisms. Alloying and microstructural effects on toughness and methods of alloying and processing that yield alpha-2 titanium aluminides with improved toughness have been identified. These improvements, though, can not easily be achieved without some loss of high temperature strength and creep resistance.

2.0 TECHNICAL PLAN

2.1 Objective and Scope

The objective of this program was to study and identify the basic mechanisms which can improve the toughness of alloys based on the intermetallic compound Ti₃Al.

The program was conducted in two separate phases. In the first phase, alloying and processing were explored in three tasks based on the following concepts:

- solid solution alloying
- alloying to produce tough second phase
- dispersoid containing alloys.

In the fourth task of Phase I, alloys were designed to make use of additive and/or synergistic effects of combining the various alloying and processing concepts. The Phase I studies entailed alloy selection, conventional and rapid solidification technology (RST) processing, extensive microstructural evaluation, and preliminary toughness and tensile measurements. In Phase II, three of the best alloy compositions from Phase I were selected for scale-up and further microstructural and property evaluation. Mechanical testing in Phase II included tensile, notched tensile, fatigue, fracture toughness, creep and stress/rupture tests.

2.2 Program Plan

A flow diagram for the program is shown in Figure 2-1. The general program plan allowed for the study of combined alloying effects through an iterative process as well as detailed mechanical property evaluation that was accomplished after alloy scale-up in Phase II.

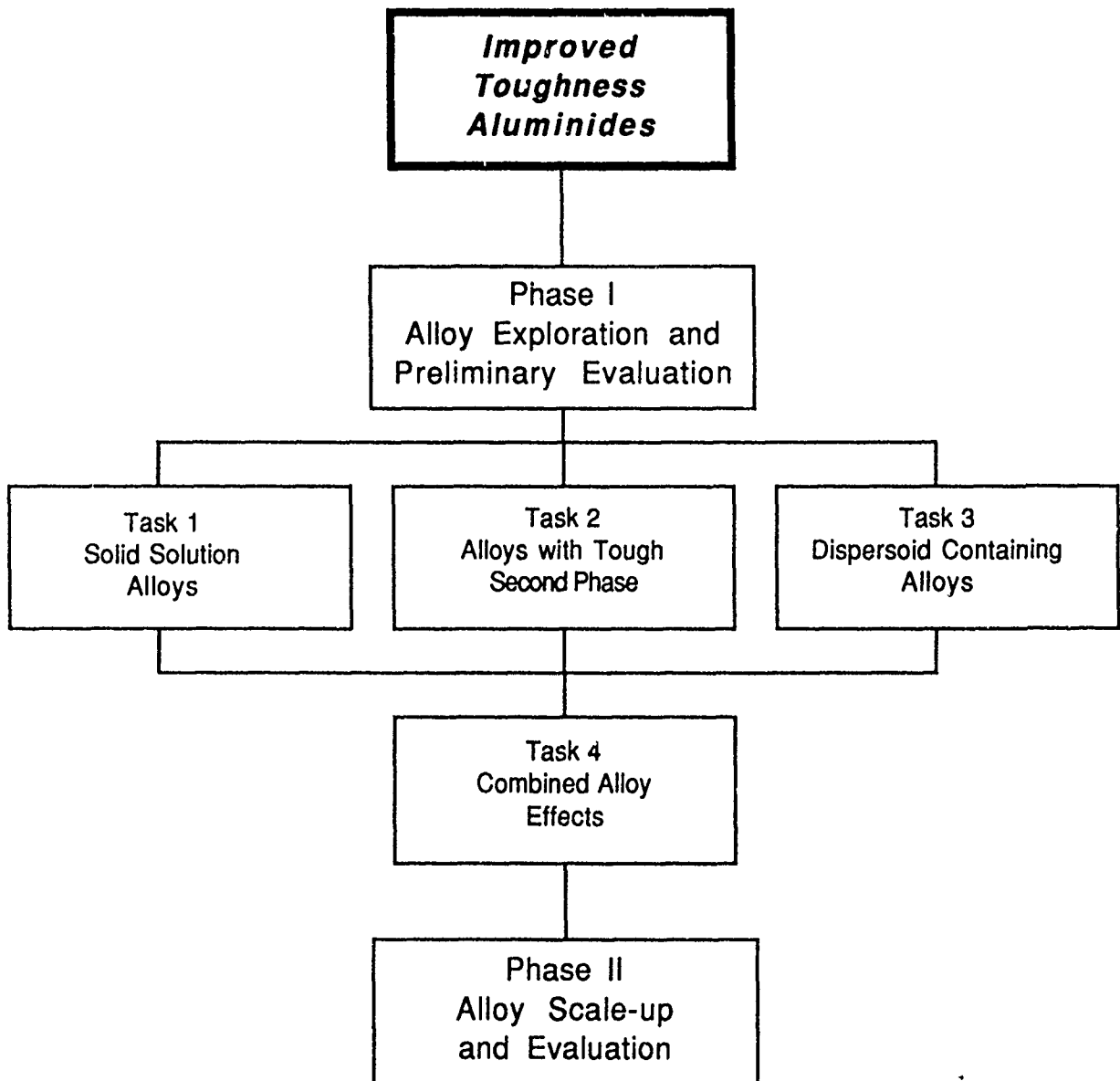


Figure 2-1 Flow diagram of overall program.

2.2.1 Phase I - Alloy Exploration and Preliminary Evaluation

The prime objective in Phase I was to identify alloying techniques which: 1) increase low temperature $c+a/2$ slip, 2) disperse planar α slip bands, and/or 3) impede general crack propagation. For each alloy system, analytical electron microscopy (AEM) together with mechanical property testing were the prime evaluation techniques. These studies were augmented by heat treatment and thermomechanical processing to define microstructure/property relationships and operative toughening mechanisms. Scanning electron microscopy (SEM) was used to determine the fracture mode of selected test specimens.

In Task 1, the effect of solid solution alloying on the toughness and ductility of Ti_3Al was evaluated. The work in this task helped to define the inherent toughness limitation of the Ti_3Al matrix. In order to assure that any toughness improvements were the result of solid solution mechanisms, AEM and optical metallography were used to evaluate:

- $c+a/2$ dislocation mobility
- alpha-2 platelet morphology
- absence of second phase particles
- planarity and distribution of a slip.

Nine alloys were selected for this task based on the results of GE studies and those reported in the literature. Conventional ingot melting and extrusion were used for processing of these alloys. Mechanical testing of all Task 1 alloys included tensile testing at room temperature, 427°C (800°F), and 649°C (1200°F), fracture toughness testing at room temperature, and small strain compression testing at room temperature, 300°C (572°F), and 500°C (932°F).

In Task 2, Ti_3Al alloys containing a tough second phase were evaluated to determine the effects of the second phase on toughness, strength, and ductility. We believed that a tough second phase might contribute to measurable improvements in toughness and ductility. However, a central issue was the extent to which the second phase might reduce high temperature strength, creep and stress/rupture properties. Key variables which were evaluated with regard to their effects on properties include:

- mobility of $c+a/2$ dislocations within the alpha-2 matrix
- structure of the tough second phase (order-disorder)
- volume fraction of tough second phase
- general morphology effects.

Seven alloys were selected for this task. Melting, processing, and testing were carried out as in Task 1.

In Task 3, alloys containing dispersoids were evaluated to determine the effect of the dispersoids on toughness. We believed that in addition to their potential benefit on toughness, the dispersoid might also improve the strength of the alloy over the entire range of operating temperatures. A few of the key features evaluated in this task include:

- volume fraction of dispersoid
- influence of matrix additions on dispersoid stability
- influence of processing and consolidation on dispersoid size/distribution
- dispersoid-dislocation interaction.

Six alloys were selected for this task. Each of the alloys was rapidly solidified in powder form by centrifugal atomization and the powder consolidated by extrusion. Microstructures were evaluated in the atomized, consolidated, and heat treated condition. Mechanical testing was carried out as in Task 1.

Based on the results of Tasks 1, 2, and 3, eight alloys were formulated, produced, and evaluated in Task 4. The goal of this task was to produce a balanced alloy system which achieved improved toughness with little or no sacrifice in other properties. Non-consumable arc-melting and extrusion were used to produce the Task 4 materials. Heat treatment studies were performed to obtain desired microstructure/property relationships. Microstructural and mechanical evaluations followed the schedule used for Tasks 1, 2, and 3 except that creep and stress/rupture testing were substituted for compression testing and deformation analysis.

2.2.2 Phase II - Alloy Scale-up

Based on the results of Phase I studies, three alloys were scaled-up for extensive evaluation and mechanical property characterization. The selected alloys were melted and processed using conventional ingot metallurgy. A thorough heat treatment study was conducted and chemical analysis and optical metallography were used to characterize the alloys. When justified, detailed AEM was used to more fully define structural details. The mechanical testing program for the Phase II alloys is outlined in Table 2-1.

Table 2-1 Mechanical Testing Program for Phase II

Test Type	Test Temperature°C (°F)	No. of Test Per Alloy
Tensile	RT, 204(400), 430(800), 540(1000) 650(1200), 760(1400)	12
Creep	540(1000), 650(1200), 760(1400)	6
Stress/Rupture	540(1000), 650(1200), 760(1400)	3
LCF	RT, 204(400), 430(800), 650(1200) 760(1400)	16
Toughness	RT, 204(400), 430(800), 650(1200) 760(1400)	6
Thermal Stability (Tensile)	RT, 430(800), 650(1200)	4
Notched Tensile	RT, 430(800), 650(1200)	<u>4</u>
	Total Tests	51

3.0 RESEARCH AND DEVELOPMENT

3.1 Phase I: Alloy Exploration

Alloy exploration was conducted in three initial tasks based on 1) solid solution strengthening, 2) alloying to produce tough second phase, and 3) dispersoid containing alloys. These tasks were followed by a fourth in which the methodologies developed in the first three tasks were combined to make use of additive and/or synergistic effects.

3.1.1 Task 1 - Solid Solution Alloys

A total of nine single phase alloys were formulated to study the affects of solid solution alloying on alpha-2 titanium aluminide alloys. These alloys are listed in Table 3-1. Since the ductilizing effect of Nb has been well documented[2-5], Nb was included in all compositions at a constant level of five atom percent. In addition, the variation of Al level was tested with Ti-20Al-5Nb-5Ga (IT-1) and Ti-25Al-5Nb-5Ga (IT-2). Other elements such as Ga, Sn, Ta, Mo, Cr, and Zr were added in an effort to identify whether these additions influence the deformation behavior of the material. Both Ga and Ta have been shown to raise the c/a ratio of the superlattice closer to unity [6] and several alloys were formulated to determine whether this has a beneficial affect on deformation behavior. The beta stabilizers Nb, Ta, Mo, and Cr are known to be effective additions for the refinement of the alpha-2 platelet size in the transformed beta. This refined microstructural condition could be beneficial to both ductility and toughness.

3.1.1.1 Processing and Heat Treatment

The Task 1 compositions were approved by the contracting officer (CO) and 6.8 kg (15 lb) ingots of each alloy were double melted by vacuum arc remelting (VAR) at the RMI Company. Each ingot was then machined to fit inside a Ti-64 can for subsequent extrusion. Prior to extrusion, the ingots measured approximately 108 mm (4.25 in) in diameter and 125 mm (5 in) in length.

Extrusion temperatures were chosen within the alpha-2 plus beta phase field in an effort to produce refined microstructures. Internally funded work at GEAE which was performed prior to this contract effort indicated that microstructural refinement could benefit both fracture toughness and ductility. In this internally funded work, Ti-24Al-11Nb material was processed by extrusion both above and below the beta transus temperature. A refined microstructure, in which both the prior beta grain size and the size of the alpha-2 transformation product were reduced, was developed in the material which was processed below the beta transus temperature. This refined microstructure was heat treated to maintain a fine distribution of equiaxed primary alpha-2 grains and small prior beta grains which consisted of fine acicular alpha-2 platelets within a near-continuous beta matrix. The beta processed material was heat treated above the beta transus temperature to produce a Widmanstatten microstructure of alpha-2 platelets within large prior beta grains. Room temperature tensile test results for the two microstructural conditions revealed that the material with a refined microstructure reached a plastic elongation of 3.3% while the material with a fully transformed beta microstructure and large prior beta grain size failed after 2.2% plastic elongation. In addition, yield strengths and rupture live for the two microstructural conditions were nearly equivalent. Due to the increased ductility associated with microstructural refinement, it was determined that refined microstructures should be produced whenever possible in this program. As such, it would be possible to explore both the effects of alloy composition and microstructural refinement on the fracture toughness of alpha-2 titanium aluminides.

Table 3-1 Compositions of Task 1 Alloys*

Alloy	Ti	Al	Nb	Ta	Ga	Mo	Other	O
IT-1	70.0 [71.2]	20.0 [11.5] (12.9)	5.0 [9.9] (9.5)		5.0 [7.4] (6.3)			(0.093)
IT-2	65.0 [67.6]	25.0 [14.7] (15.6)	5.0 [10.1] (11.4)		5.0 [7.6] (6.9)			(0.100)
IT-3	70.0 [67.7]	20.0 [10.9] (12.4)	5.0 [9.4] (8.8)				5.0 Sn [12.0 Sn] (11.8 Sn)	(0.155)
IT-4	70.0 [69.5]	20.0 [11.2] (11.0)	5.0 [9.6] (8.9)		2.5 [3.6] (3.5)		2.5 Sn [6.1 Sn] (6.2 Sn)	(0.116)
IT-5	69.0 [72.8]	25.0 [14.9] (14.2)	5.0 [10.2] (11.0)			1.0 [2.1] (2.2)		(0.094)
IT-6	69.0 [73.5]	25.0 [15.0] (15.2)	5.0 [10.3] (9.8)				1.0 Cr [1.2 Cr] (1.1 Cr)	(0.084)
IT-7	60.0 [58.4]	25.0 [13.7] (14.6)	5.0 [9.4] (9.7)				10.0 Zr [18.5 Zr] (17.0 Zr)	(0.086)
IT-8	69.0 [70.8]	22.0 [12.7] (14.0)	5.0 [9.9] (9.9)		3.0 [4.5] (4.3)	1.0 [2.1] (2.2)		(0.074)
IT-9	68.0 [66.6]	22.0 [12.2] (12.5)	5.0 [9.5] (9.4)	2.0 [7.4] (7.1)	3.0 [4.3] (3.8)			(0.122)

* The compositions which are not enclosed in brackets are aim atom percents, compositions enclosed by [] are aim weight percents, and compositions enclosed by () are measured weight percents.

All nine solid solution alloys were extruded successfully at the RMI Company. The extrusion ratio was held constant at roughly 21:1, the ram speed was approximately 2.5 cm (1 in) per second and extrusion temperatures were varied as shown in Table 3-2. These extrusion temperatures were selected after predicting beta transus temperatures [7] and assuming that extrusion must be carried out at least 30 to 85°C (50 to 150°F) below the beta transus temperature to produce a refined microstructure. After extrusion, a heat treatment matrix was established over a temperature range of 1050 to 1330°C (1925 to 2425°F) to experimentally determine the beta transus temperatures. The results from the beta transus studies are presented in Table 3-2. In addition to beta transus determination, heat treatments which produced refined microstructures containing a small fraction of primary alpha-2 were identified when possible.

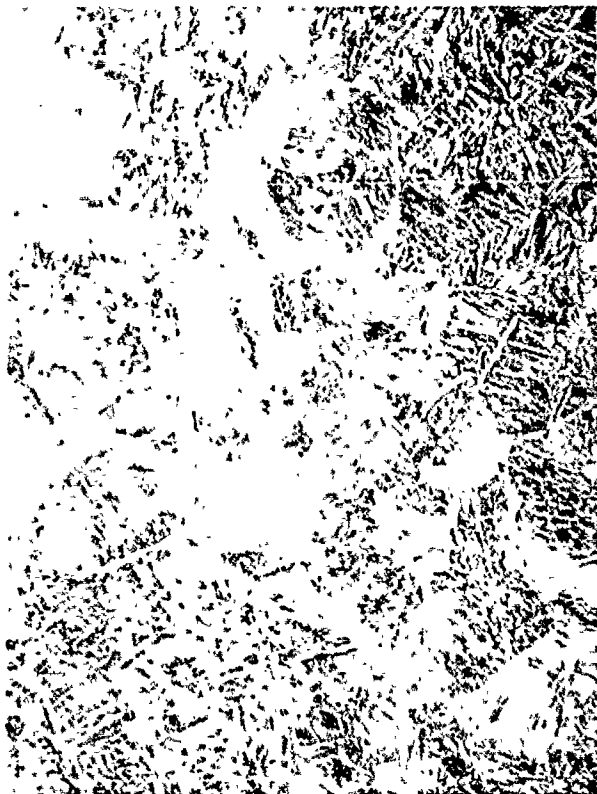
Review of the as-extruded microstructures indicated that the desired microstructural refinement produced by extrusion in the alpha-2 plus beta phase field is only accomplished when the extrusion temperature is well below the beta transus temperature. It is evident that a significant amount of adiabatic heating occurs during the extrusion process. While it is possible that the amount of adiabatic heating could vary both radially and from tip to tail of the extrusion, little evidence of this was found in the Task 1 extrusions. Although it is clear that extrusion must be carried out more than 55°C (100°F) below the beta transus temperature in order to induce microstructural refinement when using an extrusion ratio of 21:1 and ram speed of approximately 2.5 cm (1 in) per second, more detailed studies would be required to determine the ideal extrusion parameters for each specific alloy.

Several examples of the as-extruded microstructures are shown in Figure 3-1. The post-extrusion microstructure of Ti-22Al-5Nb-3Ga-2Ta (IT-9), shown in Figure 3-1a, was not sufficiently refined although its pre-extrusion temperature was 55°C (100°F) below its beta transus temperature. The alloy Ti-25Al-5Nb-1Mo (IT-5) which was extruded 100°C (180°F) below its beta transus temperature was refined to the most significant extent of all of the Task 1 alloys as shown in Figure 3-1b. The alloy Ti-20Al-5Nb-5Sn (IT-3) which was extruded more than 140°C (250°F) below the beta transus temperature and is shown in Figure 3-1c maintained a heavily worked alpha-2 microstructure. After subsequent heat treatments below the beta transus temperature, the microstructure of Ti-20Al-5Nb-5Sn (IT-3) recrystallized to form a reasonably refined microstructure.

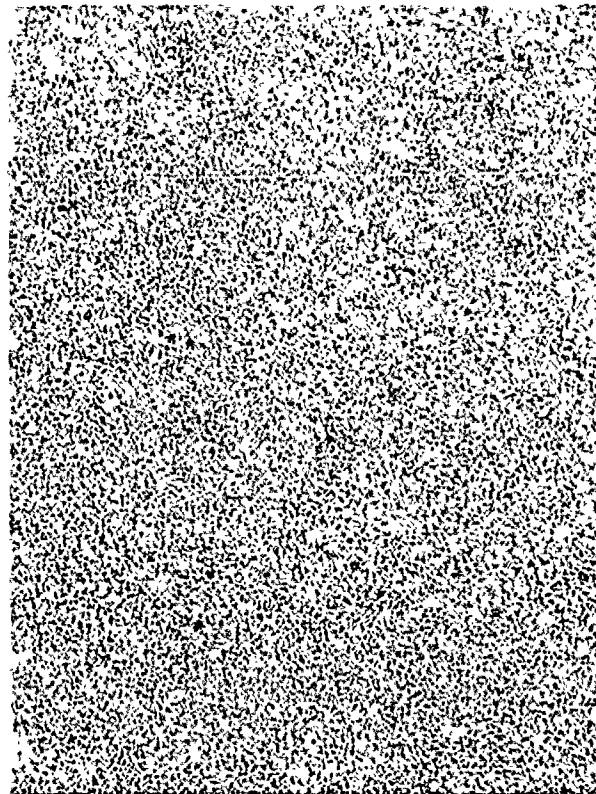
The microstructures of the Task 1 alloys following final heat treatment are shown in Figure 3-2 through 3-4. For the overall screening of mechanical properties of the Task 1 alloys, heat treatments were conducted below the beta transus temperature. For the alloys Ti-25Al-5Nb-1Mo (IT-5) and Ti-22Al-5Nb-3Ga-1Mo (IT-8), the aim microstructure which consisted of fine equiaxed primary alpha-2 grains and small prior beta grains was successfully produced as shown in Figures 3-3b and 3-4b, respectively. For many of the other Task 1 alloys, the previously discussed adiabatic heating during the extrusion process made it impossible to produce the aim microstructure. Nevertheless, heat treatments were conducted below the beta transus temperature to inhibit excessive growth of the prior beta grains.

Table 3-2 Extrusion and Beta Transus Temperatures for Task 1 Alloys

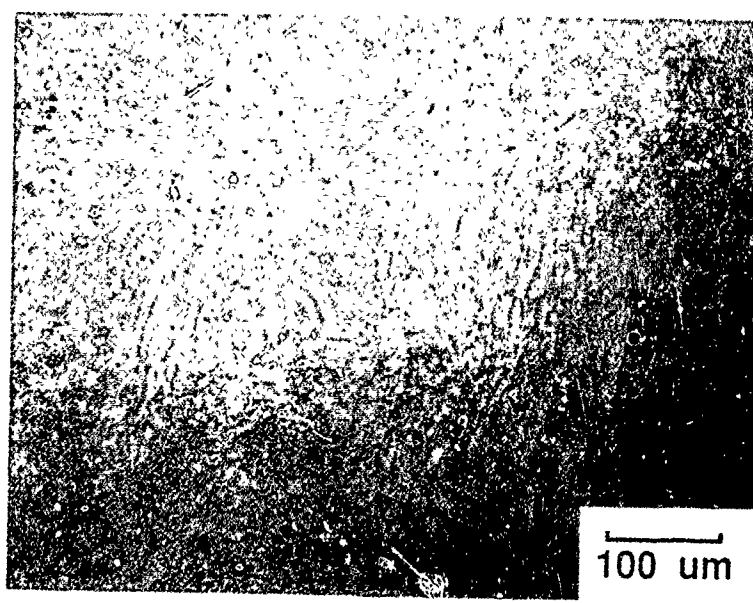
Alloy	Extrusion Temperature (°C)	Extrusion Temperature (°F)	Beta Transus Temp. (°C)	Beta Transus Temp. (°F)	Temperature Difference (°C)	Temperature Difference (°F)
IT-1	1120	2050	1150	2100	30	50
IT-2	1175	2150	1205	2200	30	50
IT-3	1175	2150	>1315	>2400	>140	>250
IT-4	1175	2150	1215	2225	40	75
IT-5	1065	1950	1165	2125	100	180
IT-6	1120	2050	1150	2100	30	50
IT-7	1065	1950	1080	1975	15	25
IT-8	1065	1950	1150	2100	85	150
IT-9	1120	2050	1175	2150	55	100



(a)



(b)



(c)

Figure 3-1 As-extruded microstructures of alloys (a) Ti-22Al-5Nb-3Ga-2Ta (IT-9), (b) Ti-25Al-5Nb-1Mo (IT-5) and (c) Ti-20Al-5Nb-5Sn (IT-3).

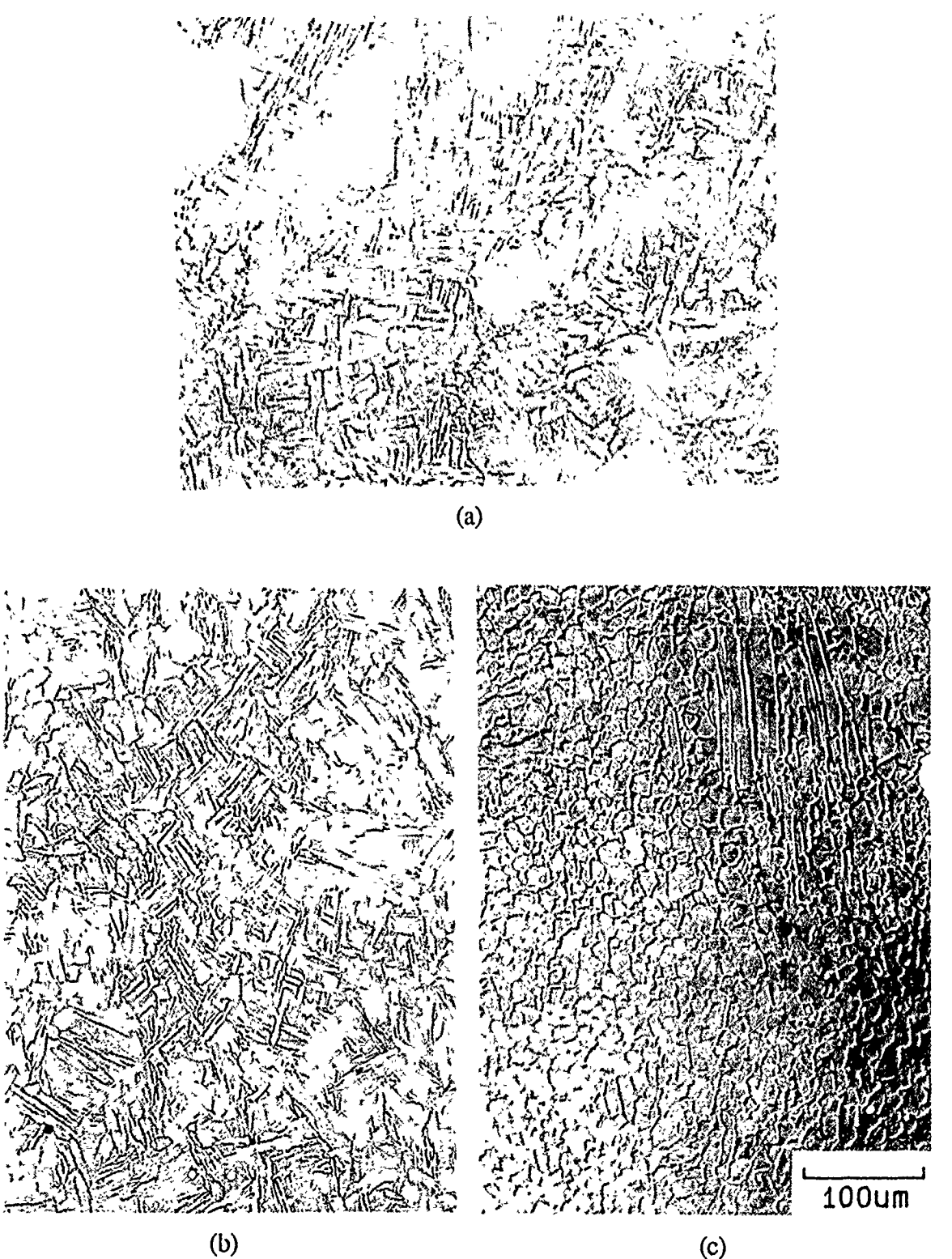


Figure 3-2 Optical micrographs of (a) Ti-20Al-5Nb-5Ga (IT-1) heat treated at 1135°C (2075°F), (b) Ti-25Al-5Nb-5Ga (IT-2) heat treated at 1177°C (2150°F) and (c) Ti-20Al-5Nb-5Sn (IT-3) heat treated at 1315°C (2400°F).

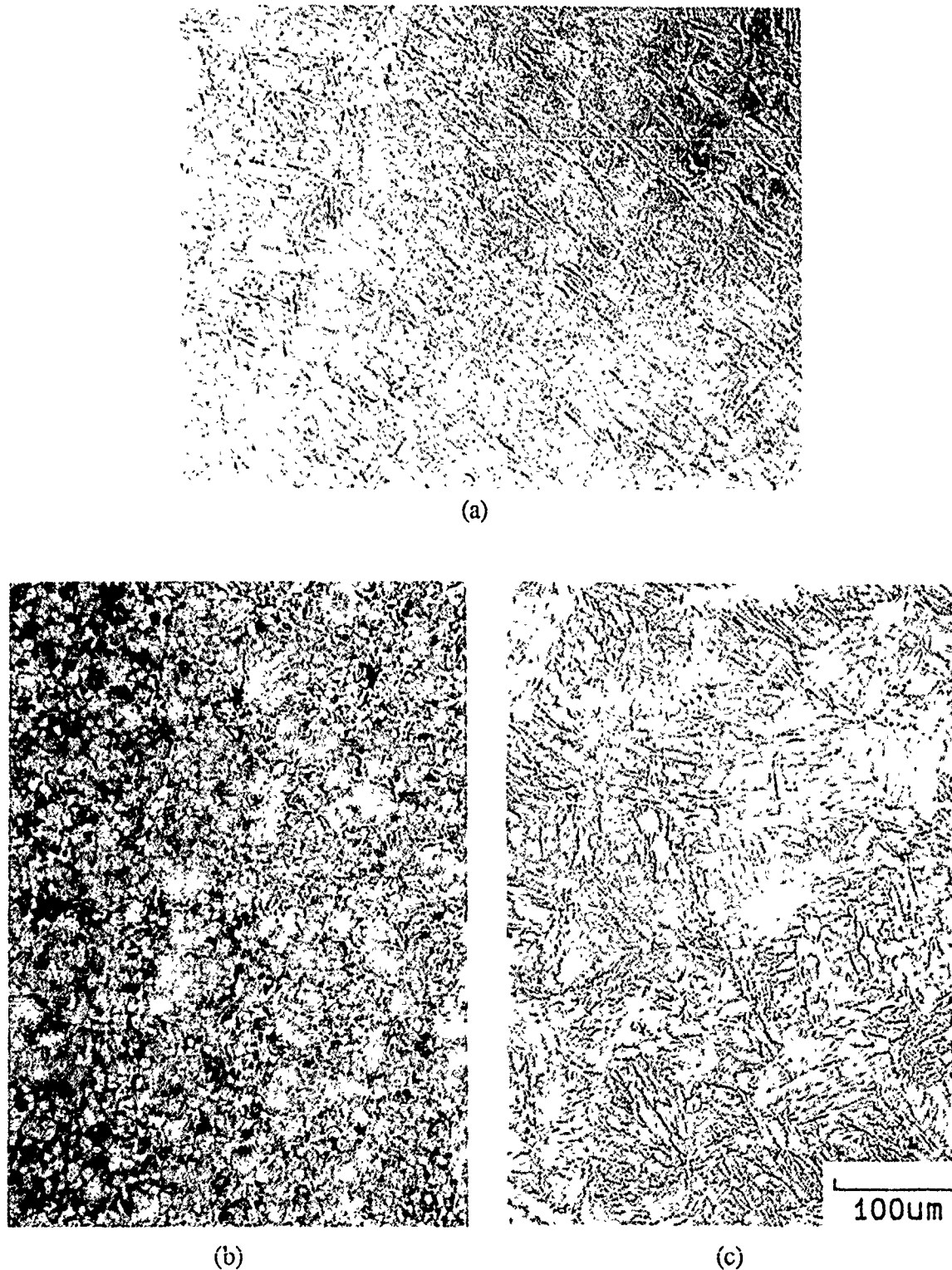


Figure 3-3 Optical micrographs of (a) Ti-20Al-5Nb-2.5Ga-2.5Sn (IT-4) heat treated at 1205°C (2200°F), (b) Ti-25Al-5Nb-1Mo (IT-5) heat treated at 1135°F (2075°F) and (c) Ti-25Al-5Nb-1Cr (IT-6) heat treated at 1135°C (2075°F).

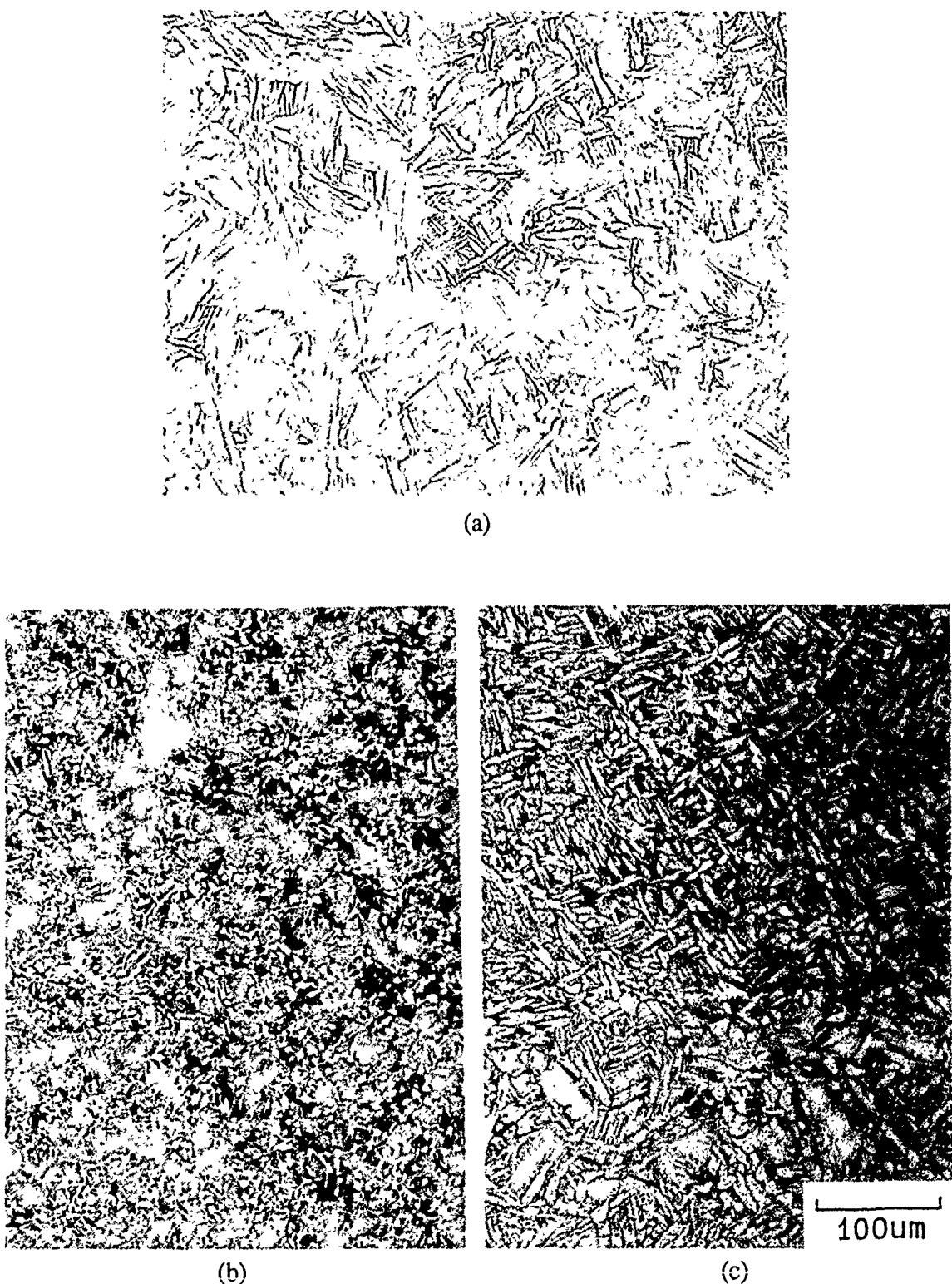


Figure 3-4 Optical micrographs of (a) Ti-25Al-5Nb-10Zr (IT-7) heat treated at 1070°C (1960°F), (b) Ti-22Al-5Nb-3Ga-1Mo (IT-8) heat treated at 1121°C (2050°F) and (c) Ti-22Al-5Nb-3Ga-2Ta (IT-9) heat treated at 1165°C (2125°F).

3.1.1.2 Mechanical Testing

Mechanical testing of all Task 1 alloys included tensile testing at room temperature, 427°C (800°F), and 649°C (1200°F), fracture toughness testing at room temperature, and small strain compression testing at room temperature, 300°C (572°F), and 500°C (932°F). The tensile specimens were machined with 1.27 cm (0.5 in) diameter threaded ends and a 3.18 cm (1.25 in) by 0.64 cm (0.25 in) diameter gage section. The fracture toughness specimens were 5.08 cm (2.0 in) long, 0.51 cm (0.2 in) wide, and 1.02 cm (0.4 in) deep with a 0.51 cm (0.2 in) notch which was not fatigue precracked prior to testing. The compression specimens were cylindrical in shape with a 0.64 cm (0.25 in) diameter and 1.91 cm (0.75 in) length.

Tensile tests were conducted at a cross head rate of 0.005 in/min through the 0.2% yield strength and then maintained at a cross head rate of 0.05 in/min through failure. Since the accuracy of measuring ductility from the change in length of broken test specimens is known to be limited for materials with low ductility, extensometers were kept in place until failure for room temperature tensile tests. Plastic deformation was then measured from load vs strain curves. The tensile test results are summarized in Table 3-3.

The tensile test results indicate that both strength and ductility are low for all of the solid solution alloy compositions. The alloys Ti-25Al-5Nb-1Mo (IT-5) and Ti-22Al-5Nb-3Ga-1Mo (IT-8) were shown to have the highest ductility across the range of test temperatures. The aim microstructure was obtained for these alloys and subsequent testing would show that the increase in ductility was due to the microstructural condition rather than chemical composition. The test results for Ti-20Al-5Nb-5Sn (IT-3) identified extremely poor ductility but the unusually high oxygen content of 0.155 weight percent may have had a significant effect on this result. For these solid solution strengthened alloys, one way to consider the results is to compare the alloys on the basis of 'effective' Al levels (Al + Ga + Sn). None of the Task 1 alloys had 'effective' Al levels below 25 atom percent, a level shown in later tasks to have an affect on room temperature ductility. The variation of Al content between Ti-20Al-5Nb-5Ga (IT-1) and Ti-25Al-5Nb-5Ga (IT-2) did not result in significant variation in ductility at RT, but at elevated temperatures, the alloy with a lower 'effective' Al level was shown to have higher ductility. In general, it is difficult to conclude from these results that either the quaternary alloying additions or variation of Al level caused any significant improvement of the room temperature tensile properties of single phase alpha-2 titanium aluminide alloys.

Duplicate fracture toughness specimens (notched but not fatigue precracked) of each of the Task 1 alloy were tested at room temperature. These three point bend tests were conducted as specified by ASTM E399 using a loading rate of 454 kg (1000 lb) per minute. Since the specimens were not fatigue precracked, valid K_{IC} measurements were not obtained. However, the fracture toughness specimens for Tasks 1 through 4 were manufactured and tested in the same manner such that relative identification of alloying effects on fracture toughness were made possible. The $K_{experimental}$ values were calculated and are given in Table 3-4.

Fractographic analyses were conducted on selected bend test specimens to aid in identifying the influence of composition and microstructure on fracture behavior. A comparison of Ti-20Al-5Nb-5Ga (IT-1) (test specimen A - 23.3 MPa \sqrt{m} (21.2 ksi \sqrt{in})) and Ti-25Al-5Nb-5Ga (IT-2) (test specimen B - 12.1 MPa \sqrt{m} (11.0 ksi \sqrt{in})) reveals that, although the fracture mode, cleavage through alpha-2 colonies, was the same for both specimens, specimen IT-1A had a much rougher fracture surface, as shown in Figure 3-5a and b. There was considerably more tearing between alpha-2 colonies in specimen IT-1A than in specimen IT-2B. Microstructural analysis indicated that some beta phase existed

between alpha-2 platelets in Ti-20Al-5Nb-5Ga (IT-1), but Ti-25Al-5Nb-5Ga (IT-2) contained only alpha-2 platelets separated by a grain boundary alpha-2 phase. Therefore, beta phase appears to have provided some resistance to crack propagation, resulting in a higher measured fracture toughness for Ti-20Al-5Nb-5Ga (IT-1).

Comparison of Ti-22Al-5Nb-3Ga-1Mo (IT-8) and Ti-20Al-5Nb-5Ga (IT-1), which had the highest fracture toughness values of the Task 1 alloys, shows cleavage through alpha-2 colonies as the primary fracture mode. The alloy Ti-22Al-5Nb-3Ga-1Mo (IT-8) has a smaller alpha-2 colony size than Ti-20Al-5Nb-5Ga (IT-1), hence there are more changes in crack propagation direction in the former, as shown in Figure 3-5a and c. The alloy Ti-22Al-5Nb-3Ga-1Mo (IT-8), like Ti-20Al-5Nb-5Ga (IT-1), contains beta phase between alpha-2 platelets and colonies which has provided resistance to fracture. There are small amounts of secondary cracking, primarily along colony boundaries, in both Ti-20Al-5Nb-5Ga (IT-1) and Ti-22Al-5Nb-3Ga-1Mo (IT-8) bend test specimens.

A correlation between fracture toughness and ductility can be made only to a small extent. The alloys Ti-25Al-5Nb-5Ga (IT-2) and Ti-20Al-5Nb-5Sn (IT-3) which showed no evidence of plastic elongation during tensile testing also demonstrated the lowest fracture toughness test results with the exception of one specimen of Ti-25Al-5Nb-1Mo (IT-5). The two test specimens of Ti-25Al-5Nb-1Mo (IT-5) showed widely different fracture toughness values, but fractographic examination of both specimens revealed remarkably similar fracture surfaces. The fracture mode was cleavage through alpha-2 colonies with tearing through the beta phase between colonies, as shown in Figure 3-6. The large difference in fracture toughness for the two Ti-25Al-5Nb-1Mo (IT-5) specimens may have been due to a test anomaly. Aside from the fracture toughness values for Ti-25Al-5Nb-5Ga (IT-2), Ti-20Al-5Nb-5Sn (IT-3) and Ti-25Al-5Nb-1Mo (IT-5), the test results varied from 15.1 MPa $\sqrt{\text{m}}$ (13.7 ksi $\sqrt{\text{in}}$) to 24.6 MPa $\sqrt{\text{m}}$ (22.4 ksi $\sqrt{\text{in}}$) with no apparent relationship to the ductility of the alloy. The fracture toughness of Ti-20Al-5Nb-5Ga (IT-1) was among the best recorded for the Task 1 alloys even though its tensile ductility was only 0.1% plastic elongation.

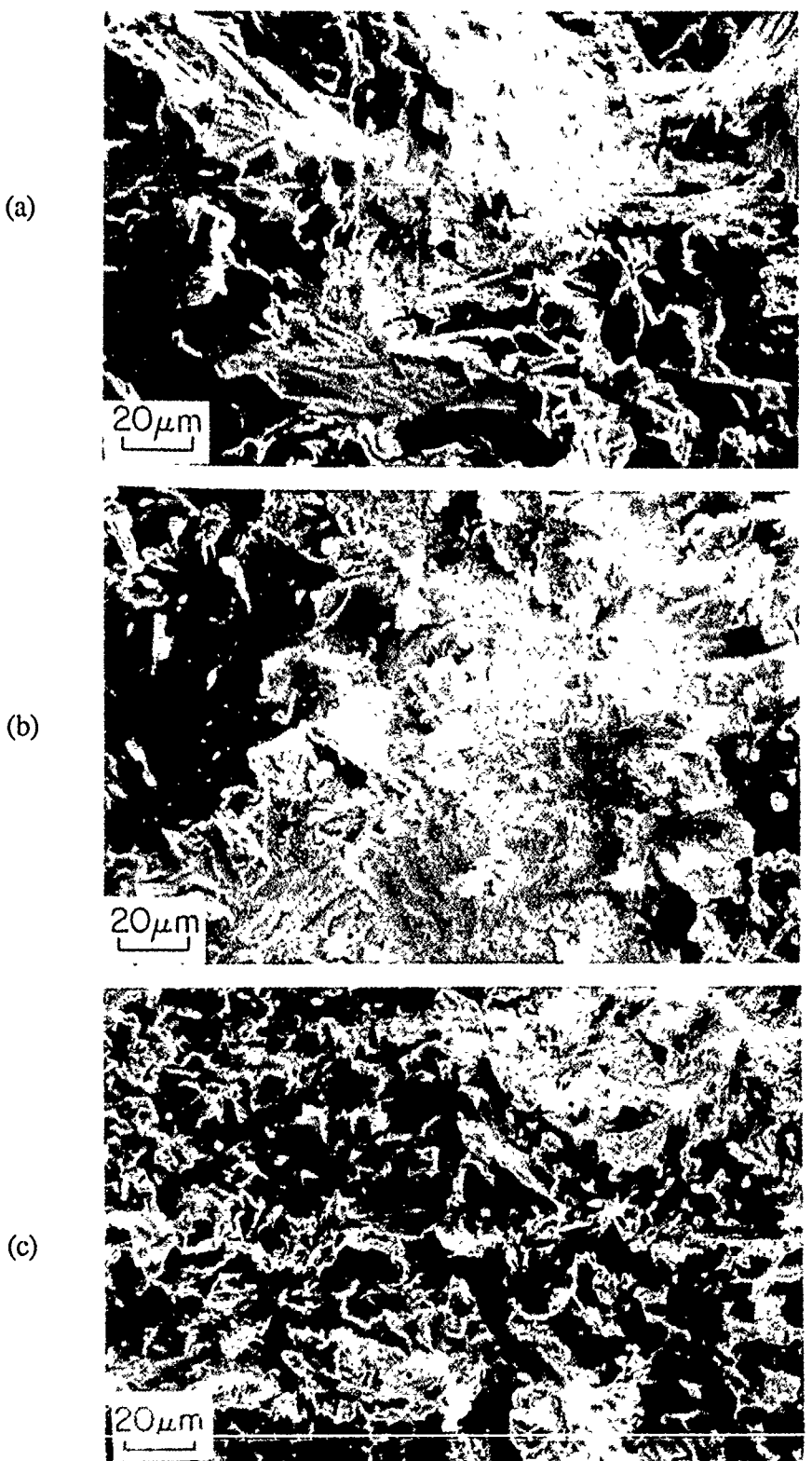


Figure 3-5 Fracture surfaces of bend test specimens of (a) alloy Ti-20Al-5Nb-5Ga (IT-1) (23.3 MPa \sqrt{m} (21.2 ksi \sqrt{in})), (b) alloy Ti-25Al-5Nb-5Ga (IT-2) (12.1 MPa \sqrt{m} (11.0 ksi \sqrt{in})), (c) alloy Ti-22Al-5Nb-3Ga-1Mo (IT-8) (24.6 MPa \sqrt{m} (22.4 ksi \sqrt{in})).

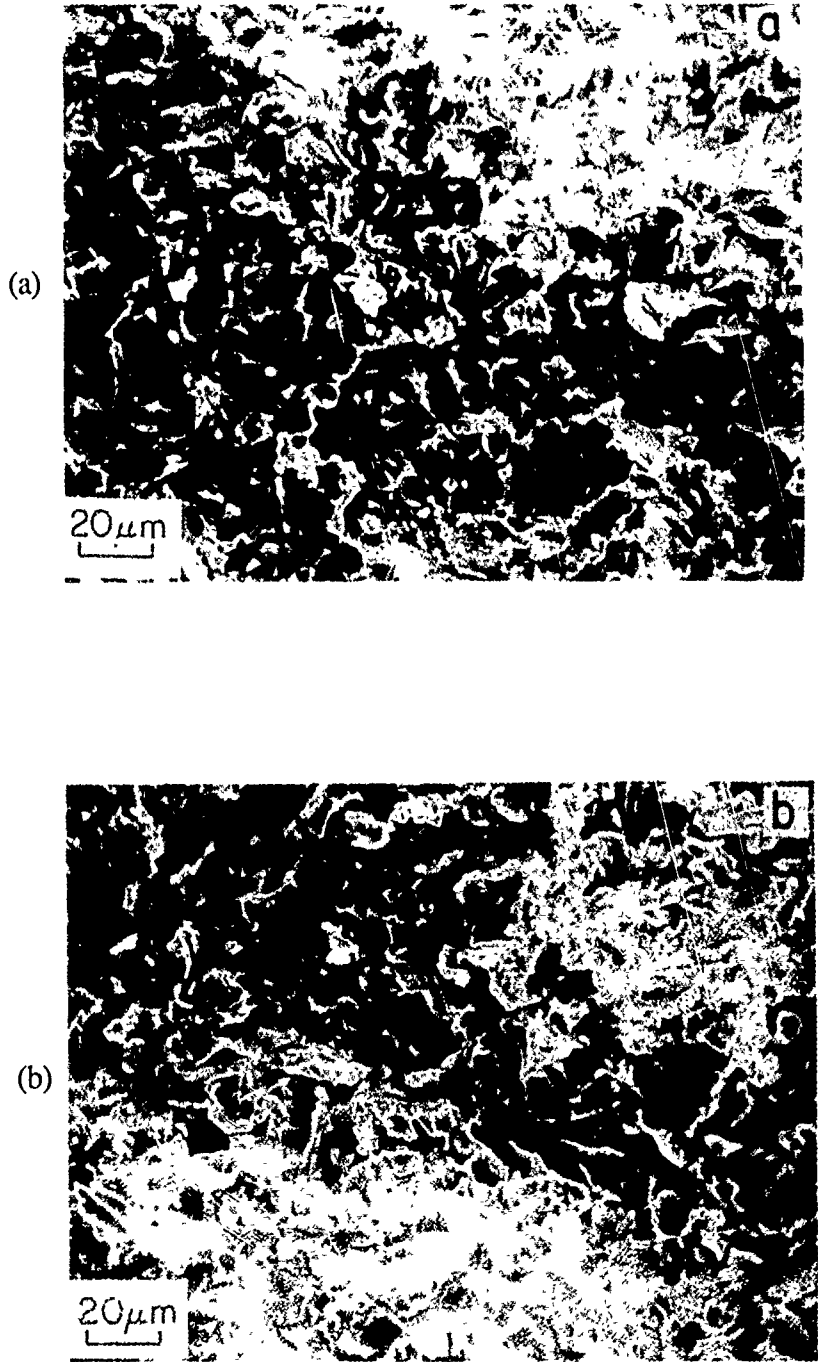


Figure 3-6 Fracture surfaces of alloy Ti-25Al-5Nb-1Mo (IT-5) bend test specimens with fracture toughness values of (a) $20.3 \text{ MPa}\sqrt{\text{m}}$ ($18.5 \text{ ksi}\sqrt{\text{in}}$) and (b) $8.5 \text{ MPa}\sqrt{\text{m}}$ ($7.7 \text{ ksi}\sqrt{\text{in}}$).

Table 3-3 Tensile Properties of Task 1 Alloys

Alloy	Temperature (°C)	Temperature (°F)	UTS (MPa)	UTS (ksi)	0.2 YS (MPa)	0.2 YS (ksi)	EL (%)	RA (%)
IT-1	24	75	788	114.4		(a)	0.1	0.0
	24	75	706	102.4		(a)	0.1	0.2
	427	800	743	107.9	562	81.6	2.5	3.3
	649	1200	602	87.4	428	62.1	5.3	10.9
IT-2	24	75	487	70.7		(a)	0.0	0.0
	24	75	542	78.7		(a)	0.0	0.2
	427	800	580	84.2	472	68.5	0.5	1.2
	649	1200	601	87.2	459	66.6	0.4	2.5
IT-3	24	75	87	12.6		(a)	0.0	(b)
	24	75	404	58.7		(a)	0.0	(b)
	427	800	517	75.1		(a)	0.0	0.0
	649	1200	491	71.3	418	60.6	1.2	2.5
IT-4	24	75	638	92.6	626	90.9	0.2	0.4
	24	75	645	93.6	634	92.0	0.2	1.0
	427	800	558	81.0	397	57.6	3.2	5.3
	649	1200	490	71.0	308	44.7	6.7	11.2
IT-5	24	75	818	118.7	728	105.7	0.9	2.0
	24	75	833	120.9	765	111.1	0.5	1.5
	427	800	837	121.5	493	71.6	9.3	11.1
	649	1200	607	88.1	394	57.2	10.6	15.1
IT-6	24	75	584	84.7		(a)	0.1	0.0
	24	75	621	90.1		(a)	0.1	0.8
	427	800	588	85.4	464	67.3	0.4	2.5
	649	1200	604	87.7	384	55.8	4.3	10.3
IT-7	24	75	914	132.6	810	117.5	0.8	0.4
	24	75	619	89.8	589	85.5	0.3	0.2
	427	800	904	131.2	602	87.4	6.1	8.4
	649	1200	697	101.2	438	63.6	4.5	8.6
IT-8	24	75	814	118.1	653	94.8	1.2	1.4
	24	75	781	113.4	651	94.5	1.1	1.8
	427	800	783	113.6	449	65.2	8.9	10.5
	649	1200	589	85.5	369	53.6	13.3	19.5
IT-9	24	75	679	98.6		(a)	0.2	0.0
	24	75	711	103.2		(a)	0.2	0.7
	427	800	699	101.5	475	69.0	2.4	5.2
	649	1200	573	83.2	406	58.9	4.6	10.0

(a) Specimen failed prior to 0.2% yield.

(b) Specimen failed in threaded region.

Table 3-4 Room Temperature Toughness of Task 1 Alloys

Alloy	K_{exp} (MPa·m ^{1/2})	K_{exp} (ksi·in ^{1/2})
IT-1	23.3 22.9	21.2 20.8
IT-2	12.1 Void Test	11.0 Void Test
IT-3	11.5 9.2	10.5 8.4
IT-4	16.7 16.2	15.2 14.7
IT-5	20.3 8.5	18.5 7.7
IT-6	15.9 15.1	14.5 13.7
IT-7	19.1 19.1	17.4 17.4
IT-8	24.6 20.6	22.4 18.7
IT-9	16.8 20.2	15.3 18.4

3.1.1.3 Analysis of Deformation Structures

Compression specimens were tested to approximately 2% plastic strain at RT, 300°C (570°F), and 500°C (930°F) prior to sectioning for AEM analysis. These specimens were prepared in an effort to determine the effect of alloying additions and temperature on the intrinsic slip mechanisms of alpha-2 titanium aluminide alloys. To accomplish this, it was necessary to determine the orientation of the stress axis with respect to the grain which was being analyzed in the AEM. Ideally, this study would have been conducted with single crystals but these would have been very difficult to grow for the Task 1 alloys and virtually impossible for the Task 2 and 3 alloys which were designed to have additional phases present. The following paragraphs describe the analytical techniques which were developed for Task 1, 2 and 3 alloys. The specific results for each Task will be described subsequently.

AEM Procedure

A technique was established for evaluating deformation behavior in polycrystalline samples. This technique involved sectioning the compression specimens longitudinally by diamond saw as shown schematically in Figure 3-7. The slices were ground down to 150 microns (6 mils) with the final grinding marks parallel to the stress axis. TEM disks were electro-discharge machined out of the central region of these slices, electropolished in a standard fashion, and mounted in a TEM tilt-rotate specimen holder with the grinding marks perpendicular to the rod axis. The last operation was performed with the specimen holder mounted on an optical microscope with a cross-hair reticule in the eyepiece set parallel to one edge of the specimen holder. The specimen was clamped in the holder and the specimen cup was then rotated until the grinding marks visible on the unpolished rim of the specimen were aligned with the reticule normal. The specimens were placed in the electron microscope and each region examined by convergent beam electron diffraction until an alpha-2 grain could be found with its c axis within 15° of the compression axis. The specimen misorientation was determined using computer driven deflection of the selected area electron diffraction pattern to measure the displacement and rotation of the (0002) g vector.

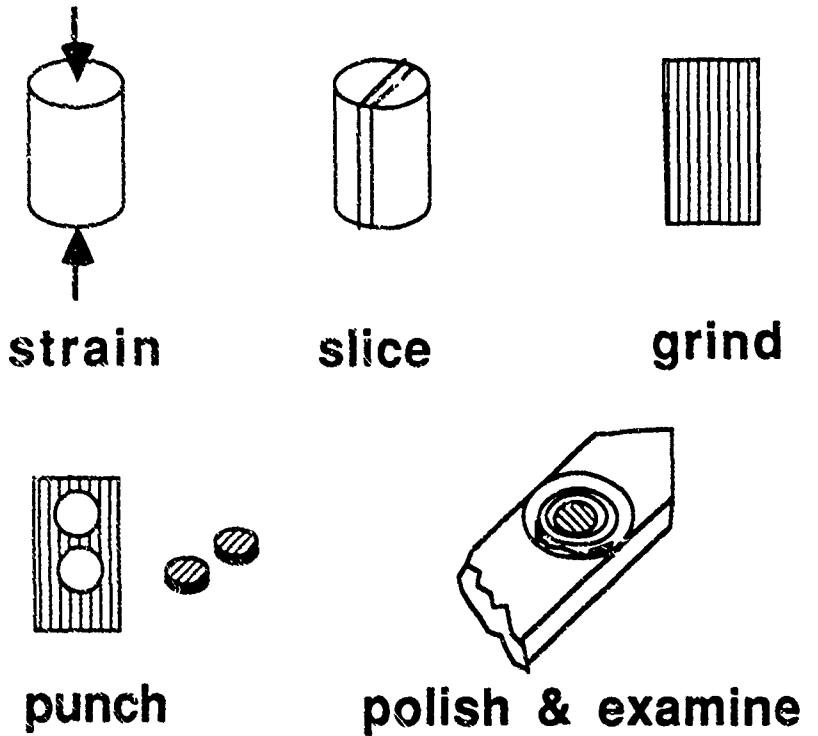


Figure 3-7 Schematic diagram of specimen preparation procedure.

The arbitrary angle of 15° had been chosen on the basis of Schmid factor calculations for a Burgers vector slip on basal planes versus $c+a/2$ slip on both {2021} and {1121} pyramidal planes (Note: see Table 3-5 for a description of Miller-Bravais notation for alpha-2 versus alpha). While it is conceivable that $c+a/2$ slip could occur on {1010}, this has not been observed and is explained on the basis of a high Peierls stress due to the corrugated nature of these planes [8]. Assuming that the ratio of the critical resolved shear stress for $c+a/2$ slip to that for a slip is at least 2:1, as found in alpha titanium [9], the locus of the transition from where $c+a/2$ slip would be expected to that where a slip would be favored is a circle approximately 15° from the [0001]. Based upon the above assumption, $c+a/2$ slip would only be anticipated within this region of the stereographic projection. The probability of an alpha-2 grain having its c axis within this angular range can be computed as 0.034. For the case of randomly oriented primary alpha-2 grains, this result can be applied directly and would mean that an average of 29 alpha-2 grains would need to be examined to find one where $c+a/2$ slip could be expected. Any texture would affect this result but preliminary work on alloys of this type and similar processing condition have not shown any significant texture [10]. The situation with alpha-2 laths is somewhat different. In this case, the orientation of the alpha-2 is determined by that of the parent beta grain (which has a much higher symmetry). For a randomly oriented beta grain, the probability of a <110> zone being within 15° of the compression axis is six times higher (about 1 in 5). Since the basal planes of the alpha-2 have to be parallel to one of these <110>'s (because of the Burger's orientation relationship), the probability of a beta grain having a colony of alpha-2 with its basal plane within this range is also 1 in 5. While this does not improve the probability for any single lath or colony, the crystallographic relationship of alpha-2 laths simplifies the search for appropriately oriented colonies. If one colony is found to have its basal plane between 15 and 45° from the compression axis, no other colonies within that prior-beta grain will be oriented with their c axes within 15° of the compression axis.

Desirable Microstructure

The refined microstructure which was set as a goal for improved mechanical properties was also beneficial for dislocation analysis. A small volume fraction of primary alpha-2 inhibits beta grain growth and improves the probability of finding an alpha-2 colony of a suitable orientation. Also, the primary alpha-2 grains are preferable to colonies when performing trace analysis since they are generally wider than any laths. This increases the distance over which a slip trace can be measured, reduces the probability of intersecting slip systems confusing the analysis, and, perhaps most important of all, improves the ability to discriminate between true 'slip' dislocations and those that are 'grown-in' during the beta to alpha-2 phase transformation. This point will be discussed more fully later.

Although the desired microstructure was not achieved for a number of alloys, the post-extrusion heat treatments were still carried out in the alpha-2 plus beta field. As a result, additional beta grain growth was inhibited while a few larger alpha-2 platelets were preserved. Thus, whenever present, primary alpha-2 grains were used for dislocation analysis but, when they were absent, the larger alpha-2 colonies were analyzed.

Definition of Slip Systems

The objective of the dislocation analysis was to measure the abundance of $c+a/2$ slip, determine the operative slip planes, and see how both varied with alloy composition and deformation temperature. In the results which follow it is important that the reader be aware of those issues which were not addressed and some caveats about the inherent

limitations of the technique. For this reason we will describe the slip systems considered in our analysis.

The operative slip systems in alpha titanium alloys with \mathbf{a} and $\mathbf{c+a}$ Burgers vectors are listed in Table 3-5. Also listed are the corresponding slip systems for the $D0_{19}$ superlattice structure of alpha-2. Note that the correct nomenclature for $\mathbf{c+a}$ dislocations in alpha-2 is $\mathbf{c+a}/2[11]$.

Table 3-5. Alpha Slip Systems and Geometrically Equivalent Alpha-2 Indices

Alpha Burgers Vector	Slip Plane	Alpha-2 Burgers Vector	Slip Plane
$1/3 <11\bar{2}0>$	{0001} (10\bar{1}0) (10\bar{1}1)	$1/6 <11\bar{2}0>^*$	{0001} (10\bar{1}0) (20\bar{2}1)
$1/3 <11\bar{2}3>$	{11\bar{2}2} (10\bar{1}1)	$1/6 <11\bar{2}6>^*$	{11\bar{2}1} (20\bar{2}1)

* These will be superpartials

In Table 3-5, we assumed that the dislocations will slip on the equivalent planes with Burgers vectors of equal magnitude in both the disordered and ordered structures. The difference in the indices of the slip planes is brought about by the fact that the ordering occurs in only the basal plane so that the lattice parameter is doubled in the \mathbf{a} direction but is unchanged in the \mathbf{c} direction. For basal and prism planes the Miller-Bravais indices are unchanged; however, for pyramidal planes the following relationship holds:

$$(h k i l)_{\text{alpha}} = (2h 2k 2i l)_{\text{alpha-2}}$$

Thus $(11\bar{2}2)_{\text{alpha}}$ is equivalent to $(22\bar{4}2)_{\text{alpha-2}}$ which reduces to $(11\bar{2}1)_{\text{alpha-2}}$. The inverse is true for directions:

$$[u v t w]_{\text{alpha}} = 1/2[u v t 2w]_{\text{alpha-2}}$$

In this case, the Burgers vector $1/3[11\bar{2}3]_{\text{alpha}}$ equals $1/6[11\bar{2}6]_{\text{alpha-2}}$. Of course, perfect dislocations (with an \mathbf{a} component) in alpha become superpartial dislocations in alpha-2. In the following analysis, we did not determine the magnitude of the Burgers vectors. Identification of $1/3<11\bar{2}0>$ superlattice dislocations split into $1/6<11\bar{2}0>$ superpartials has recently been performed by Court et al [12]. The separation of the partials, however, was determined to be about 6nm and was only detectable in weak-beam. Identification of the true Burgers vector for $\mathbf{c+a}/2$ dislocations in alpha-2 would require considerable computer image simulation. Our assumption was that there would be pairs of $1/6<11\bar{2}6>$ dislocations making a $1/3<11\bar{2}6>$ superdislocation.

Differentiation of $\mathbf{c+a}/2$ dislocations from those with a \mathbf{c} Burgers vector has been based upon which slip plane the dislocation is lying on. There are long straight dislocations which are observed aligned with the basal plane in images formed with g_{0002}

in both alpha and alpha-2 alloys and these may well be c dislocations. An example is shown in Figure 3-8 where some of these straight segments are associated with basal plane faults. These dislocations could also have a different type of $c+a$ Burger's vector such as the $1/6<20\bar{2}3>\alpha$ observed by Woodfield et al. [13]. However, these can not be slip generated $c+a$'s since these can slip only on pyramidal planes. Recent work by Thomas et al. [14] describing c slip in alpha-2 appears more likely to be residual "grown-in" dislocation structure that is not contributing to deformation[15]. Indeed, c dislocations can only slip conservatively on prism planes and, since we have not observed any $c+a/2$'s on these planes, we have not had to use further $\mathbf{g}\cdot\mathbf{b}$ analysis to differentiate between $c+a/2$ and c slip. One other difference that is associated with the slip of $c+a/2$'s is a characteristically corrugated appearance, as will be seen later. Arrays of dislocations with a c component are often present in lath boundaries. An example can be seen in the lower left hand corner of Figure 3-10c. The array stops where the two laths have joined together. The $c+a/2$'s are also observed frequently in sub-boundaries within laths. Care was taken to distinguish these from slip dislocations. The criteria used to reject dislocations from being classified as slip produced, included curvature of the "slip plane," presence of more than one type of dislocation on the same plane, and misorientation of the grain on one side of the array relative to the other as identified by changes in the bend contours passing through the array.

Our dislocation Burgers vector analysis was performed by imaging with the g_{0002} reflection and at least one other: usually g_{2021} (Note: our convention will be to use Miller-Bravais indices that refer to the $D0_{19}$ lattice unless indicated otherwise by a subscript). Slip planes were determined by tilting specimens to the point where the slip planes were parallel to the viewing direction, that is, they were then viewed edge-on. The operative slip planes were then identified by locating the \mathbf{g} vector normal to the slip trace.

In general, we have not tried to identify the operative planes for a slip except when a trace is clearly evident and conveniently oriented for analysis. We have identified both (0001) and $(10\bar{1}0)$ slip in these cases. It would appear reasonable to assume that a dislocations not lying parallel to the (0001) trace when g_{0002} is operating are slipping on $\{10\bar{1}0\}$ planes. An example of a slip in a grain that was unfavorably oriented for $c+a/2$ slip is shown in Figure 3-9. The $\mathbf{g}\cdot\mathbf{b}$ analysis is consistent with both of the two major sets of dislocations being in a screw orientation. As such, it is impossible to tell if they are lying on basal or prism planes. There are one or two small bowed segments visible which are probably on the basal plane. We are viewing this grain from the $[0001]$ direction and any dislocations lying on the prism planes would project as screw if they were of mixed character. Pure edge dislocations lying on the prism planes would be end-on from this direction so one can tell that they are not these. An examination of another grain viewed from close to the $[11\bar{2}0]$ direction is shown in Figure 3-10. Imaging with g_{0002} (Figure 3-10a) extinguishes all of the slip dislocations - arrays of c component dislocations can still be seen at the lath interfaces. The images in the other micrographs are thus of a dislocations. This time some of the dislocations are again parallel to the basal plane and probably in a screw orientation, however, a good proportion are either parallel to the prism plane and (most likely) edge, or are mixed. As before, identification of the slip plane for the screws is ambiguous but the other dislocations are on prism planes.

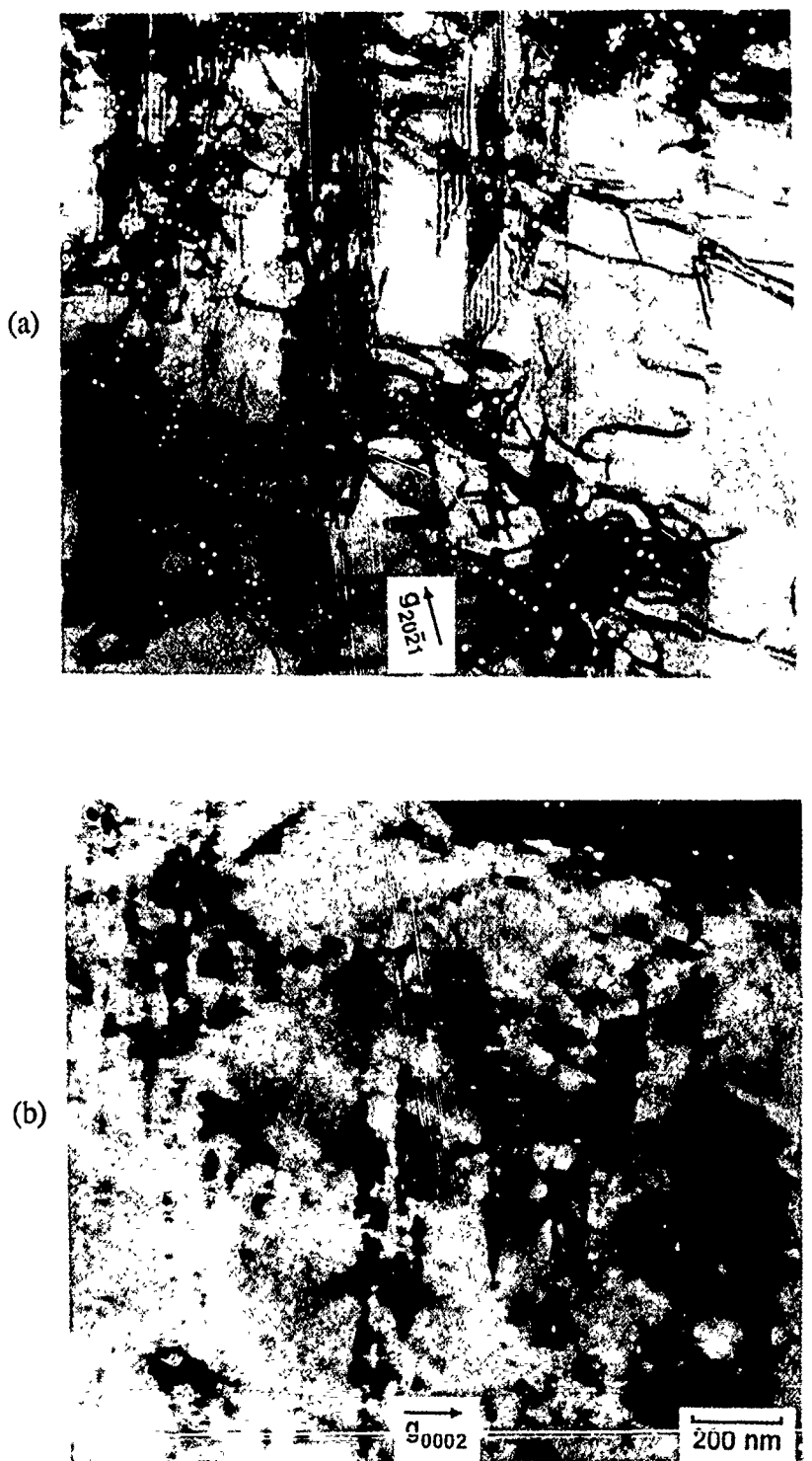


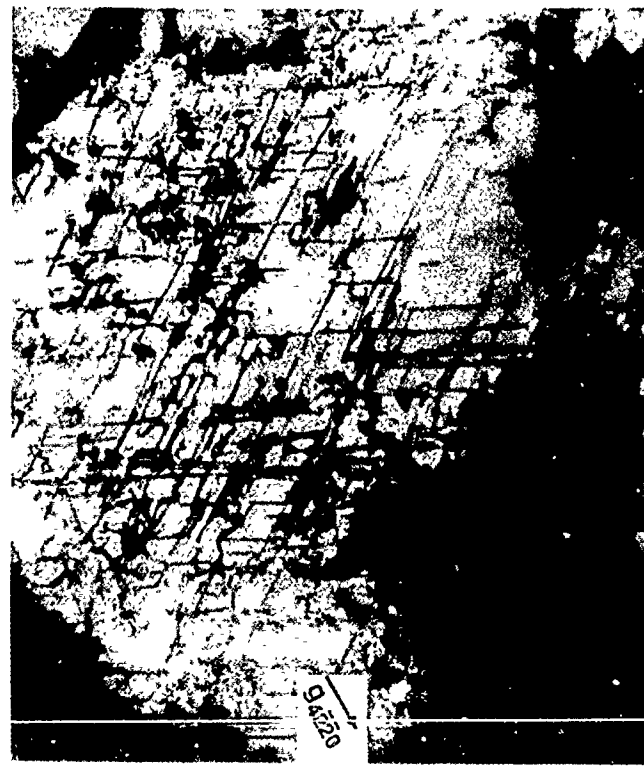
Figure 3-8 TEM micrographs of a dislocations and basal plane faults in a Ti-19.5Al-5Nb-5Ta-3Sn (IT-15) specimen deformed at room temperature.



(a)



(b)



(c)



(d)

Figure 3-9 TEM micrographs of a slip in a Ti-25Al-4Nb-2Ta-2V-1Mo (IT-11) specimen which was deformed at room temperature.

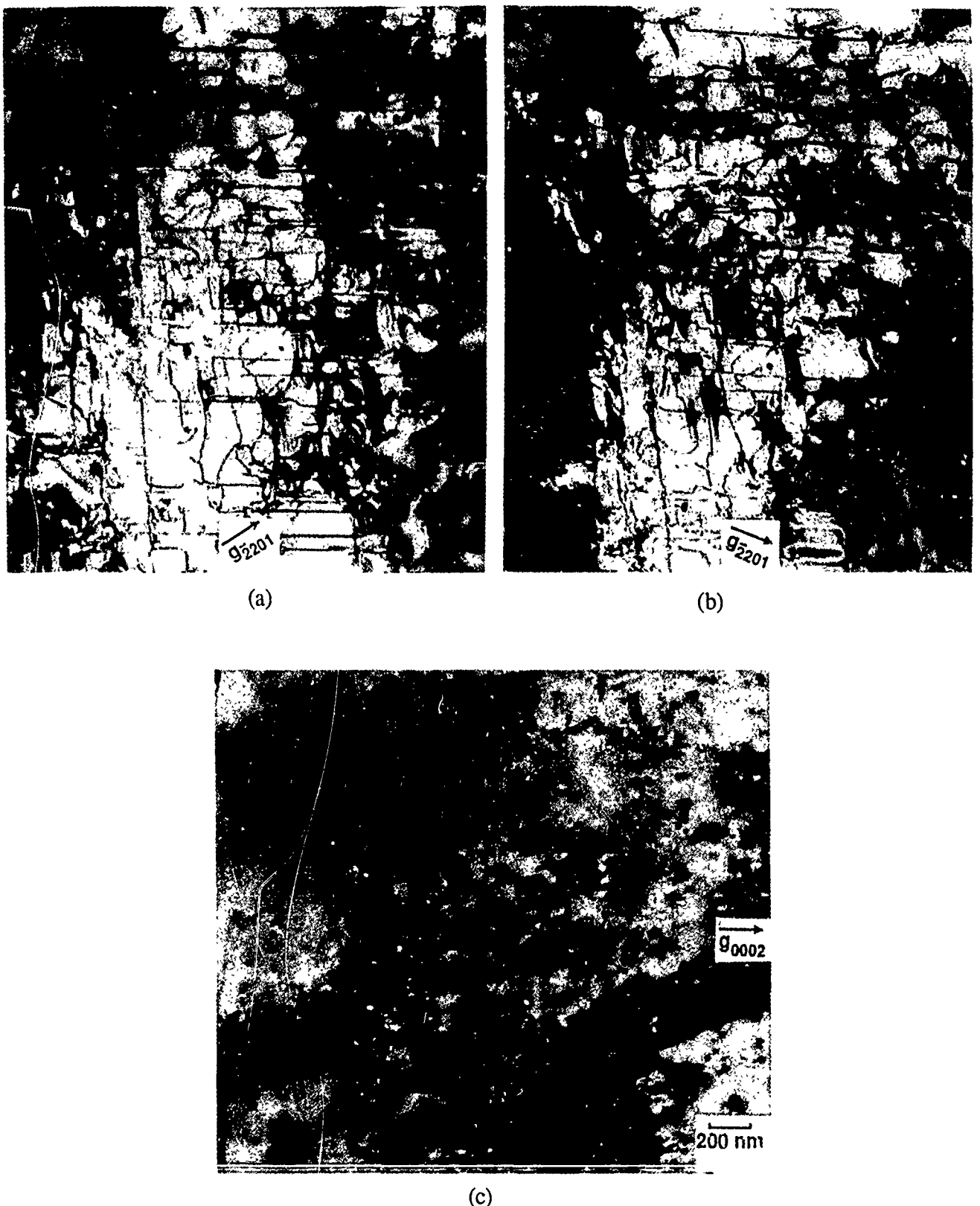


Figure 3-10 TEM micrographs of a dislocations on basal and prism planes in a Ti-25Al-4Nb-2Ta-2V-1Mo (IT-11) specimen which was deformed at room temperature.

Microstructure of Task 1 Alloys

TEM analysis was conducted after deforming each of the Task 1 alloys in compression to approximately 2% plastic strain at room temperature, 300°C (570°F) and 500°C (930°F). As a result of heat treatment within the two phase field, we recognized that some beta phase may form in the alloys and influence toughness test values; however, deformation of the alpha-2 phase could be evaluated independent of the presence or absence of beta phase. Nevertheless, each of the alloys was evaluated for beta phase and alpha-2 grain morphology. Small amounts of beta phase were found in all of the Task 1 alloys except Ti-25Al-5Nb-5Ga (IT-2). The beta phase is present generally as discontinuous thin ribbons, as shown in Figure 3-11a. Although quantitative measurements of the volume fraction of beta phase were not made, none of the alloys appeared to contain more than 1 volume percent.

Some unusual microstructures were generated by heat treatment within the alpha-2 plus beta phase field. For example, the typical Widmanstatten alpha-2 plates of Ti-25Al-5Nb-5Ga (IT-2) were separated by a continuous phase, shown in Figure 3-11b, that was also analyzed as alpha-2. Chemical analyses by EDS indicated the boundary phase to be very slightly higher in Nb and lower in Ga and Al, but the ranges were far below that expected for beta phase or for Ti_2Ga as shown in Table 3-5. Selected area and convergent beam electron diffraction produced patterns consistent with the DO_{19} structure of alpha-2.

Table 3-6 Phase Compositions of Ti-25Al-5Nb-5Ga (IT-2)

Phase	Atom Percent, by EDS		
	Al	Nb	Ga
Widmanstatten Alpha-2	24.3	5.6	5.6
Boundary phase	23.6	6.6	4.2

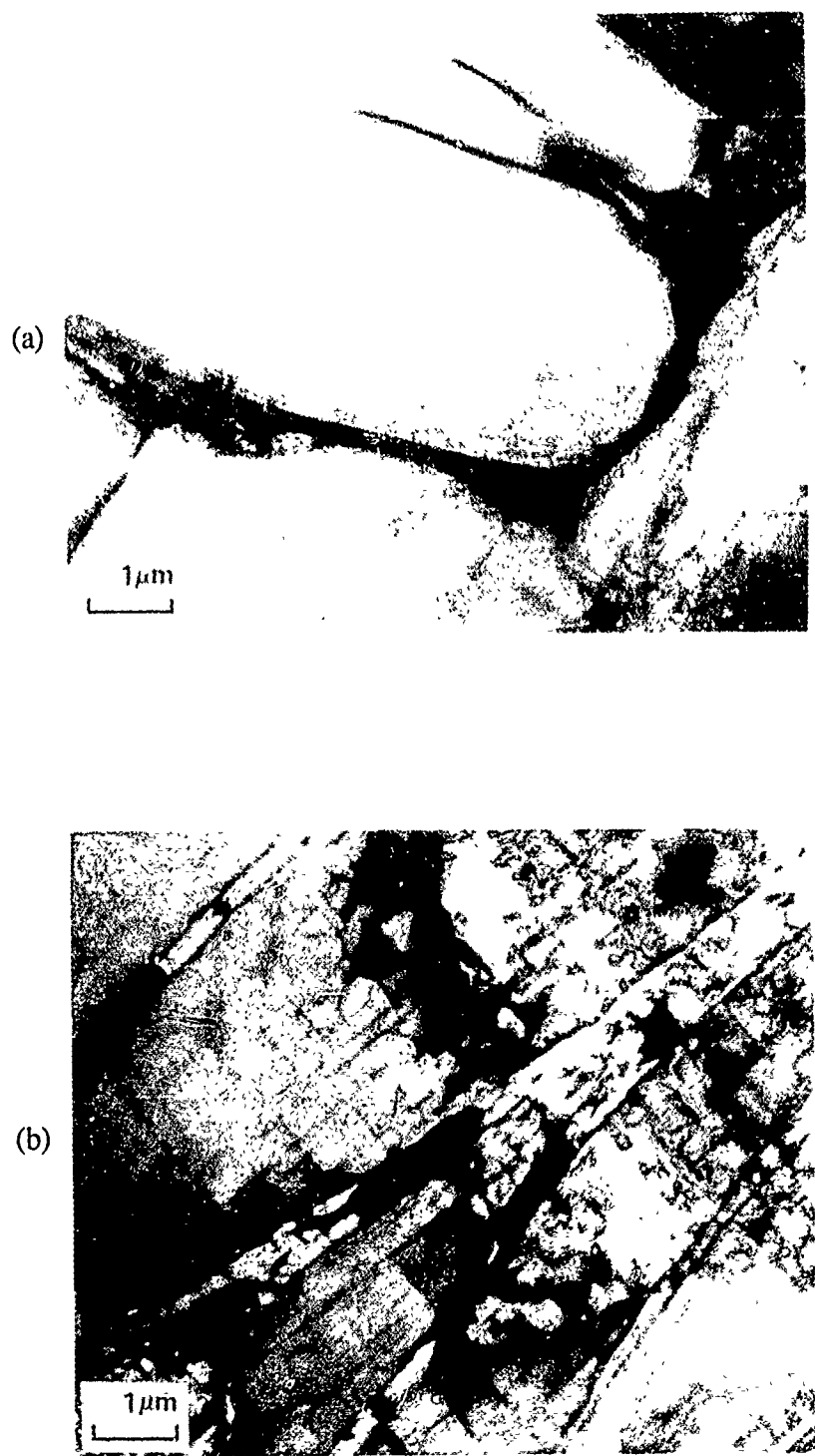


Figure 3-11 TEM micrograph of alloy (a) Ti-25Al-5Nb-1Cr (IT-6) illustrating thin, discontinuous beta phase (b) Ti-25Al-5Nb-5Ga (IT-2) demonstrating continuous alpha-2 phase separating alpha-2 Widmanstatten plates.

Temperature Effects on Deformation

Alpha-2 grains having their c-axis within 15° of the stress axis were located in only four of the nine specimens mechanically tested at room temperature. Those four were Ti-20Al-5Nb-2.5Ga-2.5Sn (IT-4), Ti-25Al-5Nb-1Mo (IT-5), Ti-25Al-5Nb-10Zr (IT-7), and Ti-22Al-5Nb-3Ga-1Mo (IT-8). In each specimen, c+a/2 slip as a compression-deformation mechanism was detected. For instance, Figure 3-12a shows c+a/2 slip in Ti-20Al-5Nb-2.5Ga-2.5Sn (IT-4), and examples from the other three alloys are shown in Figures 3-12b and 3-13. Trace analyses were not performed on all c+a/2 slip planes, but for those done, {1121} were found to be the predominant slip planes. Of the remaining five room temperature test specimens that had no alpha-2 grains oriented with their c-axis within 15° of the compression axis, Ti-25Al-5Nb-5Ga (IT-2) and Ti-22Al-5Nb-3Ga-2Ta (IT-9) exhibited some c+a/2 activity in grains oriented with their c-axis 20-40° from the stress axis. No evidence of compression-induced c+a/2 slip was detected in the unpreferentially oriented grains of Ti-20Al-5Nb-5Ga (IT-1), Ti-20Al-5Nb-5Sn (IT-3), or Ti-25Al-5Nb-1Cr (IT-6).

The 300°C (570°F) test specimens of Ti-25Al-5Nb-5Ga (IT-2), Ti-20Al-5Nb-5Sn (IT-3), and Ti-25Al-5Nb-1Mo (IT-5) had alpha-2 grains with their c-axis within 15° of the compression axis. The alloy Ti-25Al-5Nb-1Mo (IT-5) showed fairly extensive c+a/2 slip while the others exhibited only slight c+a/2 activity. Figure 3-14a shows c+a/2 slip in Ti-25Al-5Nb-1Mo (IT-5) while Figure 3-14b demonstrates c+a/2 slip in Ti-25Al-5Nb-5Ga (IT-2). The 300°C (570°F) test specimens of Ti-20Al-5Nb-5Ga (IT-1), Ti-25Al-5Nb-1Cr (IT-6), Ti-25Al-5Nb-10Zr (IT-7), and Ti-22Al-5Nb-3Ga-2Ta (IT-9) did not display alpha-2 grains with their c-axis oriented within 15° of the compression axis. However, in each of these specimens, grains were found with the c-axis within 45° of the stress axis and slight c+a/2 activity was identified.

It was not obvious if there was a small increase in the amount of c+a/2 slip activity at 300°C (570°F) for any particular alloy, and in general, c+a/2 slip was very limited. In the room temperature test specimens, only Ti-20Al-5Nb-2.5Ga-2.5Sn (IT-4) exhibited more than slight c+a/2 slip. The results of our TEM analysis clearly indicate that there was no dramatic increase in c+a/2 slip at 300°C (570°F) over that at room temperature even though tensile ductility was increased significantly as reported in Table 3-3.

Tensile test results showed that six of the Task 1 alloys exhibit ductilities ranging from 2.4 to 9.3% at 427°C (800°F), and that only Ti-25Al-5Nb-5Ga (IT-2), Ti-20Al-5Nb-5Sn (IT-3), and Ti-25Al-5Nb-1Cr (IT-6) have tensile elongations less than 1% at that temperature. If this increased ductility was the result of a more uniform distribution of c+a/2 slip, a significant change in c+a/2 dislocation densities may have been expected for the 500°C (930°F) compression specimens evaluated by TEM. Grains with their c-axis within 15° of the stress axis were identified for four of the nine 500°C (930°F) test specimens evaluated by TEM. Of these, none exhibited extensive c+a/2 slip, rather Ti-25Al-5Nb-1Mo (IT-5), Ti-22Al-5Nb-3Ga-1Mo (IT-8) and Ti-22Al-5Nb-3Ga-2Ta (IT-9) contained a few deformation induced c+a/2 dislocations, as shown in Figure 3-15. The alloy Ti-25Al-5Nb-1Cr (IT-6) had no deformation induced c+a/2 in an alpha-2 grain correctly oriented for c+a/2 slip, Figure 3-16a. No alpha-2 grains oriented for c+a/2 slip were observed in the other 500°C (930°F) test specimens, but in grains oriented from 20° to 70° off the stress axis, scant deformation induced c+a/2 slip was detected as shown by the example illustrated in Figure 3-16b.

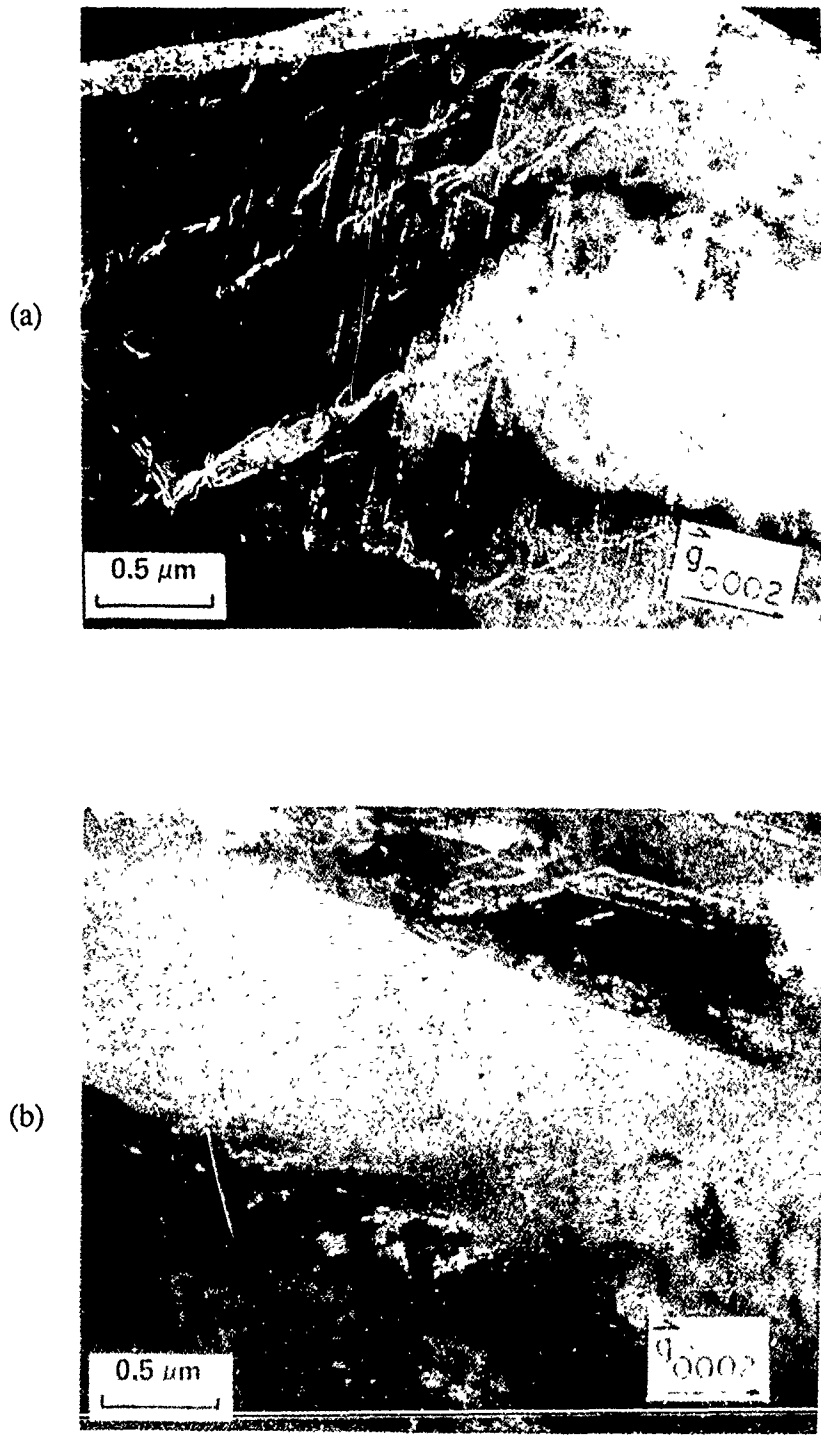


Figure 3-12 (a) TEM micrograph illustrating $c+a/2$ slip in an alpha-2 grain oriented with the c axis 6° from the stress axis in alloy Ti-20Al-5Nb-2.5Ga-2.5Sn (IT-4) tested at RT. (b) TEM micrograph showing $c+a/2$ slip in an alpha-2 grain in alloy Ti-25Al-5Nb-1Mo (IT-5) tested at RT.

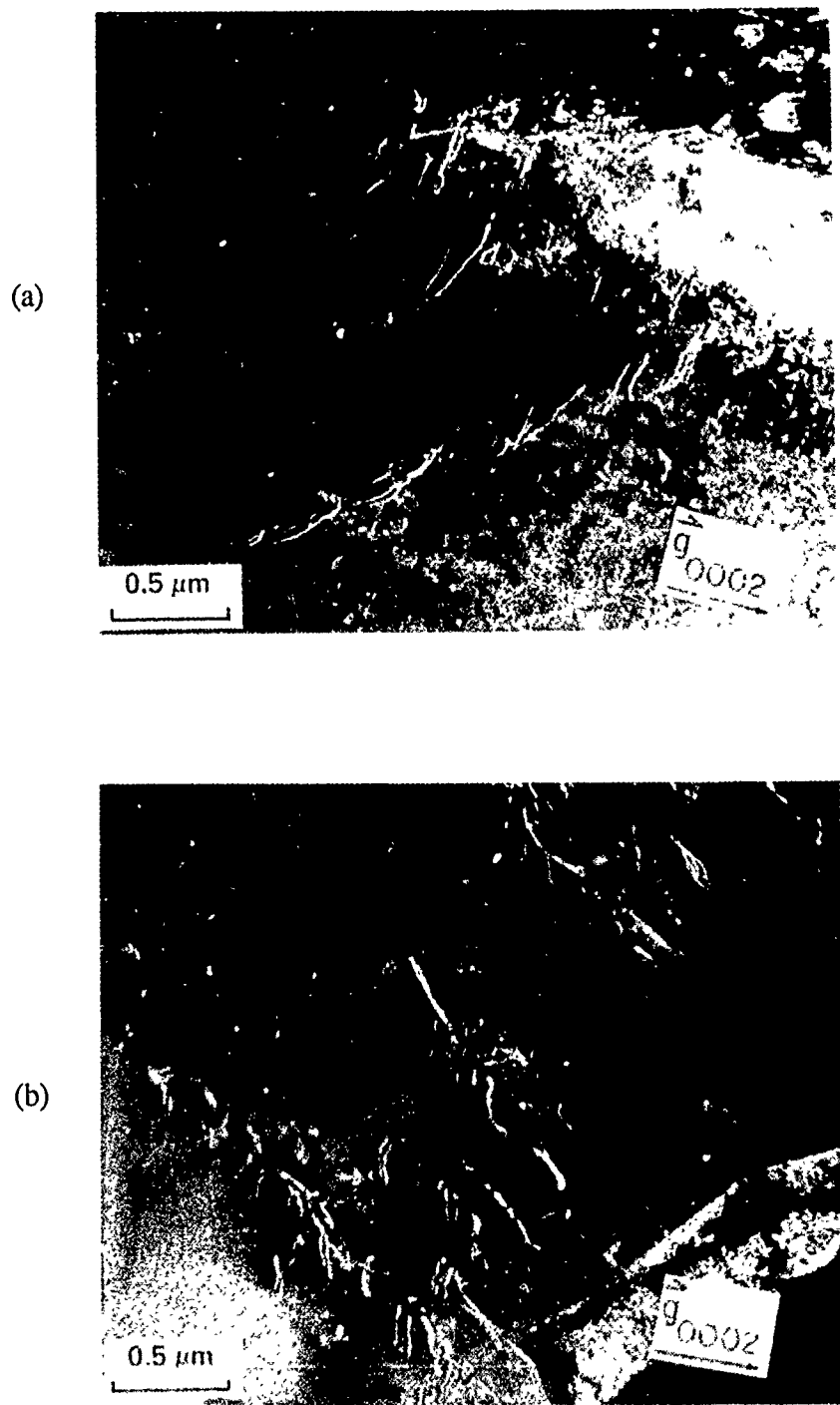


Figure 3-13 (a) TEM micrograph showing $c+a/2$ slip in an alpha-2 grain oriented with the c axis 16° from the stress axis in alloy Ti-25Al-5Nb-10Zr (IT-7) tested at RT. (b) TEM micrograph illustrating $c+a/2$ slip in an alpha-2 grain oriented with the c axis 10° from stress axis in alloy Ti-22Al-5Nb-3Ga-1Mo (IT-8) tested at RT.

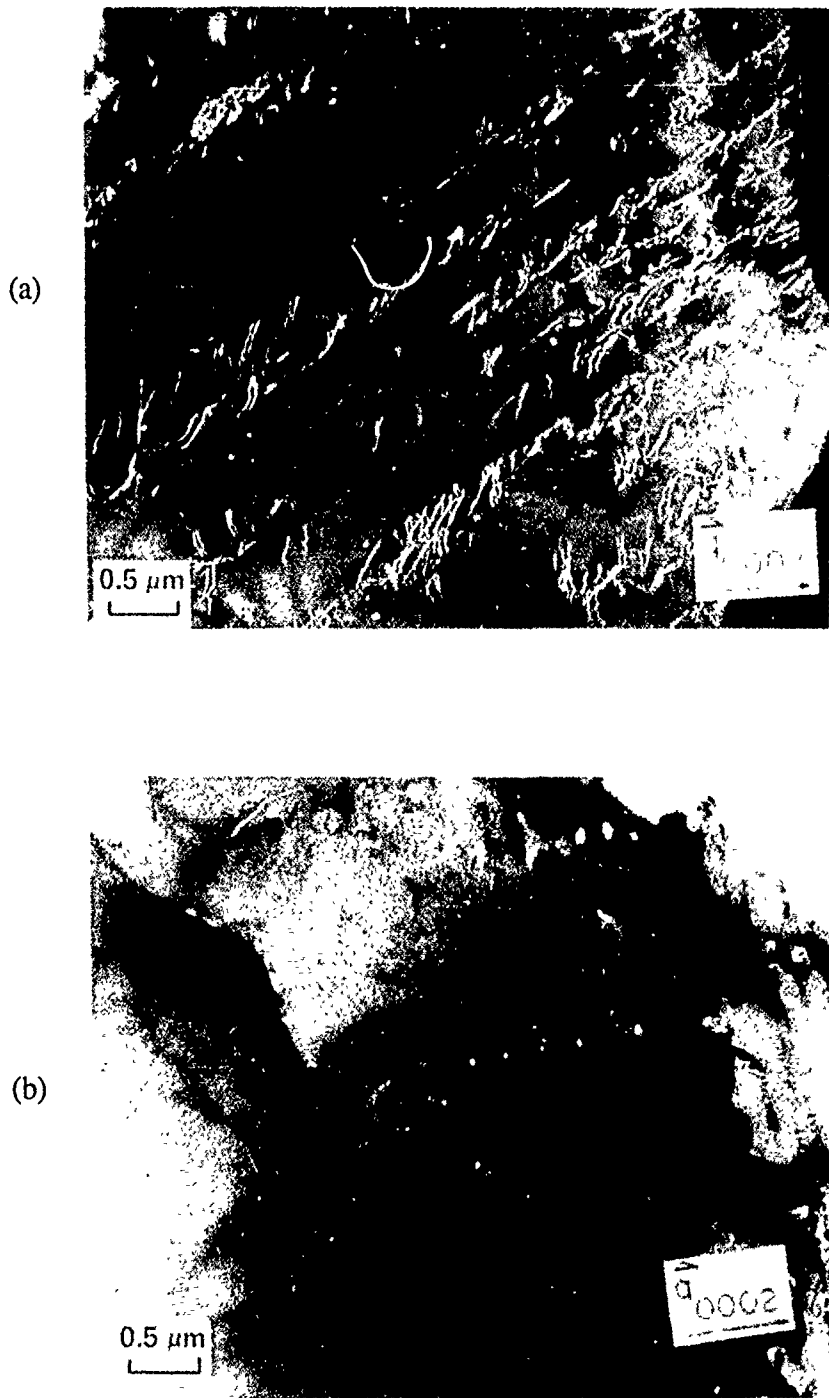


Figure 3-14 (a) TEM micrograph illustrating $c+a/2$ slip in an alpha-2 grain oriented with the c axis 13° from the stress axis in alloy Ti-25Al-5Nb-1Mo (IT-5) tested at 300°C (572°F). (b) TEM micrograph showing $c+a/2$ slip in an alpha-2 grain oriented with the c axis 12° from the stress axis in alloy Ti-20Al-5Nb-5Sn (IT-3) tested at 300°C (572°F).

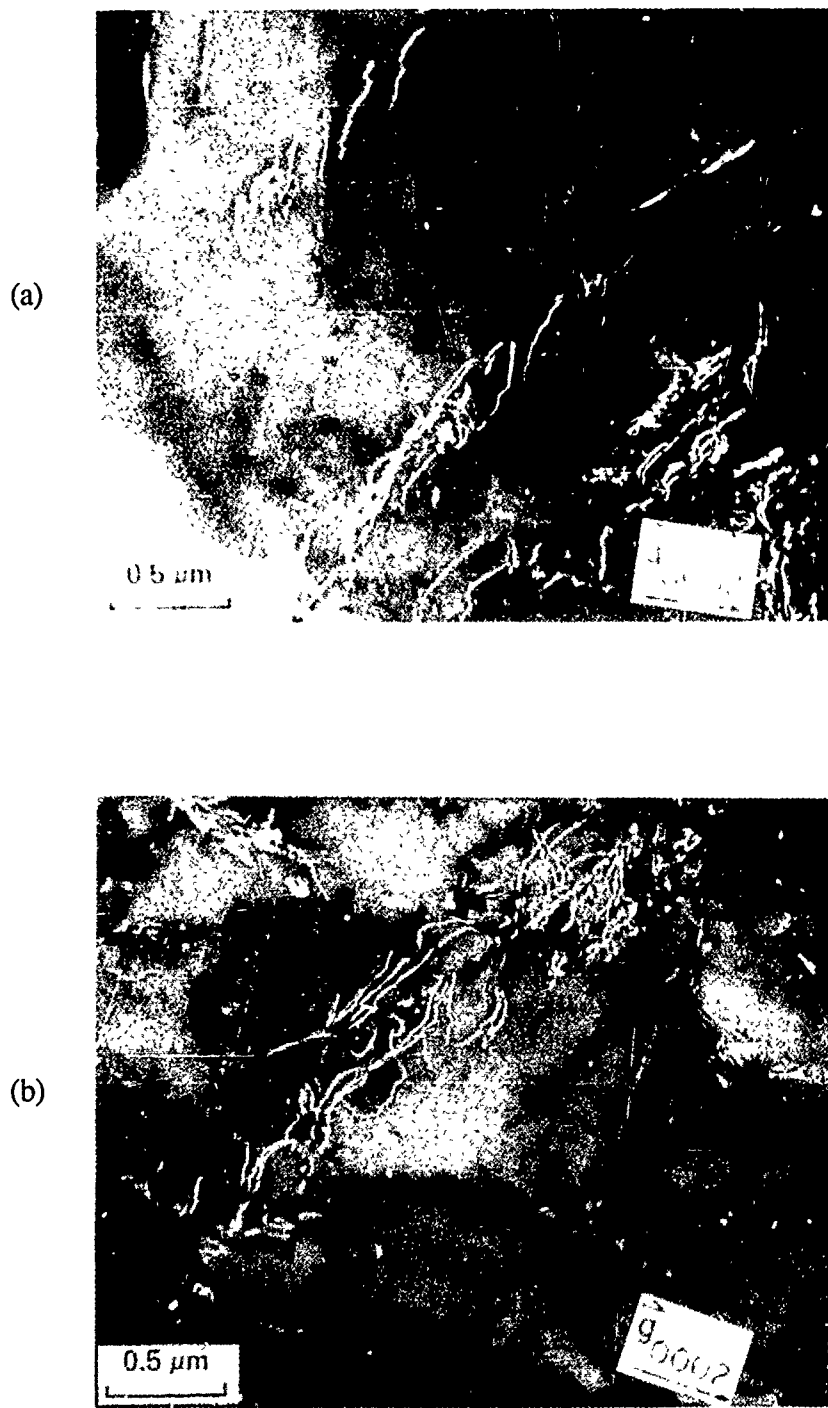


Figure 3-15 (a) TEM micrograph showing $c+a/2$ slip in an alpha-2 grain oriented with the c axis 15° from the stress axis in alloy Ti-25Al-5Nb-1Mo (IT-5) tested at 500°C (932°F). (b) TEM micrograph illustrating $c+a/2$ slip in an alpha-2 grain oriented with the c axis 10° from the stress axis in alloy Ti-22Al-5Nb-3Ga-1Mo (IT-8) tested at 500°C (932°F).

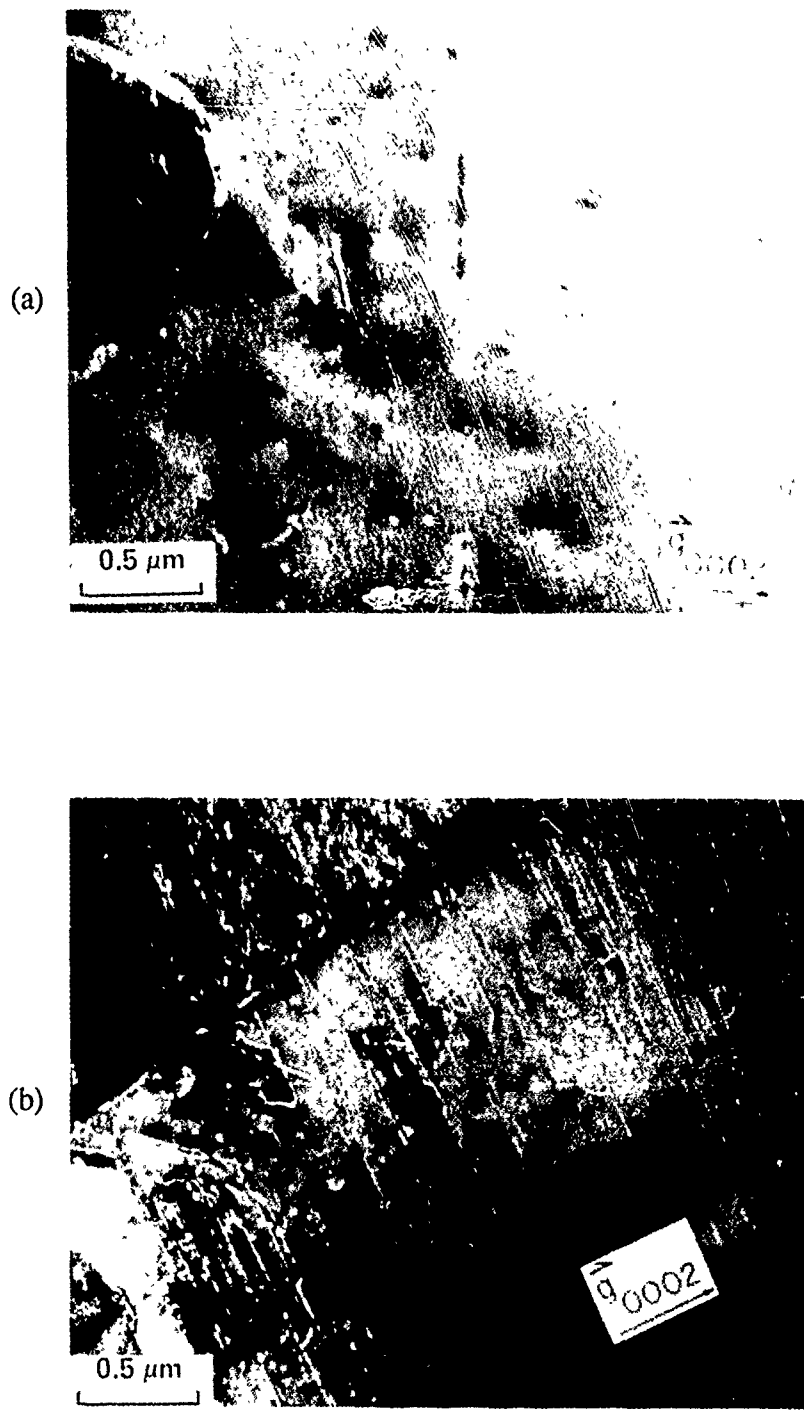


Figure 3-16 (a) TEM micrograph illustrating $c+a/2$ slip in an alpha-2 grain oriented with the c axis 6° from the stress axis in alloy Ti-25Al-5Nb-1Cr (IT-6) tested at 500°C (932°F). (b) TEM micrograph showing $c+a/2$ slip in an alpha-2 grain oriented with the c axis 31° from the stress axis in alloy Ti-25Al-5Nb-10Zr (IT-7) tested at 500°C (932°F).

Burgers Vectors

Burgers vector and slip plane analysis were both made on selected test specimens. Use of the $\mathbf{g} \cdot \mathbf{b}$ invisibility criterion and imaging with reflections in the [1120] and [1123] zones was sufficient to determine the Burgers vector. No attempts were made to determine the magnitude of the Burgers vectors. The primary slip planes for a-type dislocations in the Ti₃Al structure are {1010}, with {0001} and {2021} also possible. In the absence of slip traces on the foil surfaces, slip planes were deduced by viewing stereo pairs to estimate angles between dislocation lines and the corresponding zone axis. By comparing these estimated angles for two zone axes for each set of dislocations, a selection of one of the known slip planes could be made.

Typical a-type dislocations in the Ti-22Al-5Nb-3Ga-1Mo (IT-8) specimen which was tested at room temperature are shown in Figure 3-17. In this grain, the deviation of the c-axis from the compression axis was approximately 18°. Although only straight dislocation segments are visible in Figure 3-17a, two types of dislocations are present as identified by labels A and B. As shown in Figure 3-17b, tilting to a different zone axis and a second g-vector reveals new sets of dislocations, labelled C and D, while rendering dislocation B invisible. By imaging with 2201, 2201, 0002, 4400, 2022, and 2022 g-vectors, the invisibility criterion indicated the following Burgers vectors:

- Type A: [2110]
- Type B: [1216]
- Type C: [1120]
- Type D: [2116].

The majority of the dislocations then are a-type with occasional c+a/2 dislocations present.

The specimen of Ti-22Al-5Nb-3Ga-1Mo (IT-8) tested at 500°C (930°F) contains similar dislocations as shown in Figure 3-18. The deviation of the c-axis from the compression axis in this grain was approximately 5°. Therefore, the orientation of the grain in Figure 3-18a favors c+a/2 dislocation activity as did the orientation of the grain shown in the room temperature test specimen shown in Figure 3-17a. In addition to the straight dislocations labelled E in Figure 3-18a, there are bowed segments, such as those labelled F and I, and extremely long segments, labelled H. After imaging with 2201, 2201, 0002, 4400, 2022, and 2022 g-vectors and applying the $\mathbf{g} \cdot \mathbf{b}$ invisibility criterion, the Burgers vectors were assigned as follows:

- Type E: [2110]
- Type F: [2110]
- Type G: [1120]
- Type H: [1210]
- Type I: [2116].

As was found in the room temperature specimen, the majority of the dislocations are a-type and only a few c+a/2 dislocations were identified. A comparison of Figures 3-17a and 3-18a reveals that there are more dislocations with a [2110] Burgers vector in the latter, and that there is an additional slip plane activated which contains Type H [1210] dislocations.

Slip Planes

After identifying the Burgers vectors, the slip planes of a number of the dislocations were determined. The a -type dislocations in the room temperature test specimen were found to lie in prism planes as follows:

Type A: $[2\bar{1}\bar{1}0] (01\bar{1}0)$
Type C: $[1\bar{1}20] (1\bar{1}00)$.

Because of the imaging conditions, it was not possible to unambiguously deduce the slip planes of the $\text{c+a}/2$ dislocations. However, for the Type D dislocations in Figure 3-17a, the slip plane was either $(20\bar{2}1)$ or $(2\bar{2}01)$. For Type B dislocations, the slip plane was indeterminate.

In the 500°C (930°F) test specimen, the following slip planes were deduced for the a -type dislocations in Figure 3-18a:

Type E: $[2\bar{1}\bar{1}0] (01\bar{1}0)$
Type F: $[2\bar{1}\bar{1}0] (01\bar{1}0)$
Type G: $[1\bar{1}20] (1\bar{1}00)$
Type H: $[1\bar{2}10] (10\bar{1}0)$.

As was the case for the room temperature test specimen, imaging conditions were not sufficient for determination of the slip plane of the Type I, $\text{c+a}/2$, dislocations.

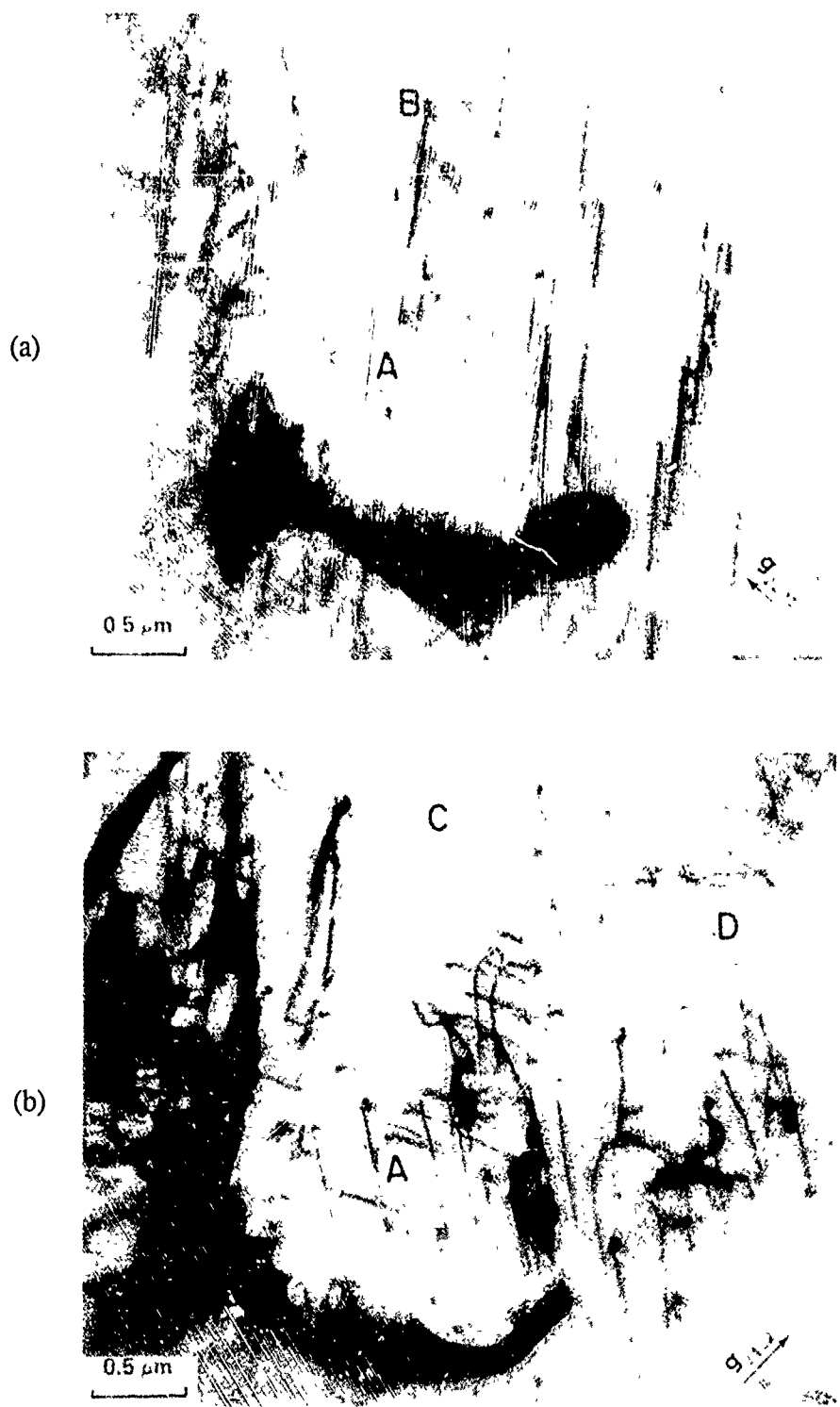


Figure 3-17 Transmission electron micrographs of dislocations in alloy Ti-22Al-5Nb-3Ga-1Mo (IT-8) compression specimen tested at room temperature. The compression axis is horizontal to the figures where (a) $g=220\bar{1}$ and (b) $g=242\bar{2}$.

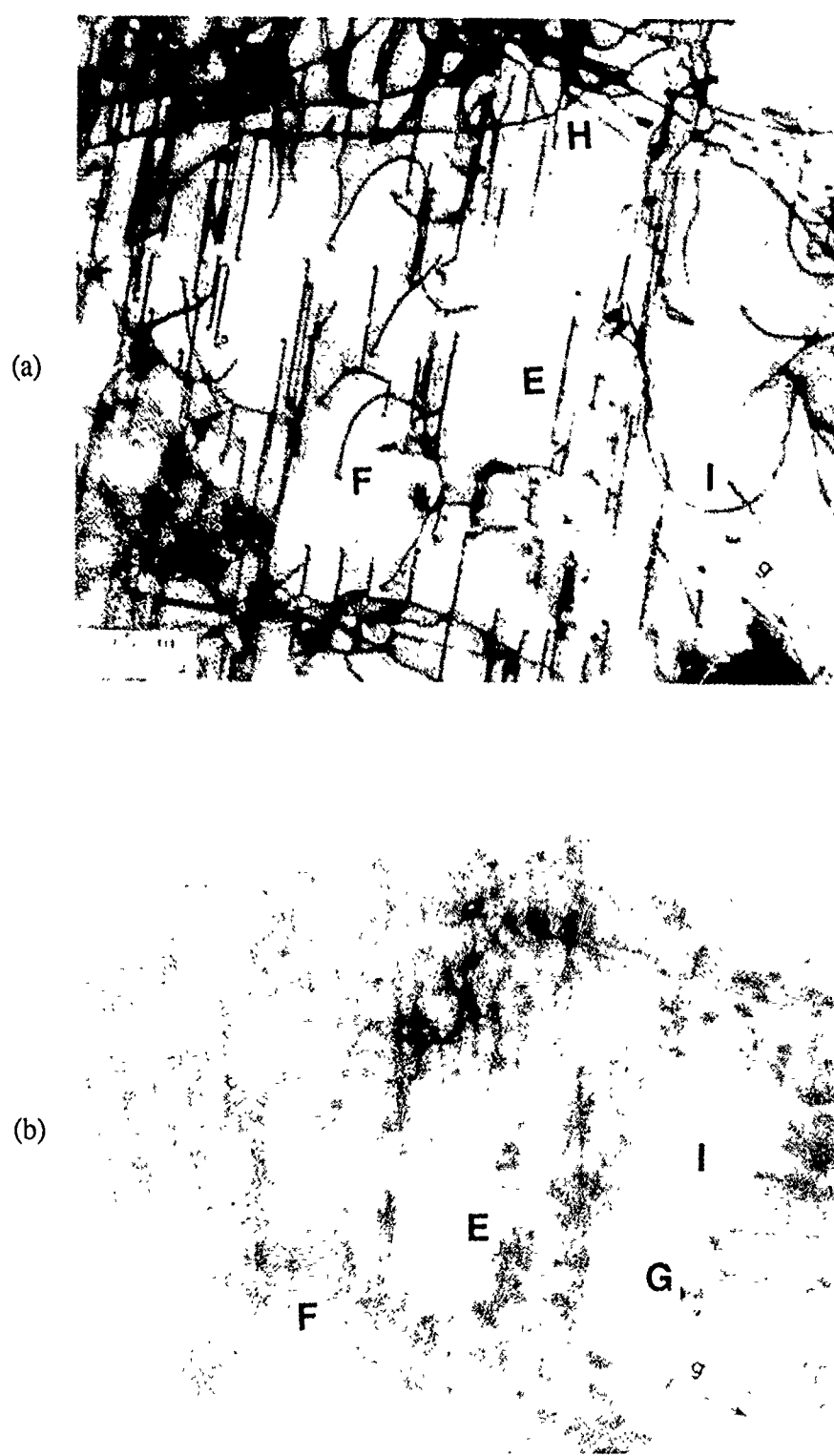


Figure 3-18 Transmission electron micrographs of dislocations in Ti-22Al-5Nb-3Ga-1Mo (IT-8) after compression testing at 500°C (930°F). The compression axis is horizontal to the figures where (a) $g=2\bar{2}01$ and (b) $g=20\bar{2}2$.

3.1.1.4 Alternate Microstructures

The alloys Ti-25Al-5Nb-1Mo (IT-5) and Ti-22Al-5Nb-3Ga-1Mo (IT-8) were selected to determine the influence of microstructure on mechanical properties. The selection of these alloys was based primarily on the favorable results achieved during the initial screening of mechanical properties and the opportunity to produce vastly different microstructures due to the degree of microstructural refinement obtained during extrusion processing. For the study of alternate microstructures, these alloys were beta solution treated and quenched to produce a fully transformed microstructure with a relatively large prior beta grain size as shown in Figures 3-19c and 3-19d. Previously, these alloys had been tested with a refined microstructural condition as shown in Figures 3-19a and 3-19b. These refined microstructures had been produced by extrusion and heat treatment below the beta transus temperature.

Evaluation of the beta solution treated material included tensile and fracture toughness testing. Tensile test results from the beta solution treated materials are compared to those of the refined microstructural condition in Table 3-7. The specimens of Ti-25Al-5Nb-1Mo (IT-5) and Ti-22Al-5Nb-3Ga-1Mo (IT-8) with a beta treated microstructure have much higher yield strengths at 427°C (800°F) and 649°C (1200°F) and higher ultimate strengths at 649°C (1200°F) than the corresponding strength levels for the refined microstructural condition. However, the specimens with a beta solution treated microstructure had considerably lower ductility at all test temperatures. At room temperature, the beta solutioned materials had very little ductility and the 0.2% yield strength was not achieved, whereas, the fine grained materials reached ductility levels up to 1.2% elongation. Clearly, the beta solution heat treatment offers some strength advantages at the expense of ductility. Furthermore, the low ductility of the beta solution treated material indicates that the ductility achieved during the initial screening of mechanical properties was the result of microstructural refinement rather than chemical composition.

Fracture toughness data for both the beta solution treated and the refined microstructures of Ti-25Al-5Nb-1Mo (IT-5) and Ti-22Al-5Nb-3Ga-1Mo (IT-8) are given in Table 3-8. In the case of Ti-25Al-5Nb-1Mo (IT-5), higher fracture toughness was associated with the beta solution treated microstructure. For Ti-22Al-5Nb-3Ga-1Mo (IT-8), the specimens with a refined microstructure and primary alpha-2, as shown in Figure 3-19d, were shown to have slightly higher fracture toughness than those with a beta solution treated microstructure. With more detailed observation of the beta solution treated microstructures, it is evident that a coarse colony microstructure was formed for Ti-25Al-5Nb-1Mo (IT-5) while a predominantly Widmanstatten microstructure with a smaller platelet size was formed for Ti-22Al-5Nb-3Ga-1Mo (IT-8). The large colonies of alpha-2 in the beta solution treated Ti-25Al-5Nb-1Mo (IT-5) test specimens promote crack branching which leads to improved fracture toughness. Although the beta grain size of the beta solution treated specimens of Ti-22Al-5Nb-3Ga-1Mo (IT-8) was large, the individual microstructural constituents (alpha-2 platelets/grains) were of similar size for the two Ti-22Al-5Nb-3Ga-1Mo (IT-8) microstructures. Neither microstructure of Ti-22Al-5Nb-3Ga-1Mo (IT-8) promoted a significant amount of crack branching and, as a result, the more ductile microstructure was also found to have slightly higher fracture toughness.

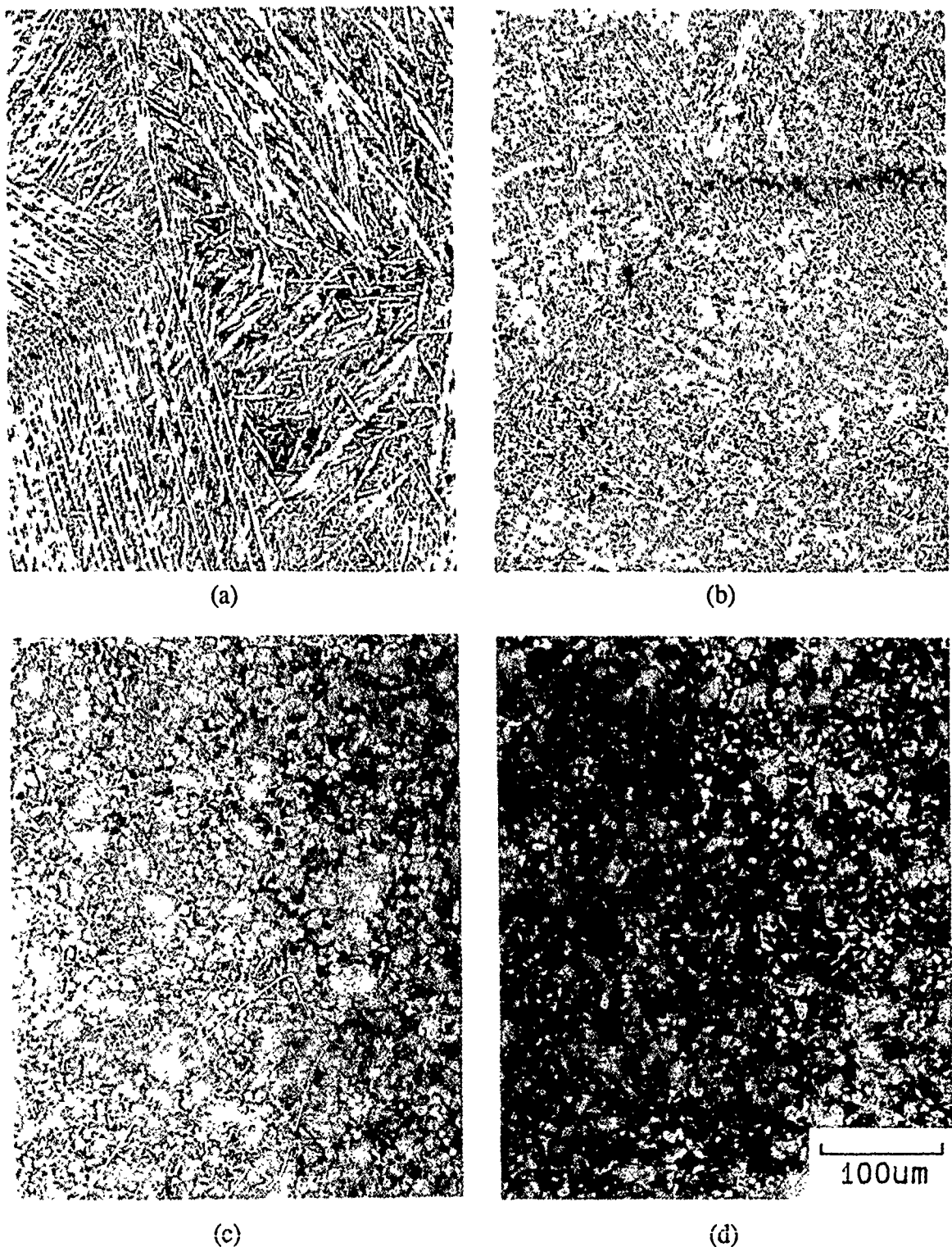


Figure 3-19 Microstructures of beta solution treated material of alloy (a) Ti-25Al-5Nb-1Mo (IT-5) and (b) Ti-22Al-5Nb-3Ga-1Mo (IT-8), and duplex microstructures produced by heat treatment within the alpha-2 plus beta phase field of alloys (c) Ti-25Al-5Nb-1Mo (IT-5) and (d) Ti-22Al-5Nb-3Ga-1Mo (IT-8).

Table 3-7 Tensile Properties for Microstructural Study of Task 1 Alloys

Alloy / Condition	Temp °C	Temp °F	0.2 YS MPa	0.2 YS ksi	UTS MPa	UTS ksi	El %	RA %
IT-5	24	75	728	105.7	818	118.7	0.6	2.0
	24	75	765	111.1	833	120.9	0.5	1.5
	427	800	493	71.6	837	121.5	9.3	11.1
	649	1200	394	57.2	607	88.1	10.6	15.1
IT-5(B)	24	75	-	-	883	128.1	<0.1	-
	24	75	-	-	760	110.3	<0.1	-
	427	800	655	95.1	765	111.0	1.1	0.8
	649	1200	541	78.5	738	107.1	3.4	8.2
IT-8	24	75	653	94.8	814	118.1	1.2	1.4
	24	75	651	94.5	781	113.4	1.1	1.8
	427	800	449	65.2	783	113.6	8.9	10.5
	649	1200	369	53.6	589	85.5	13.3	19.5
IT-8(B)	24	75	-	-	792	115.0	0.15	-
	24	75	-	-	716	103.9	0.1	-
	427	800	601	87.3	822	119.3	2.3	2.5
	649	1200	520	75.5	754	109.4	5.5	11.5

(B) = Beta Solution Heat Treatment

Table 3-8 Fracture Toughness Test Results for the Microstructural Study of Task 1 Alloys

Alloy / Condition	K _{exp} (MPa \sqrt{m})	K _{exp} (ksi \sqrt{in})
IT-5	20.3	18.5
	8.5	7.7
IT-5(B)	29.9	27.2
	22.4	20.4
IT-8	24.6	22.4
	20.6	18.7
IT-8(B)	19.3	17.5
	20.1	18.3

(B) = Beta Solution Heat Treatment

3.1.1.5 Task 1 - Summary

The Phase I, Task 1 alloys were selected to evaluate the effects of solid solution alloying. Mechanical test results indicated that two of the alloys, Ti-25Al-5Nb-1Mo (IT-5) and Ti-22Al-5Nb-3Ga-1Mo (IT-8), had approximately 1 percent tensile elongation at room temperature when processed and heat treated to produce a refined microstructure with a small volume fraction of primary alpha-2. When testing the same alloys after beta solution heat treatment, tensile elongation was reduced to less than 0.2 percent at room temperature, thus indicating that solid solution alloying was of less significance than microstructural control. Yet, the Mo additions which retard the transformation kinetics in Ti-25Al-5Nb-1Mo (IT-5) and Ti-22Al-5Nb-3Ga-1Mo (IT-8) were instrumental in achieving microstructural refinement. In all cases, the tensile strengths of the solid solution alloys were relatively low although beta solution heat treatment did improve elevated temperature strength.

Additional test results from Phase I, Task 1 indicated that fracture toughness and ductility were not closely related. The fracture toughness of an alloy such as Ti-20Al-5Nb-5Ga (IT-1) was as high as the fracture toughness of Ti-25Al-5Nb-1Mo (IT-5) and Ti-22Al-5Nb-3Ga-1Mo (IT-8) even though the tensile elongation of Ti-20Al-5Nb-5Ga (IT-1) was much lower than for Ti-25Al-5Nb-1Mo (IT-5) and Ti-22Al-5Nb-3Ga-1Mo (IT-8). Only in extreme conditions such as for Ti-25Al-5Nb-5Ga (IT-2) and Ti-20Al-5Nb-5Sn (IT-3) were both tensile elongation and fracture toughness correspondingly low. Furthermore, when studying the effect of microstructure on the mechanical properties of Ti-25Al-5Nb-1Mo (IT-5) and Ti-22Al-5Nb-3Ga-1Mo (IT-8), no relationship was established between ductility and fracture toughness. The fracture toughness of Ti-25Al-5Nb-1Mo (IT-5) was higher after beta solution heat treatment while the fracture toughness of Ti-22Al-5Nb-3Ga-1Mo (IT-8) was higher with a microstructure produced by extrusion and heat treatment below the beta transus temperature. As stated previously, specimens with a refined microstructure produced by extrusion and heat treatment below the beta transus temperature had significantly higher ductility than specimens which were beta solution treated. Therefore, it is clear that the microstructure which yields the best ductility is not always the microstructure which yields the highest fracture toughness. While a coarse colony alpha-2 microstructure can be beneficial to fracture toughness, it has generally been found to be detrimental to tensile ductility.

A significant effort was applied to analysis of the deformation structures in compression specimens of the solid solution alloys. From this work, little distinction could be made with regard to the effects of alloying on deformation behavior. When grains could be found with an appropriate orientation to the compression axis, the propensity for $c+a/2$ slip to occur was found to be very low for all of the solid solution alloys. In addition, contrary to original expectations, no clear evidence was found to indicate that the density of $c+a/2$ slip increased as the deformation temperature was increased from room temperature to 500°C (930°F) despite the fact that tensile elongation increased dramatically for a number of the alloys over this temperature range.

3.1.2 Task 2 - Tough Second Phase Alloys

Task 2 was conducted in parallel to Task 1. Seven alloys were selected to study the effects of a tough second phase on the mechanical properties of alpha-2 titanium aluminides. The aim and measured chemical compositions for these alloys are listed in Table 3-9. Since beta is the most practical second phase to introduce into alpha-two titanium aluminide materials, all of the alloys contained Nb as an alloying addition, as in Task 1, but most contained additional beta stabilizing elements as well. The distribution, morphology and properties of the beta phase in conventional alpha titanium alloys can be tailored by selective alloying and heat-treatment. A similar situation is thought to be true for the alpha-2 titanium aluminides alloys and the Task 2 alloys were selected to study the specific effects of beta phase alloying. The aluminum level and effective Al level (Al+Sn+Ga) of the Task 2 alloys was typically lower than the stoichiometric level of 25 atom percent. This reduction of aluminum additions allows for the formation of beta as a tough second phase without adding unusually high levels of heavy beta stabilizing elements.

3.1.2.1 Processing and Heat Treatment

The Task 2 compositions were approved by the CO and 6.8 kg (15 lb) ingots of each alloy were double melted by VAR at the RMI Company. Each ingot was then machined to fit inside a Ti-64 can for subsequent extrusion. Prior to extrusion, the ingots measured approximately 108 mm (4.25 in) in diameter and 125 mm (5 in) in length. Extrusion temperatures were chosen within the alpha-2 plus beta phase field in an effort to produce refined microstructures. All seven solid solution alloys were extruded successfully at the RMI Company. The extrusion ratio was held constant at roughly 21:1, the ram speed was approximately 2.5 cm (1 in) per second and extrusion temperatures were varied as shown in Table 3-10. These extrusion temperatures were selected after predicting beta transus temperatures and assuming that extrusion must be carried out at least 30 to 85°C (50 to 150°F) below the beta transus temperature to produce a refined microstructure. After extrusion, a heat-treatment matrix was established over a temperature range of 1025 to 1200°C (1875 to 2200°F) to experimentally determine the beta transus temperatures. The results from the beta transus studies are also presented in Table 3-10.

Several examples of as-extruded microstructures of the Task 2 alloys are shown in Figure 3-20. The desired microstructural refinement was achieved in most of these alloys by extruding within the alpha-2 plus beta phase field; however, adiabatic heating during the extrusion process caused fully transformed beta microstructures to be produced for Ti-22.5Al-5Nb-5Ta-3Zr (IT-14) and Ti-19.5Al-10Nb-3Ga (IT-16). As with the Task 1 alloys, it was evident that the pre-extrusion temperatures should be kept more than 55°C (100°F) below the beta transus temperature to ensure microstructural refinement when using an extrusion ratio of 21:1 and ram speed of approximately 2.5 cm (1 in) per second.

Heat treatments which resulted in microstructures with a small fraction of primary alpha-2 were identified when conducting the beta transus studies. These heat-treatments were used for the initial screening of mechanical properties. The microstructures of the Task 2 alloys produced by final heat-treatment for the evaluation of mechanical properties are shown in Figure 3-21 and 3-22.

Table 3-9 Compositions of Task 2 Alloys*

Alloy	Ti	Al	Nb	Ta	V	Mo	Other	O
IT-10	68.5 [68.1]	22.5 [12.6] (10.7)	4.0 [7.7] (7.9)	2.0 [7.5] (6.6)	2.0 [2.1] (2.1)	1.0 [2.0] (1.4)		(0.096)
IT-11	66.0 [66.3]	25.0 [14.2] (13.8)	4.0 [7.8] (8.2)	2.0 [7.6] (6.8)	2.0 [2.1] (2.0)	1.0 [2.0] (2.0)		(0.121)
IT-12	67.5 [66.5]	22.5 [12.5] (11.6)	6.0 [11.5] (11.5)	2.0 [7.4] (6.7)			2.0 Cr [2.1 Cr] (1.9 Cr)	(0.134)
IT-13	68.3 [67.3]	22.7 [12.6] (12.0)	3.0 [5.7] (5.5)	3.0 [11.2] (11.5)	3.0 [3.2] (2.9)			(0.140)
IT-14	64.5 [57.9]	22.5 [11.4] (12.1)	5.0 [8.7] (8.3)	5.0 [16.9] (14.8)			3.0 Zr [5.1 Zr] (5.1 Zr)	(0.107)
IT-15	67.5 [58.9]	19.5 [9.6] (9.3)	5.0 [8.5] (8.5)	5.0 [16.5] (16.5)			3.0 Sn [6.5 Sn] (6.1 Sn)	(0.108)
IT-16	67.5 [66.0]	19.5 [10.7] (11.4)	10.0 [19.0] (18.3)				3.0 Ga [4.3 Ga] (4.3 Ga)	(0.083)

* The compositions which are not enclosed in brackets are aim atom percents, compositions enclosed by [] are aim weight percents, and compositions enclosed by () are measured weight percents.

Table 3-10 Extrusion and Beta Transus Temperatures for Task 2 Alloys

Alloy	Extrusion Temperature (°C)	Extrusion Temperature (°F)	Beta Transus (°C)	Beta Transus (°F)	Temperature Difference (°C)	Temperature Difference (°F)
IT-10	1035	1900	1120	2050	85	150
IT-11	1035	1900	1175	2150	140	250
IT-12	1065	1950	1120	2050	55	100
IT-13	1065	1950	1135	2075	70	125
IT-14	1065	1950	1120	2050	55	100
IT-15	1120	2050	>1200	>2200	>80	>150
IT-16	1065	1950	1105	2025	40	75

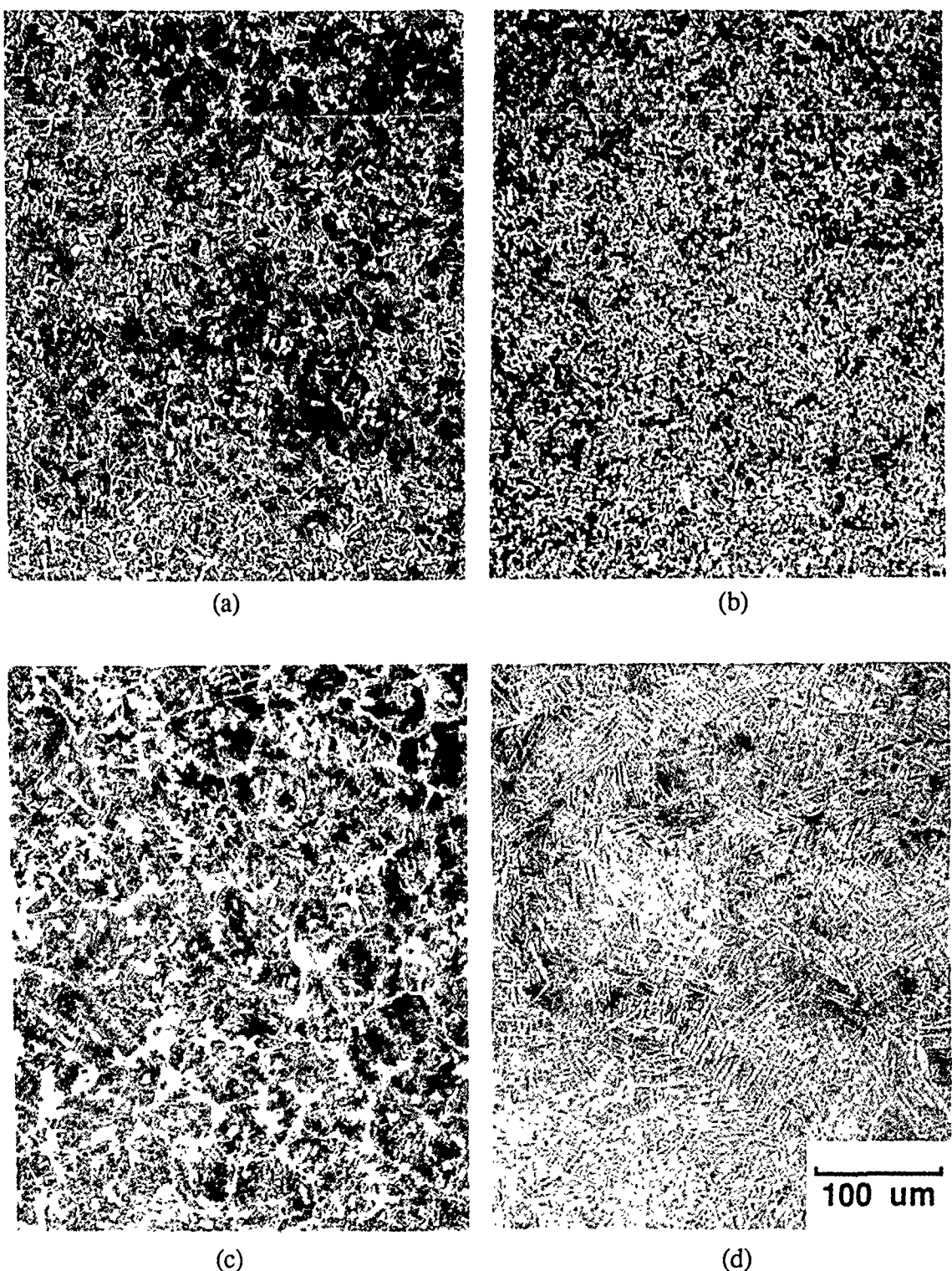
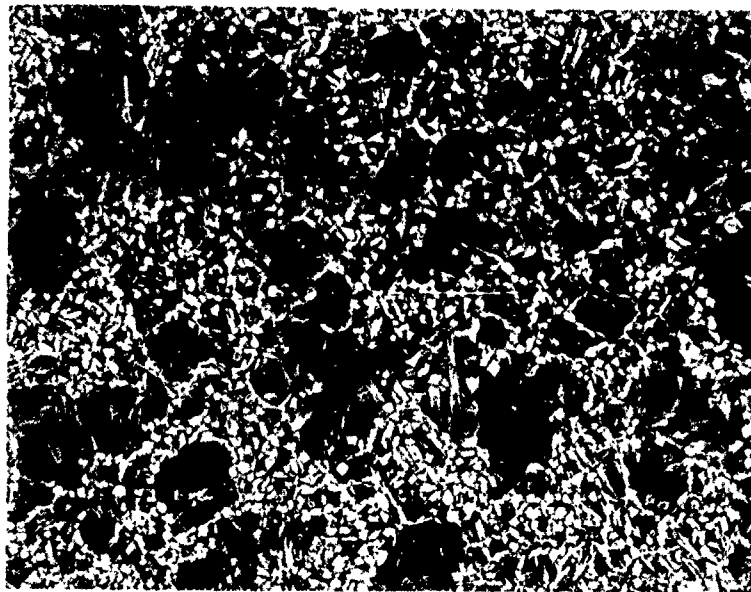


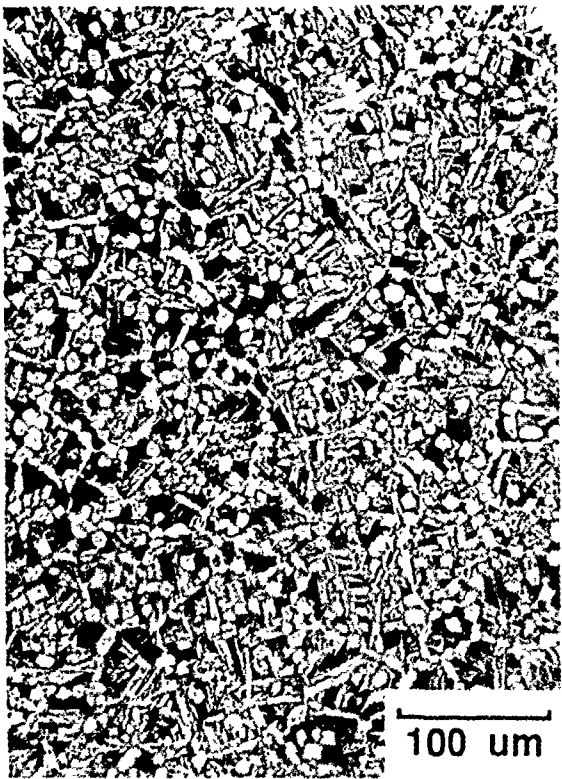
Figure 3-20 As-extruded microstructures of alloys (a) (Ti-22.5Al-4Nb-2Ta-2V-1Mo (IT-10)), (b) Ti-25.0Al-4Nb-2Ta-2V-1Mo (IT-11), (c) Ti-22.5Al-6Nb-2Ta-2Cr (IT-12) and (d) Ti-19.5Al-10Nb-3Ga (IT-16).



(a)



(b)



(c)

Figure 3-21 Optical micrographs of (a) Ti-22.5Al-4Nb-2Ta-2V-1Mo (IT-10) heat treated at 1095°C (2000°F), (b) Ti-25.0Al-4Nb-2Ta-2V-1Mo (IT-11) heat treated at 1135°C (2075°F) and (c) Ti-22.5Al-6Nb-2Ta-2Cr (IT-12) heat-treated at 1095°C (2000°F).

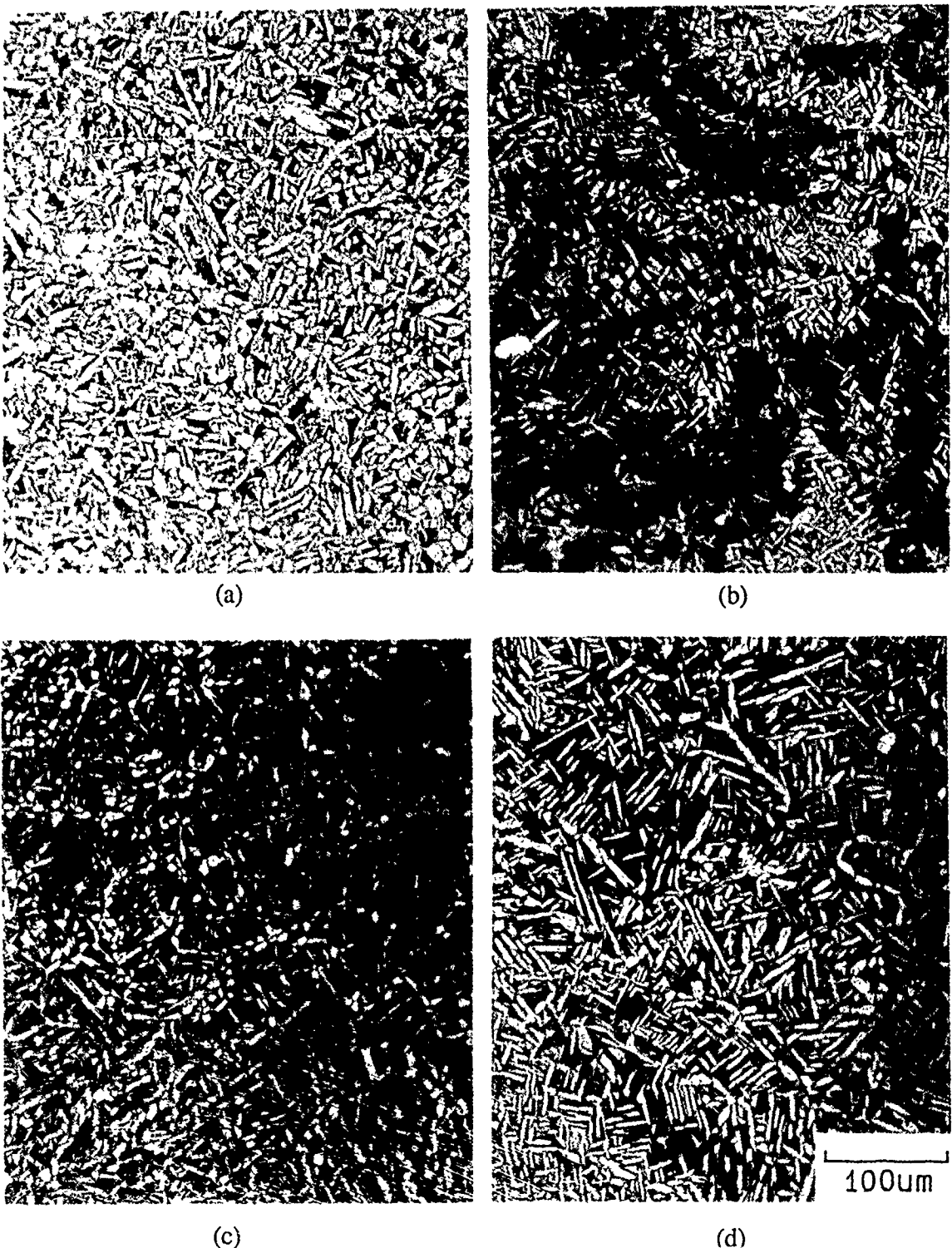


Figure 3-22 Optical micrographs of (a) Ti-22.7Al-3Nb-3Ta-3V (IT-13) heat-treated at 1095°C (2000°F), (b) Ti-22.5Al-5Nb-5Ta-3Zr (IT-14) heat-treated at 1095°F (2000°F), (c) Ti-19.5Al-5Nb-5Ta-3Sn (IT-15) heat treated at 1175°C (2150°F) and (d) Ti-19.5Al-10Nb-3Ga (IT-16) heat-treated at 1070°C (1960°F).

3.1.2.2 Mechanical Testing

Mechanical testing of all Task 2 alloys included tensile testing at room temperature, 427°C (800°F), and 649°C (1200°F), fracture toughness testing at room temperature, and small strain compression testing at room temperature, 300°C (572°F), and 500°C (932°F). The tensile specimens were machined with 1.27 cm (0.5 in) diameter threaded ends and a 3.18 cm (1.25 in) by 0.64 cm (0.25 in) diameter gage section. The fracture toughness specimens were 5.08 cm (2.0 in) long, 0.51 cm (0.2 in) wide, and 1.02 cm (0.4 in) deep with a 0.51 cm (0.2 in) notch which was not fatigue precracked prior to testing. The compression specimens were cylindrical in shape with a 0.64 cm (0.25 in) diameter and 1.91 cm (0.75 in) length.

Tensile tests were conducted at a cross head rate of 0.005 in/min through the 0.2% yield strength and then maintained at a cross head rate of 0.05 in/min through failure. Since the accuracy of measuring ductility from the change in length of broken test specimens is known to be limited for materials with low ductility, extensometers were kept in place until failure for room temperature tensile tests. Plastic deformation was then measured from load versus strain curves. The tensile test results are summarized in Table 3-11.

Encouraging tensile test results were generated for a number of the Task 2 alloys. Even though significant evidence has been generated to show that increased oxygen is detrimental to room temperature ductility [16], several of the Task 2 compositions had reasonable ductility despite having oxygen levels well above the specified limit of 0.10 weight percent. Unlike the Task 1 alloys, the 'effective' Al level of the Task 2 compositions was kept below the stoichiometric level of 25 atom percent. Undoubtedly, these lower Al levels were at least partially responsible for the increase in ductility over the Task 1 compositions. However, the success in producing refined microstructures for the Task 2 alloys was also beneficial to ductility as supported later when evaluating alternative microstructures.

Aside from increased ductility, many of the Task 2 alloys were also significantly stronger than the Task 1 alloys. This increased strength was especially evident at the lower test temperatures. In addition to increased levels of solid solution strengtheners and boundary strengthening by way of a refined alpha-2 platelet size, the Task 2 alloys were strengthened by the presence of a strong beta phase. The high strength of the beta phase in alpha-2 titanium aluminide alloy compositions has been demonstrated in recent work by Gittis and Koss [17]. Even though the strength of the Task 2 alloys was improved over that of the Task 1 alloys, only Ti-25.0Al-4Nb-2Ta-2V-1Mo (IT-11) maintained good strength at 650°C (1200°F). Since the measured compositions for Ti-22.5Al-4Nb-2Ta-2V-1Mo (IT-10) and Ti-25.0Al-4Nb-2Ta-2V-1Mo (IT-11) were nearly identical, except for Al content, it was evident that Al has a large effect on high temperature strength. The measured levels of Mo and O also vary slightly in these two alloys. While Mo may have had some effect on the high temperature strength, it is not likely that O influenced strength at temperatures as high as 650°C (1200°F). Of course, microstructure also has a significant effect on strength across the range of test temperatures, and later work on alternative microstructures indicated that the high temperature strength of the Task 2 alloys could be significantly improved by beta solution heat-treatment and rapid cooling.

Table 3-11 Tensile Properties of Task 2 Alloys

Alloy	Temp (°C)	Temp (°F)	0.2YS (MPa)	0.2YS (ksi)	UTS (MPa)	UTS (ksi)	El (%)	RA (%)
IT-10	24	75	752	109.1	923	134.0	3.0	4.7
	24	75	770	111.8	885	128.5*	1.0*	1.1*
	427	800	468	67.9	881	127.9	21.8	24.8
	649	1200	374	54.3	554	80.4	25.3	37.1
IT-11	24	75	966	140.2	1072	155.6	0.5	0.2
	24	75	907	131.6	990	143.7	0.4	0.4
	427	800	584	84.7	1005	145.9	5.1	7.5
	649	1200	488	70.8	797	115.7	5.6	7.8
IT-12	24	75	668	97.0	861	124.9	3.2	5.1
	24	75	668	97.0	899	130.5	4.8	5.0
	427	800	437	63.4	825	119.7	36.5	37.4
	649	1200	316	45.9	413	59.9	26.4	62.2
IT-13	24	75	646	93.8	895	129.9	6.7	9.5
	24	75	691	100.3	772	112.1*	0.7*	3.2*
	427	800	412	59.8	760	110.3	36.1	40.4
	649	1200	313	45.4	415	60.2	22.4	34.9
IT-14	24	75	741	107.5	905	131.4	1.2	3.2
	24	75	761	110.5	927	134.6	1.6	3.3
	427	800	482	70.0	918	133.3	20.8	21.8
	649	1200	382	55.5	546	79.2	17.5	24.2
IT-15	24	75	629	91.3	762	110.6	1.2	3.1
	24	75	694	100.7	772	112.1	0.5	1.7
	427	800	422	61.2	723	104.9	11.2	16.5
	649	1200	335	48.6	506	73.4	14.5	22.3
IT-16	24	75	794	115.3	907	131.6	0.5	1.5
	24	75	815	118.3	847	123.0	0.3	0.5
	427	800	531	77.1	931	135.1	10.9	11.8
	649	1200	435	63.2	594	86.2	4.5	12.0

* Failure initiated at Ta inclusion.

Although earlier studies had demonstrated that Ga additions may have potential for improving the ductility of alpha-2 titanium aluminides [18], testing of the Ga containing alloy, Ti-19.5Al-10Nb-3Ga (IT-16), resulted in very poor ductility even though its effective Al level (Al+Ga) was well below the stoichiometric level of 25 atom percent. This can in part be attributed to the less than ideal microstructure with a large prior beta grain size which was produced as a result of adiabatic heating during the extrusion process. Nevertheless, if Ga does have a beneficial effect on the ductility of alpha-2 titanium aluminide alloys, it is not significant enough to warrant the expense and difficulties encountered when preparing these alloys for melting.

Duplicate fracture toughness specimens (notched but not fatigue precracked) of each of the Task 2 alloy were tested at room temperature. These three point bend tests were conducted as specified by ASTM E399 using a loading rate of 454 kg (1000 lb) per minute. Since the specimens were not fatigue precracked, valid K_{IC} measurements were not obtained. However, the fracture toughness specimens for Tasks 1 through 4 were manufactured and tested in the same manner so that relative identification of alloying effects on fracture toughness were made possible. The $K_{experimental}$ values were calculated and are given in Table 3-12.

The results from fracture toughness testing of the Task 2 alloys show considerable improvement over those from the solid solution alloys tested in Task 1. Fractographic analysis as shown in Figure 3-23 revealed a definite relationship between roughness of the fracture surface and fracture toughness. Each of the Ti-22.5Al-6Nb-2Ta-2Cr (IT-12) fracture toughness specimens clearly revealed the most significant degree of surface roughness while the alloy IT-11 specimens exhibited a very smooth fracture surface. In general, there was a very strong direct relationship between fracture toughness and ductility of the Task 2 alloys. The only alloy which demonstrated any contradiction to this direct relationship was Ti-19.5Al-10Nb-3Ga (IT-16) which demonstrated reasonably high fracture toughness even though its ductility was relatively low.

Table 3-12 Room Temperature Fracture Toughness of Task 2 Alloys

Alloy	K_{exp} (MPa \sqrt{m})	K_{exp} (ksi \sqrt{in})
IT-10	33.6	30.6
	36.9	33.6
IT-11	20.9	19.0
	21.0	19.1
IT-12	46.7	42.5
	46.2	42.0
IT-13	38.0	34.6
	41.1	37.4
IT-14	34.7	31.6
	39.5	35.9
IT-15	36.7	33.4
	30.2	27.5
IT-16	32.3 Void Test	29.4 Void Test

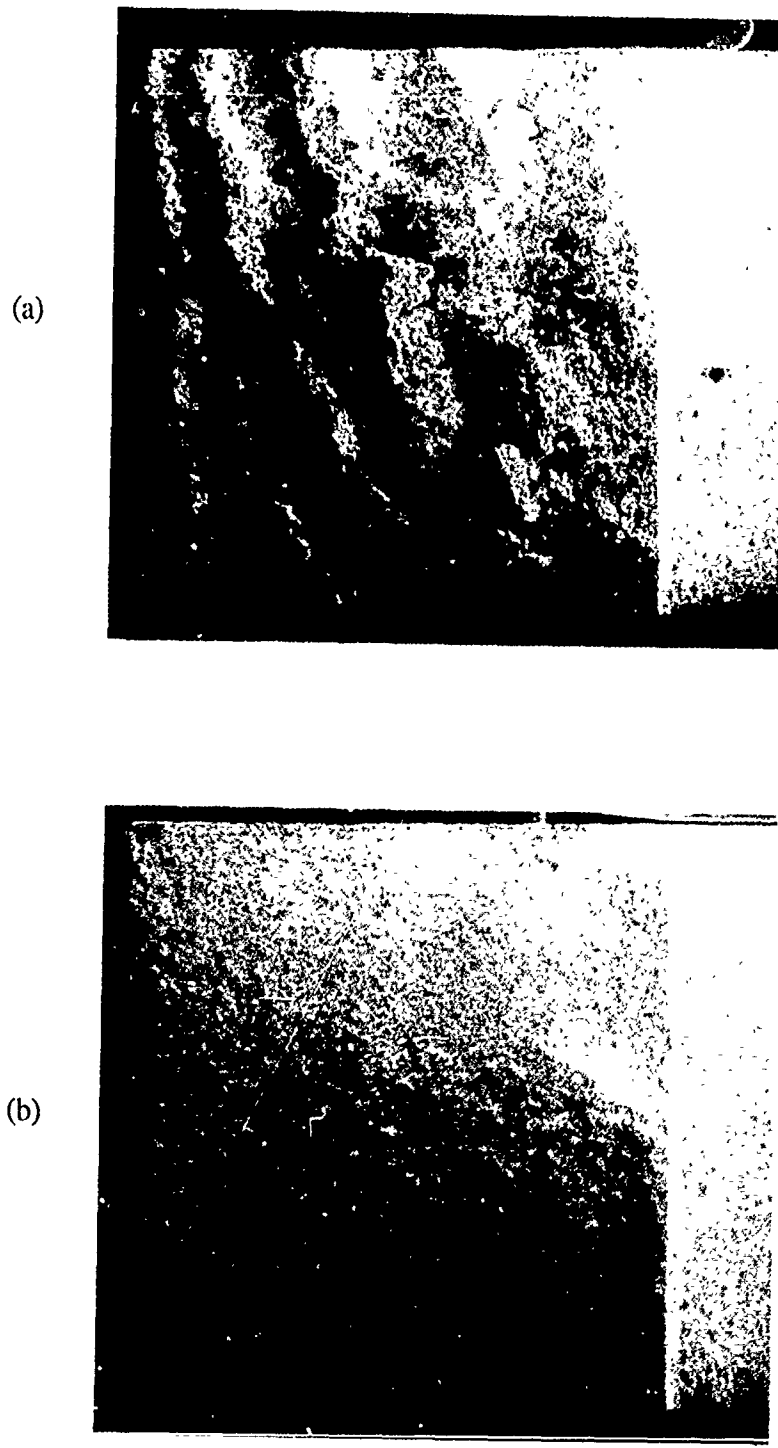


Figure 3-23 Fractographic analysis revealing overall surface roughness of fracture toughness specimens of alloys (a) Ti-22.5Al-6Nb-2Ta-2Cr (IT-12) and (b) Ti-25.0Al-4Nb-2Ta-2V-1Mo (IT-11).

3.1.2.3 Analysis of Deformation Structures

Each of the Task 2 alloys was tested in compression to approximately 2% plastic strain at room temperature, 300°C (570°F) and 500°C (930°F) and prepared for AEM analysis. The specimen preparation and evaluation procedures were conducted in the same manner as described in section 3.1.1.3 so that the orientation of a given grain was correlated to the orientation of the stress axis. Again, $c+a/2$ slip was expected only in grains with their c -axis with 15° of the compression axis.

All of the alloys showed $c+a/2$ slip when deformed at room temperature. Examples of images from this series of specimens are shown in Figures 3-24 through 3-25. In each case, the slip plane of the $c+a/2$ slip was determined to be {1121}. In some cases where the compression axis was close to the [0001] axis of the crystallite, only $c+a/2$ slip was observed but often a slip was also present. An example from the room temperature test specimen of Ti-25.0Al-4Nb-2Ta-2V-1Mo (IT-11) is seen in Figure 3-24 where some a dislocations are visible in 3-24b which were out of contrast for the g_{0002} image shown in 3-24a. One very interesting, and as yet unexplained, phenomenon observed when the {1121} slip planes of the $c+a/2$ dislocations are tilted on edge is a very thin straight line which extends along the slip plane in regions where no dislocations are present. Images using $+g$ and $-g$ are shown in Figures 3-24c and 3-24d, respectively. The reversal of contrast between this planar feature and the background is consistent with it being produced by a strain component normal to the slip plane as opposed to strain induced precipitation of a second phase. This contrast was seen in all alloys although it was not always imaged as clearly as in this example. Somewhat shorter traces can be seen in Figure 3-25 which is from Ti-22.5Al-6Nb-2Ta-2Cr (IT-12). We can see that the dislocations are coming from a lath boundary which is off to the right of the field of view. The images of the slip planes in Figure 3-25c are visible from the first groups of dislocations on each plane back to the boundary. The dislocations often appear to be grouped in pairs which might be expected to arise either from some splitting of a superdislocation into superpartials or due to the presence of dipoles. The former explanation is not supported by any evidence of APB or stacking fault contrast which would be visible when the slip plane is tilted over. If the image of the slip plane were being produced by some such fault it would be expected to go in and out of contrast after a set number of dislocations had passed. No evidence of this has been found. Figures 3-14a and 3-14b have been taken with opposite g vectors to test the hypothesis of dipoles. The oscillatory contrast of the fringes reverses uniformly for each dislocation and there is no apparent lateral shift as would be expected between dipoles. Thus the "grouping" is probably random.

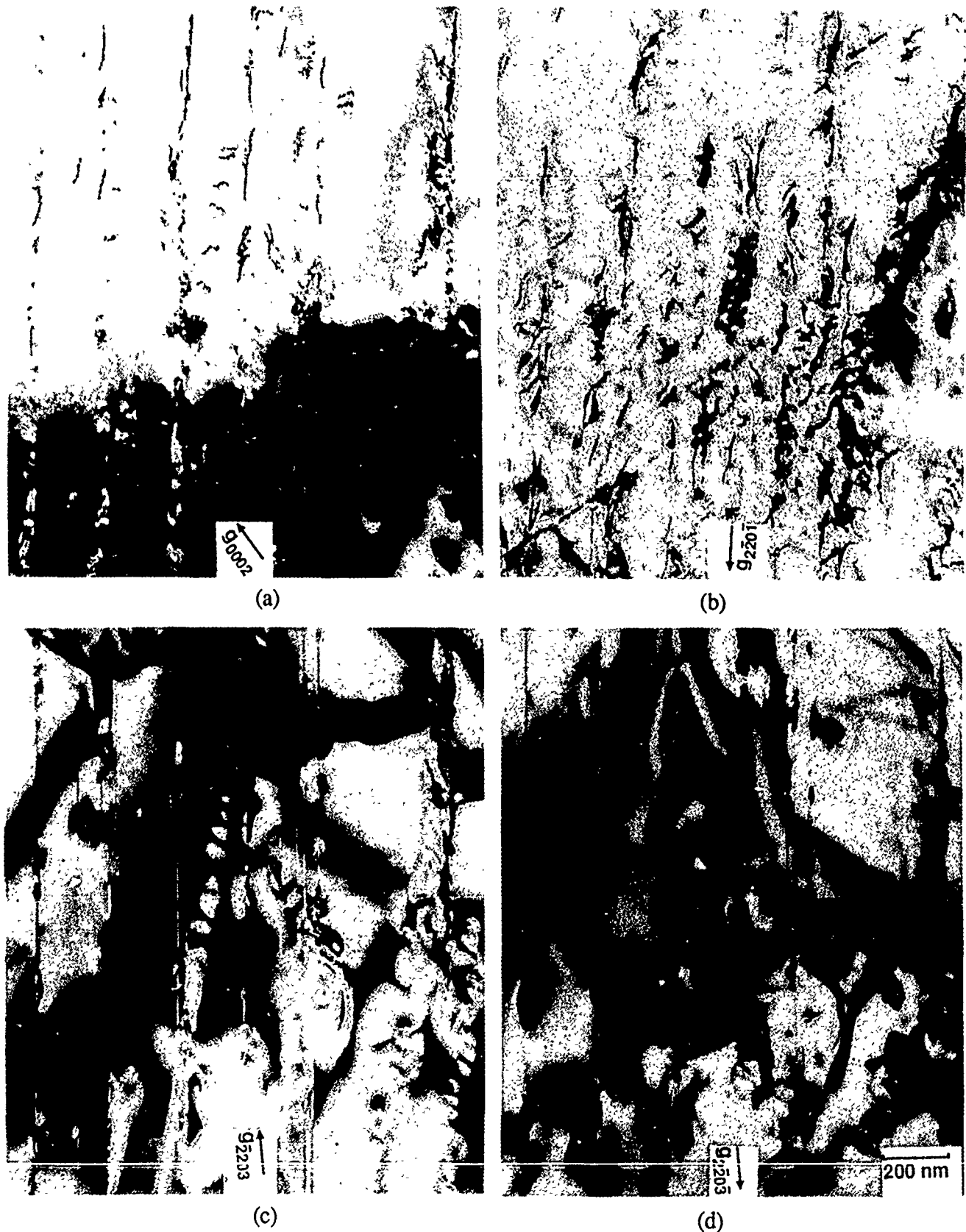


Figure 3-24 TEM micrographs of $c+a/2$ dislocations in a Ti-25.0Al-4Nb-2Ta-2V-1Mo (IT-11) specimen which was deformed at room temperature.

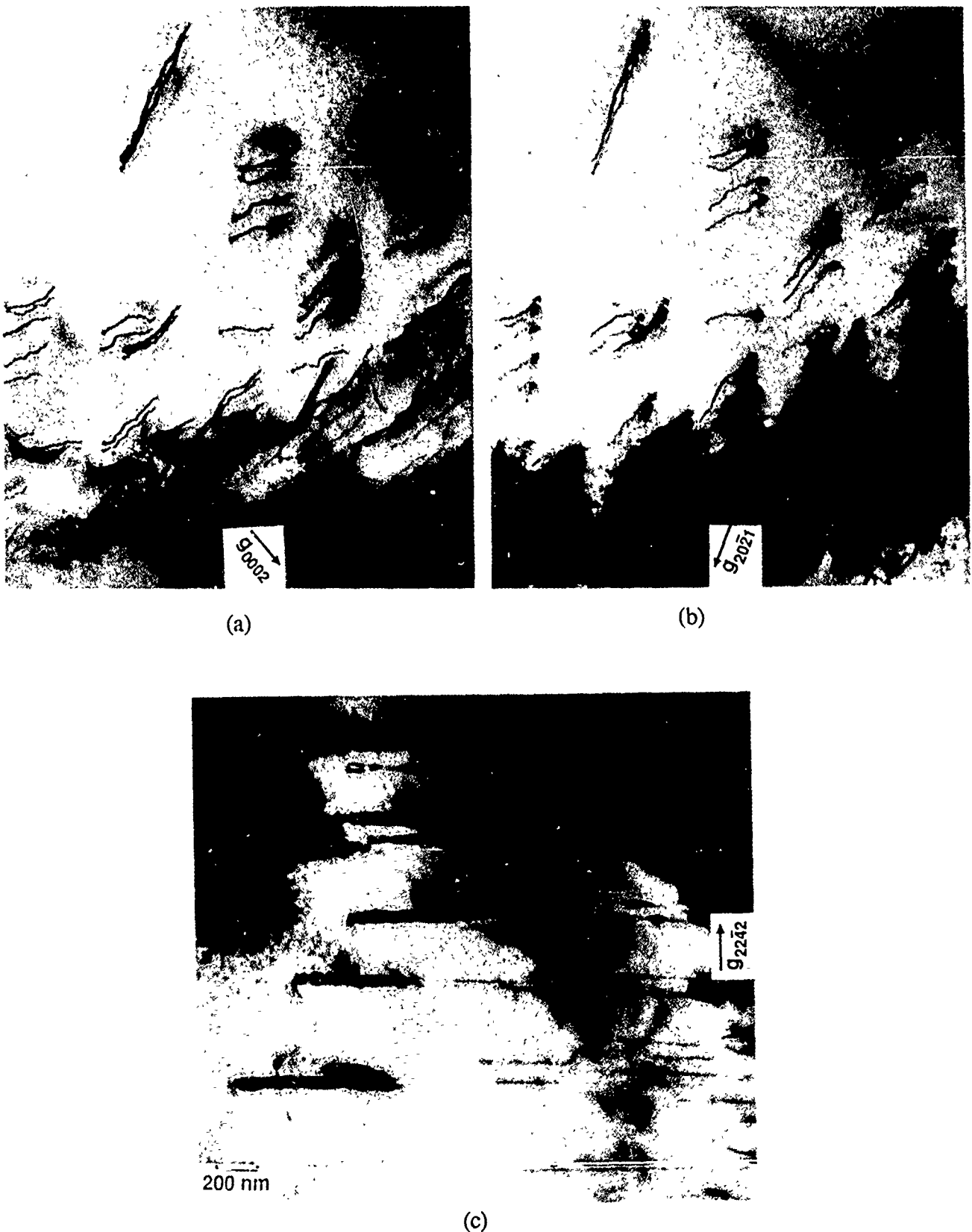


Figure 3-25 TEM micrographs of $c+a/2$ dislocations in a Ti-22.5Al-6Nb-2Ta-2Cr (IT-12) specimen which was deformed at room temperature.



(a)



(b)



(c)

Figure 3-26 TEM micrographs of $c+a/2$ and a dislocations in a Ti-22.5Al-5Nb-5Ta-3Zr (IT-14) specimen which was deformed at room temperature.

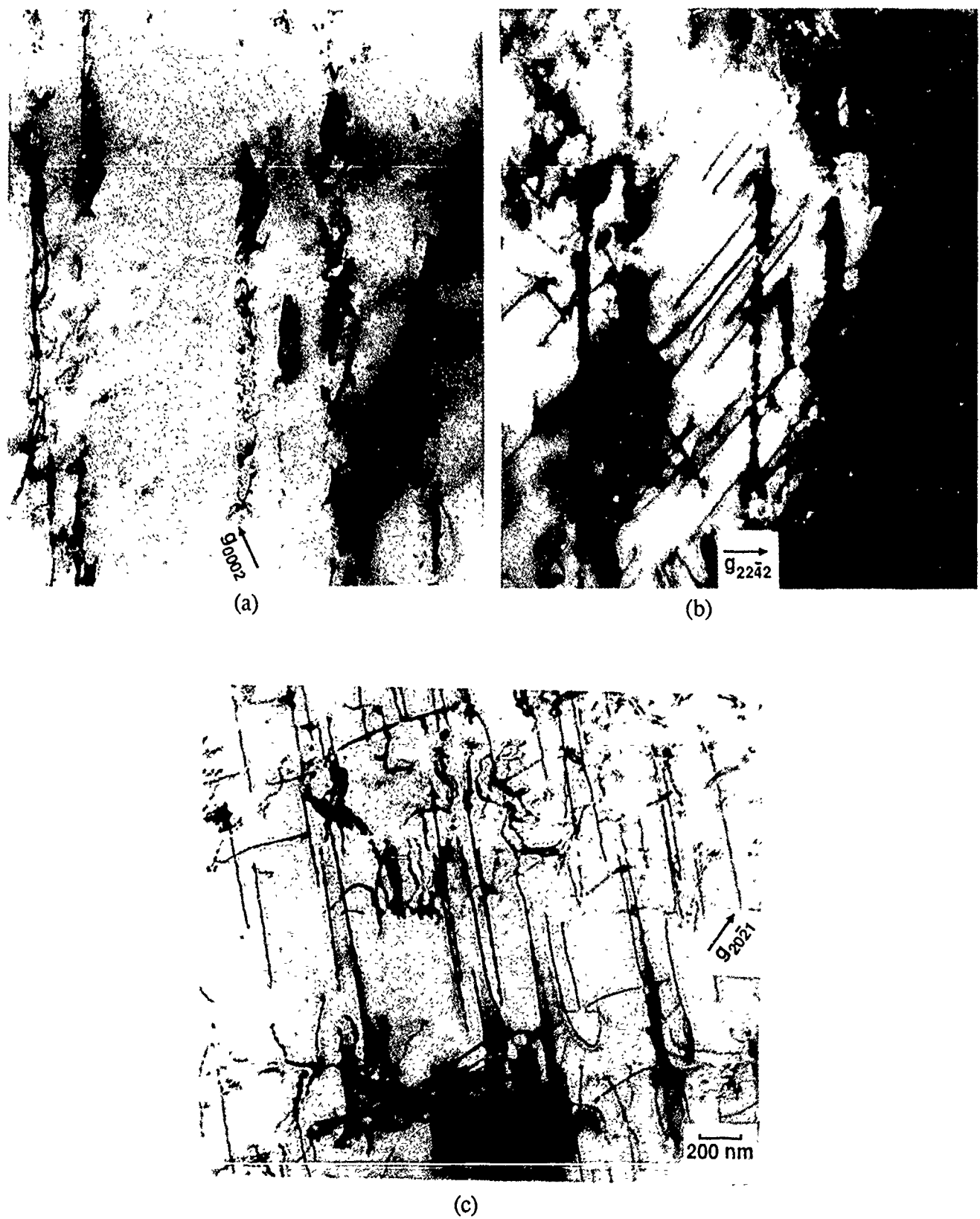


Figure 3-27 TEM micrographs of $c+a/2$ and a dislocations in a Ti-19.5Al-10Nb-3Ga (IT-16) specimen which was deformed at room temperature.

The micrographs of Ti-22.5Al-5Nb-5Ta-3Zr (IT-14), shown in Figure 3-26, show two interesting features. First, the images of the $\{11\bar{2}1\}$ slip planes are not as thin as those in the other micrographs. Some of this may be due to the slightly higher density of dislocations on the slip planes but it also appears as if interactions with dislocations on intersecting slip planes have caused some spreading of the dislocations on to other parallel planes. Secondly, the images of the a dislocations (most visible in Figure 3-26b) show some dislocation loops and other features which are evidence of more dislocation interactions. This is quite different from the situation in Figure 3-27, taken from Ti-19.5Al-10Nb-3Ga (IT-16), where the a dislocations are very straight and do not seem to have been affected by intersecting slip.

The dislocation structure did not change very much as the deformation temperature was increased to 300°C (570°F) but the incidence of $c+a$ slip in grains that were significantly off-axis decreased. Two examples are shown in Figures 3-28 through 3-30. The first figure is from Ti-22.5Al-4Nb-2Ta-2V-1Mo (IT-10) and shows a grain that has undergone considerable deformation with both $c+a$ and a slip. An additional feature of this lath was that it contained a large number of APBs. Figures 3-28b and 3-28c are both dark-field images taken with the superlattice reflection $g_{10\bar{1}1}$ but at slightly different values of s . Thermal APBs are visible in the former image and slip-produced ones can be seen in the latter. This difference in the visibility is unusual and suggests a different form of APB. Note that the slip-produced APB is due to a slip. The thermal APBs had been observed in many of the room temperature tested specimens as well, but only in the alpha-2 laths (transformed-beta) but not in the primary alpha-2 grains. More work is needed to see if their presence in Figure 3-28 was merely the result of this being a large alpha-2 lath, or whether the temperature itself is playing a role. Figure 3-29 is a series of micrographs which show dislocations in Ti-22.5Al-6Nb-2Ta-2Cr (IT-12). The specimen shows very little difference from the room-temperature strained specimen and contains both a and $c+a$ slip. The dark contrast features were identified by EDS as being Cr rich and have been assumed to be $TiCr_2$. One alloy which still showed a significant amount of $c+a$ slip at this intermediate temperature was Ti-22.7Al-3Nb-3Ta-3V (IT-13) and it is shown in Figure 3-30. All three sets of slip planes have been identified as $\{11\bar{2}1\}$.

The alloy Ti-22.7Al-3Nb-3Ta-3V (IT-13) was also the only one to show a significant amount of $c+a$ slip at the highest temperature tested, 500°C (930°F). This is illustrated in Figure 3-31 which shows $c+a$ slip, again on $\{11\bar{2}1\}$, and a slip on prism planes. More typical of the other alloys tested at this temperature is Ti-19.5Al-10Nb-3Ga (IT-16), as shown in Figure 3-32. In the large alpha-2 lath visible in Figure 3-32a, there is very little $c+a$ or a slip. The fine alpha-2 laths of the transformed beta show a much higher dislocation density. It appears that the large lath, which is at almost the ideal angle for $c+a$ slip to be favored, must be elastically hard compared to the adjacent colonies. Indeed, this was the most surprising aspect of this dislocation study : contrary to expectation, the proportion of $c+a$ slip actually decreased as the deformation temperature was raised.

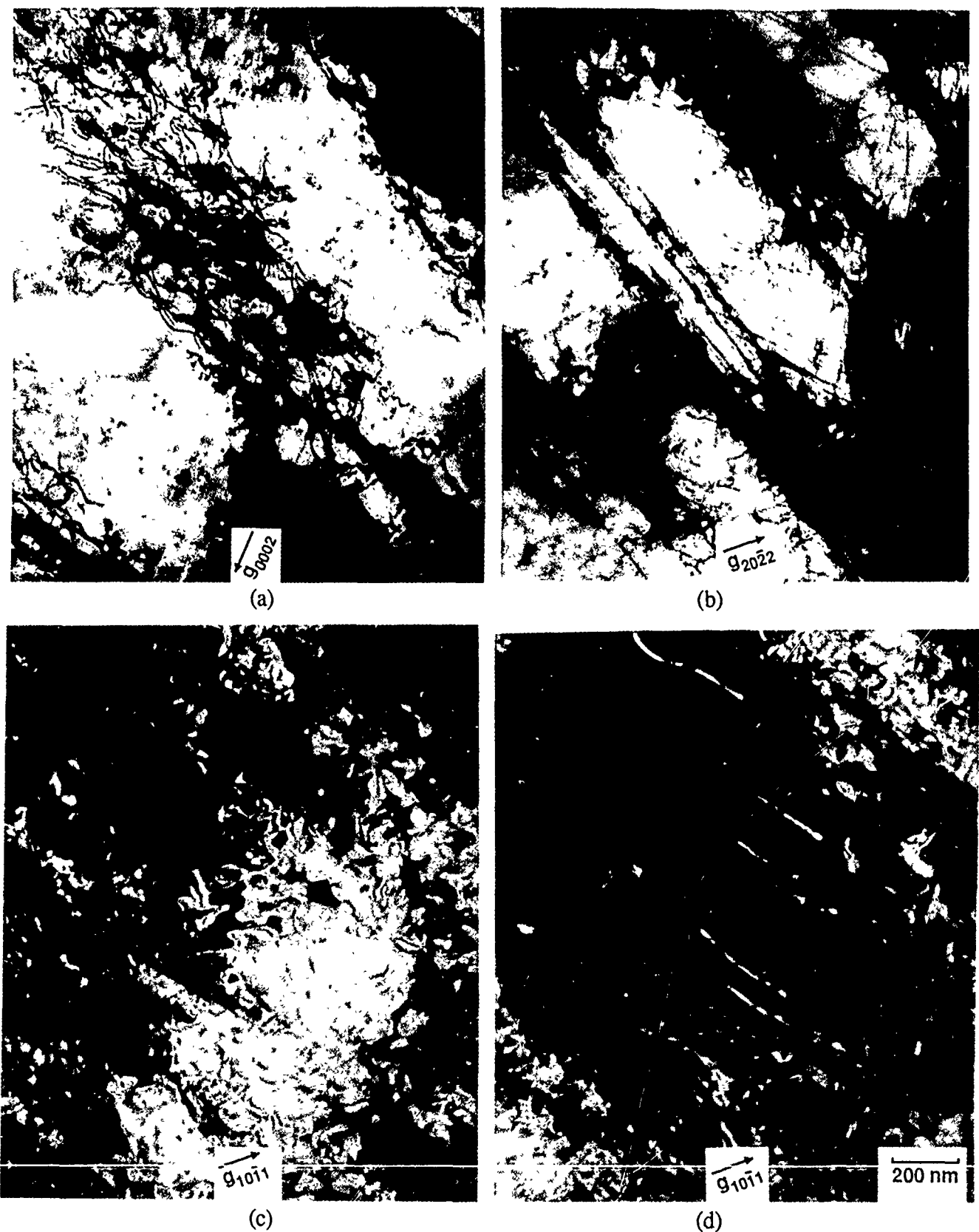


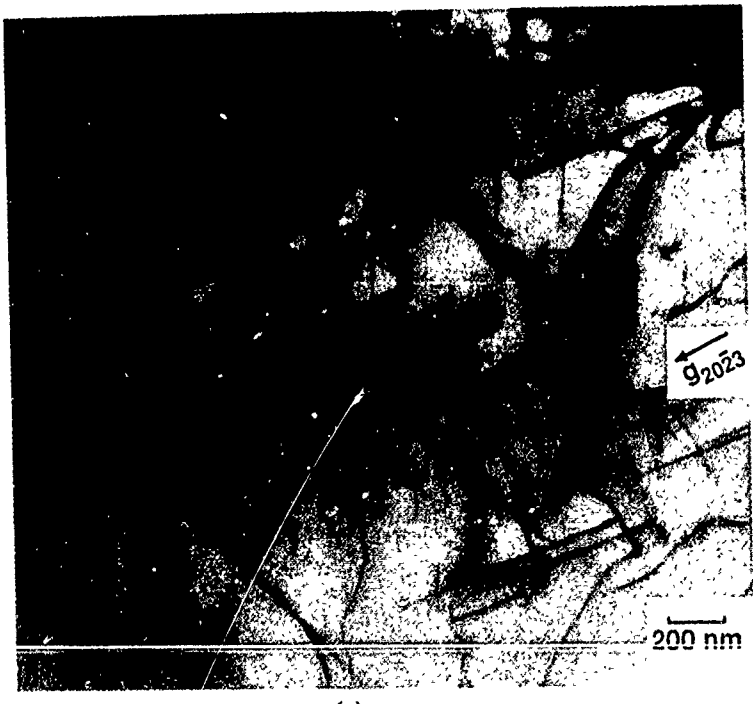
Figure 3-28 TEM micrographs of $c+a/2$ and a dislocations plus APB's in a Ti-22.5Al-4Nb-2Ta-2V-1Mo (TT-10) specimen which was deformed at 300°C (570°F).



(a)



(b)



(c)

Figure 3-29 TEM micrographs of $c+a/2$ and a dislocations in a Ti-22.5Al-6Nb-2Ta-2Cr (IT-12) specimen which was deformed at 300°C (570°F).

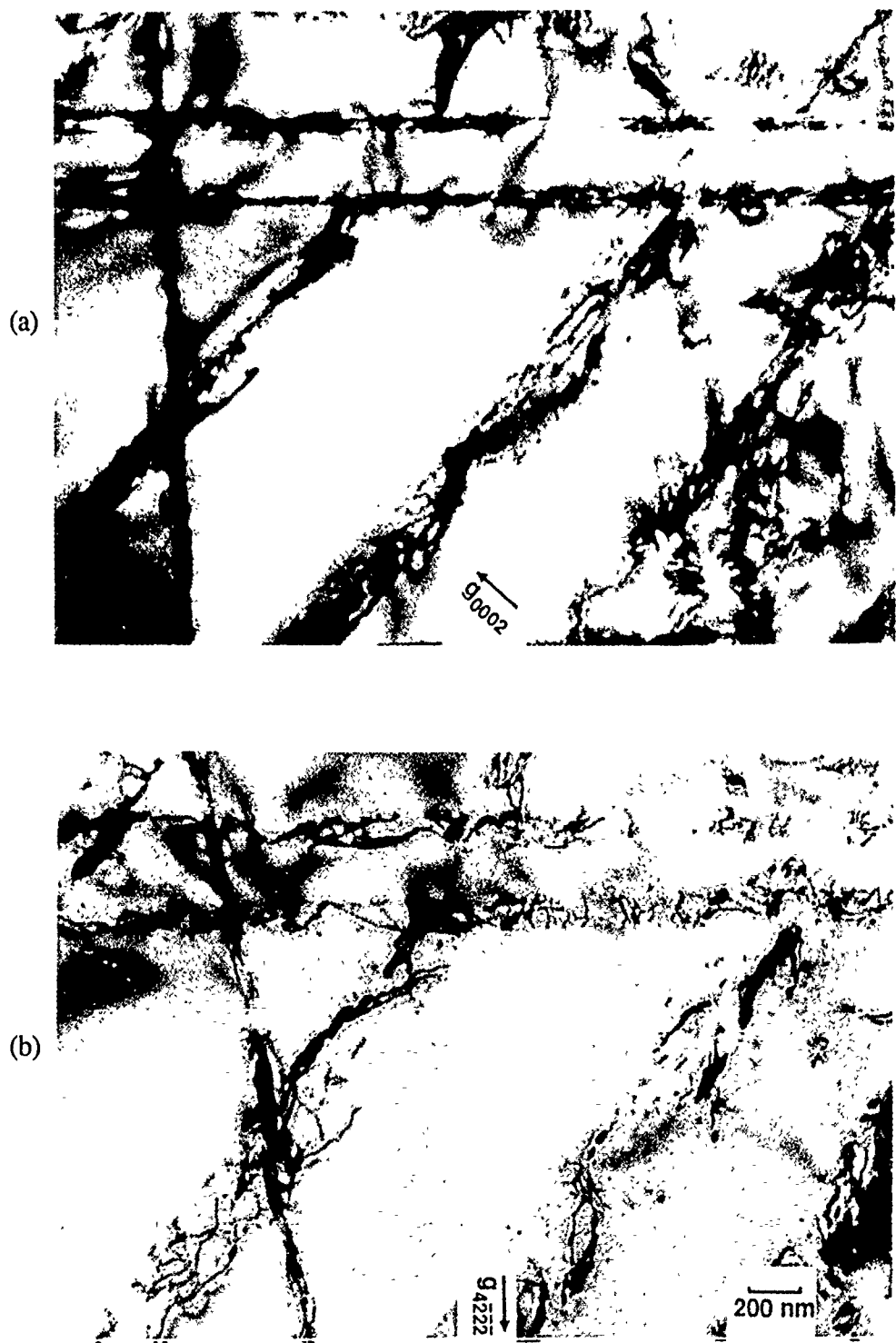


Figure 3-30 TEM micrographs of $c+a/2$ dislocations in a Ti-22.7Al-3Nb-3Ta-3V (IT-13) specimen which was deformed at 300°C (570°F).

This observation raises the question of how the c component accommodations are achieved at these intermediate temperatures where we know that the ductility is increasing. At least in this series of alloys, it appears that the accommodation is achieved in the beta phase, by interface sliding, and/or by deformation of the surrounding colonies. In effect, the alpha-2 grains with c axes oriented parallel to the stress axis do not have to deform. They appear to act as hard particles while the surrounding "soft" grains produce the necessary accommodation strains.

Deformation of the beta phase itself is difficult to judge in most of these alloys since the beta ribs are thin and there is little opportunity to observe well defined slip traces. In addition, the beta stabilizing elements tend to be of high atomic number, making penetration by the electron beam harder than for the alpha-2 phase of equivalent thickness. If these effects were not sufficient, the additional strain effects associated with omega phase in leaner alloys compounds the difficulty. One alloy which clearly showed the deformation modes of the beta phase was Ti-22.5Al-6Nb-2Ta-2Cr (IT-12). Figure 3-33a and 3-33b show how simply slip transfer can occur between the alpha-2 and beta for basal slip. The Burgers orientation relationship between the alpha-2 and beta produces parallel close packed planes and directions:

$$(0001)_{\text{alpha-2}} \parallel (110)_{\text{beta}} \\ [11\bar{2}0]_{\text{alpha-2}} \parallel [1\bar{1}1]_{\text{beta}}$$

It might be expected therefore that $1/6[11\bar{2}0]$ superpartials could transfer to the beta phase and become $1/2[1\bar{1}1]$ dislocations without generating a lot of debris, and consequently, without generating a lot of backstress. Offsets can clearly be seen at the alpha-2/beta interfaces although we should note that the step marked by the arrow is in the opposite sense to the smaller ones in the adjacent laths. Also, it is not quite aligned with the dominant slip trace. These large angular steps were seen fairly frequently in many alloys and may be a result of the beta->alpha transformation. We plan on examining some unstrained specimens to check out this hypothesis. The features certainly would be expected to be stress raisers and could possibly play a role in nucleating the coarse slip. The compound formation and associated cusps in the alpha-2 / beta interface shown in Figure 3-33c may play a similar role.

One other consequence of the Burgers relationship is that the following two sets of pyramidal planes in the alpha-2 are also very nearly parallel to $\{110\}$ planes in the beta. Specifically :

$$(2\bar{2}01)_{\text{alpha-2}} \text{ 1.6° from } \parallel (011)_{\text{beta}} \\ (\bar{2}201)_{\text{alpha-2}} \text{ 1.6° from } \parallel (101)_{\text{beta}}$$

These $\{20\bar{2}1\}_{\text{alpha-2}}$ planes are equivalent to $\{10\bar{1}1\}_{\text{alpha}}$ on which a slip has been observed in alpha titanium alloys. These planes contain the same $[11\bar{2}0]$ Burgers vector which is again parallel to the $[1\bar{1}1]$ in the beta. Thus it is conceivable that "cross-slip" could also occur between these two systems. Heavy slip on these $\{110\}$ planes is observed in Figure 3-33 but very little, if any, appears to have crossed into the alpha-2. Two hypotheses are put forward to explain this: 1) this is simply because $\{20\bar{2}1\}$ has a very high Peierls stress in alpha-2, or 2) the dislocations in the beta do not have the necessary Burgers vector to translate to a slip. The latter explanation results from the existence of two $<111>$ directions in each $\{011\}$ plane. Because of the Burgers orientation

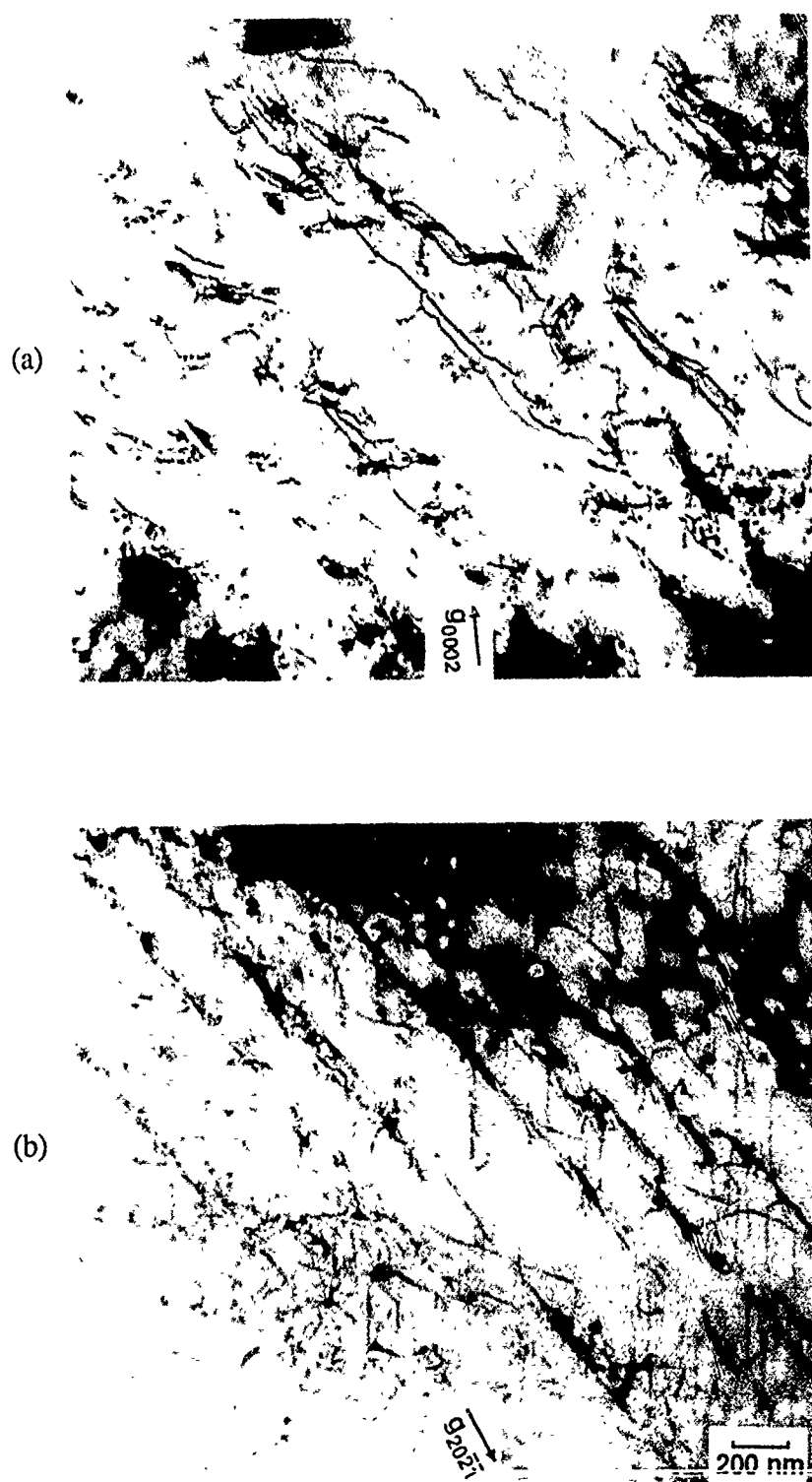


Figure 3-31 TEM micrographs of $c+a/2$ and a dislocations in a Ti-22.7Al-3Nb-3Ta-3V (IT-13) specimen which was deformed at 500°C (930°F).

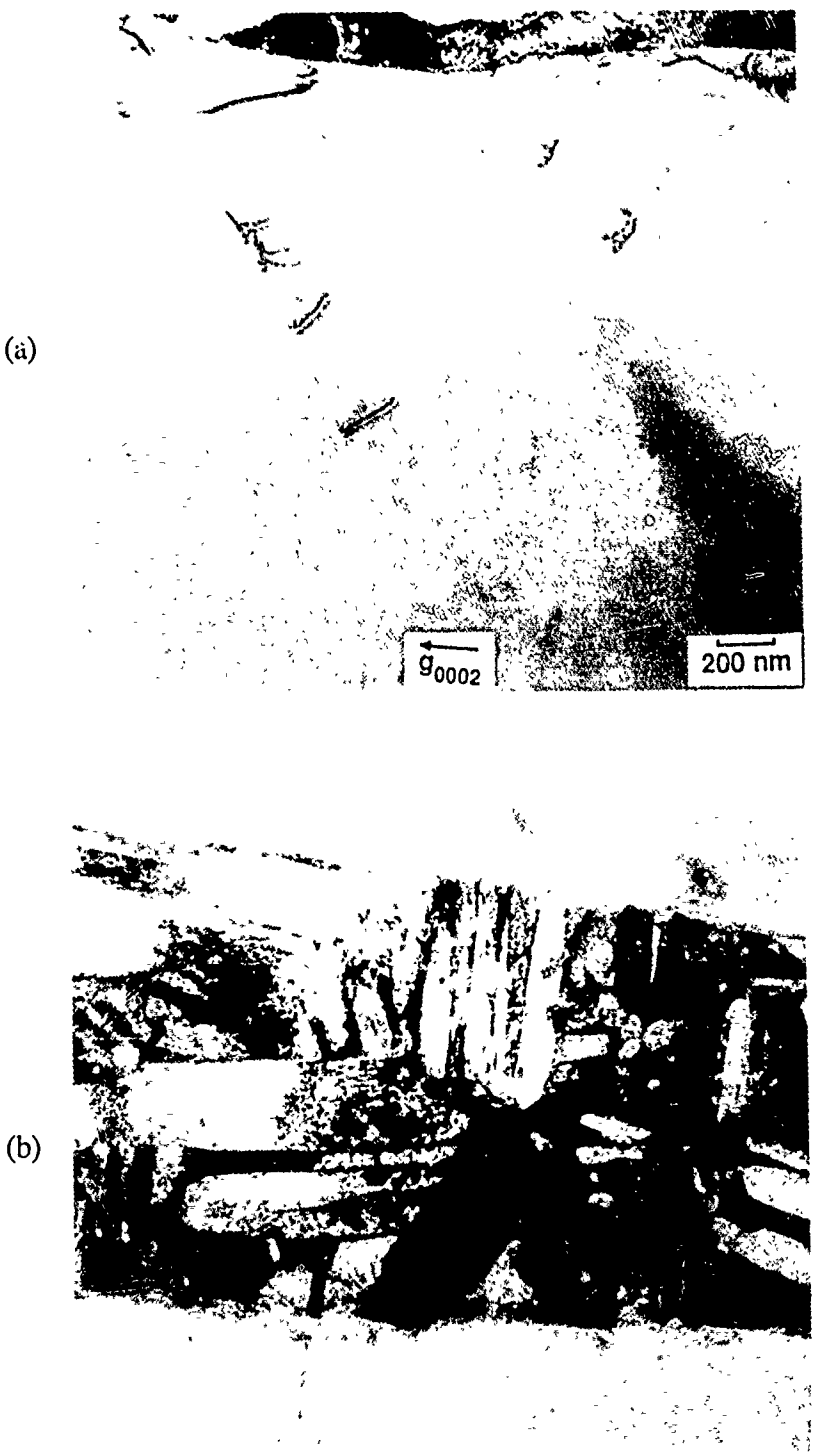


Figure 3-32 TEM micrographs of inhomogeneous slip distribution in a Ti-19.5Al-10Nb-3Ga (IT-16) specimen which was deformed at 500°C (930°F).

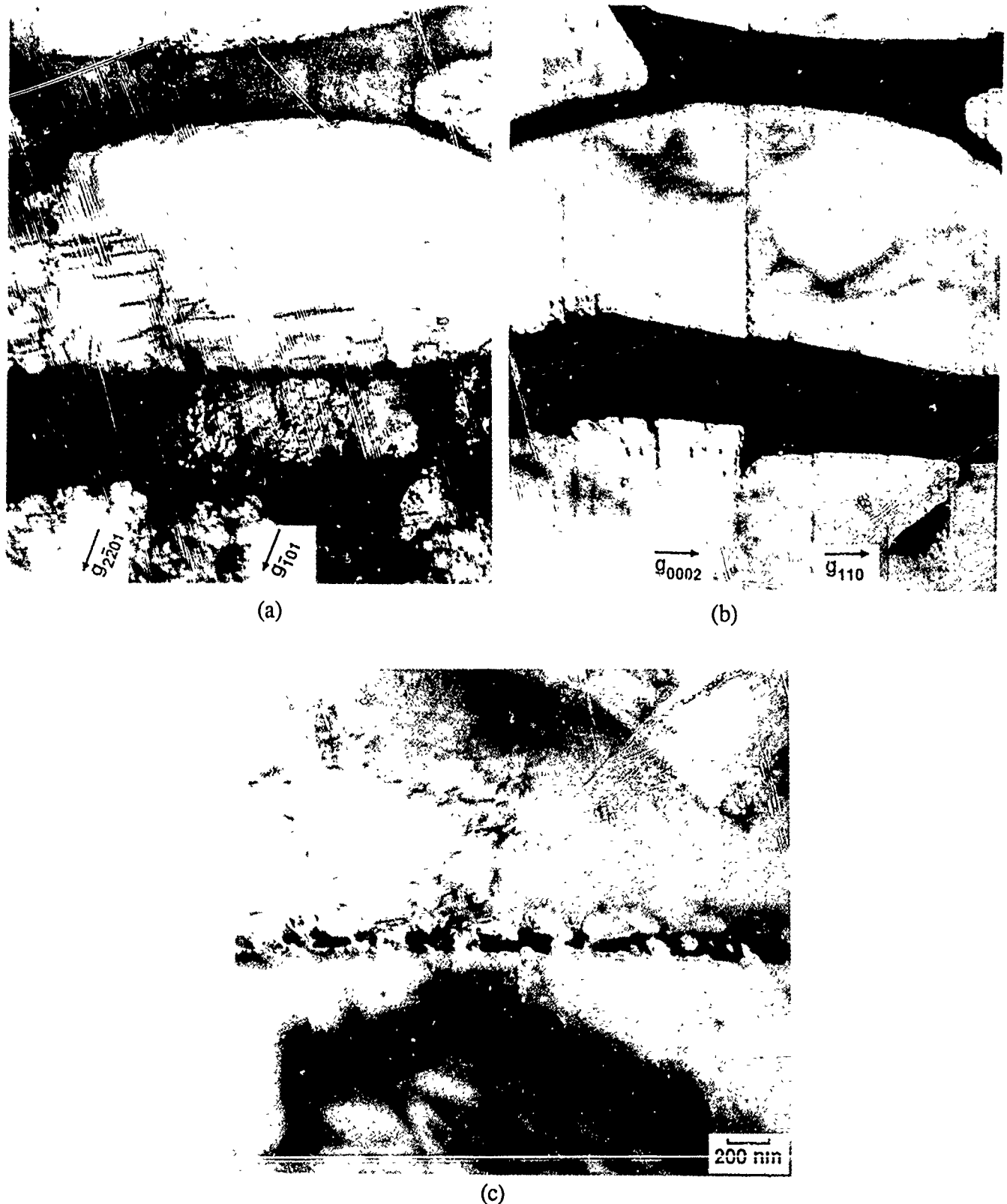


Figure 3-33 TEM micrographs of a slip transfer across an alpha-2/beta interface in a Ti-22.5Al-6Nb-2Ta-2Cr (IT-12) specimen which was deformed at 300°C (570°F).

relationship, only one $\langle 111 \rangle$ is parallel to a $\langle 11\bar{2}0 \rangle$ in the alpha-2. The other $\langle 111 \rangle$ is 3.1° away from a $\langle 11\bar{2}6 \rangle$ direction. If the operative Burgers vectors in Figure 3-33 were of this type, they would thus have to transfer to $c+a/2$ slip with an increase in the magnitude of the Burgers vector. This would require a complex interaction between successive $\{111\}$ dislocations and would probably be disfavored.

3.1.2.4 Alternate Microstructure

The alloys Ti-22.5Al-6Nb-2Ta-2Cr (IT-12) and Ti-22.7Al-3Nb-3Ta-3V (IT-13) were selected for additional study of the microstructure/property relationships of alloys which contain a small fraction of retained beta phase. Each of these alloys was given a beta solution heat-treatment to produce the microstructures shown in Figure 3-34c and 3-34d. Previously, these alloys were produced with a refined microstructure consisting of primary alpha-2 in a transformed beta matrix as shown in Figures 3-34a and 3-34b.

The tensile test results from the two microstructures of Ti-22.5Al-6Nb-2Ta-2Cr (IT-12) and Ti-22.7Al-3Nb-3Ta-3V (IT-13) are presented in Table 3-13. These results are very similar to the results of the microstructure/property study conducted on the solid solution alloys in Task 1 since higher strength levels are achieved in the beta solution treated materials at the expense of ductility. During room temperature testing of both Ti-22.5Al-6Nb-2Ta-2Cr (IT-12) and Ti-22.7Al-3Nb-3Ta-3V (IT-13), one beta solution treated specimen failed prior to reaching the 0.2% yield strength and the duplicate room temperature test specimen failed just after reaching 0.2% elongation. Room temperature testing of the refined microstructures of each alloy resulted in ductility levels as high as 4.8 and 6.7% elongation for Ti-22.5Al-6Nb-2Ta-2Cr (IT-12) and Ti-22.7Al-3Nb-3Ta-3V (IT-13), respectively. Moreover, during the initial screening of the Task 2 alloy tensile properties, all of the alloys which were processed and heat treated in the alpha-2 plus beta phase field were shown to have higher ductility than the beta solution treated versions of Ti-22.5Al-6Nb-2Ta-2Cr (IT-12) and Ti-22.7Al-3Nb-3Ta-3V (IT-13). Clearly, this indicates that the subject variations in microstructure have had a more significant effect on ductility than the variations in chemical composition studied in Task 2.

The fracture toughness data for the two microstructures of Ti-22.5Al-6Nb-2Ta-2Cr (IT-12) and Ti-22.7Al-3Nb-3Ta-3V (IT-13) are given in Table 3-14. For both alloys, the material with a refined microstructure exhibited higher fracture toughness than the material with a microstructure produced by beta solution treatment. Neither of the microstructures produced by beta solution treatment of Ti-22.5Al-6Nb-2Ta-2Cr (IT-12) and Ti-22.7Al-3Nb-3Ta-3V (IT-13) contained large alpha-2 colonies which could promote crack branching for improved fracture toughness. In fact, observation of the fracture surfaces of these Task 2 alloys indicates that there is much more secondary cracking and a more tortuous fracture path with a refined microstructure produced by extrusion and heat-treatment below the beta transus temperature than for a fine Widmanstatten microstructure produced by beta solution heat-treatment. Therefore, the microstructure which promoted the highest ductility was also associated with higher fracture toughness.

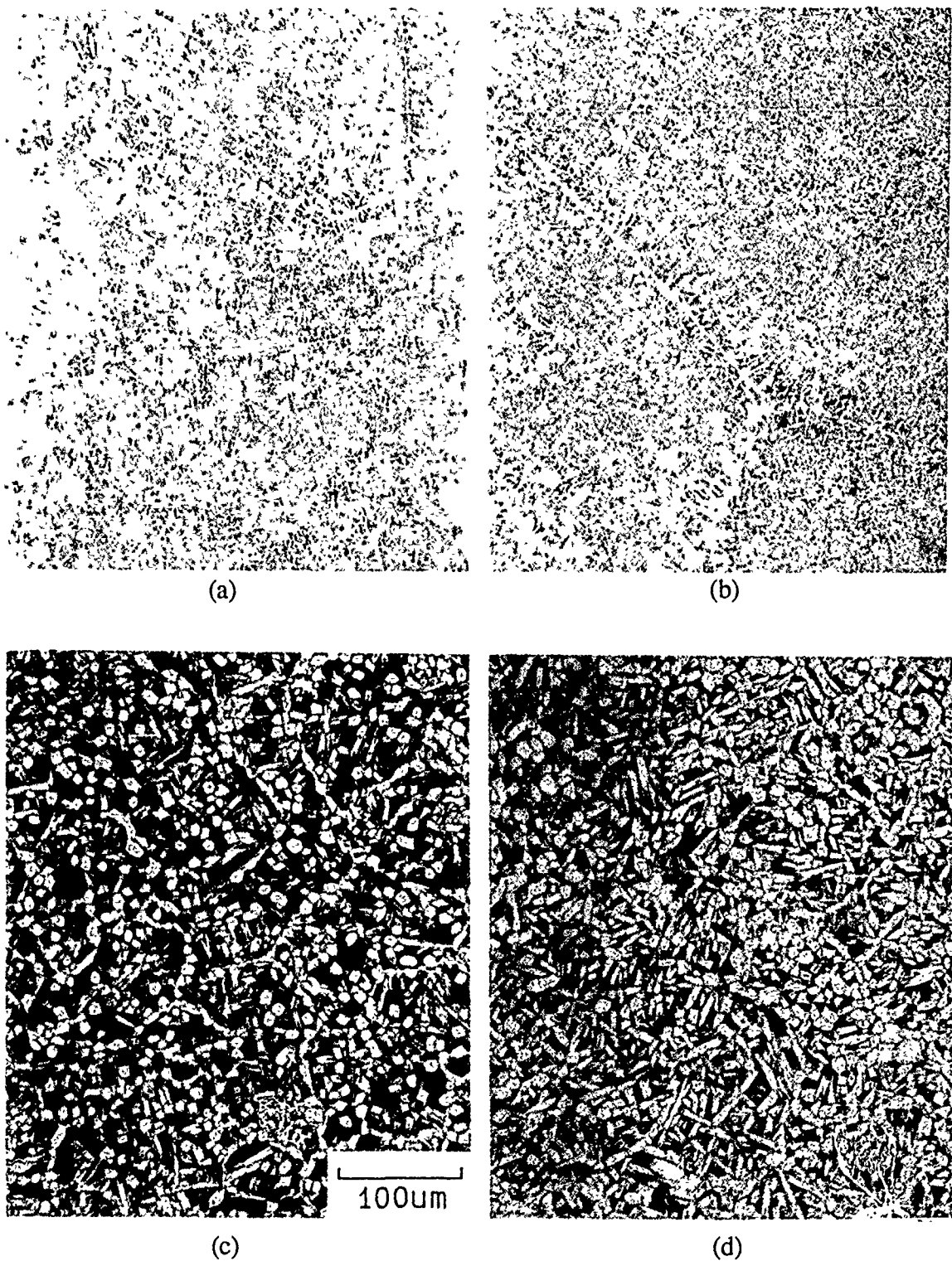


Figure 3-34 Microstructures of beta solution treated material of (a) Ti-22.5Al-6Nb-2Ta-2Cr (IT-12) and (b) Ti-22.7Al-3Nb-3Ta-3V (IT-13), and duplex microstructures produced by heat-treatment within the alpha-2 plus beta phase field of alloys (c) IT-12 and (d) IT-13.

Table 3-13 Tensile Properties for Microstructural Study of Task 2 Alloys

Alloy / Condition	Temp °C	Temp °F	0.2YS MPa	0.2YS ksi	UTS MPa	UTS ksi	El %	RA %
IT-12	24	75	668	97.0	861	124.9	3.2	5.1
	24	75	668	97.0	899	130.5	4.8	5.0
	427	800	437	63.4	825	119.7	36.5	37.4
	649	1200	316	45.9	413	59.9	26.4	62.2
IT-12(B)	24	75	-	-	1032	149.8	0.1	-
	24	75	986	143.1	986	143.1	0.2	-
	427	800	649	94.2	882	128.0	9.7	13.2
	649	1200	462	67.1	611	88.7	12.7	21.8
IT-13	24	75	646	93.8	895	129.9	6.7	9.5
	24	75	691	100.3 *	772	112.1 *	0.7 *	3.2 *
	427	800	412	59.8	760	110.3	36.1	40.4
	649	1200	313	45.4	415	60.2	22.4	34.9
IT-13(B)	24	75	1038	150.7	1047	151.9	0.25	-
	24	75	-	-	1010	146.6	0.1	-
	427	800	758	110.0	967	140.3	6.7	9.7
	649	1200	524	76.1	714	103.6	4.3	7.6

(B) = Beta Solution Heat Treatment

* = Specimen failed at Ta defect

Table 3-14 Fracture Toughness Test Results for the Microstructural Study of Task 2 Alloys

Alloy / Condition	K_Q (MPa \sqrt{m})	K_Q (ksi \sqrt{in})
IT-12	46.7	42.5
	46.2	42.0
IT-12(B)	32.6	29.6
	34.7	31.5
IT-13	38.0	34.6
	41.1	37.4
IT-13(B)	30.8	28.0
	38.2	34.7

(B) = Beta Solution Heat Treatment

3.1.2.5 Task 2 - Summary

The Phase I, Task 2, alpha-2 plus beta alloy compositions were produced by adding larger amounts of beta stabilizing additions and lower levels of Al. As expected, these alloys were generally shown to have higher ductility and fracture toughness than the solid solution alloys. In addition, clear relationships were established between microstructural variables and mechanical properties. For the alloys Ti-22.5Al-6Nb-2Ta-2Cr (IT-12) and Ti-22.7Al-3Nb-3Ta-3V (IT-13), ductility was significantly higher for the refined microstructure produced by extrusion and heat treatment below the beta transus temperature than for the microstructure produced by beta solution heat treatment. Likewise, fracture toughness was improved by processing and heat treatment which refined the microstructure. As with the solid solution alloys, strength was improved with beta solution heat treatment; however, it is difficult to justify this heat treatment due to the associated reduction of ductility and fracture toughness.

Analysis of the deformation structures of the Phase I, Task 2 compression specimens revealed findings similar to those of Phase I, Task 1. No specific alloying addition was found to have a clear influence on the density of $c+a/2$ slip, and the density of $c+a/2$ slip was not found to increase with increasing test temperature. In fact, it was evident that the density of $c+a/2$ slip actually decreased with increasing test temperature at the small strain levels (~2.0% plastic strain) studied in this program. Furthermore, an inhomogenous distribution of deformation was found to be prevalent in the elevated temperature test specimens. That is, it was common to find adjacent grains in the elevated temperature test specimens with very high and very low densities of a slip. This variation in dislocation density was clearly a function of the orientation of the grain with respect to the compression axis. At room temperature, this dislocation density effect was less obvious.

3.1.3 Task 3 - Dispersoid Containing Alloys

The chemical compositions of the Task 3 alloys are given in Table 3-15. In general, the aim of Task 3 was to assess whether the presence of a dispersion of Er_2O_3 particles might impart some ductility to Ti_3Al by reducing the planarity of slip. For this reason, it was considered important to study some alloys without the retained beta phase. If the dispersed oxide was the only second phase present, the influence of the dispersion on mechanical properties could be determined. The alloys Ti-25Al-5Nb-1.5%Er (IT-18) and Ti-25Al-5Nb-3.0%Er (IT-19) were chosen as base compositions. Niobium was added to these alloys since the binary compound exhibits such a lack of ductility and a more practical assessment of the rôle of a dispersion might be achieved in an alloyed version of the compound. Niobium was chosen as an alloying addition since it is known to impart ductility to alloys based on Ti_3Al ; however, the alloying level was set at 5 atom percent since it was considered important to maintain a single phase matrix. The different levels of Er for these alloys were chosen to determine the influence of the volume fraction of Er_2O_3 on mechanical properties. A third 'single phase' alloy, Ti-25Al-5Nb-5Ga-1.5%Er (IT-20), was chosen on the basis of previous work which showed an improvement in ductility with Ga additions. There is some controversy concerning the role of Ga. Some workers have identified the presence of Ti_2Ga which was thought to improve ductility while others suggest that improved ductility results from a reduced c/a ratio and lower anti-phase boundary energy caused by Ga additions.

Several additional alloys which contain retained beta phase were also selected for evaluation in Task 3. The beta containing alloys Ti-24Al-11Nb-1.5%Er (IT-17), Ti-25Al-5Nb-5Ta-1.5%Er (IT-21), and Ti-25Al-5Nb-5Ta (IT-22) were chosen on the basis of the ductility already exhibited by alloys without the Er addition. With these alloys, it is possible to explore any synergistic or additive effects of the Er_2O_3 dispersion and beta phase on mechanical properties. In addition, the alloy Ti-25Al-5Nb-5Ta (IT-22) was selected as a baseline alloy to monitor the effects of powder processing which are unrelated to the addition of Er.

3.1.3.1 Consolidation and Extrusion

Extrusion of the atomized powders became an iterative process due to the use of previously untested parameters. Sufficient material was required of each alloy so that an appropriate number of test samples would be available for the mechanical testing program. In each case, we thought that approximately 150 g (0.33 lb) of powder would be sufficient for each alloy. However, the alloys were to be extruded using the facilities at WRDC which require the use of a rather large extrusion can, with a volume of approximately 700 cm^3 (43 in³). Therefore, it was necessary to make use of a thick-walled can. In the first attempt at extrusion, the cans were fabricated from Ti-6-4 with a wall thickness of approximately 2.5 cm (1.0 in). The welded cans were heated to the extrusion temperature 1040°C (1900°F), loaded into the press, and extruded directly at a ratio of 8:1. The resulting aluminide core material varied in diameter significantly and only partial densification was achieved. We thought that two factors might have contributed to the poor quality of the extruded material. Firstly, the thickness of the extrusion can was significant so that much of the deformation induced during extrusion was taken up in the material of the can. As a result, the powders were not sufficiently deformed to permit densification and inter-particle bonding. Secondly, the cans were extruded directly, without being hot-compacted by blind-die extrusion.

Table 3-15 Compositions of Task 3 Alloys

Alloy	Ti	Al	Nb	Ga	Ta	Er
atom %, aim; volume % Er aim						
IT-17	65	24	11			1.5
IT-18	70	25	5			1.5
IT-19	70	25	5			3.0
IT-20	65	25	5	5		1.5
IT-21	65	25	5		5	1.5
IT-22	65	25	5		5	
weight %, aim/(actual)						
IT-17	65.1	13.5 (13.0)	21.4 (19.9)	.		1.3
IT-18	74.6	15.0 (15.3)	10.3 (9.3)			1.4
IT-19	74.6	15.0	10.3			2.3
IT-20	67.7	14.7 (15.2)	10.1 (9.0)	7.6 (6.9)		1.3
IT-21	60.4	13.1 (12.5)	9.0 (8.7)		17.5 (15.5)	1.2
IT-22	60.4	13.1 (12.7)	9.0 (8.8)		17.5 (16.7)	

A second set of atomized powders of the six alloys were produced, canned, and submitted for extrusion due to the poor quality of the first extrusions. The second set of cans had thinner walls (approximately 1.9 cm (0.75 in)) and the powder quantity in each can was increased to approximately 250 g (0.5 lb). Prior to extrusion, the cans were blind-die extruded, re-coated with lubricant, and subsequently extruded using the same conditions as listed above. These extrusions were only marginally better than those done initially. Once again, the diameter of the aluminide core varied along the length of the extrusion indicating inhomogenous compaction and in some cases full densification and bonding had not been achieved.

The use of thick-walled cans for the extrusion of powders of these alloys is not recommended. It appears that too much work is done in deforming the can instead of the powders. Any further work involving small lots of powders such as those used in this program would benefit from the use of an extrusion press which accepts small cans, such as that at GE Corporate Research and Development. In addition, it seems that pre-compaction of the powders may be advisable, using a process such as hot isostatic pressing (HIP) to aid in particle bonding.

3.1.3.2 Characterization of Extruded Powders

The microstructures of the extruded alloys were characterized by AEM. Since the purpose of the dispersed particles is to inhibit the development of planar slip morphologies by either hardening active slip systems or promoting bypass of particles on parallel slip planes, and not to develop strengthening through an Orowan mechanism, the size of the particles is not very critical. However, to be effective in inhibiting planar slip, the density of particles within the matrix should remain high and the diameters of the particles should remain somewhat less than roughly 50 nm for the volume fractions used in this program. Therefore, in assessing the microstructures of the extruded materials, particular note is paid to the form of the distribution of particles following extrusion. Samples of alloys from both extrusions have been studied. In the following discussion, two micrographs are presented for each alloy; in each case, (a) represents the first set of extrusions, whereas (b) represents the second set of extrusions.

In the Ti-Al-Nb-Er alloys (IT-17 to IT-19), the microstructures consist of a rather coarse dispersion of Er_2O_3 in a matrix of alpha-2, as shown in Figures 3-35 through 3-37 respectively. In addition, for Ti-24Al-11Nb-1.5%Er (IT-17), there are also particles of retained beta, as expected from this alloy composition. As can be seen, the dispersed particles are fairly large with diameters typically in the range of 0.1-0.5 μm . Such coarsening of particles during extrusion is not due to exposure to the temperature of the extrusion, but to a somewhat higher temperature. Presumably, it is the adiabatic heating accompanying the extrusion process that is causing the temperature rise. The inhomogenous nature of the dispersion is most probably due to the samples being raised in temperature above their respective alpha-2/beta transus temperatures rather than remaining at an elevated temperature in the alpha-2 phase field. Similar observations have been noted in the case of alpha Ti-Er alloys. Clearly, this is not the optimum dispersion for the purposes described above. It is interesting to note that the dislocation density remains fairly high in the case of Ti-24Al-11Nb-1.5%Er (IT-17), whereas there is evidence of recovery and recrystallization in Ti-25Al-5Nb-1.5%Er (IT-18) and Ti-25Al-5Nb-3.0%Er (IT-19). Finally, the most attractive microstructure of these three alloys is that exhibited in Figure 3-37b corresponding to Ti-25Al-5Nb-3.0%Er (IT-19) taken from the second set of extrusions. However, even this dispersion is not sufficiently refined to inhibit planar slip.

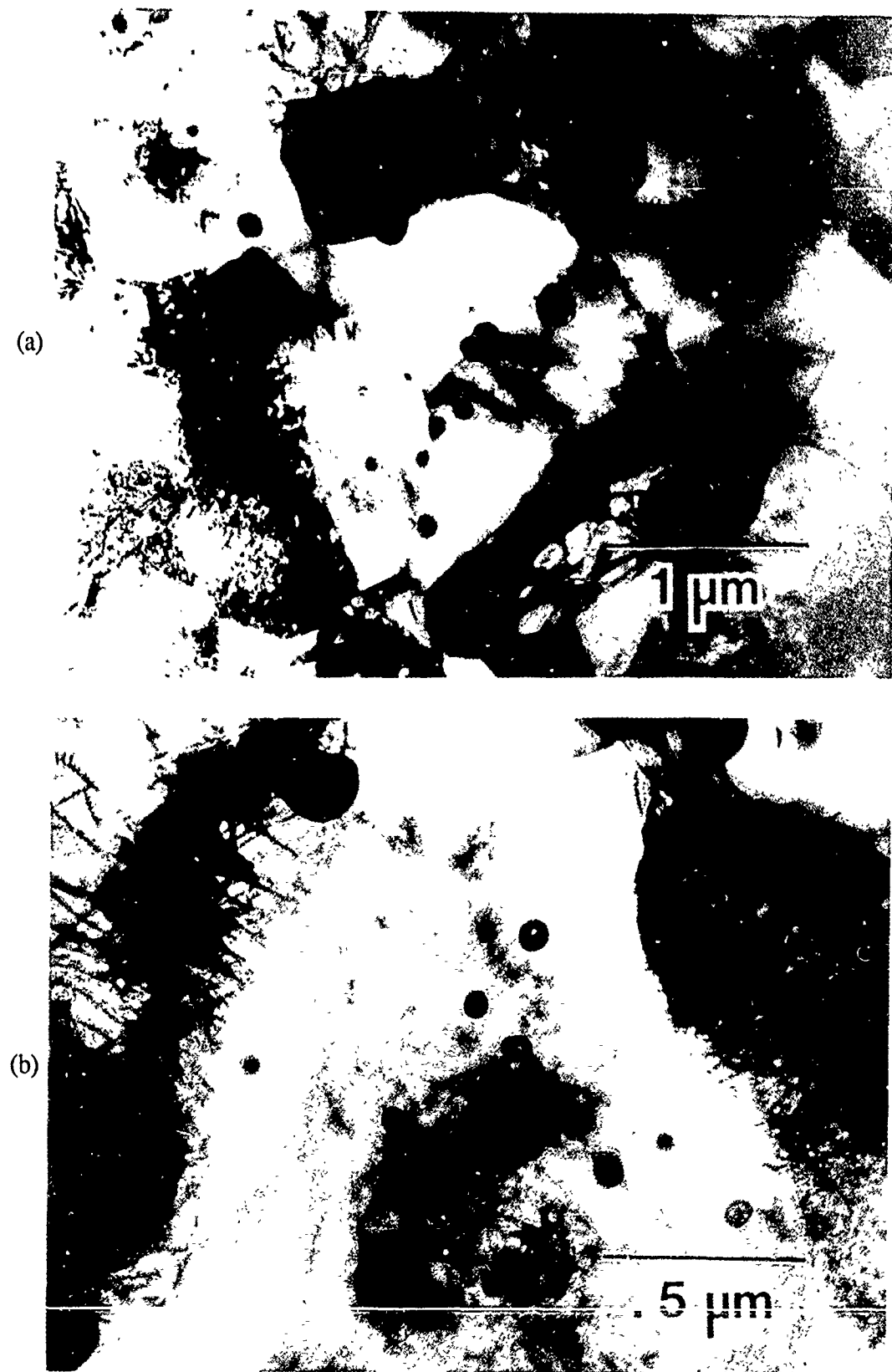


Figure 3-35 Bright-field electron micrographs of as-extruded Ti-24Al-11Nb-1.5%Er (IT-17) showing coarsened dispersoids and heavy deformation after (a) direct extrusion and (b) compaction plus extrusion.

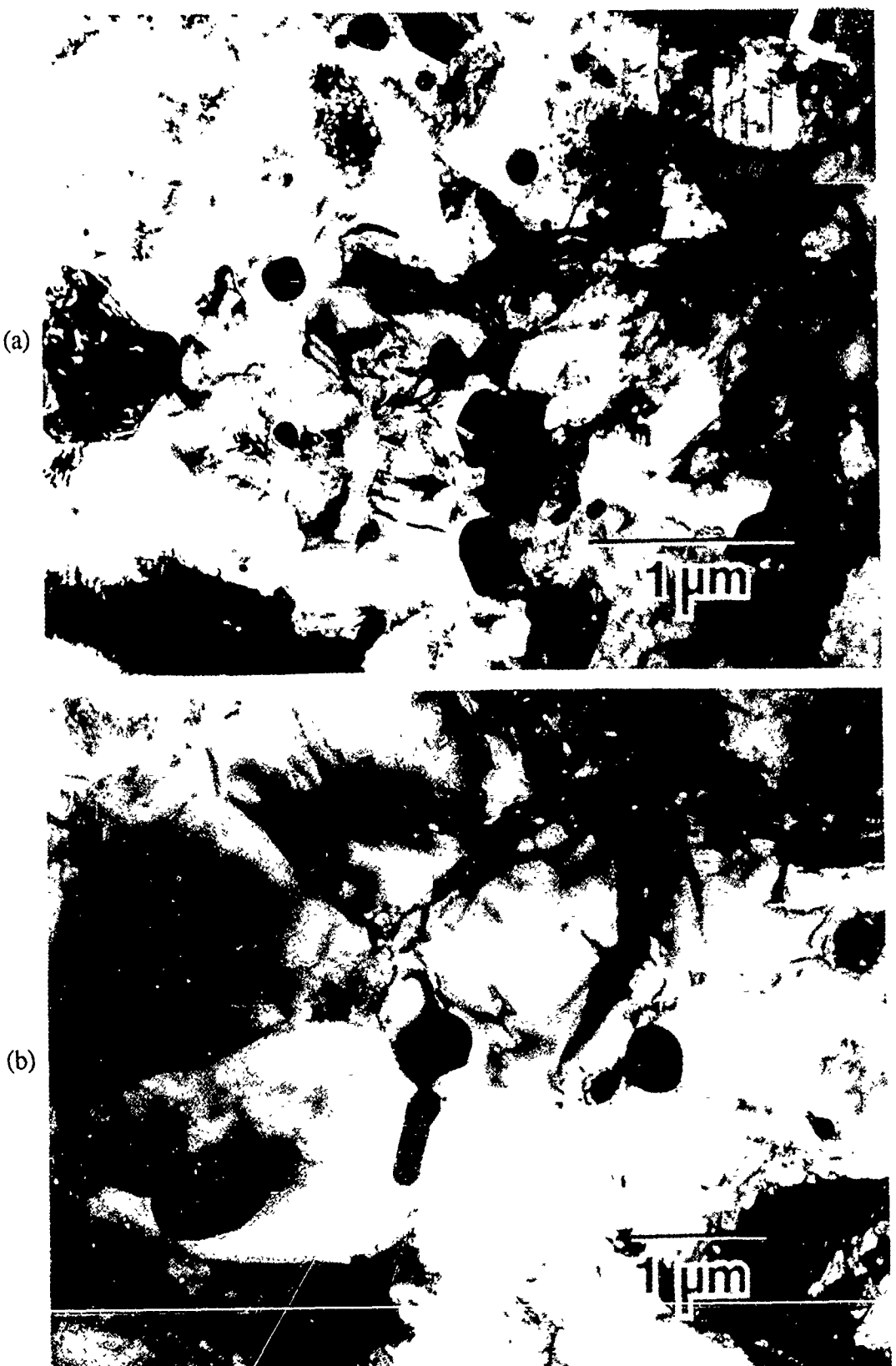


Figure 3-36 Bright-field electron micrographs of as-extruded Ti-25Al-5Nb-1.5%Er (IT-18) showing coarse dispersoids after (a) direct extrusion and (b) compaction plus extrusion.

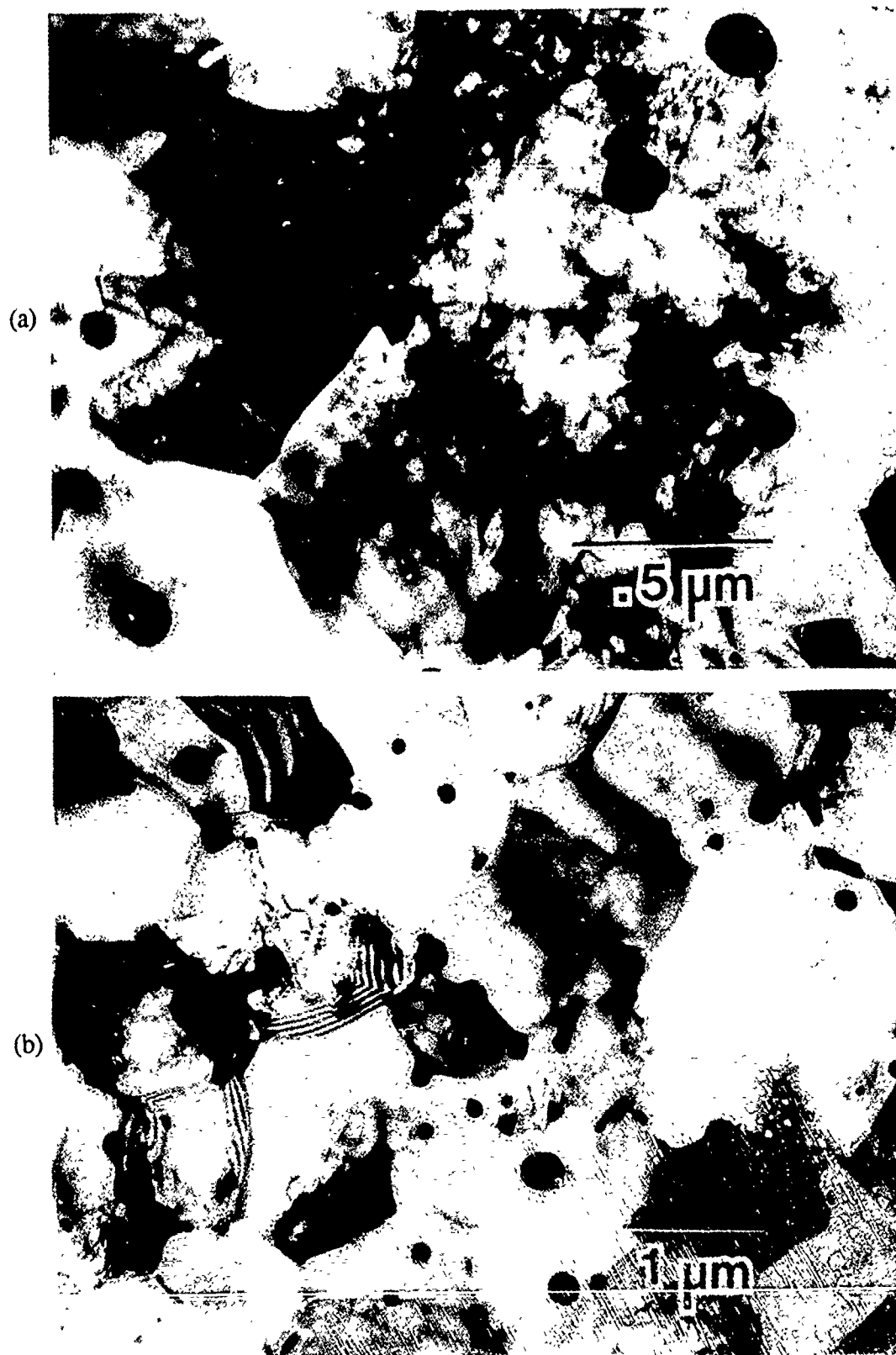


Figure 3-37 Bright-field electron micrographs of as-extruded Ti-25Al-5Nb-3.0%Er (IT-19) illustrating coarse dispersoids and recrystallized grains after (a) direct extrusion and (b) compaction plus extrusion.

The microstructure of Ti-25Al-5Nb-5Ga-1.5%Er (IT-20) following extrusion is shown in Figure 3-38. As can be seen, a dispersion of Er₂O₃ particles is present in a matrix of alpha-2. X-ray energy dispersive spectroscopy reveals that the Ga is present in the matrix of this alloy as expected from previous work. The large dispersed particles range in size from approximately 50-500 nm. The matrix appears to have recovered and recrystallized during the extrusion process.

Examples of the as-extruded microstructures of Ti-25Al-5Nb-5Ta-1.5%Er (IT-21) and Ti-25Al-5Nb-5Ta (IT-22), Ti-Al-Nb-Ta with and without Er, are shown in Figures 3-39 and 3-40, respectively. In the first alloy, Ti-25Al-5Nb-5Ta-1.5%Er (IT-21), once again the particles are rather large with sizes ranging from roughly 100 to 800 nm. The matrices of both of the alloys consist of heavily deformed alpha-2 which has not recovered significantly nor recrystallized. This is in common with the observation of Ti-24Al-11Nb-1.5%Er (IT-17). In addition to the alpha-2 phase, retained beta is also present in this alloy due to the high Nb+Ta content.

In each case, the dispersion of Er₂O₃ particles has coarsened considerably during extrusion. This is presumed to be due to the adiabatic heat which is generated during this process. If the required microstructure is to be preserved during consolidation, thermal excursion above approximately 1100°C (2000°F) must be avoided. The adiabatic heating caused by extrusion may be reduced by lowering both the extrusion ratio and the speed of extrusion. However, in the past, such experiments have resulted in incomplete inter-particle bonding. If such experiments are to be successful, it is most likely that a combination of processes will need to be used. For example, shock consolidation could be carried out prior to extrusion. In this way, considerable inter-particle bonding may be achieved at low temperatures prior to the extrusion process.

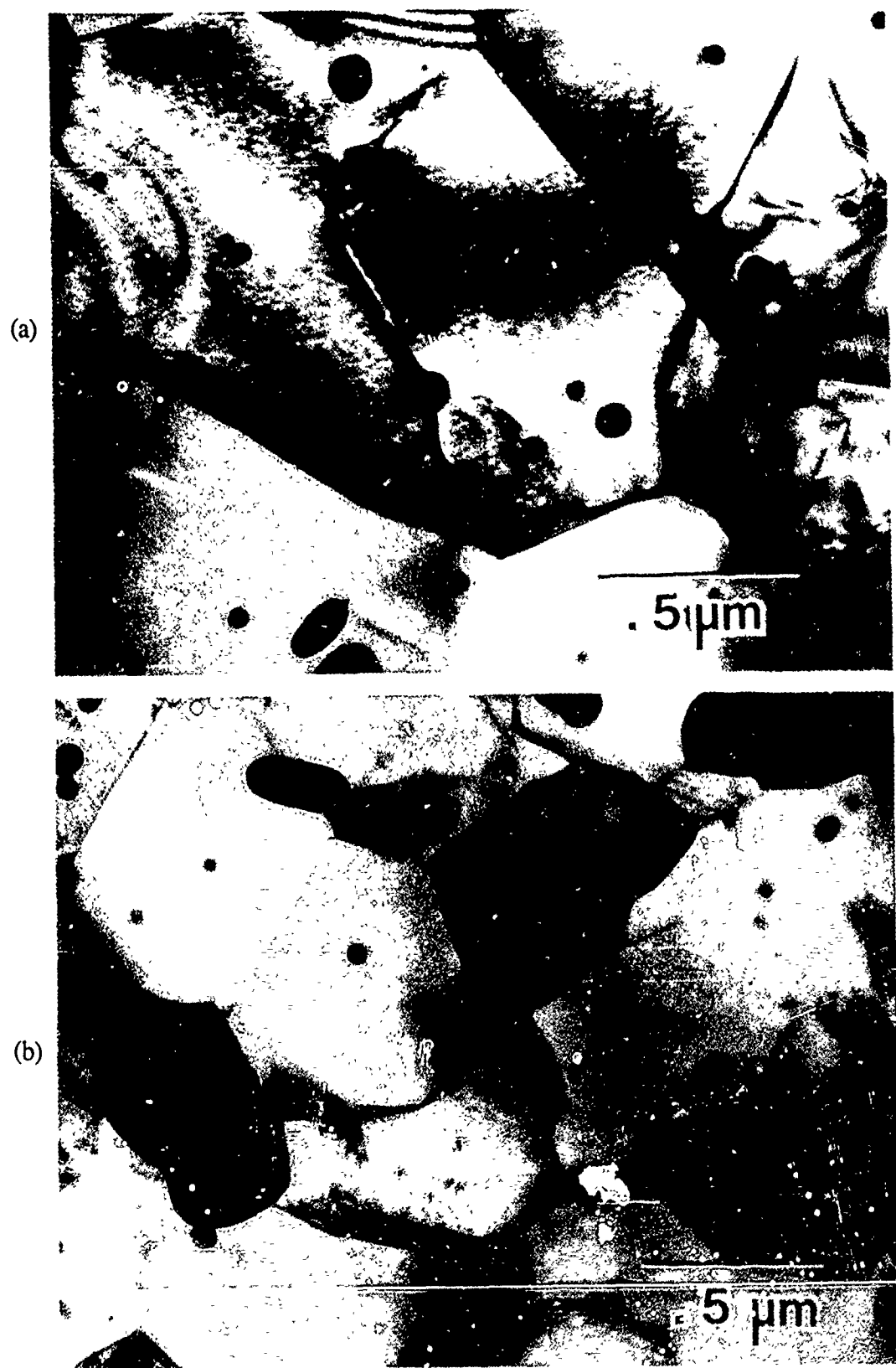


Figure 3-38 Bright-field electron micrographs of as-extruded Ti-25Al-5Nb-5Ga-1.5%Er (IT-20) showing recovered and recrystallized grains with large dispersoids after (a) direct extrusion and (b) compaction plus extrusion.

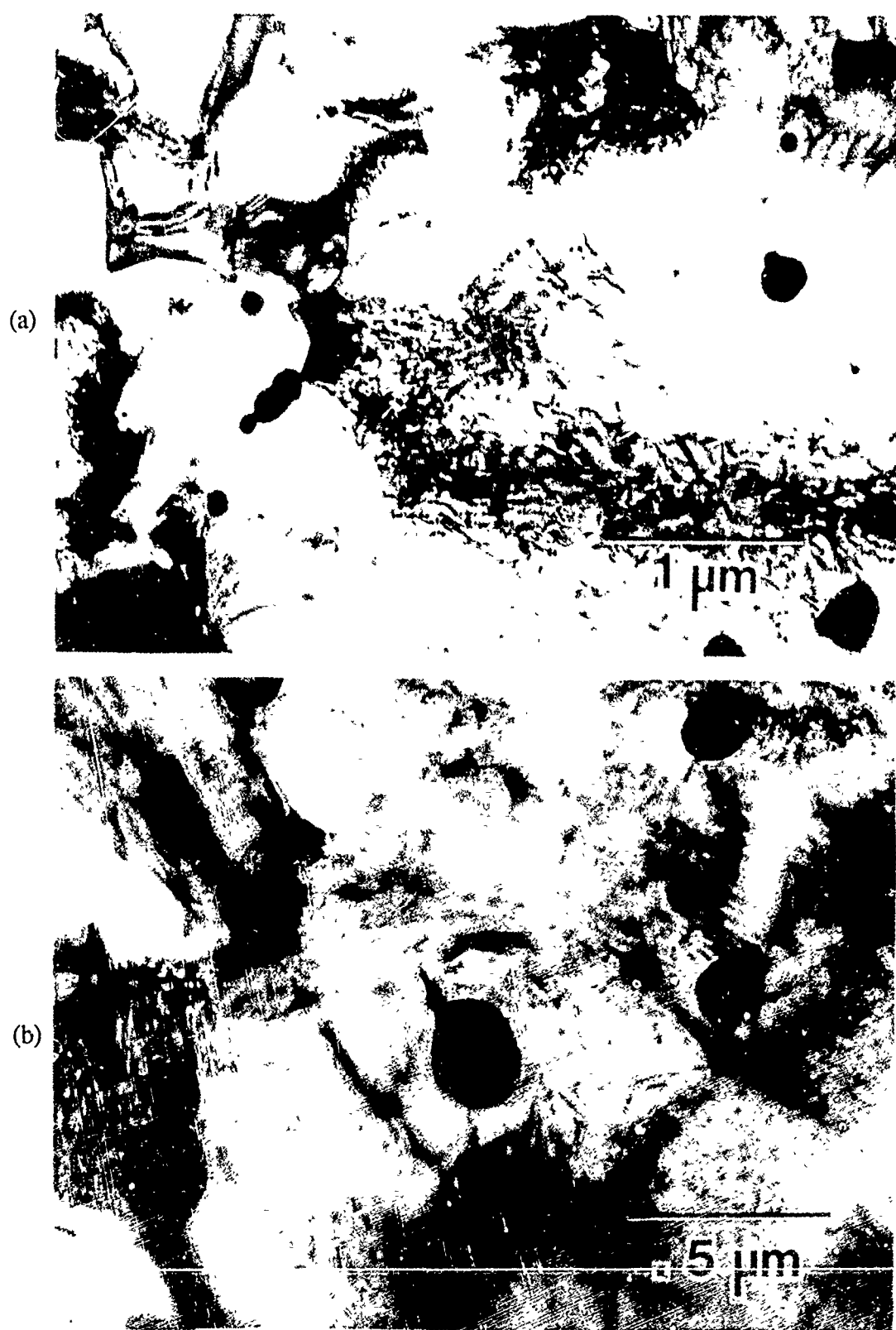


Figure 3-39 Bright-field electron micrographs of as-extruded Ti-25Al-5Nb-5Ta-1.5%Er (IT-21) illustrating heavy deformation, coarse dispersoids, and beta phase after (a) direct extrusion and (b) compaction plus extrusion.



Figure 3-40 Bright-field electron micrographs of as-extruded Ti-25Al-5Nb-5Ta (IT-22) showing heavy deformation and beta phase after (a) direct extrusion and (b) compaction plus extrusion.

3.1.3.3 Mechanical Testing

The results from the tensile tests presented in Table 3-16 are, of course, disappointing. However, this is not surprising in view of the poor quality of the extruded material. The extrusions of Ti-25Al-5Nb-5Ga-1.5%Er (IT-20) were so poor that no mechanical test specimens were successfully prepared. Only three elevated temperature test specimens showed evidence of some plastic deformation. The fact that many of the specimens failed outside the gage section indicated that these results are in fact defect controlled, and do not represent the intrinsic properties of the materials. Consequently, it is not possible to draw qualified conclusions from these tests.

Table 3-16 Tensile Strength of Task 3 Alloys

Alloy		Temperature °C	Temperature °F	Tensile Strength MPa	Tensile Strength ksi
IT-17	20	70		235	34.0
	650	1200		302*#	43.8
IT-18	425	800		597#	86.5
	650	1200		196	28.4
IT-19	425	800		358*	51.9
	650	1200		248	35.9
IT-21	20	70		421*	61.0
	425	800		224*	32.5
	650	1200		346	50.1
IT-22	425	800		719*	104.2
	650	1200		496#	71.9

* failed outside gauge section.

some plastic deformation.

Samples from each consolidated alloy were compressed at room temperature, 300°C (572°F) and 500°C (932°F) to about 2% strain. Values of the compressive 0.2% proof strengths are presented in Table 3-17. For the room temperature tests, the results are an average of two samples. These samples were then prepared for electron microscopy so that the dislocation microstructures could be studied in some detail.

Table 3-17 0.2% Compressive Yield Strength of Task 3 Alloys

Alloy	Temperature		Yield Strength	
	°C	°F	MPa	ksi
IT-17	20	70	939	136.1
	300	572	620	89.8
	500	932	631	91.4
IT-18	20	70	641	92.9
	300	572	488	70.7
	500	932	412	59.7
IT-19	20	70	1248	180.8
	300	572	1015	147.1
	500	932	908	131.5
IT-20	20	70	1600*	231.8
	300	572	1507*	218.4
	500	932	1341*	194.3
IT-21	20	70	1010	146.3
	300	572	794	115.0
	500	932	701	101.5
IT-22	20	70	1098	159.1
	300	572	798	115.6
	500	932	765	110.8

* brittle failure

The room temperature compressive yield strengths show an interesting variation with alloy composition. Of the Ti-Al-Nb-Er alloys, the alloy exhibiting the highest yield strength is Ti-25Al-5Nb-3.0%Er (IT-19) which contains a large amount of Er. It is interesting to note that the as-extruded microstructure of this alloy consists of a fine, equiaxed grain morphology resulting from recrystallization, Figure 3-37b. The Er apparently plays a role in maintaining this fine grain size which may well account for the strength of this alloy. The alloy Ti-25Al-5Nb-5Ga-1.5%Er (IT-20) exhibits the highest strength, and this may be due to the presence of solute zones or fine precipitates, as discussed below. The Ta containing alloys (Ti-25Al-5Nb-5Ta-1.5%Er (IT-21), Ti-25Al-5Nb-5Ta (IT-22)) also exhibit high strengths, similar to Ti-24Al-11Nb-1.5%Er (IT-17). Of course, as expected from the microstructures of the extruded samples, the dispersoids present in samples IT-17 through IT-21 are not expected to play a role in inducing increased ductility.

Duplicate fracture toughness specimens of each of the Task 3 alloys were tested at room temperature. The three point bend specimens were notched but not fatigue precracked. The tests were conducted as specified by ASTM E399-83 using a loading rate of 90.8 kg (200 lb) per minute. The K_{exp} values were then calculated and are presented in Table 3-18. All of the specimens failed by cleavage with little or no surface roughness. However, the specimens which contained some beta phase, (Ti-24Al-11Nb-1.5%Er (IT-17), Ti-25Al-5Nb-5Ta-1.5%Er (IT-21), and Ti-25Al-5Nb-5Ta (IT-22)) all had higher fracture toughness values than those which did not contain beta phase. When comparing the results from Ti-25Al-5Nb-5Ta-1.5%Er (IT-21) which contained dispersoids and Ti-25Al-5Nb-5Ta (IT-22) which did not contain a dispersoid, it is apparent that the coarse dispersoids were not effective in improving the fracture toughness of these alpha-2 titanium alloys.

Table 3-18 Room Temperature Fracture Toughness of Task 3 Alloys

Alloy	K_{exp} (MPa \sqrt{m})	K_{exp} (ksi \sqrt{in})
IT-17	20.8	18.9
	20.2	18.4
IT-18	10.2	9.3
	8.7	7.9
IT-19	8.8	8.0
	10.1	9.2
IT-20	5.8	5.3
	10.8	9.8
IT-21	12.7	11.5
	11.7	10.6
IT-22	18.6	16.9
	19.4	17.6

3.1.3.4 Analysis of Deformation Structures

This analysis involves a determination of the Burgers vector (\mathbf{b}) of the dislocations, their slip planes, and the morphology of slip. In this work, including that done in parallel studies, it has been shown that dislocations with $\mathbf{b}=\mathbf{a}$ glide on $\{10\bar{1}0\}$. Particular interest is paid here to the nature of the dislocations with $\mathbf{b}\neq\mathbf{a}$, since it is thought that these dislocations play an important rôle in the room temperature ductility of the compound. In each case, a grain is chosen so that the compression axis lies within $\sim\pm 8^\circ$ of the $[0001]$ direction. In this way, it is known that a significant shear stress acts on the given slip system so that dislocations of this type are expected to be present as a result of glide. The initial analysis reported here has concentrated primarily on the dislocation microstructure of Ti-25Al-5Nb-5Ga-1.5%Er (IT-20). This alloy was chosen because of the extremely high strength exhibited in compression as reported in Table 3-17.

A grain of Ti-25Al-5Nb-5Ga-1.5%Er (IT-20) oriented as described above was analyzed in the AEM. Some of the dislocations present in this grain are shown in Figure 3-41 which was recorded with the diffraction vector, $\mathbf{g} = \bar{2}021$. In this image, dislocations with $\mathbf{b}=\mathbf{a}$ and $\mathbf{b}\neq\mathbf{a}$ are imaged. Those dislocations whose Burgers vectors lie inclined to the basal plane are conveniently imaged with $\mathbf{g} = \pm 0002$, where dislocations with $\mathbf{b}=\mathbf{a}$ are out of contrast. Such an image, with $\mathbf{g} = 0002$ is shown in Figure 3-42. The Burgers vectors of these dislocations may be determined from the images given in Figure 3-43 and 3-44, recorded with $\mathbf{g} = 02\bar{2}1$ and $\bar{2}021$ respectively. In these images, the dislocations which are in contrast in Figure 3-42 are now out of contrast. These results show uniquely that the Burgers vector of the dislocations is parallel to $[\bar{1}1\bar{2}6]$. The magnitude of the Burgers vector has not been determined; if the dislocations are of the type $1/3<11\bar{2}6>$, then this would result in an extremely large Burgers vector of rather high energy. It is more likely that the dislocations have $\mathbf{b} = 1/6<11\bar{2}6>$ and since these would be super-partial, presumably they glide in pairs. A large number of observations made in parallel studies are consistent with the fact that these dislocations do indeed glide in the form of loosely coupled pairs.

Trace analysis has revealed that these particular dislocations glide on $(11\bar{2}1)$. It is interesting to note that the c-component dislocations lie in bands, i.e. rather inhomogeneously, and this is not altered by the presence of the large dispersoids. Two other observations have been made concerning the microstructure of this alloy. The first of these concerns the fine contrast exhibited in the background of Figure 3-41, 3-43 and 3-44. These same contrast features are not visible in Figure 3-42. Such contrast features have not been observed in other more dilute alloys characterized in parallel studies. In principle, these features correspond to centers of strain, and it is possible for these to be surface impurities introduced during preparation of the thin foils. However, this is thought to be unlikely because of their sensitivity to diffraction contrast (i.e. exhibiting no contrast when imaged with $\mathbf{g} = 0002$). If these features are intrinsic, one may speculate that the contrast arises from formation of solute-rich zones or the refined precipitation of a second phase. If this is so, the origin of the high compressive yield strength of this alloy may be understood. The second observation of interest is the presence of faults shown in Figure 3-41. Trace analysis reveals that these faults lie on the basal planes. Previous work has shown that such basal faults in alpha Ti are produced during growth of this phase from beta

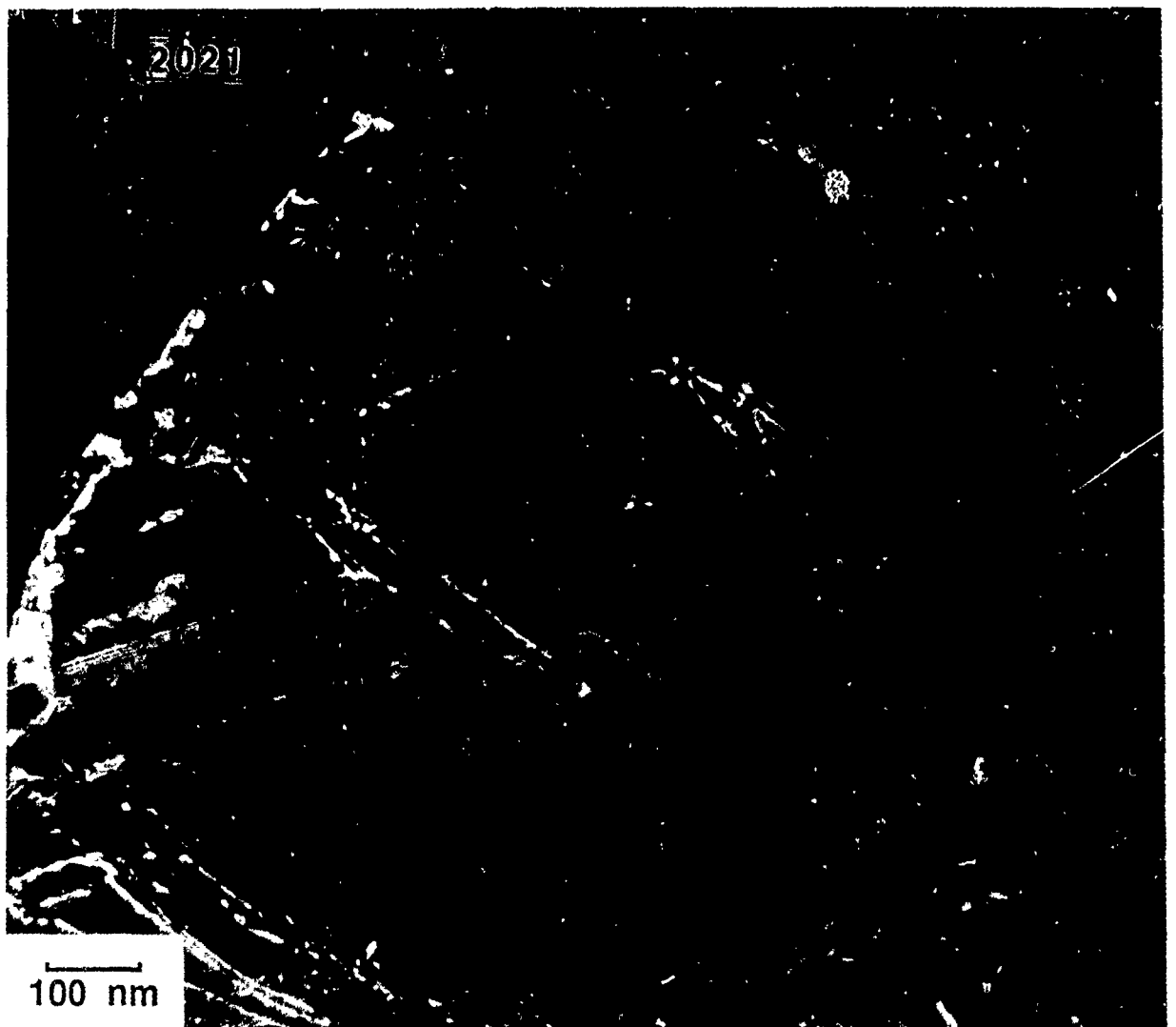


Figure 3-41 Weak-beam dark-field electron micrograph of the dislocation microstructure of Ti-25Al-5Nb-5Ga-1.5%Er (IT-20) after RT compression testing.

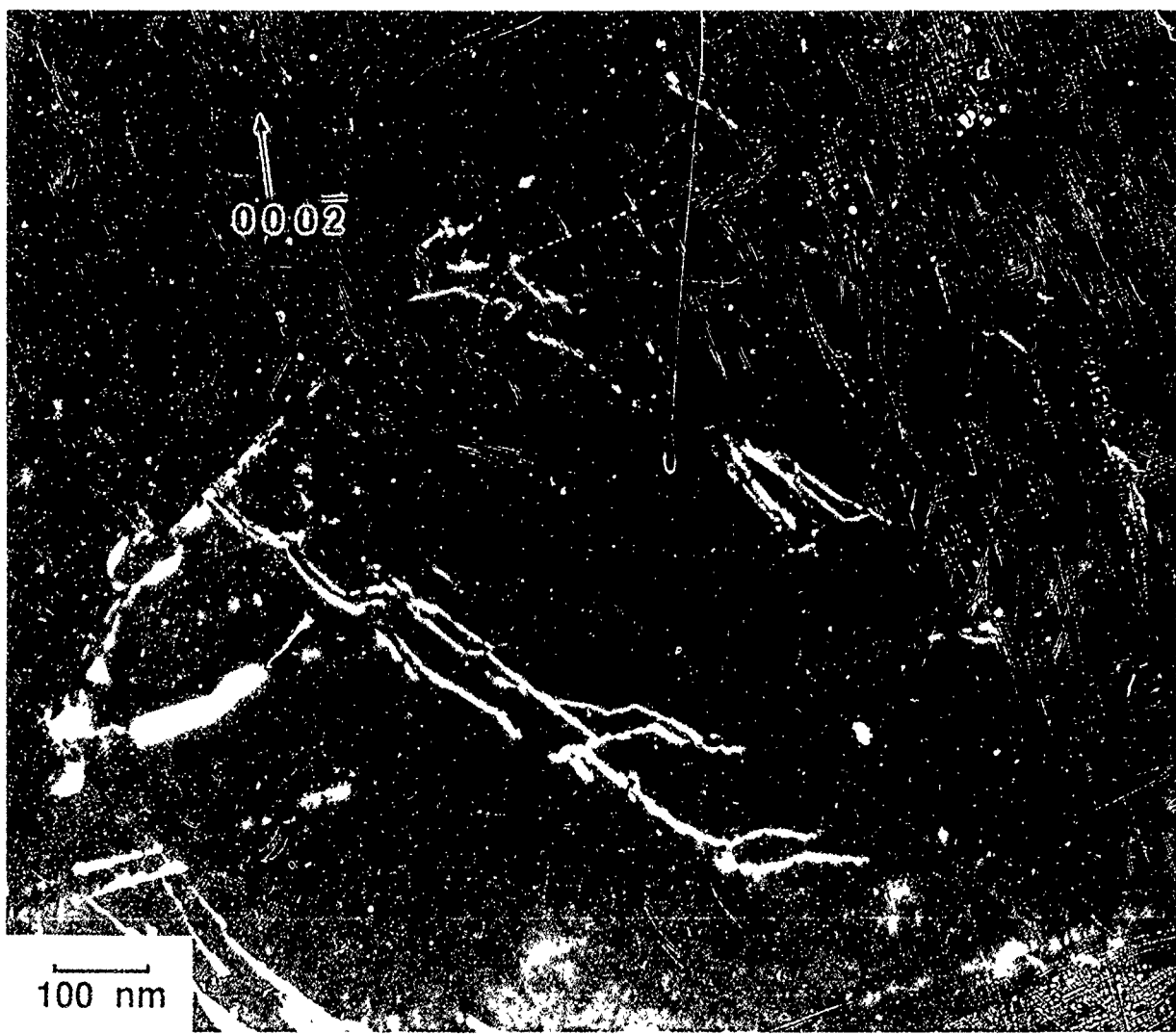


Figure 3-42 Weak-beam dark-field electron micrograph of $c+a/2$ dislocations in Ti-25Al-5Nb-5Ga-1.5%Er (IT-20) after RT compression testing.

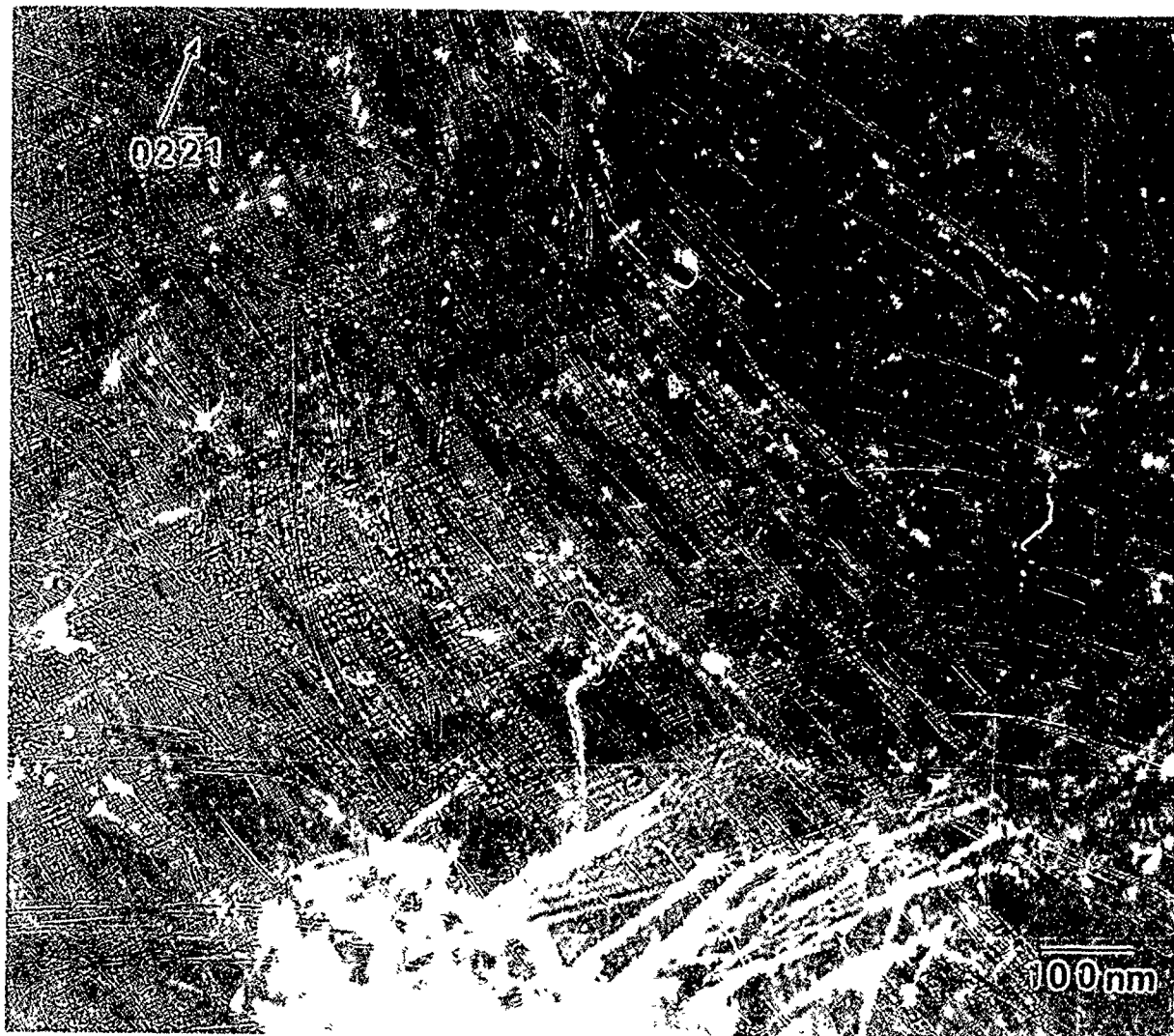


Figure 3-43 Weak-beam dark-field electron micrograph of Ti-25Al-5Nb-5Ga-1.5%Er (IT-20) after room temperature compression testing with $g = 02\bar{2}1$ and the beam direction close to $[1\bar{2}10]$.

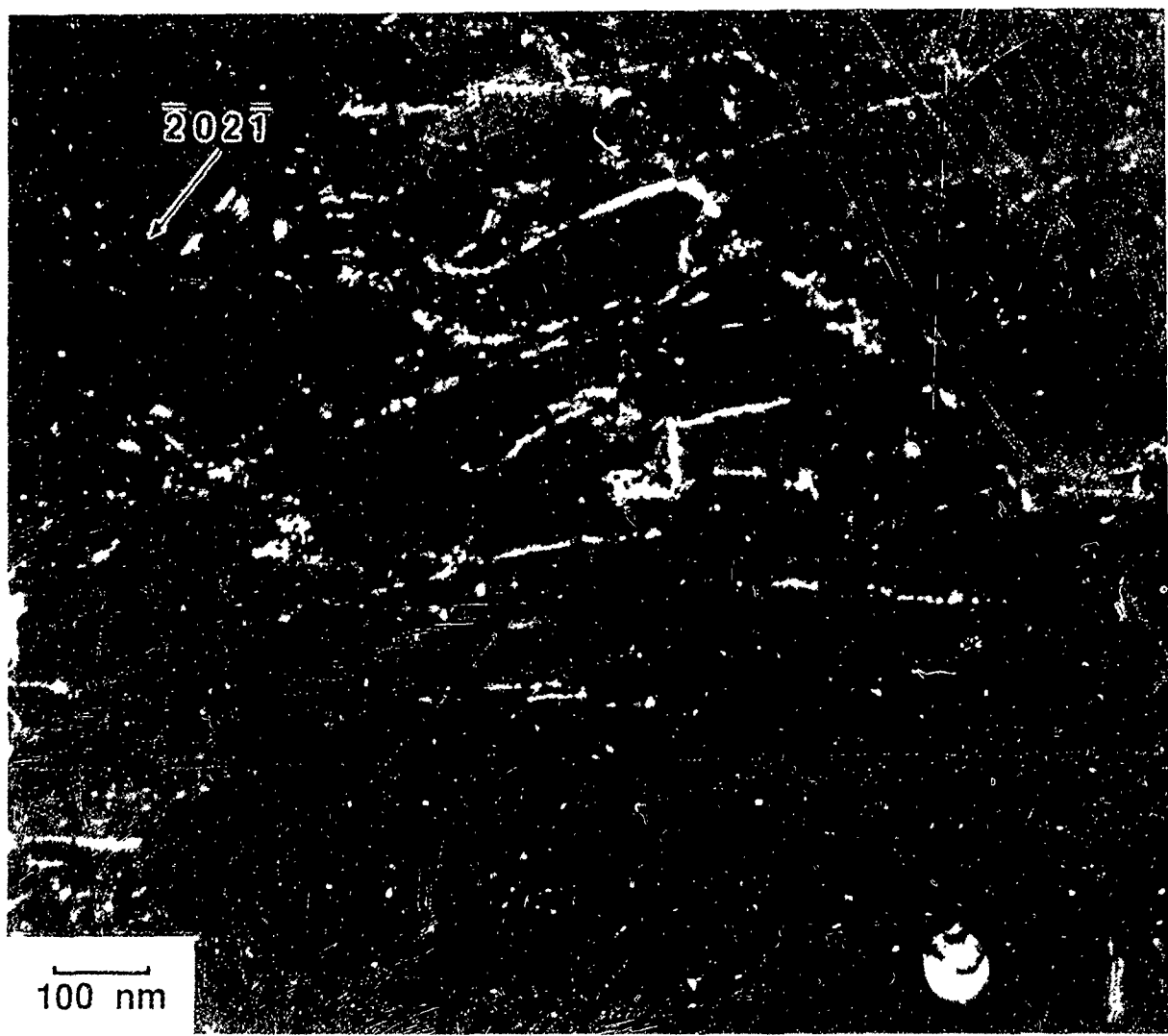


Figure 3-44 Weak-beam dark-field electron micrograph of Ti-25Al-5Nb-5Ga-1.5%Er (IT-20) after RT compression testing with $g = \bar{2}0\bar{2}1$ and the beam direction close to $[1\bar{1}02]$.

titanium. Such faults are bounded by dislocations of the type $\mathbf{b} = 1/6<20\bar{2}3>$. In the present study, the dislocations bounding the faults are out of contrast when imaged with $\mathbf{g} = 0002$ (Figure 3-42) and do not correspond to $\mathbf{b} = 1/6<20\bar{2}3>$. In fact, the dislocation bounding the end of the fault at A in Figure 3-41 is essentially out of contrast in Figure 3-43, and this is consistent with \mathbf{b} being parallel to $[\bar{2}110]$. If this is the case, the presence of the fault may be consistent with glide of super-partials with $\mathbf{b} = 1/6<11\bar{2}0>$ on the basal plane. This is somewhat unexpected, but these samples have experienced quite high shear stresses which may induce slip on the basal plane.

The dislocation microstructures of samples of Ti-25Al-5Nb-5Ta (IT-22) compressed at room temperature are shown in Figure 3-45 through 3-48. The general features of the microstructure are similar to those shown for the case of Ti-25Al-5Nb-5Ga-1.5%Er (IT-20). The c-component dislocations are imaged in Figure 3-24 where again they are found to lie in bands. These dislocations are largely out of contrast in Figure 3-47 which is consistent with their Burgers vector being parallel to either $[\bar{2}11\bar{6}]$ or $[1\bar{1}26]$. There is also evidence of the same refined contrast features in Figure 3-45 and 3-47 but not in Figure 3-46. This is consistent with the results described for Ti-25Al-5Nb-5Ga-1.5%Er (IT-20), and it is interesting to note that this alloy has a significant solute concentration. In addition, along the bands of dislocations with $\mathbf{b} = \mathbf{c+a}/2$, there is considerable debris present. This debris is imaged in Figure 3-45 and 3-47 but not in Figure 3-46. Presumably, the debris is a result of intersection of dislocations having $\mathbf{b} = \mathbf{a}$ with those having $\mathbf{b} = \mathbf{c+a}/2$. An image of the debris is shown at higher magnification in Figure 3-48.

The dislocation microstructures of samples deformed above room temperature have not been studied in detail at this time. However, a preliminary set of observations has been obtained on this alloy (Ti-25Al-5Nb-5Ta (IT-22)) deformed at 500°C (930°F). The dislocation microstructure is shown in Figure 3-49 and 3-50. As can be seen, the morphology is similar to that shown in Figures 3-45 through 3-47. It appears that the dislocations in the band marked A in Figure 3-50 are out of contrast in Figure 3-49 with $\mathbf{g} = 20\bar{2}1$. This is again consistent with \mathbf{b} being parallel to $<11\bar{2}6>$.

3.1.3.5 Task 3 - Summary

The Phase I, Task 3 alloys which contained a rare earth oxide dispersion were produced by rapid solidification processing. Mechanical test results for the powder metallurgy alloys were poor even for Ti-25Al-5Nb-5Ta (IT-22) which did not contain a rare earth oxide dispersion. A more extensive study of these alloys which includes careful analysis of processing effects would be necessary to determine the potential of the Task 3 alloying procedures. At this time, the study of alpha-2 titanium aluminide alloys which contain rare earth oxide dispersions has not been encouraging.

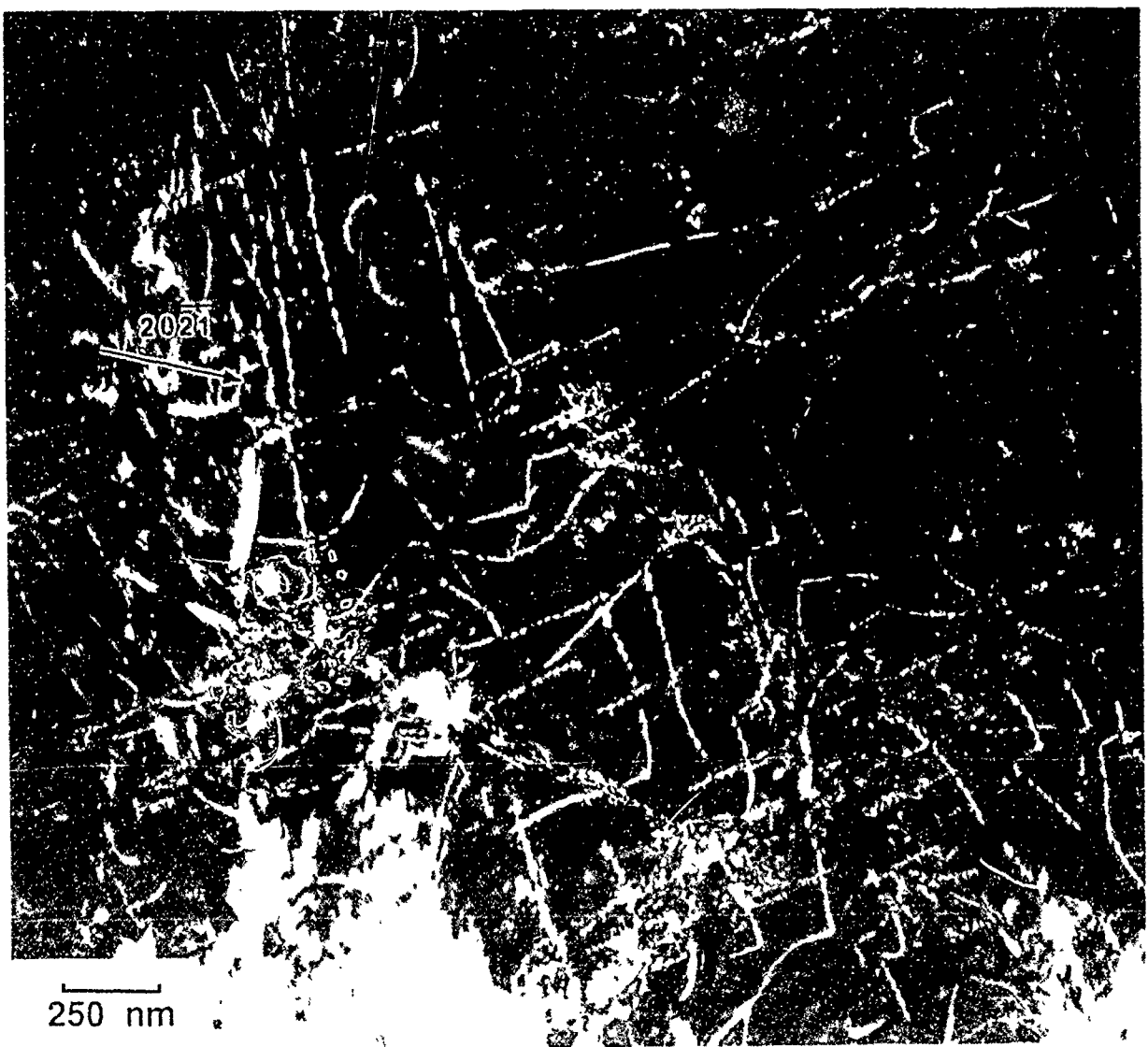


Figure 3-45 Weak-beam dark-field electron micrograph of the dislocation microstructure in Ti-25Al-5Nb-5Ta (IT-22) after RT compression testing.

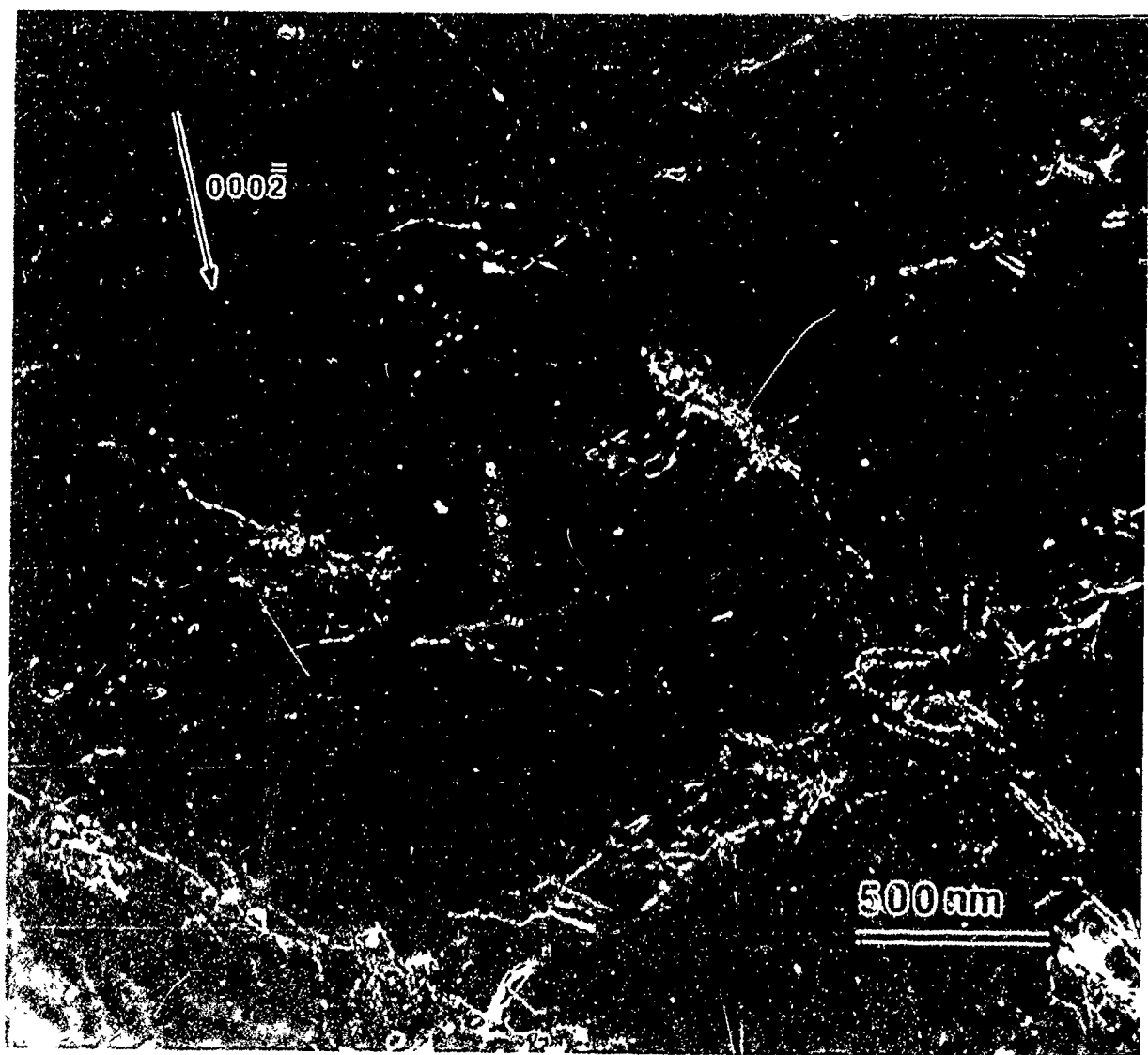


Figure 3-46 Weak-beam dark-field electron micrograph of $c+a/2$ dislocations in Ti-25Al-5Nb-5Ta (IT-22) after RT compression testing.

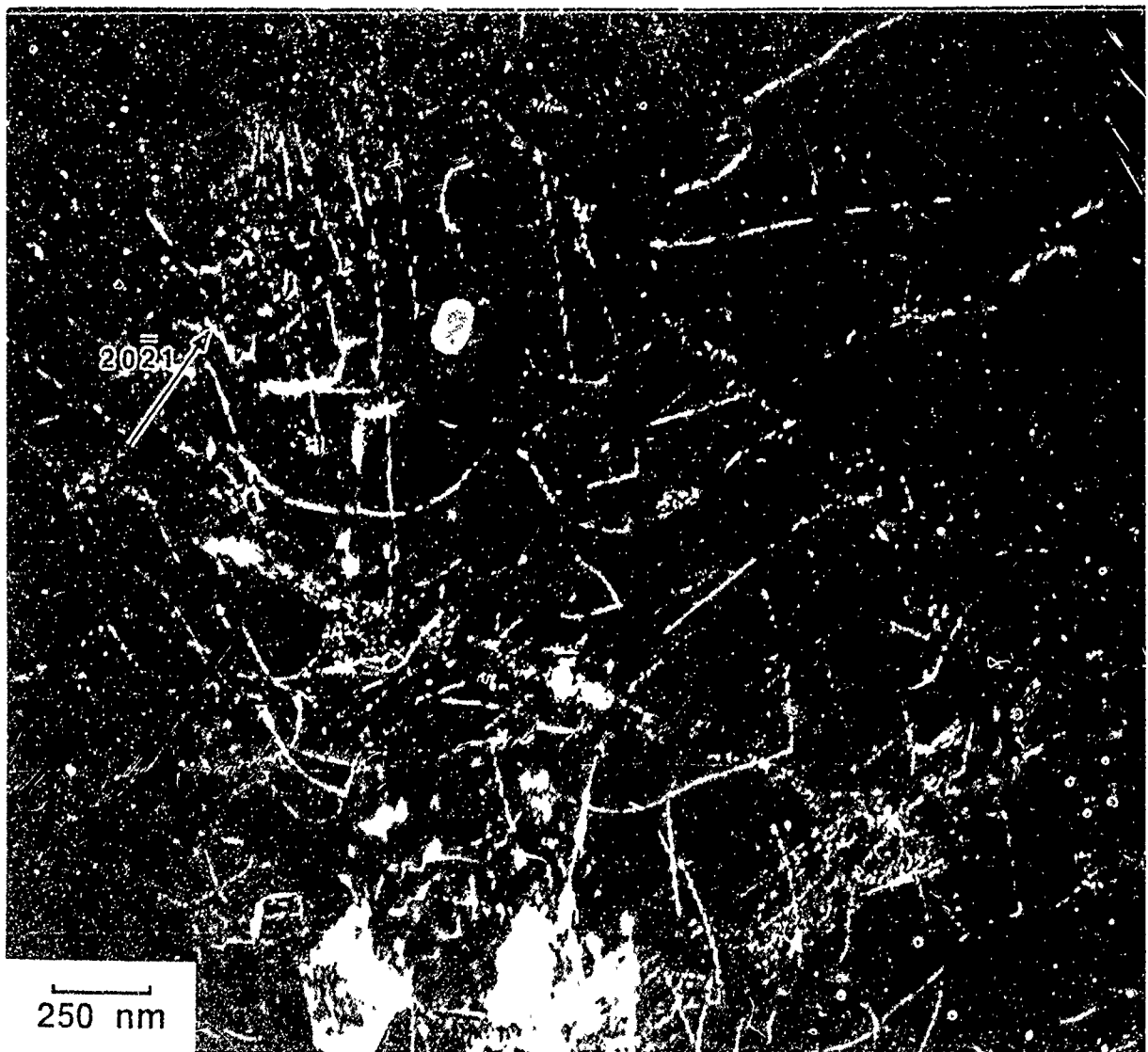


Figure 3-47 Weak-beam dark-field electron micrograph of Ti-25Al-5Nb-5Ta (IT-22) after RT compression testing with $g = 20\bar{2}1$ and the beam direction close to $[1\bar{2}10]$.

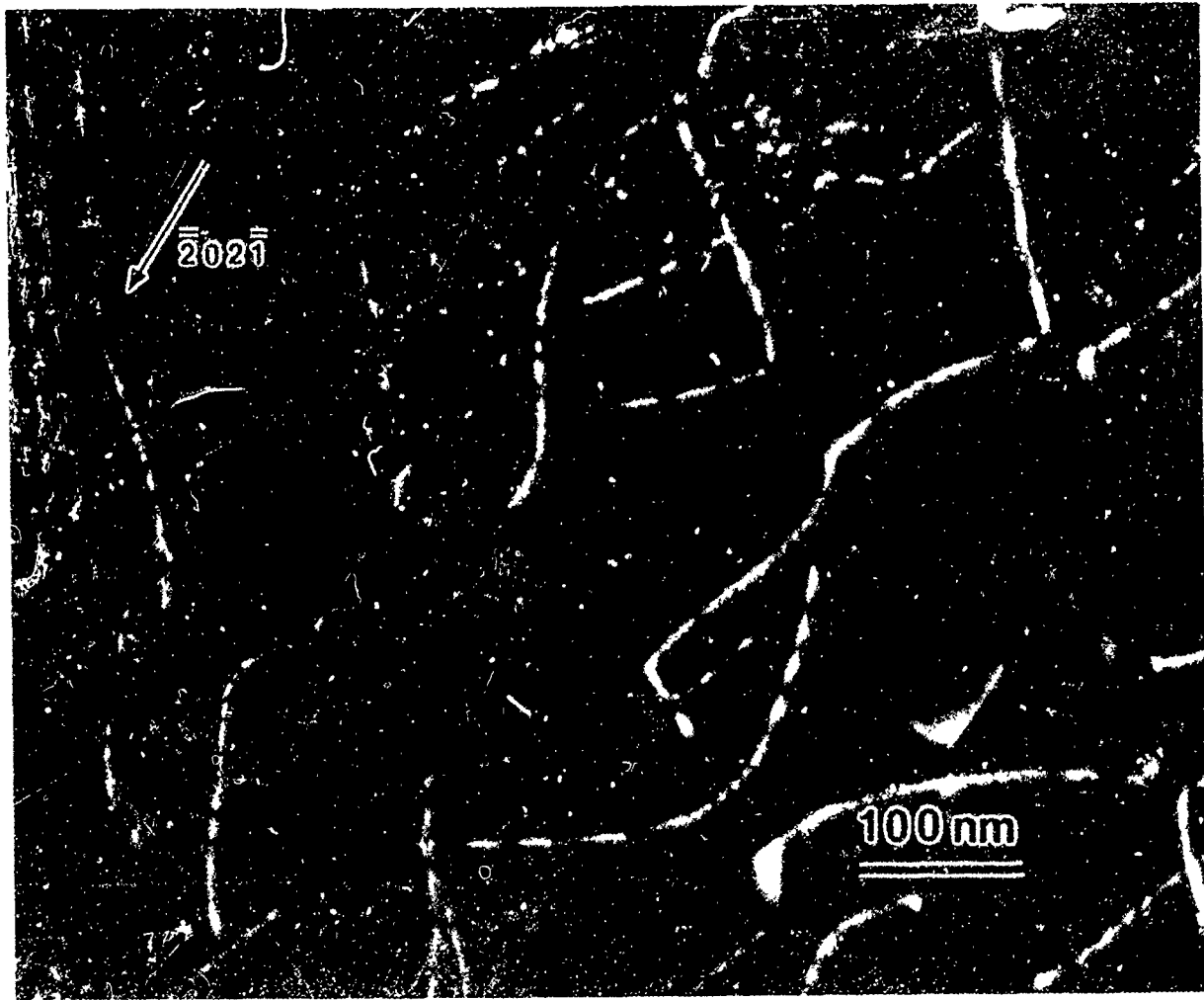


Figure 3-48 Weak-beam dark-field electron micrograph of the dislocation debris observed in the bands of c-component dislocations in Ti-25Al-5Nb-5Ta (IT-22) after RT compression testing. The beam direction is close to [1 $\bar{2}$ 10] and $g = \bar{2}02\bar{1}$.

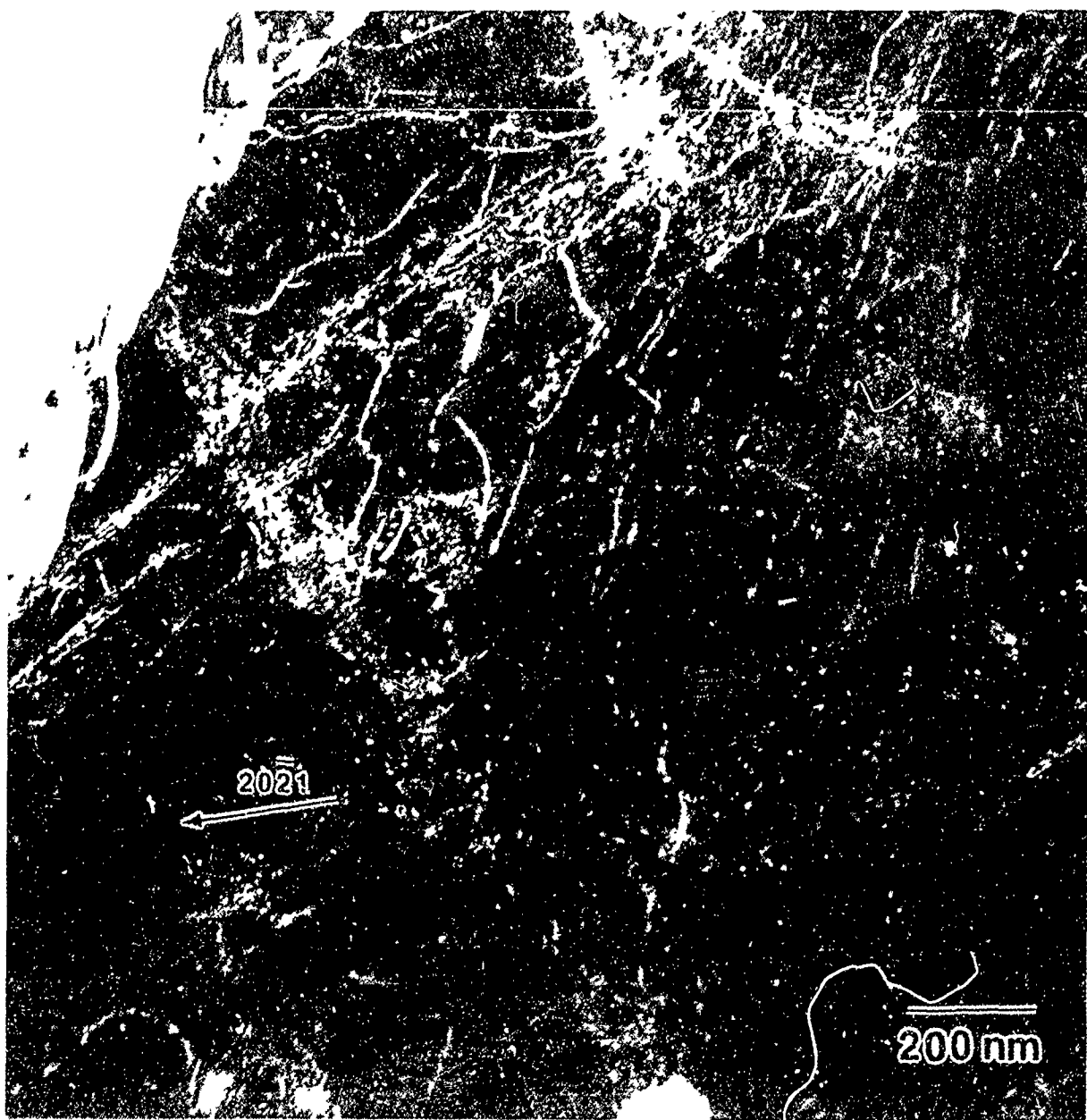


Figure 3-49 Weak-beam dark-field electron micrograph of the dislocation microstructure in Ti-25Al-5Nb-5Ga-1.5%Er (IT-20) following compression testing 500°C (932°F) with the beam direction close to [1\bar{2}10] and $g = 20\bar{2}1$.



Figure 3-50 Weak-beam dark-field electron micrograph of $c+a/2$ dislocations in Ti-25Al-5Nb-5Ga-1.5%Er (IT-20) after compression testing at 500°C (932°F). The beam direction is close to $[1\bar{2}10]$ and $g = 0002$.

3.1.4 Task 4 - Combination Alloys

Eight combination alloys were selected based on the results of the first three tasks of this program, and approval for the melting and processing of these alloys was received from the CO. Aim and measured chemical compositions are presented in Table 3-19. These alloys were selected on the premise that a balance of properties is needed over the range of expected operating temperatures. With this in mind, alloys such as Ti-25.0Al-4Nb-2Ta-2V-1Mo (IT-11) which had high elevated temperature strength but limited room temperature ductility were modified by increasing the level of beta stabilizing elements. Other alloys such as Ti-22.5Al-6Nb-2Ta-2Cr (IT-12) and Ti-22.7Al-3Nb-3Ta-3V (IT-13) which had adequate room temperature ductility but limited elevated temperature strength were modified by increasing the Al content and the level of solid solution strengtheners. In an effort to assess the balance of properties achieved in these alloys, creep and stress/rupture tests were conducted as a part of this task rather than compression testing and deformation analysis.

3.1.4.1 Processing and Heat Treatment

The alloys for Task 4 were produced by non-consumable arc-melting at GE Corporate R&D. Each of the alloys was melted in the form of a 2.5 cm (1 in) diameter by 10 cm (4 in) long ingot. These ingots were then extruded at a 10:1 ratio within the alpha-2 plus beta phase field. The extruded material was then heat-treated to produce the microstructures shown in Figures 3-51 thru 3-54. In general, the microstructures which were produced by heat treatment contain a small fraction of primary alpha-2 grains surrounded by relatively small prior beta grains which consisted of fine acicular alpha-2 platelets within a near continuous beta matrix. The alloy Ti-25Al-8Nb-3V-3Ta (IT-24), however, was heat-treated above its beta transus temperature and, as a result, had a larger prior beta grain size and did not contain any primary alpha-2.

3.1.4.2 Mechanical Testing

Mechanical testing of the Task 4 alloys included tensile testing at room temperature, 427°C (800°F), and 649°C (1200°F), fracture toughness testing at room temperature, creep testing at 649°C (1200°F) and stress/rupture testing at 649°C (1200°F). The tensile, creep and stress/rupture specimens were machined with 0.64 cm (0.25 in) diameter threaded ends and a 1.9 cm (0.75 in) by 0.35 cm (0.14 in) diameter gage section. The fracture toughness specimens were 5.08 cm (2.0 in) long, 0.25 cm (0.1 in) wide, and 0.51 cm (0.2 in) deep with a 0.25 cm (0.1 in) notch which was not fatigue precracked prior to testing.

Tensile tests were conducted at a cross head rate of 0.005 in/min through the 0.2% yield strength and then maintained at a cross head rate of 0.05 in/min through failure. Since the accuracy of measuring ductility from the change in length of broken test specimens is known to be limited for materials with low ductility, extensometers were kept in place until failure for room temperature tensile tests. Plastic deformation was then measured from load versus strain curves. The tensile test results are summarized in Table 3-20.

The yield and ultimate strength levels of the Task 4 alloys are much higher than those which were previously reported for the Task 2 compositions. These higher strengths reflect the effects of an increase in Al content as well as an increased number and level of beta stabilizing additions. Furthermore, the very fine transformed beta microstructure which was produced on rapid cooling can also be associated with higher strength levels. Along with the high strength levels, lower ductility has been identified. Thread failures which occurred during the room temperature testing of these alloys have been associated

with a test specimen configuration problem which was encountered when reducing material quantities for the Task 4 alloys. A study was conducted on alloy IT-5 from Task 1 of this program to identify the effects of specimen configuration. Tensile data is reported in Table 3-21 which was gathered from previous tensile testing of alloy IT-5 using conventional test specimens and from the testing of subscale specimens which were identical to those used for testing in Task 4. The data indicates that no thread failures occurred when using the standard specimen configuration which was used for Tasks 1 and 2 while a thread failure did occur during the testing of the subscale specimens. Nevertheless, it was evident that the ductility of the Task 4 alloys was inadequate and that adjustments which would improve ductility needed to be incorporated into the scale-up alloy selections for Phase II.

Table 3-19 Compositions of Task 4 Alloys*

Alloy	Ti	Al	Nb	V	Ta	Mo	Other	O
IT-23	63.0 [61.0]	25.0 [13.6]	6.0 [11.3]	3.0 [3.1]	3.0 [11.0]	-	-	-
	-	(13.6)	(12.1)	(3.2)	(10.5)	-	-	(0.107)
IT-24	61.0 [58.0]	25.0 [13.4]	8.0 [14.8]	3.0 [3.0]	3.0 [10.8]	-	-	-
	-	(13.4)	(15.4)	(3.0)	(10.5)	-	-	(0.101)
IT-25	63.0 [61.5]	25.0 [13.8]	6.0 [11.3]	2.0 [2.1]	2.0 [7.4]	2.0 [3.9]	-	-
	-	(13.9)	(11.6)	(2.1)	(7.9)	(4.2)	-	(0.117)
IT-26	61.0 [58.5]	25.0 [13.5]	8.0 [14.9]	2.0 [2.0]	2.0 [7.3]	2.0 [3.8]	-	-
	-	(13.7)	(15.3)	(2.0)	(7.8)	(4.2)	-	(0.104)
IT-27	63.0 [58.8]	23.0 [12.1]	6.0 [10.9]	3.0 [3.0]	3.0 [10.6]	-	2.0 Sn [4.6] Sn (4.7) Sn	-
	-	(12.3)	(11.7)	(3.0)	(10.2)	-	-	(0.109)
IT-28	63.0 [57.4]	25.0 [12.9]	5.0 [8.8]	-	5.0 [17.2]	2.0 [3.7]	-	-
	-	(13.0)	(9.2)	-	(17.0)	(3.9)	-	(0.095)
IT-29	65.0 [64.7]	25.0 [14.0]	6.0 [11.6]	-	2.0 [7.5]	-	2.0 Cr [2.2] Cr (2.2) Cr	-
	-	(14.2)	(11.7)	-	(7.8)	-	-	(0.107)
IT-30	65.0 [62.9]	23.0 [12.5]	6.0 [11.3]	-	2.0 [7.3]	2.0 [3.9]	2.0 Cr [2.1] Cr (2.0) Cr	-
	-	(12.4)	(11.5)	-	(7.5)	(3.9)	-	(0.106)

* The compositions which are not enclosed in brackets are aim atom percents, compositions enclosed by [] are aim weight percents, and compositions enclosed by () are measured weight percents.

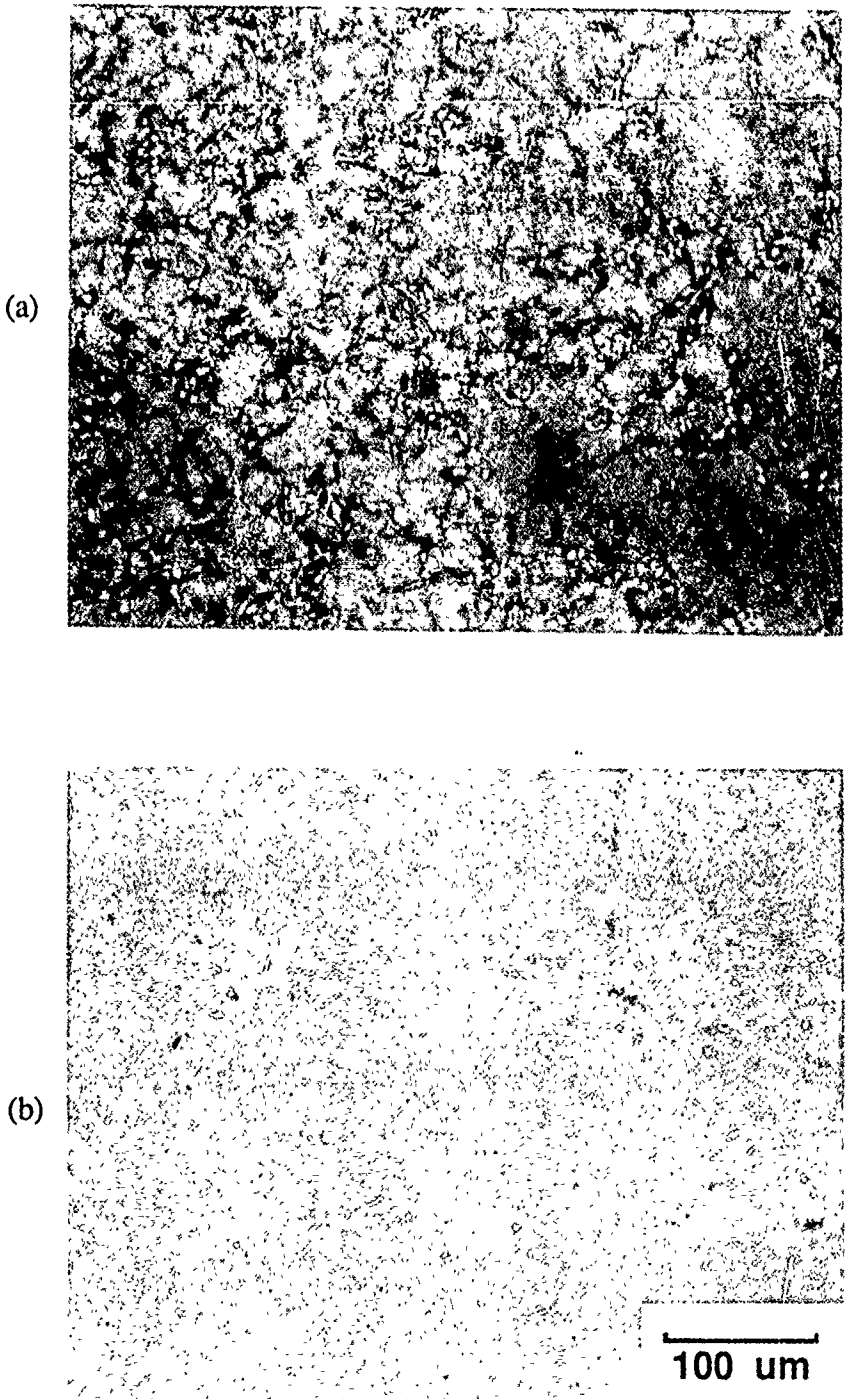


Figure 3-51 Optical micrographs of (a) Ti-25Al-6Nb-3V-3Ta (IT-23) and (b) Ti-25Al-8Nb-3V-3Ta (IT-24) after heat treatment at 1120°C (2050°F).

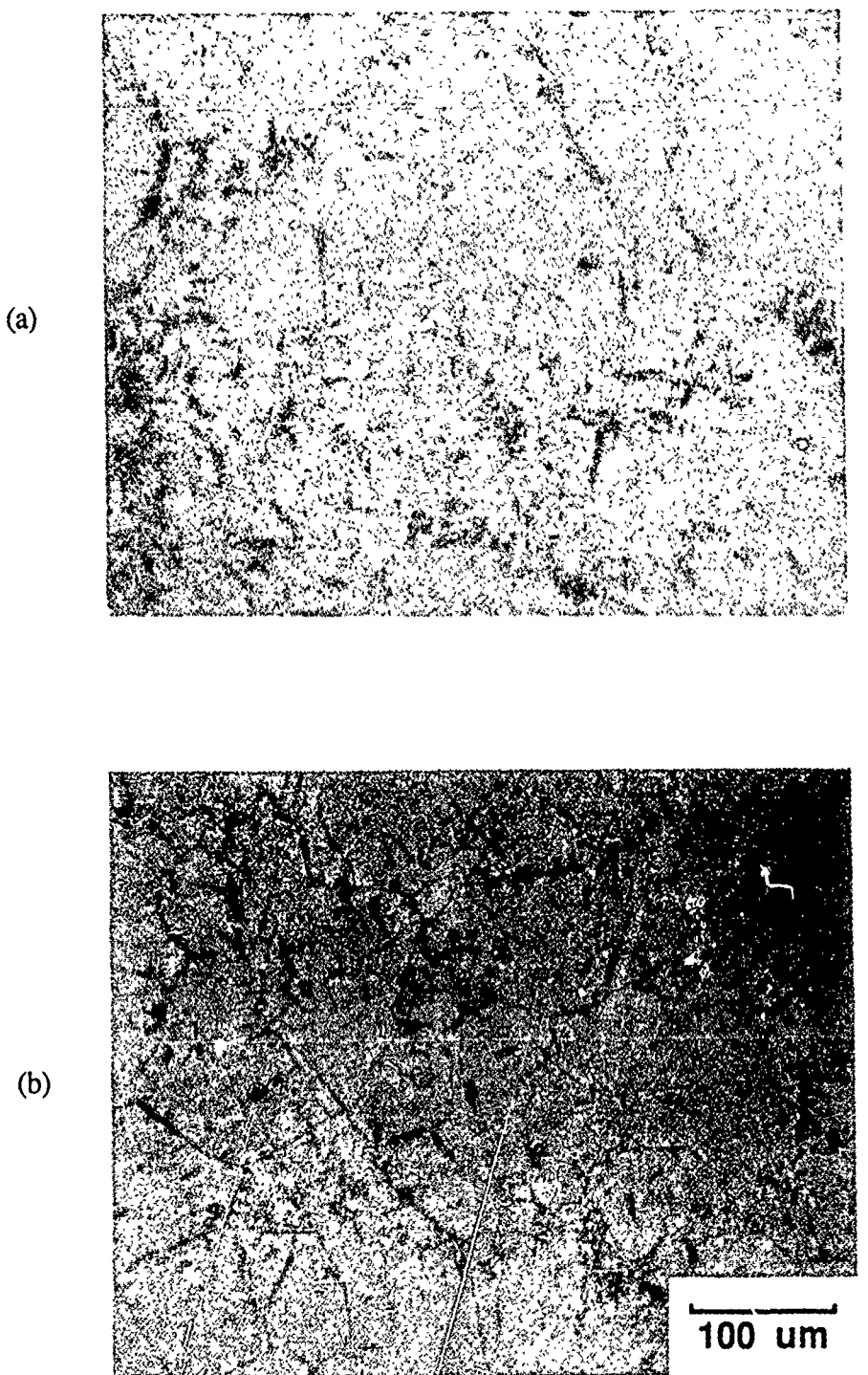


Figure 3-52 Optical micrographs of (a) Ti-25Al-6Nb-2V-2Ta-2Mo (IT-25) after heat-treatment at 1120°C (2050°F) and (b) Ti-25Al-8Nb-2V-2Ta-2Mo (IT-26) after heat-treatment at 1105°C (2025°F).

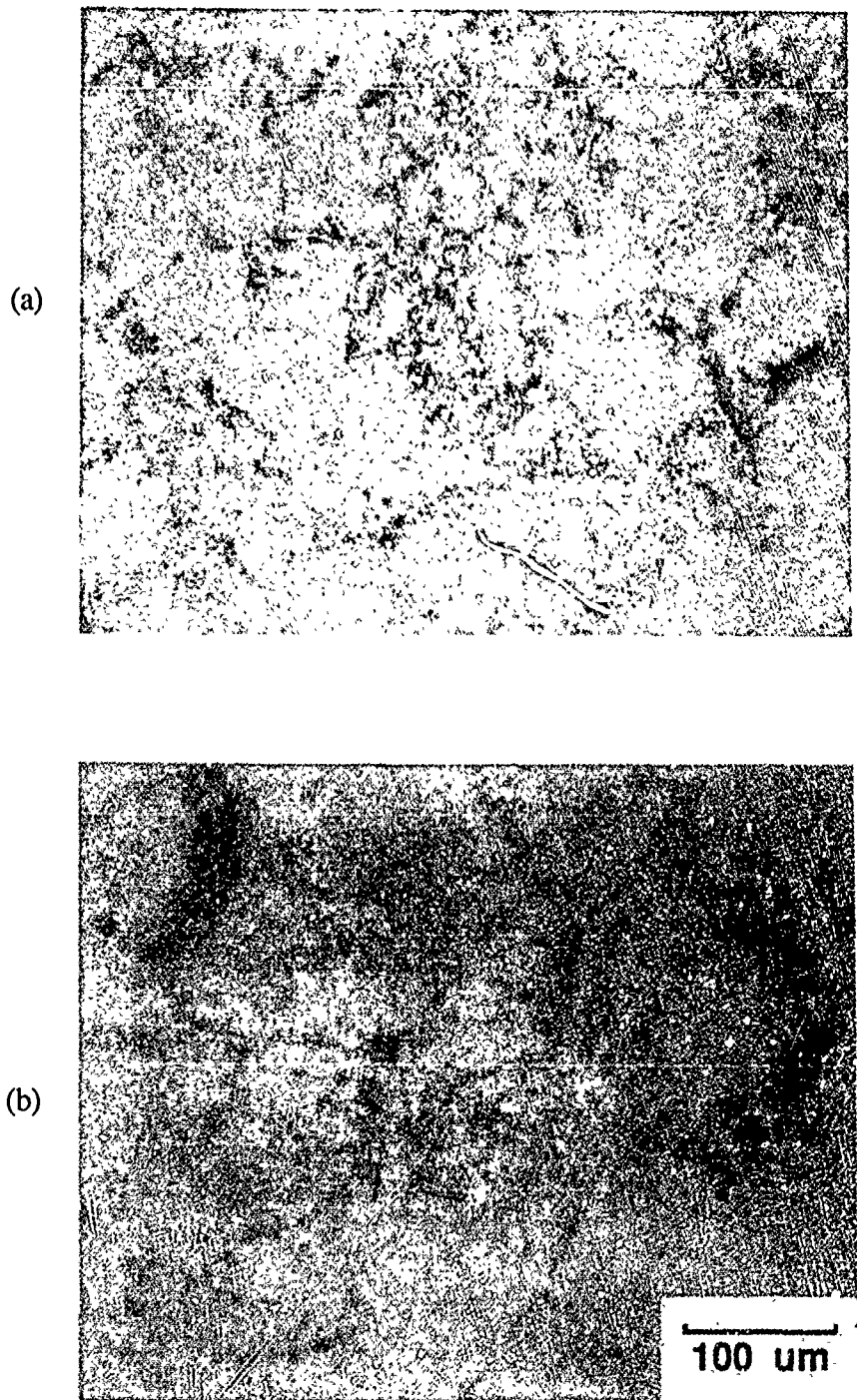


Figure 3-53 Optical micrographs of (a) Ti-23Al-6Nb-3V-3Ta-2Sn (IT-27) after heat treatment at 1160°C (2125°F) and (b) Ti-25Al-5Nb-5Ta-2Mo (IT-28) after heat treatment at 1120°C (2050°F).

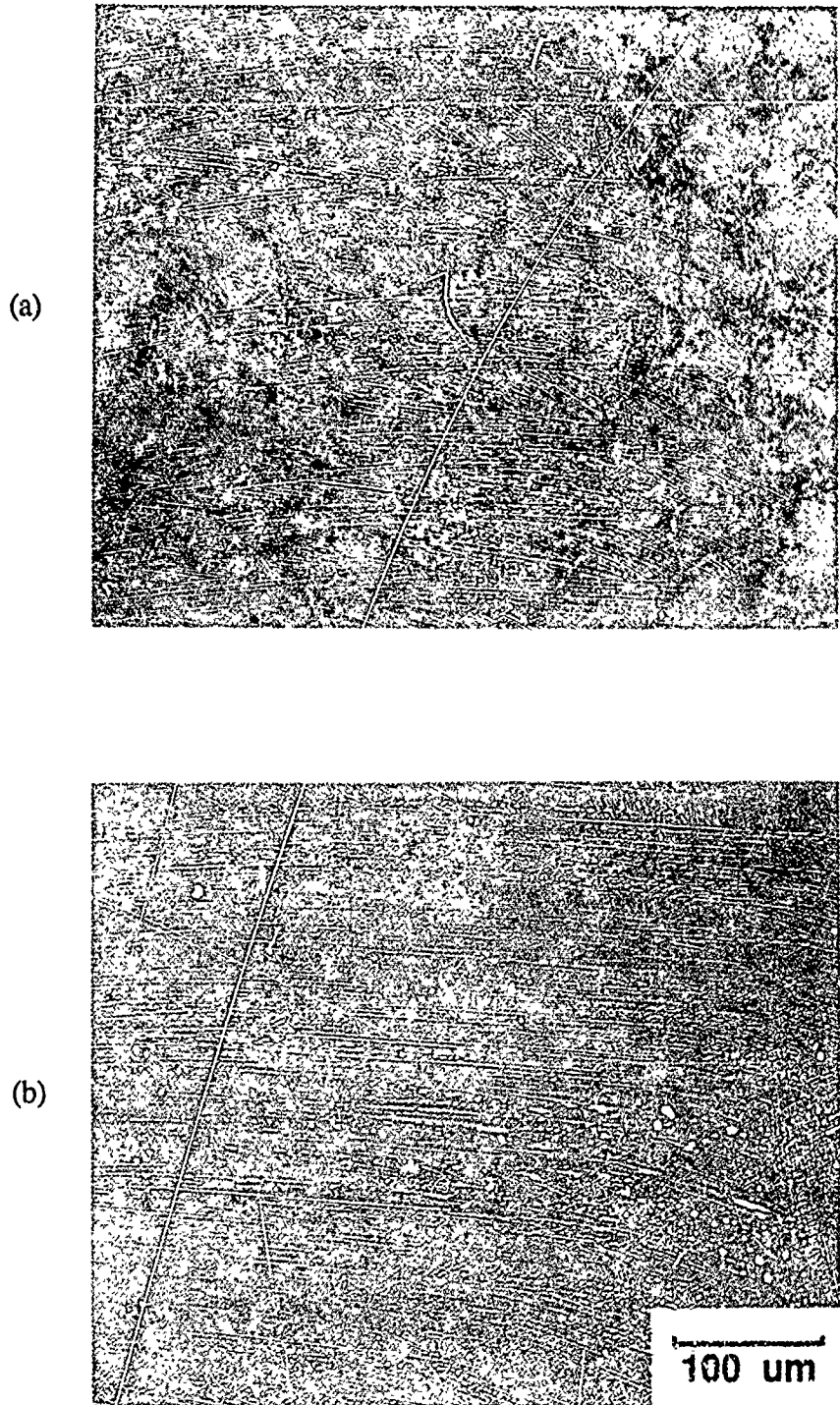


Figure 3-54 Optical micrographs of (a) Ti-25Al-6Nb-2Ta-2Cr (IT-29) after heat-treatment at 1105°C (2025°F) and (b) Ti-23Al-6Nb-2Ta-2Mo-2Cr (IT-30) after heat treatment at 1065°C (1950°F).

Table 3-20 Task 4 Tensile Properties

Alloy	Test Temperature (°C)	Test Temperature (°F)	0.2% YS (MPa)	0.2% YS (ksi)	UTS (MPa)	UTS (ksi)	E _l (%)	RA (%)
IT-23	24 649	75 1200	- 625	- 90.7	805 925	116.8 134.3	* 5.3	- 5.6
IT-24	24 427 649	75 800 1200	846 719 622	122.8 104.4 90.3	928 1082 848	134.7 157.0 123.1	* 15.3 7.8	- 13.8 9.5
IT-25	24 427 649	75 800 1200	- 693 646	- 100.6 93.8	878 1084 876	127.4 157.3 127.1	* 5.5 2.7	- 11.2 5.0
IT-26	24 427 649	75 800 1200	- 775 661	- 112.5 96.0	776 1143 914	112.6 165.9 132.7	* 13.8 6.4	- 11.3 6.3
IT-27	24 427 649	75 800 1200	- 693 608	- 100.6 88.2	636 1016 863	92.3 147.4 125.2	* 6.5 3.8	- 5.7 4.3
IT-28	24 649	75 1200	- 684	- 99.3	759 883	110.1 128.1	* 2.2	- 1.9
IT-29	24 427 649	75 800 1200	- 650 609	- 94.4 88.4	812 933 774	117.9 135.4 112.4	0.1+ 3.3 2.2	- 5.0 3.8
IT-30	24 427 649	75 800 1200	- 865 555	- 125.5 80.6	617 1242 925	89.6 180.3 134.2	0.0 13.6 3.1	- 15.6 8.1

* = Specimen failed in threaded region.

Table 3-21 Task 1 Tensile Properties as a Function of Specimen Configuration

Alloy	Test Temperature (°C)	Test Temperature (°F)	0.2% YS (MPa)	0.2% YS (ksi)	UTS (MPa)	UTS (ksi)	El (%)	RA (%)
IT-5X	24	75	728	105.7	818	118.7	0.6	2.0
	24	75	765	111.1	833	120.9	0.5	1.5
	427	800	493	71.6	837	121.5	9.3	11.1
	649	1200	394	57.2	607	88.1	10.6	15.1
IT-5Y	24	75	772	112.1	824	119.6	0.3	-
IT-5BX	24	75	-	-	883	128.1	<0.1	-
	24	75	-	-	760	110.3	<0.1	-
	427	800	655	95.1	765	111.0	1.1	0.8
	649	1200	541	78.5	738	107.1	3.4	8.2
IT-5BY	24	75	*	*	697	101.2	*	*
	649	1200	551	80.0	765	111.0	4.4	2.5

B = Beta solution heat treatment.

X = Specimen configuration with 0.50-13 threads and 0.25 inch gage diameter.

Y = Specimen configuration with 0.25-20 threads and 0.14 inch gage diameter.

* = Specimen failed in threaded region.

The results from creep testing of the Task 4 alloys are shown in Table 3-22. In addition, Larson-Miller parameters for the time to 0.2% creep for each of the Task 4 alloys have been calculated and plotted along with those of average Ti-24Al-11Nb data [19] in Figure 3-55. It is evident from the Larson-Miller plot that considerable improvement in creep properties can be achieved in relation to the alloy Ti-24Al-11Nb. In part, the improved creep properties can be associated with the higher Al levels of these alloys. The alloy with the lowest Al level, Ti-23Al-6Nb-2Ta-2Mo-2Cr (IT-30), had the lowest creep resistance of the Task 4 alloys but higher creep resistance than Ti-24Al-11Nb. Furthermore, the average Ti-24Al-11Nb data is based on material which was given a beta solution treatment and age which resulted in a microstructure with a large prior beta grain size. Therefore, the Ti-24Al-11Nb material had a larger grain size than the Task 4 alloys. The Task 4 alloying additions including Ta, Mo, V and Cr have resulted in significant improvement in overall creep resistance. Each of these elements would be expected to strengthen the beta phase of the alloy, and strengthening of the beta phase is certain to be related to improved creep resistance.

The results of stress/rupture testing of the Task 4 alloys are reported in Table 3-23. Specimens of Ti-25Al-6Nb-3V-3Ta (IT-23), Ti-25Al-8Nb-3V-3Ta (IT-24), Ti-25Al-6Nb-2V-2Ta-2Mo (IT-25), Ti-23Al-6Nb-3V-3Ta-2Sn (IT-27), and Ti-25Al-6Nb-2Ta-2Cr (IT-29) all had test lives of more than 100 hours when tested at 650°C (1200°F) and 345 MPa (50 ksi). These results show significant improvement over the alloy Ti-24Al-11Nb which has a rupture life of far less than 100 hours under the same test conditions. The test results

from the alloys Ti-25Al-6Nb-3V-3Ta (IT-23) and Ti-25Al-8Nb-3V-3Ta (IT-24) indicate that increasing the level of beta stabilizing elements from 12 to 14 atom percent is detrimental to rupture life. This conclusion is further supported by the test results from Ti-25Al-6Nb-2V-2Ta-2Mo (IT-25) and Ti-25Al-8Nb-2V-2Ta-2Mo (IT-26) which represent a similar comparison of 12 and 14 atom percent beta stabilizing elements. However, the specimens of the alloys Ti-25Al-8Nb-2V-2Ta-2Mo (IT-26) and Ti-25Al-5Nb-5Ta-2Mo (IT-28) failed at thermocouple attachments. As was the case for the creep test results, the Ti-25Al-6Nb-2Ta-2Cr (IT-29) specimen displayed the highest rupture resistance. Overall, the encouraging creep and stress/rupture results indicate that several of these alloys show potential for high temperature applications.

The fracture toughness test results for the Task 4 alloys are shown in Table 3-24. In general, the Task 4 alloys have much lower fracture toughness than the Task 2 alloys. As with tensile ductility, the lower fracture toughness is thought to be a function of the higher Al levels of the Task 4 alloys. However, due to the smaller size of the extruded bars evaluated in Task 4, a smaller specimen configuration was used and this may have influenced test results.

Table 3-22 Task 4 Creep Properties

Alloy	Temperature (°C) (°F)	Stress (MPa) (ksi)	Time to 0.1% (hours)	Time to 0.2% (hours)	LMP
IT-23	650 1200	155 22.5	11.8	56.0	23.7
IT-24	650 1200	172 25.0	2.4	15.8	22.7
IT-25	650 1200	172 25.0	15.6	107.0	24.1
IT-26	650 1200	172 25.0	11.1	94.0	24.0
IT-27	650 1200	172 25.0	18.6	103.0	24.1
IT-28	650 1200	172 25.0	48.0	285.0	24.8
IT-29	650 1200	155 22.5	635*	1270*	26.0
IT-30	650 1200	172 25.0	0.3	2.7	21.5

LMP = Larson-Miller Parameter = $T \times (12.5 + \log t) \times 10^{-3}$

* = Test stopped before 0.1% creep, time to 0.1 and 0.2% creep is calculated.

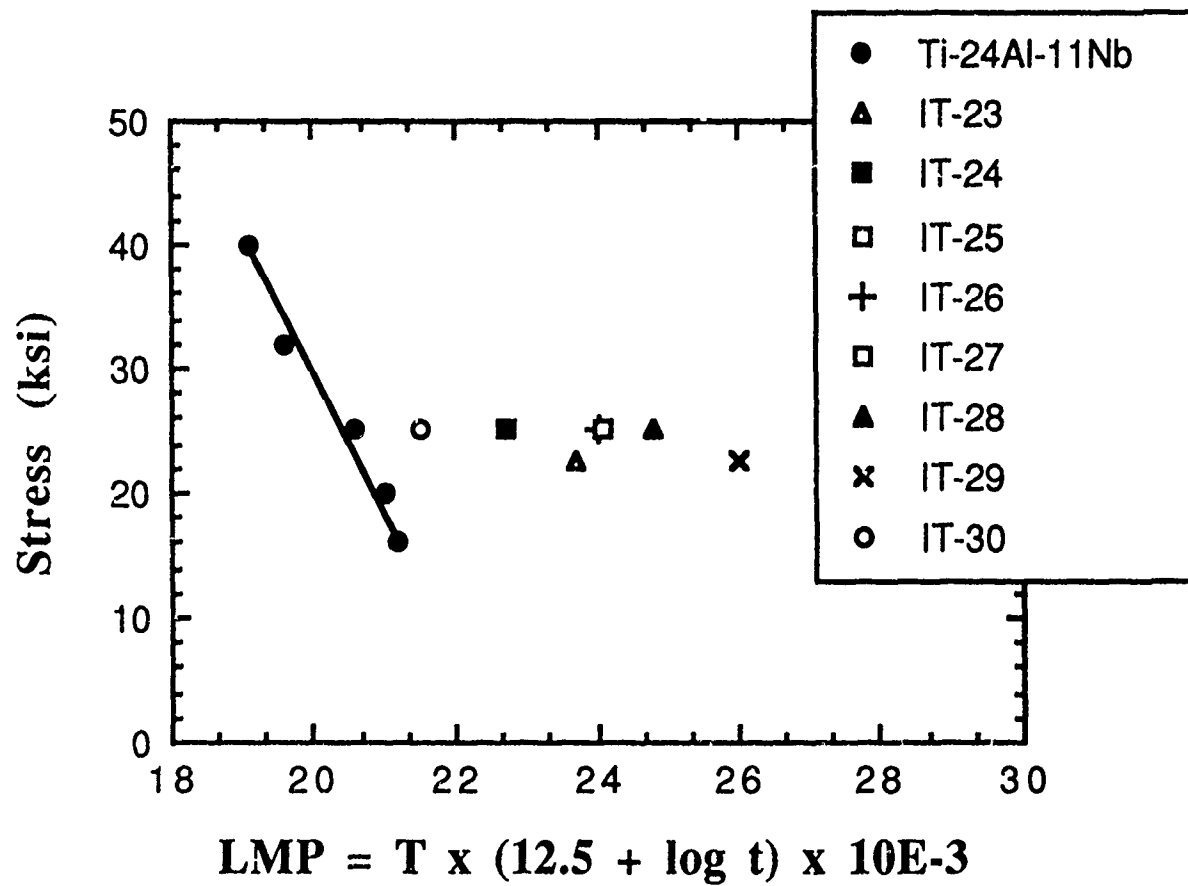


Figure 3-55 Larson-Miller plot for the time to 0.2% creep of Ti-24Al-11Nb and the Task 4 alloys where T is in °R.

Table 3-23 Task 4 Stress/Rupture Properties

Alloy	Temperature (°C)	Temperature (°F)	Stress (MPa)	Stress (ksi)	Time to Failure (hours)	Elongation at Failure (%)
IT-23	650	1200	345	50	616.0	7.7
IT-24	650	1200	345	50	206.0	6.5
IT-25	650	1200	345	50	143.2	1.5
IT-26	650	1200	345	50	92.2*	0.6*
IT-27	650	1200	345	50	588.4	4.2
IT-28	650	1200	345	50	16.3*	0.7*
IT-29	650	1200	345	50	770.0**	**
IT-30	650	1200	345	50	89.5#	#

* = Specimen failed at thermocouple attachment.
 ** = Specimen unloaded prior to failure.
 # = Specimen failed in threaded region.

Table 3-24 Task 4 Room Temperature Fracture Toughness Properties

Alloy	K _{exp} (MPa \sqrt{m})	K _{exp} (ksi \sqrt{in})
IT-23	24.3	22.1
IT-24	26.0	23.6
IT-25	18.5	16.8
IT-26	20.6	18.7
IT-27	20.7	18.8
IT-28	20.1	18.3
IT-29	12.5	11.4
IT-30	24.5	22.3

3.1.4.3 Alternate Microstructures

As in Tasks 1 and 2, two alloys were selected for a study of the influence of microstructure on mechanical properties. Based on trends which were identified in previous work, it was determined that more favorable microstructures for a balance of mechanical properties could be produced for Ti-25Al-8Nb-3V-3Ta (IT-24) and Ti-23Al-6Nb-2Ta-2Mo-2Cr (IT-30). Therefore, these alloys were selected for the study of microstructural effects. The alloy Ti-25Al-8Nb-3V-3Ta (IT-24), which was initially given a beta solution heat treatment, was heat-treated below the beta transus temperature to maintain a refined microstructure. The alternate heat treatment for the alloy Ti-23Al-6Nb-2Ta-2Mo-2Cr (IT-30) was conducted at the same alpha-2 plus beta solution temperature of 1065°C (1950°F) but was then cooled at a slower rate to coarsen the alpha-2 platelet size from that produced by the original heat treatment.

Tensile test results for Ti-25Al-8Nb-3V-3Ta (IT-24) and Ti-23Al-6Nb-2Ta-2Mo-2Cr (IT-30) are reported as a function of microstructure in Table 3-25. The data for Ti-25Al-8Nb-3V-3Ta (IT-24) indicates that heat treatment within the alpha-2 plus beta phase field yielded material with higher room temperature ductility and strength. The two representative microstructures for Ti-25Al-8Nb-3V-3Ta (IT-24) are shown in Figure 3-56. The tensile data for Ti-23Al-6Nb-2Ta-2Mo-2Cr (IT-30) shows that the slowly cooled material had greater ductility which resulted in a higher ultimate strength at low temperatures. In addition, the ductility of the slowly cooled material increases constantly with temperature while the ductility of the rapidly cooled material decreases at elevated temperature thus indicating microstructural instability. A more thorough discussion of the stability of similar alpha-2 titanium aluminide alloys is included in the Phase II results. As expected, the high temperature strength of the more ductile, slowly cooled material was measurably lower than the rapidly cooled material. The representative microstructures for the alloy Ti-23Al-6Nb-2Ta-2Mo-2Cr (IT-30) are shown in Figure 3-57.

Table 3-25 Tensile Properties for the Microstructural Study of Task 4 Alloys

Alloy	Heat Treatment	Test Temp. (°C)	Test Temp. (°F)	0.2% YS (MPa)	0.2% YS (ksi)	UTS (MPa)	UTS (ksi)	EI (%)
IT-24	alpha-2 plus beta	24	74	969	140.7	1133	164.5	1.1
		427	800	794	115.3	1192	173.0	12.4
IT-24	beta solution	24	74	846	122.8	928	134.7	*
		427	800	719	104.4	1082	157.0	15.3
		650	1200	622	90.3	848	123.1	7.8
IT-30	alpha-2 plus beta (rapid cool)	24	74	-	-	617	89.6	0.0
		427	800	865	125.5	1242	180.3	13.6
		650	1200	555	80.6	925	134.2	3.1
IT-30	alpha-2 plus beta (slow cool)	24	74	779	113.0	889	129.1	0.5
		650	1200	460	66.8	725	105.2	16.5

* Specimen failed in threaded region.

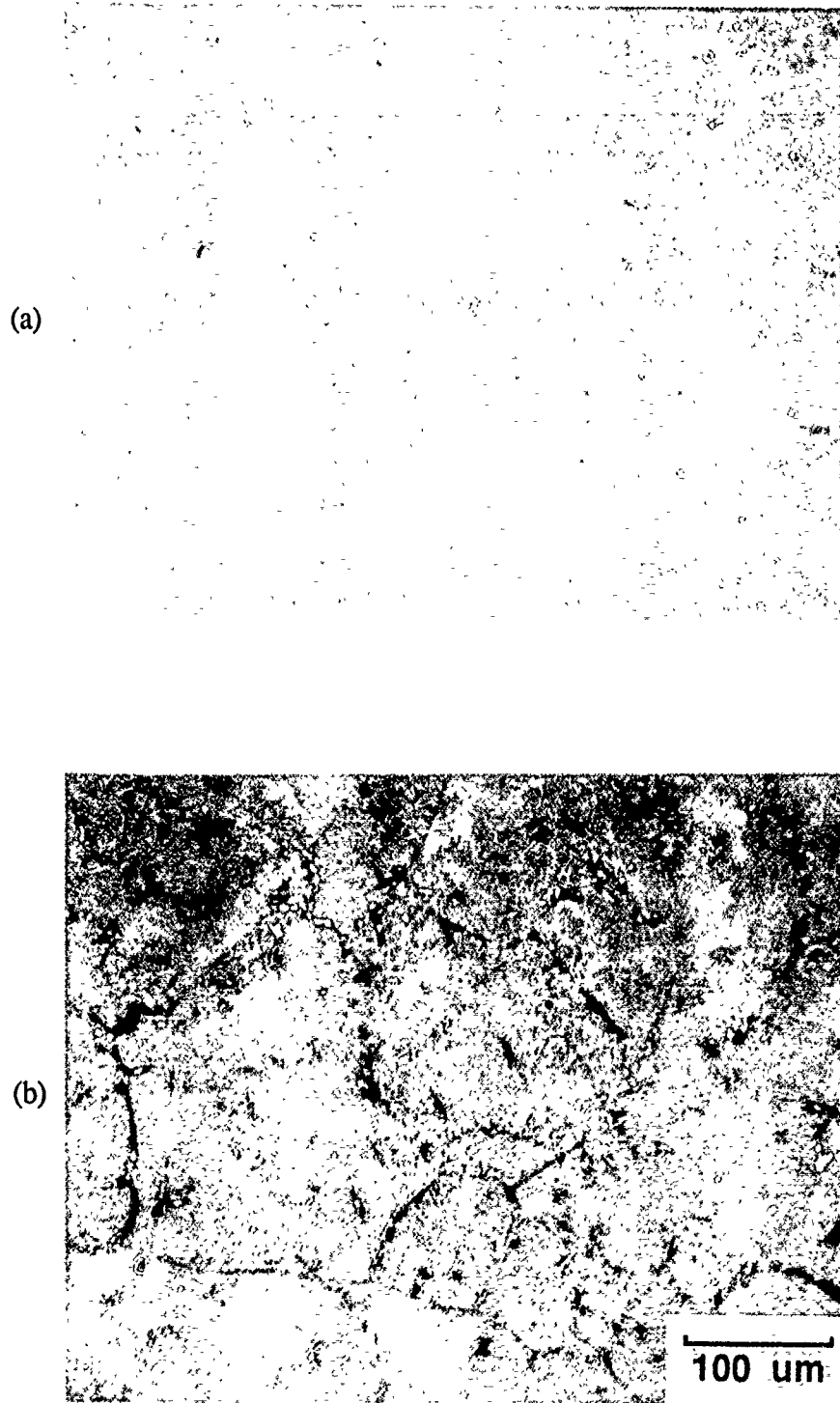


Figure 3-56 Microstructure of Ti-25Al-8Nb-3V-3Ta (IT-24) after (a) beta solution heat-treatment and (b) heat-treatment in the alpha-2 plus beta phase field.

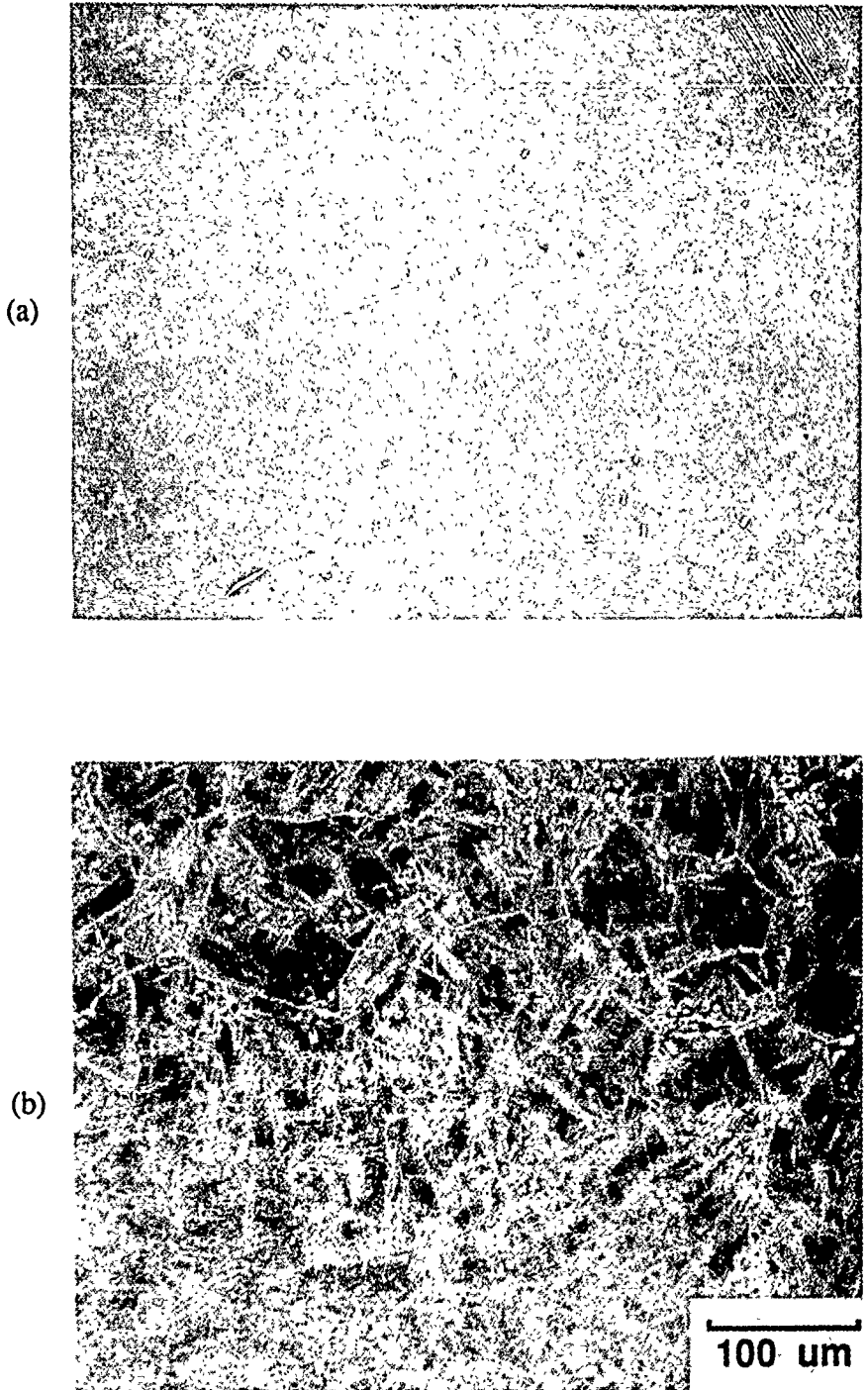


Figure 3-57 Microstructure of Ti-23Al-6Nb-2Ta-2Mo-2Cr (IT-30) after heat-treatment in the alpha-2 plus beta phase field and cooling rates of (a) 40°C (75°F) per minute and (b) 20°C (35°F) per minute.

The results from creep testing of the microstructural variations of Ti-25Al-8Nb-3V-3Ta (IT-24) and Ti-23Al-6Nb-2Ta-2Mo-2Cr (IT-30) are listed in Table 3-26 along with calculated Larson-Miller parameter values. The alloy Ti-23Al-6Nb-2Ta-2Mo-2Cr (IT-30) creep data shows that primary creep was not a function of cooling rate or transformed beta platelet size within this material which was processed and heat-treated in the alpha-2 plus beta phase field. The creep data for Ti-25Al-8Nb-3V-3Ta (IT-24) indicates that there was little difference between the primary creep properties of specimens with alpha-2 plus beta and beta heat-treated microstructures. Although the difference was statistically insignificant, the specimen which had an alpha-2 plus beta heat treatment and a smaller prior beta grain size actually had slightly better creep properties than the specimen which was given a beta solution heat treatment. This data implies that some microstructural refinement and corresponding ductility improvement can be achieved in these alloys without degrading creep properties. However, we should note that the Ti-25Al-8Nb-3V-3Ta (IT-24) material which was heat-treated in the alpha-2 plus beta phase field did not have an extremely fine prior beta grain size.

Table 3-26 Creep Test Results for the Microstructural Study of Task 4 Alloys after Testing at 650°C (1200°F) / 172 MPa (25 ksi)

Alloy	Heat treatment	Time to 0.1% (hours)	Time to 0.2% (hours)	LMP for 0.2% (C=12.5)
IT-24	alpha-2 plus beta	3.3	21.0	22.9
IT-24	beta solution	2.4	15.8	22.7
IT-30	alpha-2 plus beta (rapid cool)	0.3	2.7	21.5
IT-30	alpha-2 plus beta (slow cool)	0.6	2.7	21.5

The room temperature fracture toughness properties for the microstructural variations of the Task 4 alloys are listed in Table 3-27. In Task 2, alloys with retained beta phase were shown to have higher fracture toughness with a refined microstructure produced by alpha-2 plus beta processing and heat treatment than with a large grain microstructure produced by beta solution heat treatment. The results for Ti-25Al-8Nb-3V-3Ta (IT-24) indicate the opposite relationship between fracture toughness and microstructure. The results shown in Table 3-27 show that the Ti-25Al-8Nb-3V-3Ta (IT-24) specimen which was given a beta solution heat treatment had slightly higher fracture toughness than the specimen which was processed and heat-treated in the alpha-2 plus beta phase field. The difference in fracture toughness for the two Ti-25Al-8Nb-3V-3Ta (IT-24) microstructures is, however, relatively small. Fracture toughness was shown to be a stronger function of microstructure with the alloy Ti-22.5Al-6Nb-2Ta-2Cr (IT-12) from Task 2 which had a significantly lower Al level. In addition, the difference in prior beta grain size for the alloy Ti-22.5Al-6Nb-2Ta-2Cr (IT-12) microstructures was much greater than for the Ti-25Al-8Nb-3V-3Ta (IT-24) microstructures which are shown in Figure 3-56. The additional results, shown in Table 3-27, indicate that fracture toughness was not found to be a function of cooling rate or alpha-2 platelet size for Ti-23Al-6Nb-2Ta-2Mo-2Cr (IT-30).

Table 3-27 Fracture Toughness Test Results for the Microstructural Study of Task 4 Alloys

Alloy	Heat Treatment	K_{exp} (MPa \sqrt{m})	K_{exp} (ksi \sqrt{in})
IT-24	alpha-2 plus beta	23.2	21.1
IT-24	beta solution	26.0	23.6
IT-30	alpha-2 plus beta (rapid cool)	24.5	22.3
IT-30	alpha-2 plus beta (slow cool)	24.3	22.1

3.1.4.4 Task 4 - Summary

After the first three tasks of Phase I were completed in parallel, a fourth task was completed as a second iteration. The alloys which were selected for Task 4 were derived from trends which were identified during the first three tasks of Phase I. Since the most promising results were achieved with the alpha-2 plus beta alloys evaluated in Task 2, the Task 4 alloys were all alpha-2 plus beta compositions with higher levels of beta stabilizing additions and higher Al levels than those studied in Task 2. The primary impetus behind this selection of compositions was to attempt to achieve improved strength over a range of temperatures without sacrificing the ductility and toughness levels achieved in Task 2.

The mechanical property test results for the Task 4 alloys indicate that improved tensile strength and creep strength were achieved but at considerable expense to low temperature ductility and fracture toughness. With Al levels of approximately 25 atom percent, a small increase in beta stabilizing additions was clearly not sufficient to maintain the ductility and fracture toughness achieved in Task 2. In Task 4, studies of microstructural effects on mechanical properties included cooling rate variations for Ti-23Al-6Nb-2Ta-2Mo-2Cr (IT-30). Faster cooling rates increased the tensile strength and reduced the ductility of this alloy but did not influence creep resistance or fracture toughness.

3.2 Phase II: Alloy Scale-up

The alloy compositions which were selected for evaluation in Phase II are shown in Table 3-28. These alloys were selected on the basis of results obtained in Phase I of this program. From the evaluation of alloys in Tasks 2 and 4 of Phase I, it was clear that compositions with less than 23 atom percent Al have limited high temperature strength and creep resistance while those with Al levels greater than or equal to 25 atom percent have limited room temperature ductility. As a result, the aim Al level of 24.5 atom percent was chosen for the Phase II alloys in an effort to obtain an appropriate balance between creep resistance and room temperature ductility.

The total level of beta stabilizing additions also has significant influence on mechanical properties. Data obtained in Phase I, Task 1 indicate that alloys with total beta stabilizing additions of less than about 10 atom percent lack both strength and ductility. Furthermore, Task 4 testing indicated that alloys with 14 atom percent beta stabilizer have shorter rupture lives than those with 12 atom percent beta stabilizer. All three of the Phase II alloys were designed to have a total of 12 atom percent beta stabilizer. Of the beta stabilizers, Nb has been shown to be of considerable importance for improvement of ductility and toughness in work dating back as far as 1960 as reported by McAndrew and Simcoe [2]. In addition, other beta stabilizers are of use in more modest amounts. The addition of Mo is useful for improvement of creep resistance, strength and modulus as well as for microstructural refinement; however, large amounts of Mo are known to be detrimental to ductility [20]. As a result, Mo was included in all of the Phase II alloys at a constant level of 2 atom percent. Although there is some evidence that V decreases environmental resistance, it was added to the alloy Ti-24.5Al-6Nb-2Mo-2Ta-2V (IT-A) for its solid solution strengthening effect while Ta was added to all three Phase II alloys for solid solution strengthening. The final alloying addition, Cr, was added to the alloy Ti-24.5Al-6Nb-2Mo-2Ta-2Cr (IT-C) for its potential improvement of fracture toughness as demonstrated by the alloy Ti-22.5Al-6Nb-2Ta-2Cr (IT-12) which had the highest fracture toughness of any alloy tested in this program.

Table 3-28 Phase II Alloy Compositions*

Alloy	Ti	Al	Nb	V	Ta	Mo	Cr	O
IT-A	63.5 [61.7] -	24.5 [13.5] (13.4)	6.0 [11.4] (12.3)	2.0 [2.1] (1.7)	2.0 [7.4] (7.0)	2.0 [3.9] (3.4)	- -	- -
IT-B	63.5 [60.9] -	24.5 [13.2] (12.6)	8.0 [14.9] (14.4)	- -	2.0 [7.2] (7.0)	2.0 [3.8] (3.5)	- -	- -
IT-C	63.5 [61.9] -	24.5 [13.4] (13.4)	6.0 [11.3] (3.7)	- -	2.0 [7.4] (7.2)	2.0 [3.9] (3.7)	2.0 [2.1] (2.1)	- -

* The compositions which are not enclosed in brackets are aim atom percents, compositions enclosed by [] are aim weight percents, and compositions enclosed by () are measured weight percents.

The alloy Ti-24.5Al-6Nb-2Mo-2Ta-2V (IT-A) was produced by an induction melting technique and cast into a 7 cm (2.75 in) diameter graphite mold. This ingot was then HIP'ed and 'homogenized' above the beta transus temperature for 4 hours. After HIP'ing, the Ti-24.5Al-6Nb-2Mo-2Ta-2V (IT-A) material was extruded below the beta transus temperature at a ratio of 23:1. Final heat-treatment of Ti-24.5Al-6Nb-2Mo-2Ta-2V (IT-A) was conducted high in the alpha-2 plus beta phase field at 1120°C (2050°F) followed by a salt quench at 870°C (1600°F). This heat-treatment was selected after an extensive study of the effects of solution temperature and cooling rate on microstructure. As shown by the backscatter electron micrograph in Figure 3-58a, the final microstructure was very inhomogenous. Considerable segregation was found in all test bars of the Ti-24.5Al-6Nb-2Mo-2Ta-2V (IT-A) which were analyzed metallographically. As a result of these findings and examination of other induction melted ingots (with and without Ta), it was evident that significant amounts of segregation existed in all induction melted alpha-2 titanium aluminide ingots. This chemical segregation appears to result from insufficient amounts of super heat and mixing during the induction melting process. Subsequent 'homogenization' heat-treatment and extrusion processing were not effective in eliminating the inhomogeneity. While beta forging prior to the alpha-2 plus beta extrusion processing may improve homogeneity, this defeats the purpose of producing cast-to-size ingots by induction melting.

Alternative routes for the melting and processing of Ti-24.5Al-8Nb-2Mo-2Ta (IT-B) and Ti-24.5Al-6Nb-2Mo-2Ta-2Cr (IT-C) were chosen. Rather than induction melting and direct extrusion, these alloys were melted to 15.2 cm (6 in) diameter ingot by a VAR process and then forged to 7 cm (2.75 in) diameter billet. Beta forging was followed by extrusion and heat-treatment processing procedures which were identical to the induction melted ingot, Ti-24.5Al-6Nb-2Mo-2Ta-2V (IT-A). This processing included extrusion below the beta transus temperature at a 23:1 ratio and heat-treatment high in the alpha-2 plus beta phase field. Figure 3-58b shows that the final microstructures of the VAR melted alloys were very homogeneous. However, due to a clerical error at the melting vendor, the chemical composition of the alloy Ti-24.5Al-6Nb-2Mo-2Ta-2Cr (IT-C) was far from the aim composition. This discrepancy was not identified until testing of the alloy was well underway. As a result, testing was completed on the measured chemical composition of IT-C which will be referred to as Ti-23.5Al-2Nb-2Mo-2Ta-2Cr (IT-C) from this point on. The microstructures of each of the three Phase II alloys after final heat-treatment and aging are shown in Figure 3-59.

The smooth bar tensile properties of the Phase II alloys are shown in Tables 3-29 and 3-30. These properties and the notched tensile properties shown in Table 3-31 are representative of material which was aged for 1 hour at 760°C (1400°F) following heat-treatment high in the alpha-2 plus beta phase field and salt quenching. The smooth bar tensile properties shown in Table 3-32 were produced from material which was given an additional 100 hour thermal exposure at 705°C (1300°F). Tensile testing was conducted at a strain rate of 0.004 per minute. Plastic elongations for room temperature tests were measured by an extensometer while elongations for elevated temperature tests were measured by the standard procedure of marking the gage section and measuring the length before and after testing.

The tensile test results for Ti-24.5Al-6Nb-2Mo-2Ta-2V (IT-A) and Ti-24.5Al-8Nb-2Mo-2Ta (IT-B) show that the elongation of these alloys increases with test temperature to 427°C (800°F) and then decreases at 538 and 649°C (1000 and 1200°F) before increasing again at 760°C (1400°F). It is possible that this behavior could be the result of

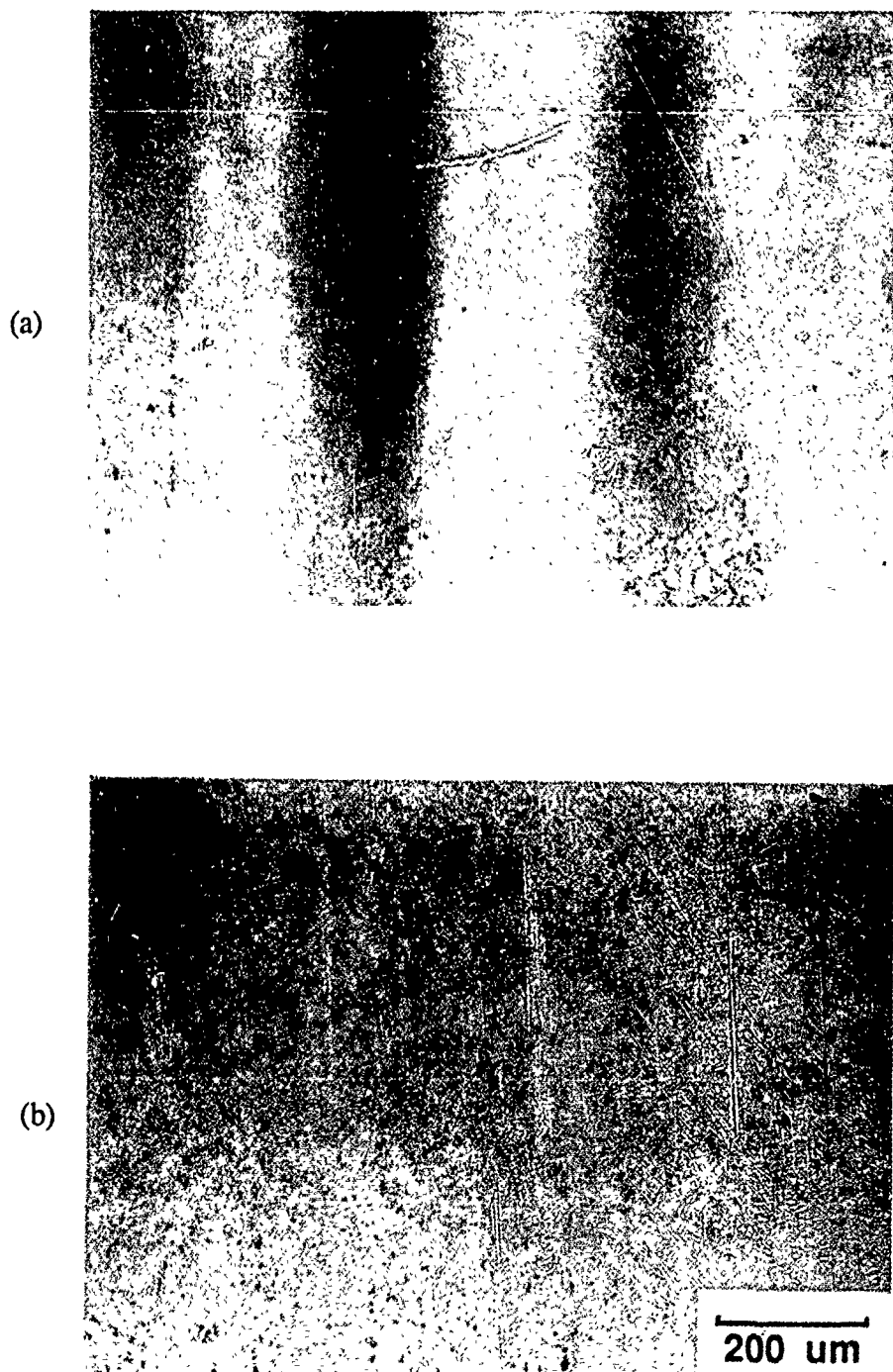
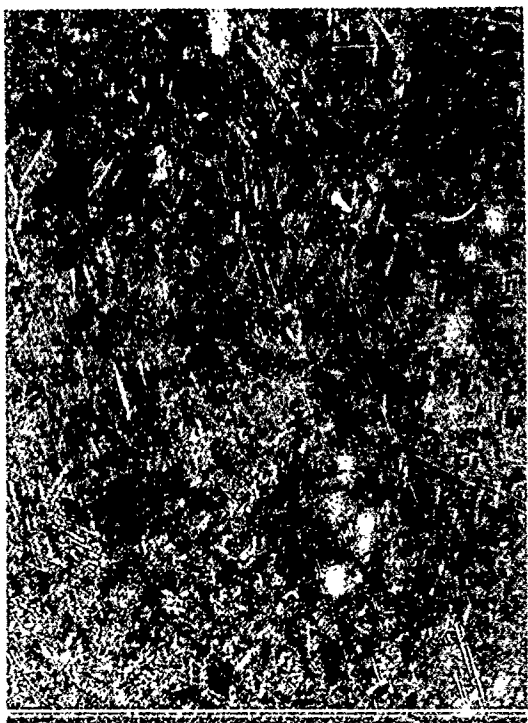


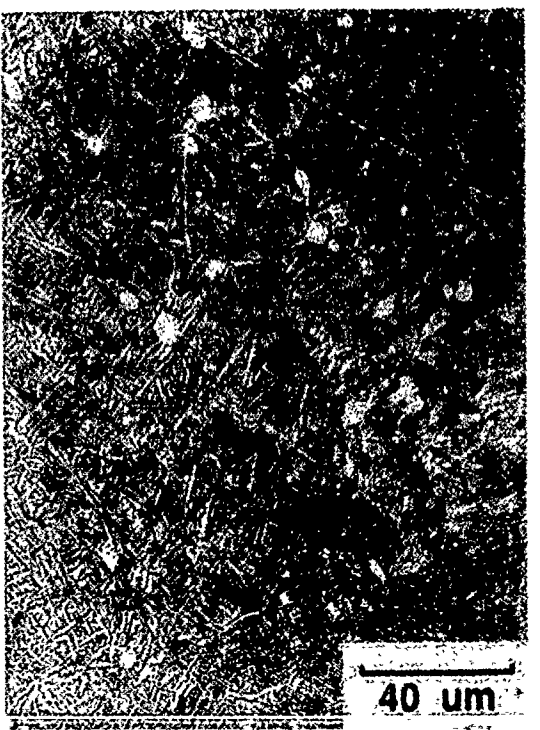
Figure 3-58 Backscattered electron micrographs showing (a) inhomogenous microstructure of Ti-24.5Al-6Nb-2Mo-2Ta-2V (IT-A) and (b) homogeneous microstructure of Ti-23.5Al-2Nb-2Mo-2Ta-2Cr (IT-C).



(a)



(b)



(c)

Figure 3-59 Optical metallography following final heat-treatment of (a) Ti-24.5Al-6Nb-2Mo-2Ta-2V (IT-A), (b) Ti-24.5Al-8Nb-2Mo-2Ta (IT-B) and (c) Ti-23.5Al-2Nb-2Mo-2Ta-2Cr (IT-C).

Table 3-29 Tensile Properties of Alloys IT-A and IT-B

Alloy	Temperature (°C)	Temperature (°F)	0.2% YS (MPa)	0.2% YS (ksi)	UTS (MPa)	UTS (ksi)	Elongation (%)	R of A (%)
IT-A	24	75	781.1	113.2	923.9	133.9	0.7	-
IT-A	24	75	771.4	111.8	876.3	127.0	0.5	-
IT-A	204	400	657.6	95.3	850.8	123.3	1.8	2.6
IT-A	204	400	663.1	96.1	874.9	126.8	1.5	1.8
IT-A	427	800	593.4	86.0	959.8	139.1	*	4.5
IT-A	427	800	576.8	83.6	959.8	139.1	8.2	6.9
IT-A	538	1000	600.3	87.0	881.8	127.8	7.3	8.9
IT-A	538	1000	550.6	79.8	901.8	130.7	5.3	9.1
IT-A	649	1200	536.8	77.8	756.9	109.7	5.8	13.2
IT-A	649	1200	549.9	79.7	792.1	114.8	6.5	11.2
IT-A	760	1400	382.3	55.4	639.6	92.7	12.4	26.2
IT-A	760	1400	389.2	56.4	628.6	91.1	12.0	19.9
IT-B	24	75	792.1	114.8	942.5	136.6	1.0	-
IT-B	24	75	770.0	111.6	908.0	131.6	0.9	-
IT-B	204	400	616.2	89.3	881.8	127.8	1.5	2.8
IT-B	204	400	660.3	95.7	872.2	126.4	*	1.8
IT-B	427	800	528.5	76.6	930.1	134.8	15.1	17.1
IT-B	427	800	538.9	78.1	941.2	136.4	12.4	15.7
IT-B	538	1000	517.5	75.0	826.6	119.8	10.6	9.4
IT-B	538	1000	476.1	69.0	748.7	108.5	8.3	11.4
IT-B	649	1200	494.0	71.6	735.5	106.6	4.2	12.0
IT-B	649	1200	463.0	67.1	692.1	100.3	7.0	12.6
IT-B	760	1400	326.4	47.3	516.1	74.8	18.0	48.4
IT-B	760	1400	332.6	48.2	564.4	81.8	#	#

* = Failure occurred outside of gage marks.

= Specimen failed at W inclusion.

Table 3-30 Tensile Properties of Alloy IT-C

Alloy	Temperature (°C)	Temperature (°F)	0.2% YS (MPa)	0.2% YS (ksi)	UTS (MPa)	UTS (ksi)	Elongation (%)	R of A (%)
IT-C	24	75	807.3	117.0	834.9	121.0	0.3	-
IT-C	24	75	787.3	114.1	892.9	129.4	0.7	0.6
IT-C	204	400	684.5	99.2	886.7	128.5	2.4	1.4
IT-C	204	400	680.3	98.6	748.7	108.5	*	*
IT-C	427	800	607.2	88.0	980.5	142.1	10.4	-
IT-C	427	800	622.4	90.2	926.0	134.2	6.0	-
IT-C	538	1000	511.3	74.1	841.8	122.0	9.5	14.7
IT-C	538	1000	574.1	83.2	859.7	124.6	11.1	14.4
IT-C	649	1200	443.7	64.3	636.2	92.2	20.5	50.7
IT-C	649	1200	437.5	63.4	643.8	93.3	17.2	42.3
IT-C	760	1400	314.0	45.5	485.1	70.3	24.7	82.2
IT-C	760	1400	287.0	41.6	449.2	65.1	15.3	42.9

* = Specimen failed in threaded region.

Table 3-31 Notched Tensile Properties of Phase II Alloys

Alloy	Temperature (°C) (°F)		NTS (MPa)	NTS (ksi)	NTS / UTS
IT-A	24	75	463.7	67.2	0.52
IT-A	24	75	513.4	74.4	0.57
IT-A	427	800	1055.7	153.0	1.10
IT-A	649	1200	698.3	101.2	0.90
IT-B	24	75	603.8	87.5	0.65
IT-B	24	75	568.6	82.4	0.61
IT-B	427	800	1012.9	146.8	1.08
IT-B	649	1200	712.1	103.2	1.00
IT-C	24	75	431.3	62.5	0.50
IT-C	24	75	429.9	62.3	0.50
IT-C	427	800	818.3	118.6	0.86
IT-C	649	1200	845.9	122.6	1.32
$K_t = 3.5$					

Table 3-32 Post Thermal Exposure Tensile Properties of Phase II Alloys

Alloy	Temperature (°C)	Temperature (°F)	0.2% YS (MPa)	0.2% YS (ksi)	UTS (MPa)	UTS (ksi)	Elongation (%)	R of A (%)
IT-A	24	75	802.5	116.3	930.1	134.8	0.8	-
IT-A	24	75	809.4	117.3	886.0	128.4	0.4	-
IT-A	427	800	559.6	81.1	902.5	130.8	8.3	8.3
IT-A	649	1200	532.7	77.2	803.9	116.5	6.5	13.4
IT-B	24	75	767.3	111.2	874.2	126.7	0.7	-
IT-B	24	75	799.0	115.8	879.1	127.4	0.5	-
IT-B	427	800	576.2	83.5	846.6	122.7	3.5	4.9
IT-B	649	1200	483.7	70.1	726.6	105.3	12.6	12.6
IT-C	24	75	761.1	110.3	776.3	112.5	0.2	-
IT-C	24	75	726.6	105.3	809.4	117.3	0.5	-
IT-C	427	800	568.6	82.4	676.9	98.1	1.8	2.2
IT-C	649	1200	447.1	64.8	681.7	98.8	11.0	17.4

microstructural instability; therefore, specimens of each alloy were given 100 hours of exposure at 705°C (1300°F) to test this possibility. The elongation of the Phase II alloys is shown graphically with and without thermal exposure in Figure 3-60a. No clear change in elongation was noted as result of thermal exposure for Ti-24.5Al-6Nb-2Mo-2Ta-2V (IT-A) while the elongation of Ti-24.5Al-8Nb-2Mo-2Ta (IT-B) at 427°C (800°F) was significantly reduced after thermal exposure. However, the 427°C (800°F) specimen of Ti-24.5Al-8Nb-2Mo-2Ta (IT-B) failed outside of the gage marks and there is some question of the validity of that data point. No clear differences were identified in the fracture morphologies of the exposed and unexposed specimens of Ti-24.5Al-8Nb-2Mo-2Ta (IT-B) except for a small variation of prior beta grain size. Furthermore, as discussed below, no significant variations in microstructure were identified by TEM of the base heat-treatment and thermally exposed conditions.

When viewed in terms of reduction of area as shown in Figure 3-60b, the ductility of Ti-24.5Al-6Nb-2Mo-2Ta-2V (IT-A) shows a normal temperature dependence while the ductility of Ti-24.5Al-8Nb-2Mo-2Ta (IT-B) shows a less pronounced reduction of ductility at intermediate temperatures. This may indicate that the plateau or decrease in ductility at intermediate test temperatures occurs as a result of a transition from uniform deformation at lower test temperatures to more localized deformation at high temperatures as has been suggested previously [21]. Tensile specimens for each test temperature of Ti-24.5Al-8Nb-2Mo-2Ta (IT-B) are shown in Figure 3-61. While a great deal of surface roughness was found after 427°C (800°F) testing, the deformation was generally uniform with no evidence of necking. Likewise, there was no significant evidence of necking for the 540 and 650°C (1000 and 1200°F) test specimens. There was, however, some secondary cracking at the surface of the 540 and 650°C (1000 and 1200°F) specimens. This onset of surface cracking at intermediate test temperatures appears to cause the reduction of intermediate temperature ductility for this particular alloy and microstructural condition. Apparently, reduced intermediate temperature ductility of alpha-2 titanium aluminide alloys can be caused by both the onset of surface cracking and the localization of deformation (necking). For the alloy Ti-24.5Al-8Nb-2Mo-2Ta (IT-B), we were unable to establish any relationship between surface cracking and localized deformation.

Tensile testing of Ti-23.5Al-2Nb-2Mo-2Ta-2Cr (IT-C) resulted with a normal dependence between test temperature and ductility for both the as-heat-treated and thermally exposed conditions. This is true for both elongation and reduction of area as shown in Figure 3-60. Thermal exposure did cause a significant decrease in elevated temperature elongation. Again, this was revealed by both elongation and reduction of area measurements.

Transmission electron microscopy was conducted on the Phase II materials before and after thermal exposure. Figure 3-62 shows thinning of the beta ribs and thickening of the alpha-2 platelets which occurred in Ti-24.5Al-6Nb-2Mo-2Ta-2V (IT-A) after the aging and thermal exposure heat-treatments. No other microstructural changes were identified after the aging process. Although it is clear that thinning of the beta ribs does occur during the 1 hour age at 760°C (1400°F), it was not evident that additional thinning of the beta ribs occurs during the 100 hour thermal exposure at 705°C (1300°F). As a result, it was not evident that reduced ductility after thermal exposure was caused by microstructural instability.

The microstructure of Ti-24.5Al-8Nb-2Mo-2Ta (IT-B) as observed by TEM is shown after its base heat-treatment in Figure 3-63a. Fairly straight Widmanstatten alpha-2 plates are observed surrounded by an almost continuous beta matrix. Short lengths of what

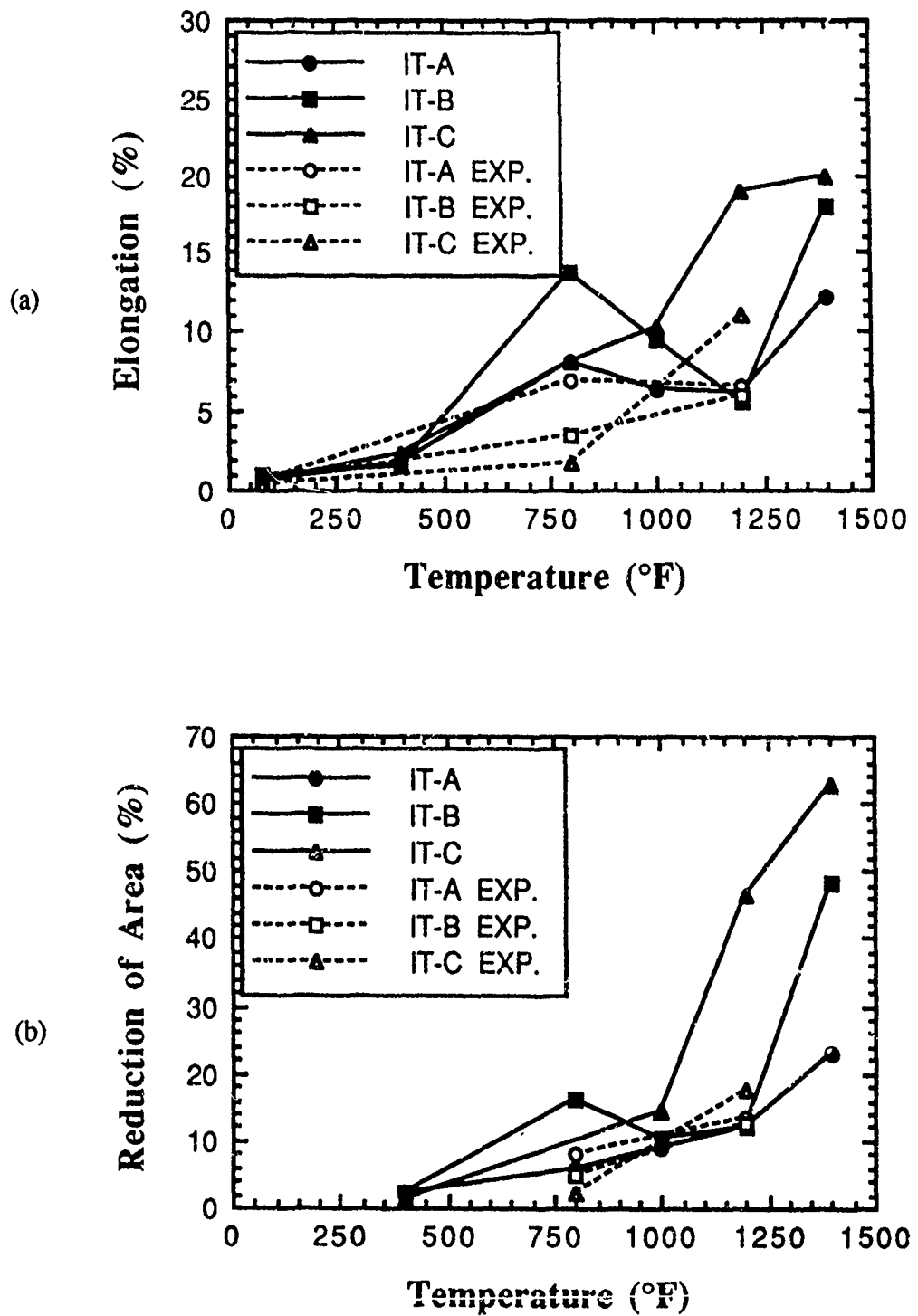


Figure 3-60 Ductility of Phase II alloys before and after a 100 hour thermal exposure at 705°C (1300°F) as determined by (a) elongation and (b) reduction of area.

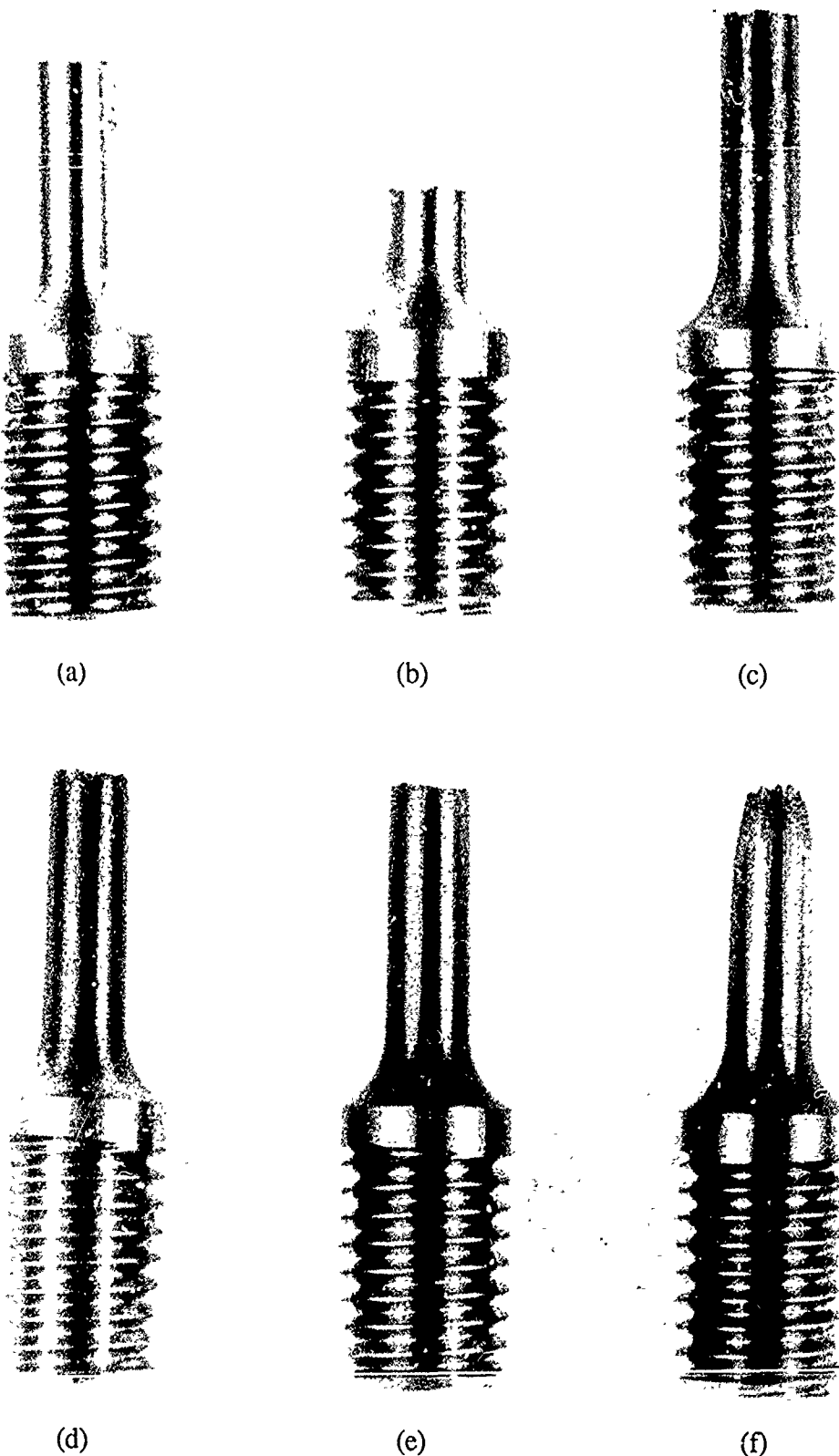


Figure 3-61 Macro photographs of tensile specimens of the alloy Ti-24.5Al-8Nb-2Mo-2Ta (IT-B) tested at (a) room temperature, (b) 205°C (400°F), (c) 425°C (800°F), (d) 540°C (1000°F), (e) 650°C (1200°F) and (f) 760°C (1400°F).

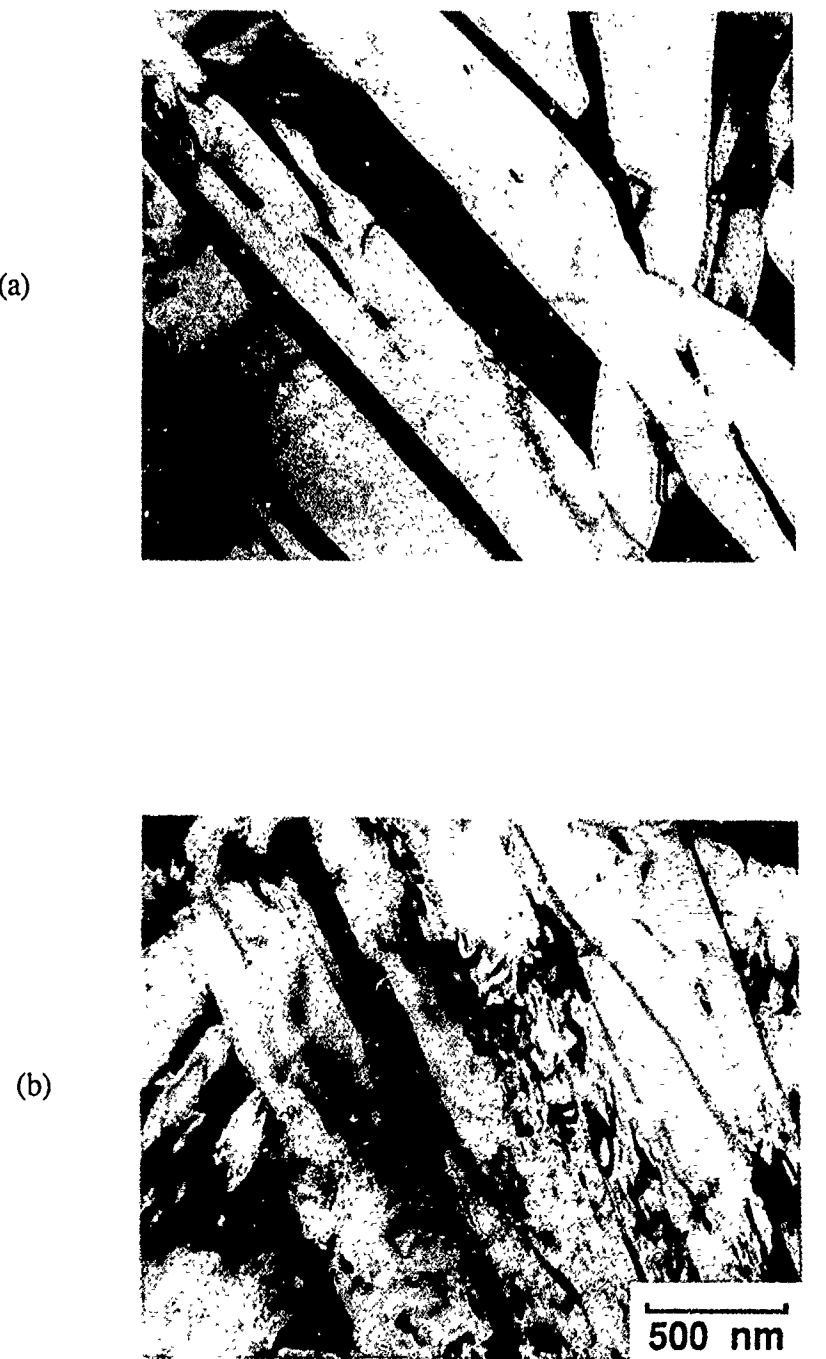


Figure 3-62 TEM micrographs of Ti-24.5Al-6Nb-2Mo-2Ta-2V (IT-A) showing the (a) microstructure after salt quench and (b) thinning of beta ribs after a 100 hour thermal exposure at 705°C (1300°F).

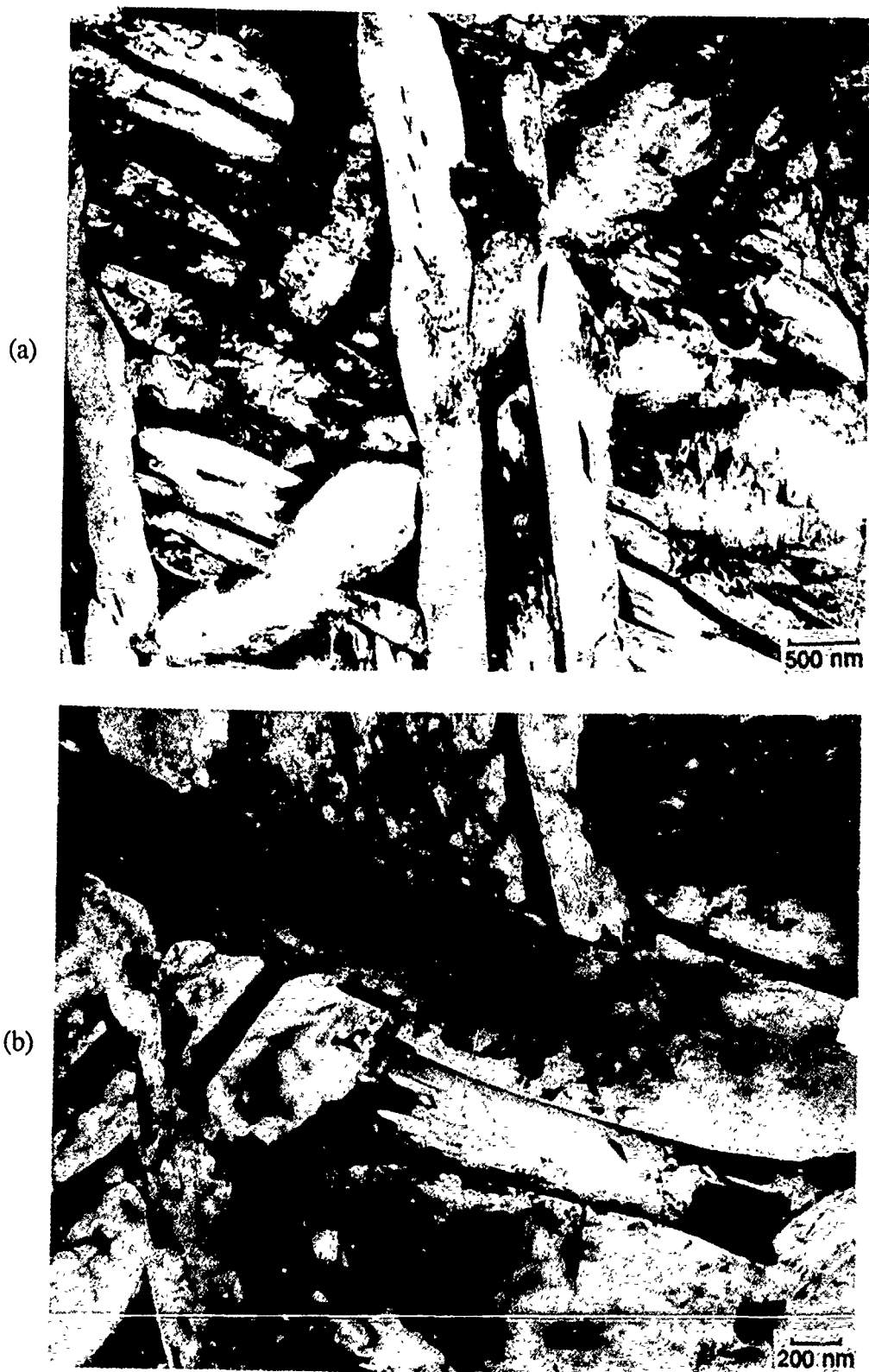


Figure 3-63 Bright-field TEM micrographs of Ti-24.5Al-8Nb-2Mo-2Ta (IT-B) showing (a) Widmanstatten alpha-2 plates with thin beta ribs and precipitation within alpha-2 and (b) precipitation of alpha-2 within the beta phase.

also appears to be beta phase exist toward the centerline of the larger plates. Since specimens from each step of the heat-treatment sequence have not been evaluated it is not clear at which point this constituent formed. It could either be residual beta that was left as two similarly oriented alpha-2 laths grew together, or actual precipitation within the plates during aging. Figure 63b is a higher magnification view that also shows some precipitation of alpha-2 within the beta phase. A morphology that occurs at some prior-beta boundaries is shown in Figure 3-64. This sideplate structure has very large regions of parallel plates with a common basal plane orientation. The beta phase is confined to narrow ribs between each lath.

Exposing Ti-24.5Al-8Nb-2Mo-2Ta (IT-B) for an additional 100 hours at 705°C (1300°F) produced relatively little change to the Widmanstatten plate structure shown originally. However, as can be seen in Figure 3-65, the interphase interfaces appear to have more regular dislocation structures.

TEM micrographs of Ti-23.5Al-2Nb-2Mo-2Ta-2Cr (IT-C) are shown in Figure 3-66. The beta ribs throughout the microstructure of this alloy were clearly thinner than for Ti-24.5Al-6Nb-2Mo-2Ta-2V (IT-A) and Ti-24.5Al-8Nb-2Mo-2Ta (IT-B). It is likely that this low fraction of beta phase influenced the tensile behavior of the alloy and accounted for the lower ductility.

The strength of each of the Phase II alloys remains high through the range of test temperatures and, the ultimate strengths at elevated temperature show a significant advantage over conventional titanium alloys such as Ti-6242. The strength of each of these alloys is only affected slightly by thermal exposure. This is shown graphically for the alloy Ti-24.5Al-6Nb-2Mo-2Ta-2V (IT-A) in Figure 3-67. The notched tensile strengths for all of the scale-up alloys at $K_t = 3.5$ are given in Table 3-31. The notched tensile strength of Ti-24.5Al-6Nb-2Mo-2Ta-2V (IT-A) is shown graphically in Figure 3-67 along with smooth bar properties. At room temperature, each of the scale-up alloys shows considerable notch weakening. At 427°C (800°F), Ti-24.5Al-6Nb-2Mo-2Ta-2V (IT-A) and Ti-24.5Al-8Nb-2Mo-2Ta (IT-B) demonstrate notch strengthening at a factor of approximately 1.1 while Ti-23.5Al-2Nb-2Mo-2Ta-2Cr (IT-C) shows notch weakening. At 650°C (1200°F), Ti-24.5Al-6Nb-2Mo-2Ta-2V (IT-A) and Ti-24.5Al-8Nb-2Mo-2Ta (IT-B) have roughly equivalent notched and smooth bar strength while Ti-23.5Al-2Nb-2Mo-2Ta-2Cr (IT-C) is notch strengthened by a factor of 1.32.

The results from creep testing of the Phase II alloys are given in Table 3-33 along with Larson-Miller parameter values for the time to 0.2% creep. The constant for the Larson-Miller equation was estimated by extrapolating the data to find the value which resulted in a straight line fit between the data for high and low stress levels. This extrapolation process, which shows a reasonable straight line fit for a constant of 12.5, is illustrated in Figure 3-68. The high stress region of the Larson-Miller curve was approximated by using the 0.2% yield stress data from 540 to 760°C (1000 to 1400°F) testing and estimating the time to 0.2% plastic strain to be 0.1 hours. A full working curve for the time to 0.2% creep, using a constant of 12.5 in the Larson-Miller equation, is shown for Ti-24.5Al-6Nb-2Mo-2Ta-2V (IT-A) in Figure 3-69. With the use of this curve, it has been determined that the temperature capability of Ti-24.5Al-6Nb-2Mo-2Ta-2V (IT-A) in the alpha -2 plus beta processed condition is approximately 85°C (150°F) higher than for beta processed Ti-6242. The alloys Ti-24.5Al-8Nb-2Mo-2Ta (IT-B) and Ti-23.5Al-2Nb-2Mo-2Ta-2Cr (IT-C) have lower creep resistance and lower measured Al levels than Ti-24.5Al-6Nb-2Mo-2Ta-2V (IT-A). This relationship between creep resistance and Al content is consistent with the general relationship established in Phase I of this program.

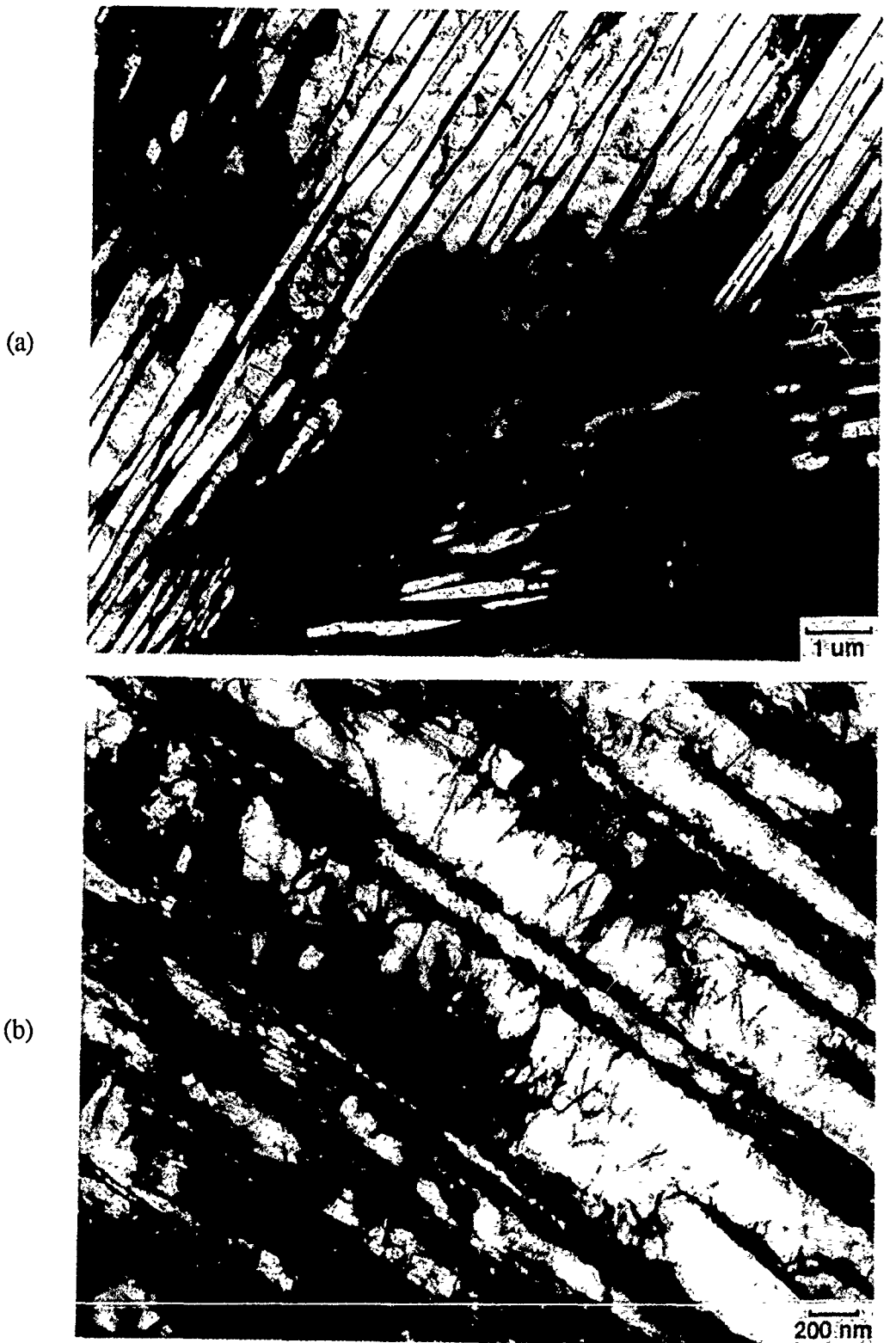


Figure 3-64 Bright-field TEM micrograph of alpha-2 sideplate colony at a prior-beta boundary of the alloy Ti-24.5Al-8Nb-2Mo-2Ta (IT-B). (a) Low magnification and (b) higher magnification with specimen tilted so that alpha-2/beta interfaces are parallel to the beam.



Figure 3-65 Bright-field TEM micrograph of Ti-24.5Al-8Nb-2Mo-2Ta (IT-B) after the base heat-treatment plus a 705°C (1300°F) / 100 hour exposure that has narrowed the beta ribs and produced regular dislocation arrays at the boundaries.

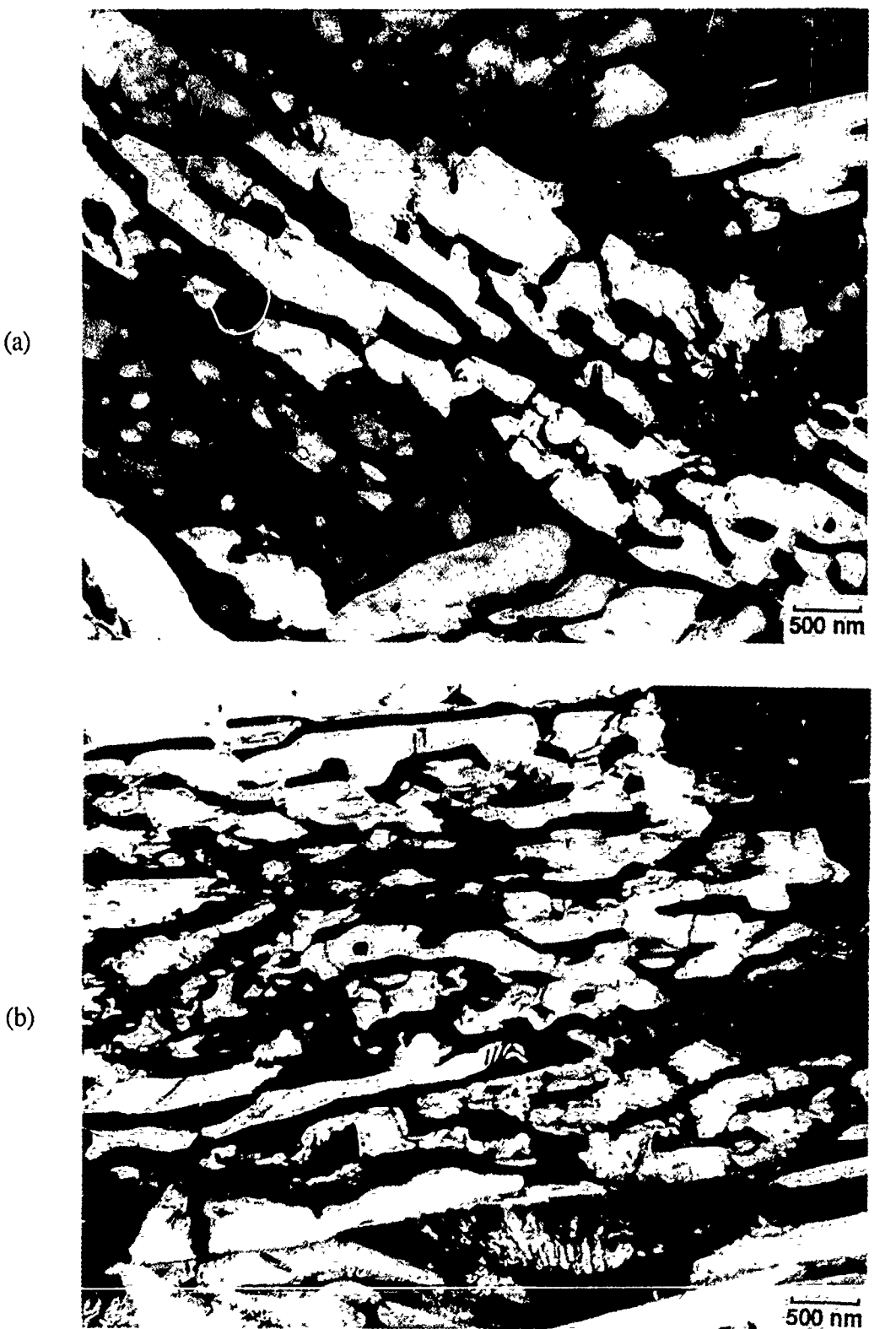


Figure 3-66 Bright-field TEM micrograph of Ti-23.5Al-2Nb-2Mo-2Ta-2Cr (IT-C) showing (a) general view of a colony which reveals a tendency to facet when tilted as in (b).

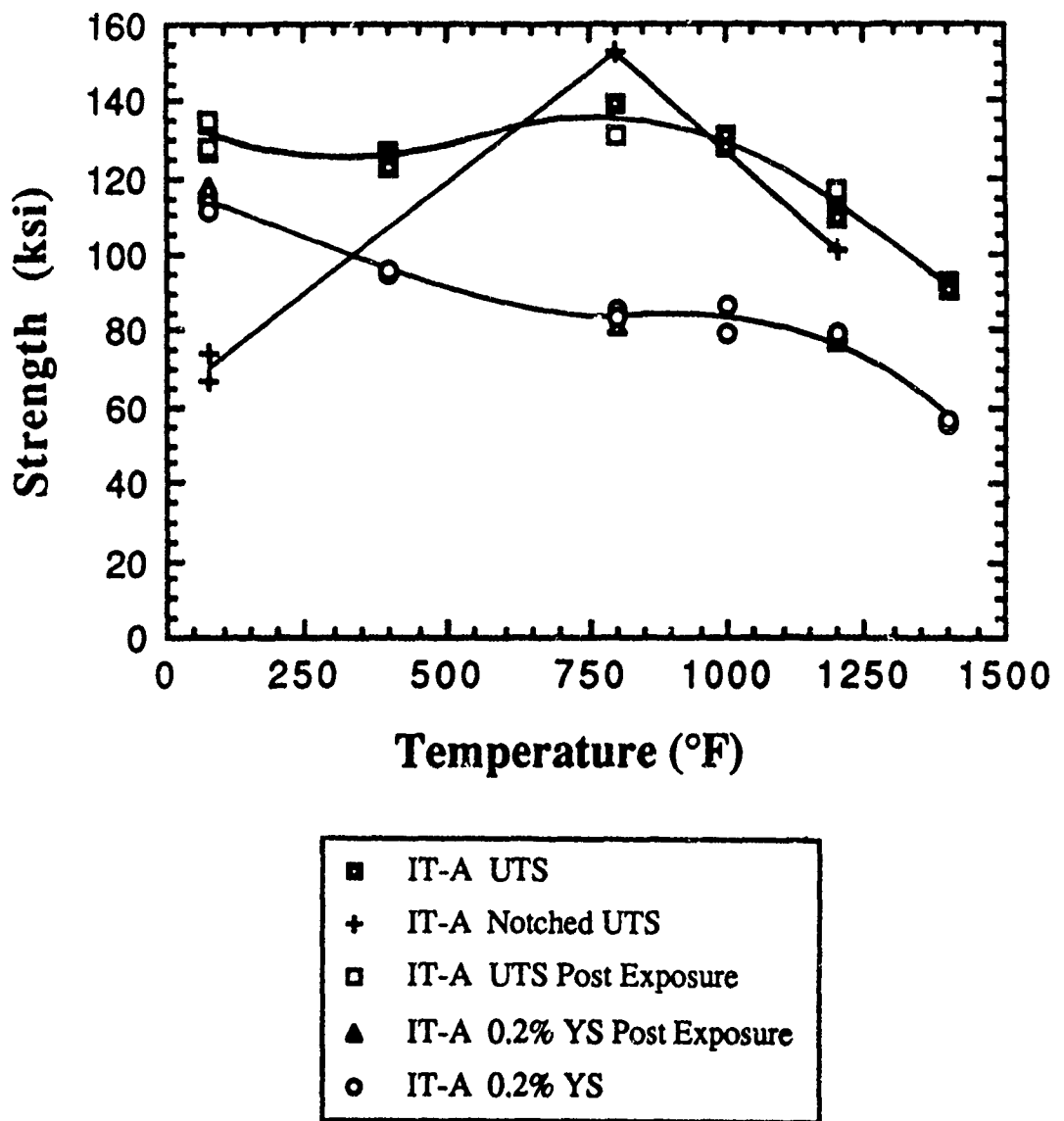


Figure 3-67 Smooth bar tensile properties of Ti-24.5Al-6Nb-2Mo-2Ta-2V (IT-A) before and after thermal exposure and notched bar tensile properties without thermal exposure.

Table 3-33 Creep Properties of Phase II Alloys

Alloy	Temperature (°C)	Temperature (°F)	Stress (MPa)	Stress (ksi)	Time to 0.2% (hours)	LMP
IT-A	538	1000	276.0	40	688	22.39
IT-A	538	1000	241.5	35	997	22.63
IT-A	649	1200	172.5	25	19	22.87
IT-A	649	1200	138.0	20	60	23.70
IT-A	760	1400	103.5	15	2.6	24.02
IT-A	760	1400	69.0	10	6.6	24.77
IT-B	538	1000	276.0	40	573	22.28
IT-B	538	1000	241.5	35	627	22.33
IT-B	649	1200	172.5	25	9.9	22.40
IT-B	649	1200	138.0	20	40	23.41
IT-B	760	1400	103.5	15	1.2	23.40
IT-B	760	1400	69.0	10	4.7	24.50
IT-C	538	1000	276.0	40	91	21.11
IT-C	538	1000	241.5	35	163	21.48
IT-C	649	1200	172.5	25	5.9	22.03
IT-C	649	1200	138.0	20	8.7	22.31
IT-C	760	1400	103.5	15	0.5	22.69
IT-C	760	1400	69.0	10	1.4	23.52

LMP = T(12.5 + log t) x 10⁻³ where T is in °R

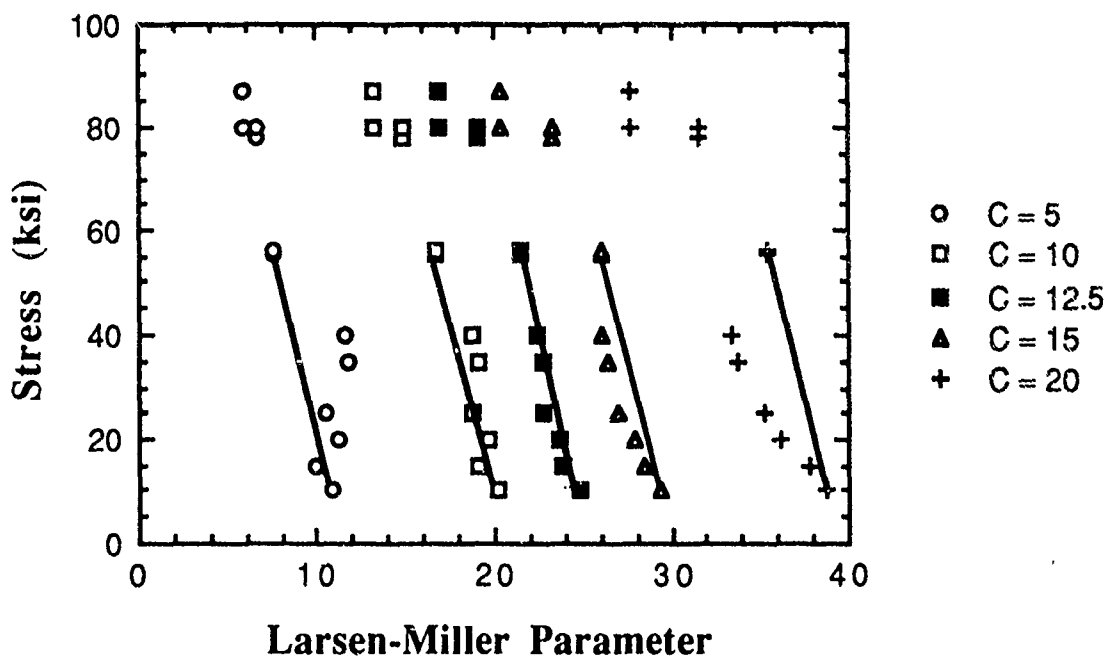


Figure 3-68 Extrapolation process used for determination of the constant in the Larson-Miller equation.

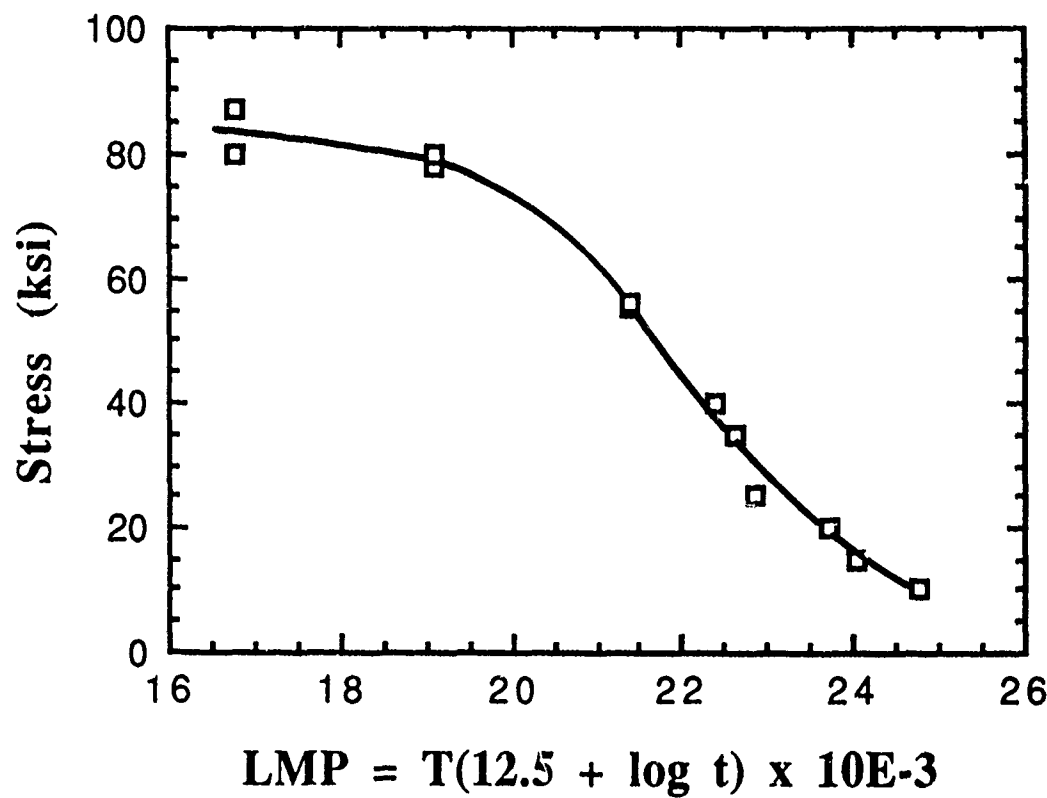


Figure 3-69 Larson-Miller curve for the time to 0.2% creep of Ti-24.5Al-6Nb-2Mo-2Ta-2V (IT-A) determined from test results over the temperature range of 540 to 760°C (1000 to 1400°F). The LMP value is calculated with temperature on the Rankine scale.

Severe surface cracking of tensile and creep/rupture specimens has been documented for the alloy Ti-24Al-11Nb [22]. In order to obtain a better understanding of what conditions lead to surface cracking, all of the creep specimens of the scale-up alloys have been examined visually and a number of them have been sectioned and evaluated metallographically for surface cracking. The creep specimens in this program were all unloaded prior to failure. Even under the most severe test conditions, no surface cracking was found on any of the creep specimens. Several of the 760°C (1400°F) test specimens were on test for approximately 200 hours with final creep strains as high as 2.7% without surface cracking. At 650°C (1200°F), test times were as long as 670 hours and final creep strains reached 0.85% without surface cracking. At 540°C (1000°F), one test was continued for 1434 hours without any signs of surface cracking. Clearly, when tested at constant load and temperature, surface cracking does not occur under relatively low strain, short life test conditions.

Several of the Phase II creep specimens were sectioned and analyzed in an electron microprobe to determine the depth of the oxygen rich layer as a function of test time and temperature. Figure 3-70 shows two examples of the data which was produced for the alloys Ti-24.5Al-6Nb-2Mo-2Ta-2V (IT-A) and Ti-24.5Al-8Nb-2Mo-2Ta (IT-B). The data shown in Table 3-34 indicates that Ti-24.5Al-6Nb-2Mo-2Ta-2V (IT-A) and Ti-24.5Al-8Nb-2Mo-2Ta (IT-B) have a temperature advantage over Ti-6242 for resistance to 'alpha case' formation of approximately 110°C (200°F).

Three specimens of Ti-24.5Al-8Nb-2Mo-2Ta (IT-B) were examined after creep testing by AEM. The identifications and test conditions for these specimens are identified in Table 3-35. The specimens have been evaluated for temperature effects on creep mechanisms. This comparison is not completely ideal since the specimens were tested to different strain levels as well as exposure times. However, the examination has resulted in some interesting observations which indicate that microstructural response during creep deformation appears to be playing a major role in controlling creep behavior.

After testing at 540°C (1000°F) / 242 MPa (35 ksi), the deformation found in the alpha-2 phase was mainly a component as determined by g•b experiments. This deformation is shown in Figure 3-71. Some additional mottling was found for certain diffraction conditions. This was consistently observed throughout this series of specimens and no complete explanation has yet been found. However, some of the mottling was stronger when viewed with superlattice reflections, suggesting that it could be APB related.

Several methods of specimen preparation were used to ensure that deformation features were not thin-foil artifacts. Of particular concern were the various morphologies of hydride phases or 'interface phase' that can be produced by electropolishing. Our experience has shown that both near-alpha and near-alpha-2 alloys are very susceptible to this artifact. The only certain way to avoid this is to ion-mill specimens from blank. Ion-milling to 'clean-up' electropolished foils is rarely successful since the hydride precipitates internally. Even if the ion-milling 'dehydrates' the foil, residual deformation structures frequently remain. This is clearly unsatisfactory when trying to determine bulk deformation characteristics. Ion-milling, unfortunately, is not an ideal solution either since beam-damage introduces mottling (and sometimes surface irregularities) that interferes somewhat with g•b analysis. For the evaluation of creep specimens, we resorted to a combination of the techniques to gain as much information as possible.

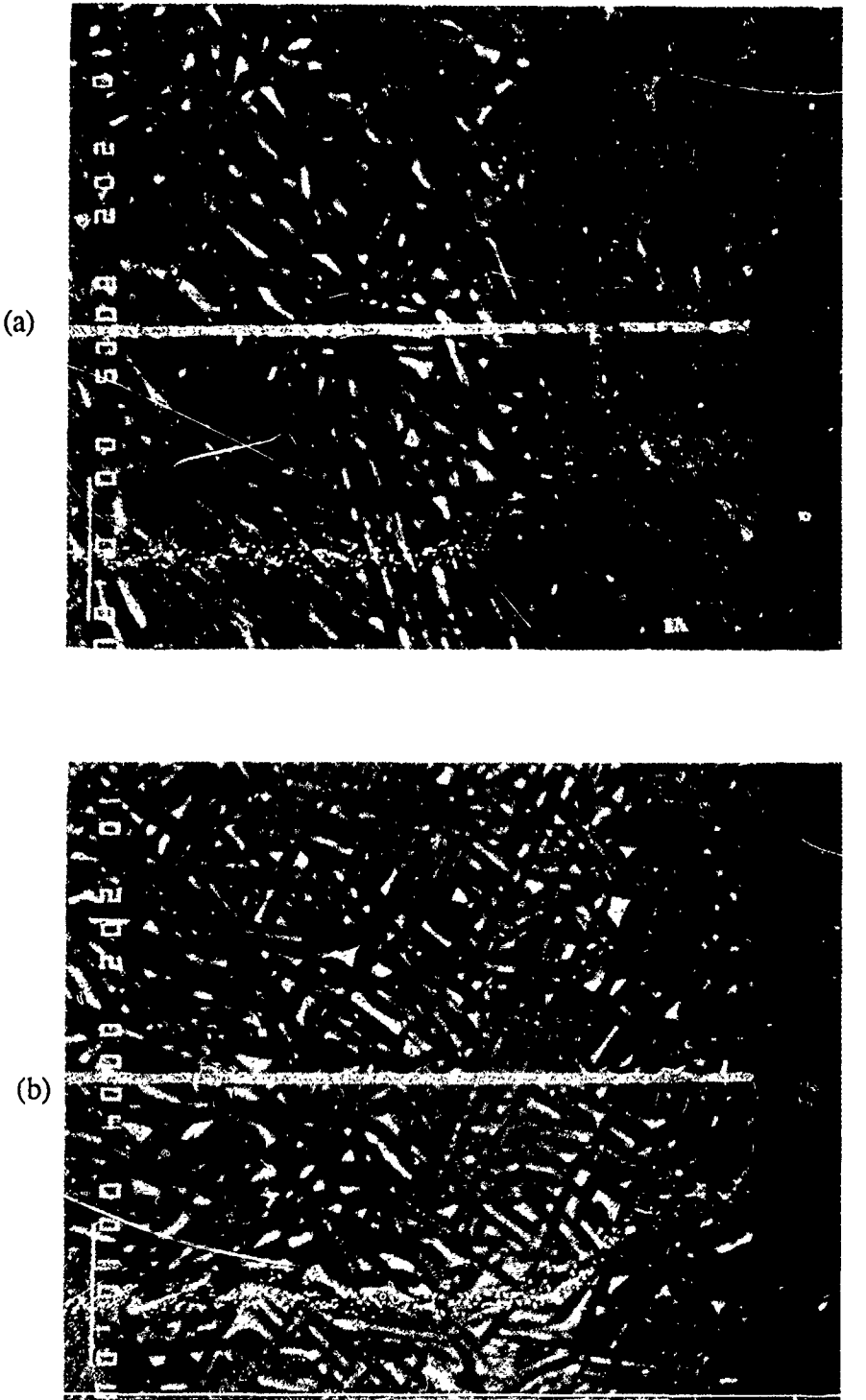


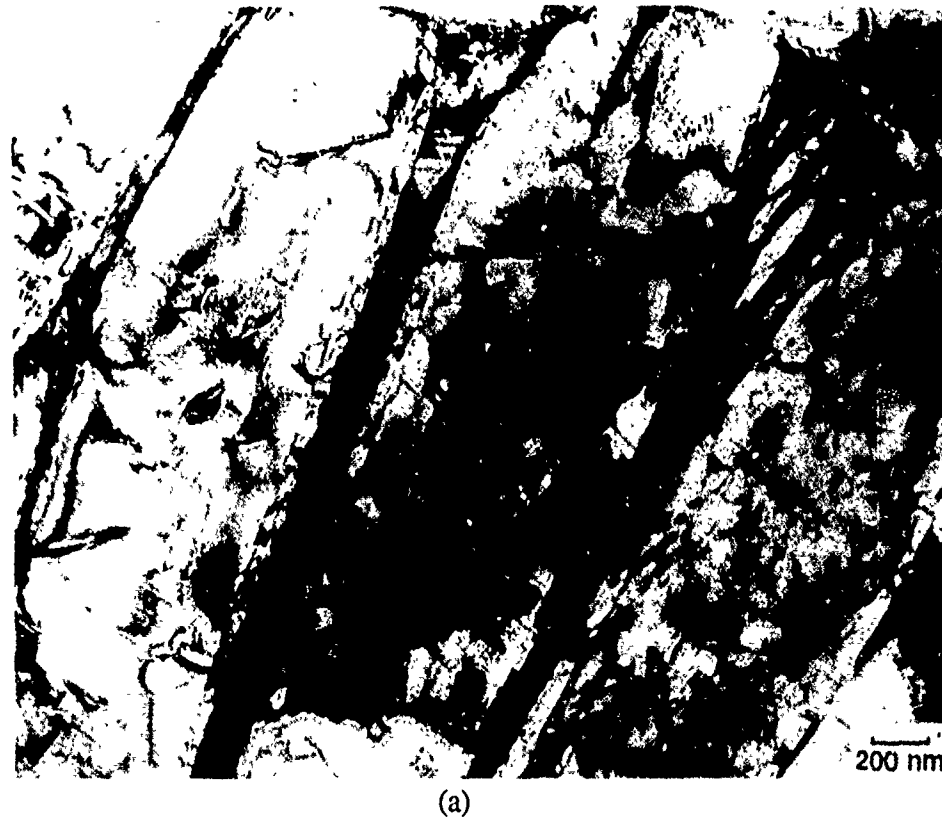
Figure 3-70 Microprobe analysis of oxygen rich layer on creep specimens of (a) Ti-24.5Al-6Nb-2Mo-2Ta-2V (IT-A) tested at 760°C (1400°F) for 194 hours and (b) Ti-24.5Al-8Nb-2Mo-2Ta (IT-B) tested at 650°C (1200°F) for 350 hours.

Table 3-34 Depth of Oxygen Rich Layer on Phase II Creep Specimens

Alloy	Temperature (°C)	Temperature (°F)	Time at Temperature (hours)	Depth of Oxygen Layer (microns)	Depth of Oxygen Layer (mils)
IT-A	540	1000	1434	3.5	0.15
IT-A	650	1200	671	16.5	0.65
IT-A	760	1400	194	18	0.70
IT-B	540	1000	725	2.5	0.10
IT-B	650	1200	350	11	0.45
IT-B	760	1400	200	26	1.05

Table 3-35 Creep Parameters of Specimens Evaluated by AEM

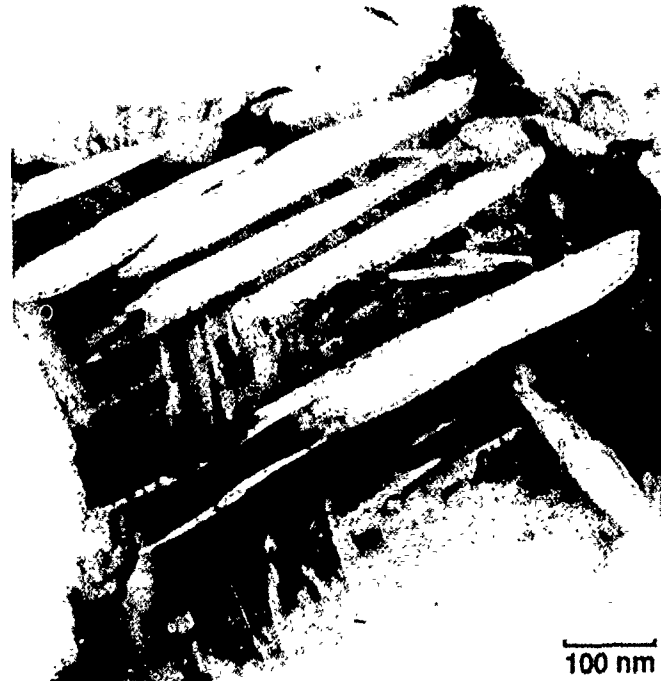
Specimen	Temperature (°C)	Temperature (°F)	Stress (MPa)	Stress (ksi)	Time (hours)	Strain (%)
B13	540	1000	242	35	722	0.21
B20	650	1200	138	20	353	0.51
B21	760	1400	69	10	194	1.48



(a)



(b)



(c)

Figure 3-71 Bright-field TEM micrograph from 540°C (1000°F) creep specimen of Ti-23.5Al-2Nb-2Mo-2Ta-2Cr (IT-C) showing (a) mottled appearance of alpha-2 colony with mostly clear beta ribs; (b) and (c) higher magnification views showing various morphologies of alpha-2 laths which precipitate during creep in the wider beta regions at colony boundaries.

The observation of dislocations in the beta phase was strongly hampered by a high volume fraction of alpha-2 precipitation. This occurs predominantly in the wider regions of beta as shown in Figure 3-71b. For the most part this occurs as individual plates which frequently intersect each other. But the precipitation in a region adjacent to a primary alpha-2 grain as shown in Figure 3-71c has taken on more of a colony morphology. This network of plates would be expected to stiffen these beta regions and probably restrict dislocation activity. We should note that very low dislocation densities were observed in the primary alpha-2 grains. A well defined network is shown in Figure 3-72. The absence of the mottling observed in the laths permitted Burgers vector determination of individual dislocations by $\mathbf{g} \cdot \mathbf{b}$ experiments as shown in Figure 3-72. These dislocations were identified as having a Burgers vectors. (The low dislocation density was also an indication that the foil preparation technique was appropriate.)

After creep testing at 760°C (1400°F) / 69 MPa (10 ksi), there was no precipitation of alpha-2 in the beta phase and it was apparent that the dislocation density was extremely low as shown in Figure 3-73. This low dislocation density was found despite the fact that this specimen was tested to the highest strain level. The regular arrays of dislocations at the alpha-2/beta interfaces as shown in Figure 3-73b are an indication that recovery was taking place. Recovery was probably occurring dynamically and may have caused a different creep mode. In separate internally funded work on different alpha-2 titanium aluminide compositions, similar low densities of deformation were found in the beta phase even when the specimens were water quenched from the 760°C (1400°F) test temperature. Figure 3-73c shows a weak beam image of dislocations within one of the alpha-2 laths of the 760°C (1400°F) / 69 MPa (10 ksi) specimen. The image was taken under weak-beam conditions such that dislocation images alone would be much narrower than this. In this case, the mottling in the background was from ion-milling.

Twinning was also observed in some regions of the specimens as shown in Figure 3-74. At first, it was suspected that this was deformation twinning but similar features were observed in sections taken from the heads of the creep specimens. Thin foils were prepared by both ion-milling and electropolishing, with extreme care being taken to ensure that the foils were not mishandled during preparation. Despite this, the features remained. Crystallographic analysis showed that the 'twins' had a {1010} habit plane. As the diffraction pattern in Figure 3-74d shows, there was also an orthorhombic distortion present. We were left to conclude that this was either, a martensitic transition/mechanical instability associated with stress relaxation in thin foils, or possibly a phase transformation similar to alpha-2 to Ti₂AlNb. Close observation of the 'twins' in Figure 3-74b shows that they did not extend fully across the alpha-2 laths. This may have been due to a compositional effect.

One additional morphological observation made on the 760°C (1400°F) specimen was that the phase inside the alpha-2 laths had coarsened. Dark-field experiments such as the one shown in Figure 3-75 were used to tentatively identify these regions as beta (since they light up at the same time as the beta phase). However, this was not conclusive proof and the regions were too thin to confirm crystal structure by convergent beam electron diffraction.

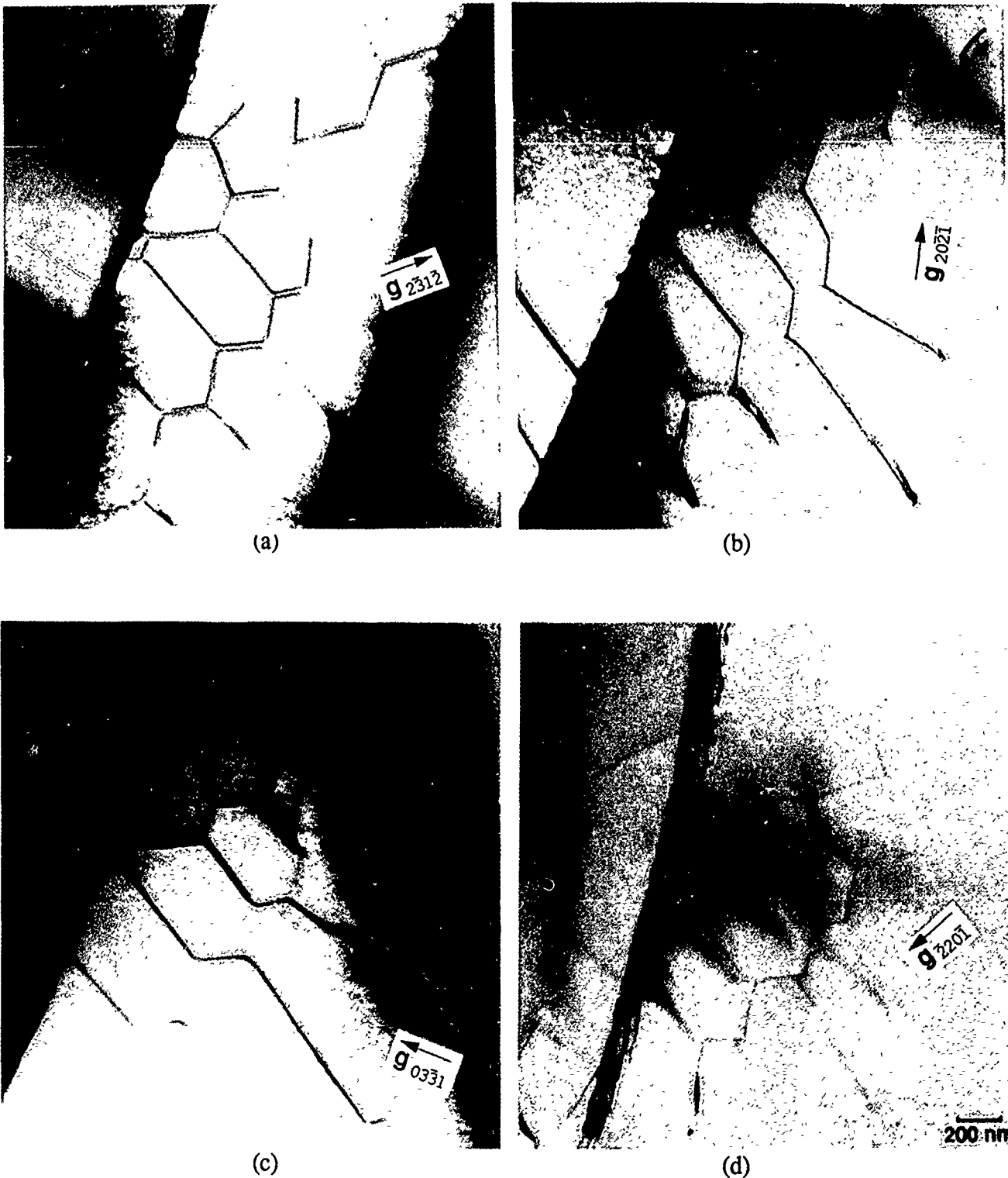


Figure 3-72 Bright-field TEM micrographs from primary alpha-2 region in same specimen as Figure 3-71 showing a network of dislocations which were identified as having $\langle a \rangle$ Burgers vectors by $\mathbf{g} \cdot \mathbf{b}$ experiments such as (b)-(d). The individual segments are mostly in screw orientations.

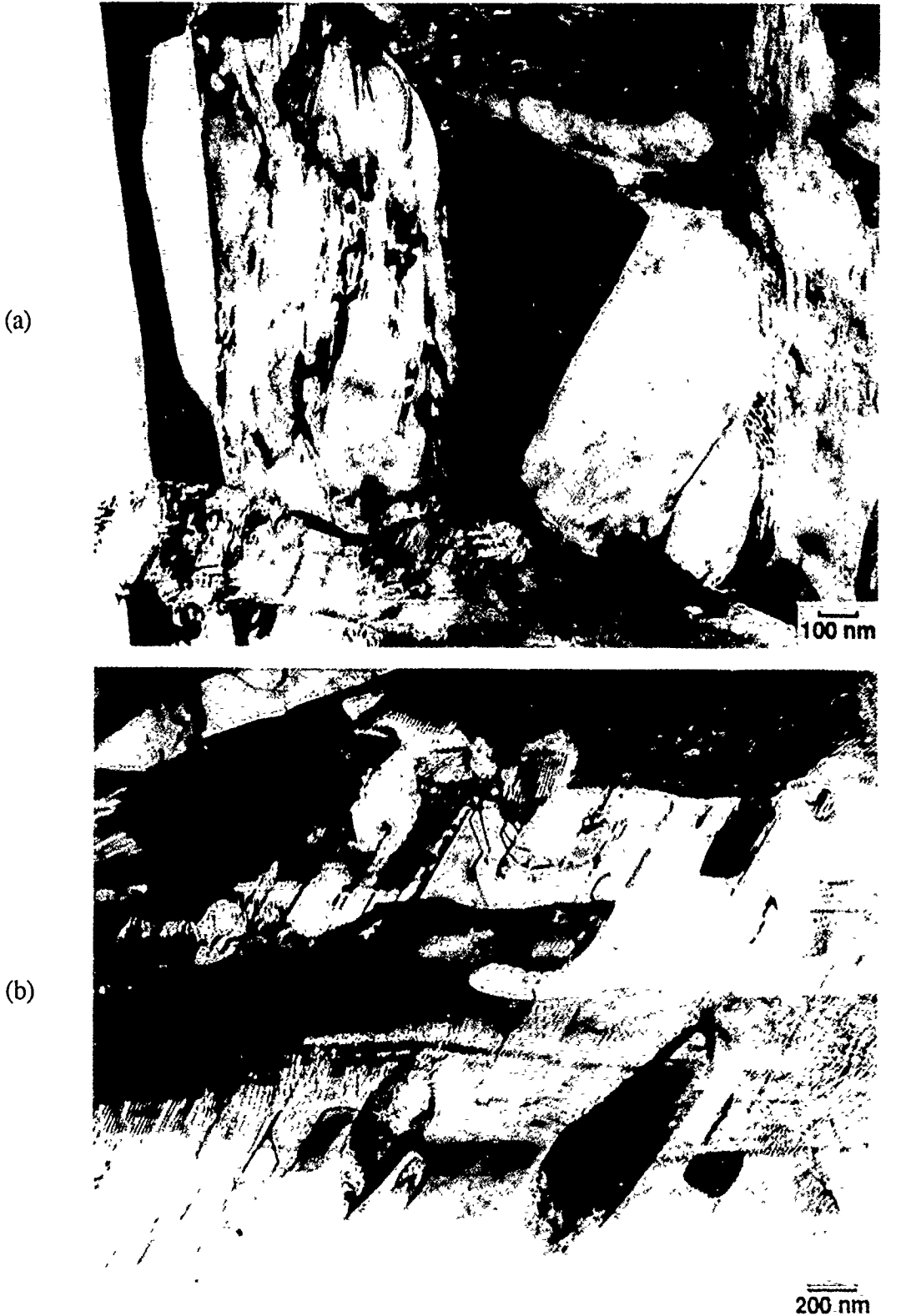


Figure 3-73 Bright-field TEM micrographs from 760°C (1400°F) creep specimen of Ti-23.5Al-2Nb-2Mo-2Ta-2Cr (IT-C) showing (a) precipitate & dislocation-free beta region with and (b) regular arrays of dislocations at the alpha-2/beta interfaces.

(c)

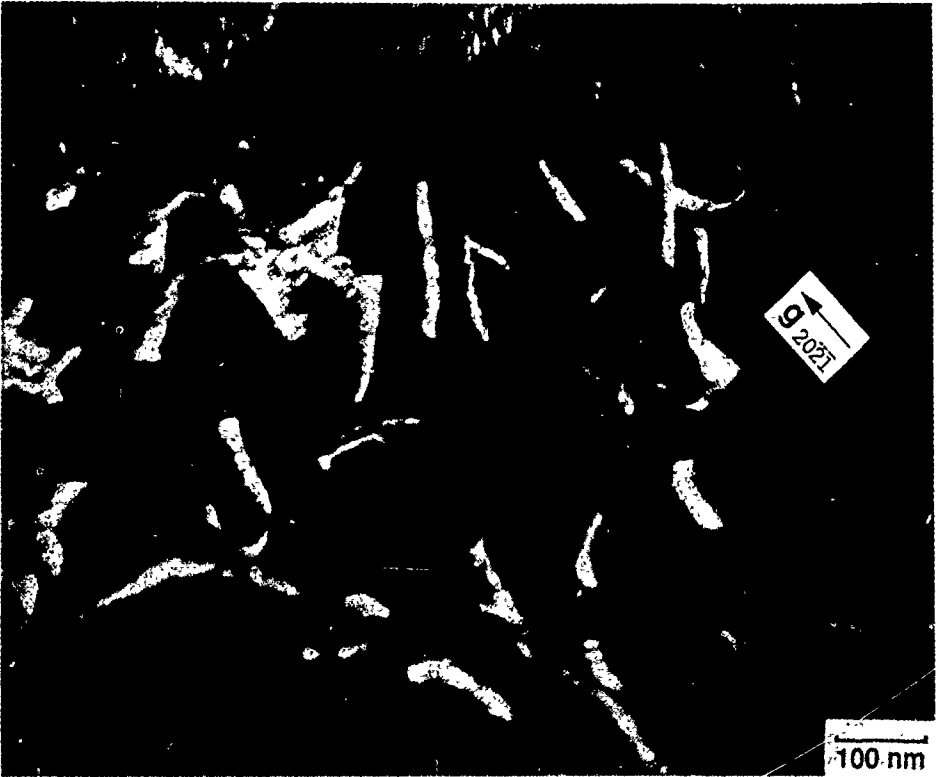


Figure 3-73 (Continued) Weak-beam dark-field TEM micrograph from 760°C (1400°F) creep specimen of Ti-23.5Al-2Nb-2Mo-2Ta-2Cr (IT-C) showing (c) possible decomposition at dislocations in the alpha-2 phase.

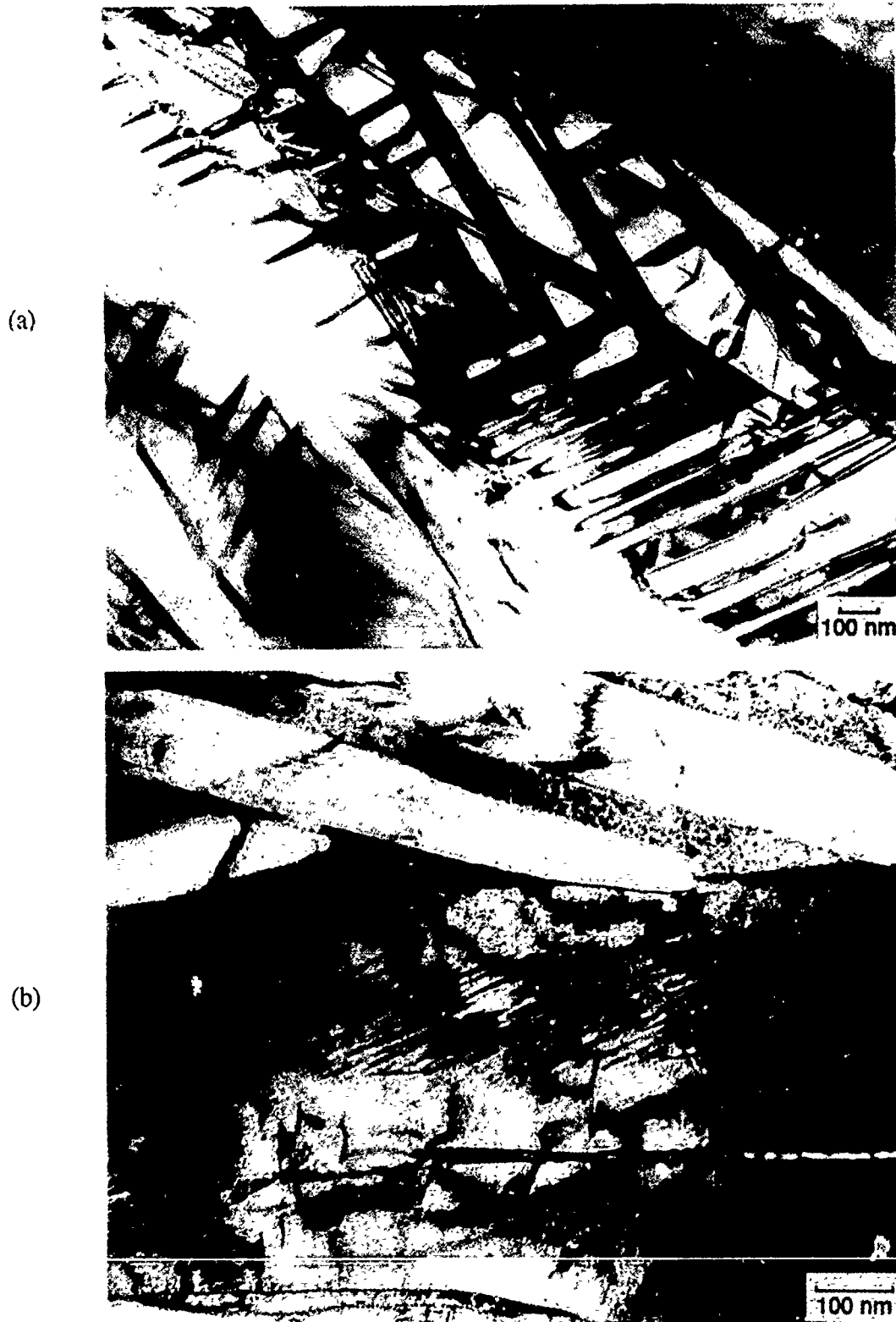


Figure 3-74 Bright-field TEM micrographs of specimen in Figure 3-73 showing (a) faulting/twinning that is (b) sometimes wholly contained within an alpha-2 lath.

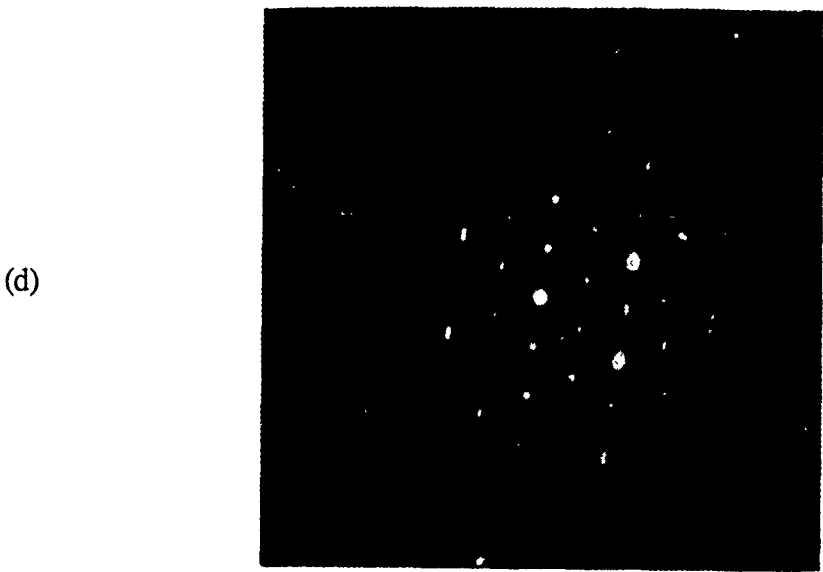


Figure 3-74 (Continued) Tilting the specimen as in (c) yields a selected-area electron diffraction pattern (d) which shows an orthorhombic distortion in the (0001) zone with 'twins' lying on $\{10\bar{1}0\}$ habit planes.

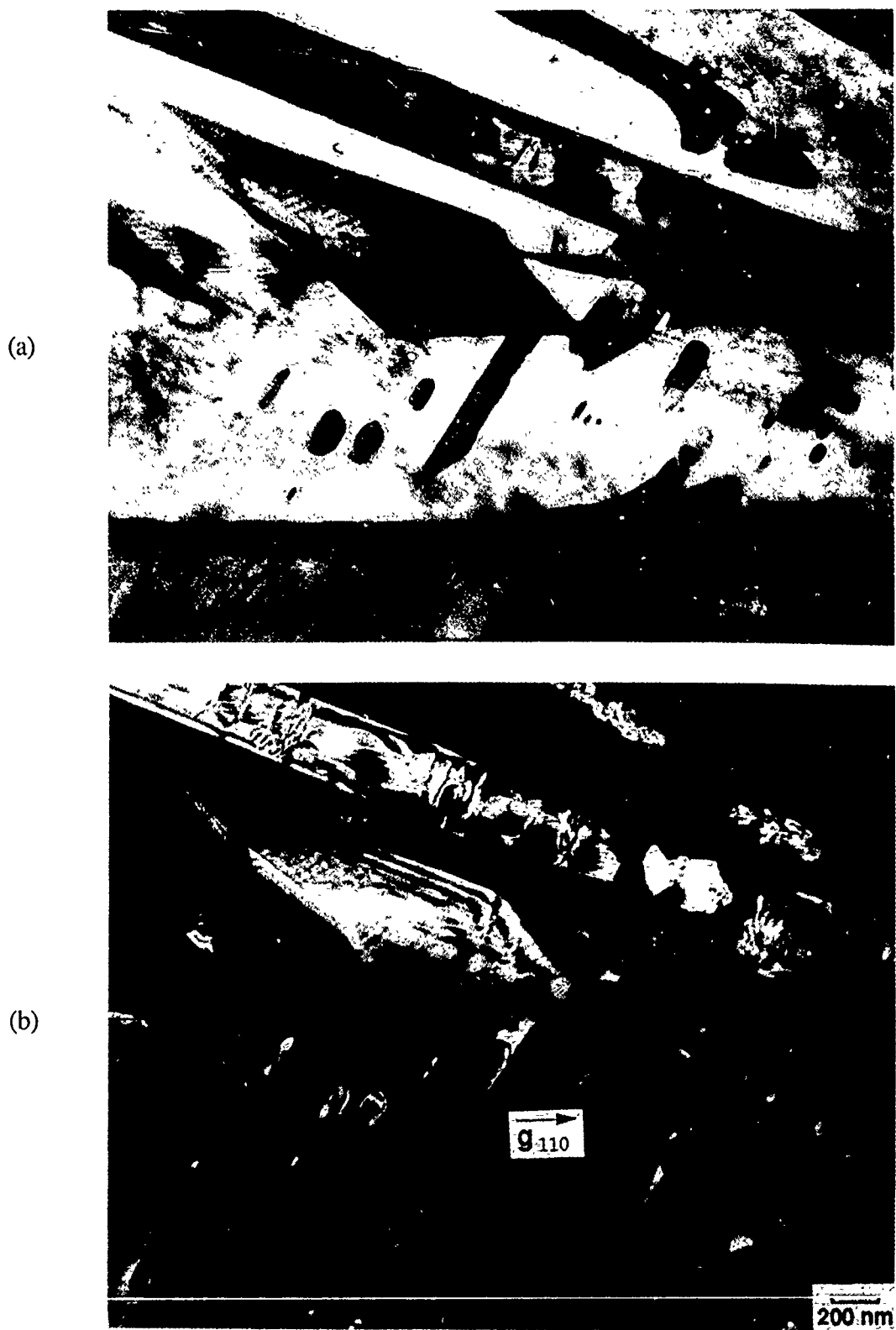


Figure 3-75 (a) Bright-field TEM micrograph of specimen in Figure 3-73 showing a region with coarsened precipitates within the alpha-2 phase which light up in the dark-field micrograph (b) imaged with the (110) beta diffraction vector.

The stress/rupture test results for the Phase II alloys are listed in Table 3-36. Once the high temperature tests were completed and the ultimate strengths were available from tensile testing, Larson-Miller curves were produced in a manner similar to that described for the time to 0.2% creep. The Larson-Miller curve for Ti-24.5Al-8Nb-2Mo-2Ta (IT-B) is shown in Figure 3-76. After the Larson-Miller curve was available, it was evident that each of the 540°C (1000°F) tests would run several thousand hours without failure and, as a result, the 540°C (1000°F) tests were discontinued prior to failure. The 650°C (1200°F) and 760°C (1400°F) specimens of Ti-24.5Al-6Nb-2Mo-2Ta-2V (IT-A) both failed at thermocouple attachments located on the gage section. Similar thermocouple attachments had no effect on the failure of Ti-24.5Al-8Nb-2Mo-2Ta (IT-B) and Ti-23.5Al-2Nb-2Mo-2Ta-2Cr (IT-C). At 760°C (1400°F), the alloy Ti-23.5Al-2Nb-2Mo-2Ta-2Cr (IT-C) test specimens elongated more than 50 percent and necked down to a fine point before failure. The 760°C (1400°F) / 210 MPa (45 ksi) test specimens for each of the three scale-up alloys are shown in Figure 3-77 to depict the clear difference in failure mode. At 650°C (1200°F), the Ti-23.5Al-2Nb-2Mo-2Ta-2Cr (IT-C) rupture specimen failed without necking or evidence of void nucleation as did the alloys Ti-24.5Al-6Nb-2Mo-2Ta-2V (IT-A) and Ti-24.5Al-8Nb-2Mo-2Ta (IT-B).

The rupture specimens of the Phase II alloys have been examined metallographically to document surface cracking. All of the specimens which were tested through failure showed some degree of surface cracking away from the primary fracture surface. At 760°C (1400°F), the Ti-24.5Al-6Nb-2Mo-2Ta-2V (IT-A) and Ti-24.5Al-8Nb-2Mo-2Ta (IT-B) test specimens exhibited secondary cracks as deep as 1000 microns even though the test times were very short. The average secondary crack depth in the 760°C (1400°F) specimens of the alloys Ti-24.5Al-6Nb-2Mo-2Ta-2V (IT-A) and Ti-24.5Al-8Nb-2Mo-2Ta (IT-B) was less than 100 microns. At 650°C (1200°F) and longer test times, the secondary cracking was present but not as severe as at the higher test temperature. The average crack depth in the 650°C (1200°F) test specimens of Ti-24.5Al-6Nb-2Mo-2Ta-2V (IT-A) and Ti-24.5Al-8Nb-2Mo-2Ta (IT-B) was less than 50 microns while a few cracks in excess of 100 microns were found in the Ti-24.5Al-8Nb-2Mo-2Ta (IT-B) test specimen. Examples of the secondary cracking found on Ti-24.5Al-8Nb-2Mo-2Ta (IT-B) specimens tested at 650 and 760°C (1200 and 1400°F) are shown in Figure 3-78. The secondary cracks appear to grow normal to the loading direction with no relationship to the microstructural features.

The results from fracture toughness testing of the scale-up alloys are presented in Table 3-37. The test specimens were 5.1 cm (2.0 in) in length, 1.0 cm (0.4 in) deep, and 0.5 cm (0.2 in) wide with a 0.5 cm (0.2 in) deep EDM notch. Fatigue precracking was conducted at room temperature prior to testing. K_{Ic} values were not obtained due to the small size of the specimens. The number of criteria which were not met according to ASTM E399 is also listed in Table 3-37. The fracture toughness values in Table 3-37 are given in terms of K_q and KEE. The equivalent energy fracture toughness (KEE) measurement provides an economical and simple method of determining fracture toughness values of specimens which are quite small [23].

The equivalent energy fracture toughness data for the scale-up alloys is plotted as a function of test temperature in Figure 3-79. The relationship for fracture toughness versus test temperature is similar to that previously shown for notched tensile properties. The alloys Ti-24.5Al-6Nb-2Mo-2Ta-2V (IT-A) and Ti-24.5Al-8Nb-2Mo-2Ta (IT-B) both demonstrate increasing fracture toughness and notched tensile strength up to 427°C (800°F) and then decreasing fracture toughness and notched tensile strength at temperatures above 427°C (800°F). For Ti-23.5Al-2Nb-2Mo-2Ta-2Cr (IT-C), fracture toughness and notched

Table 3-36 Stress/Rupture Properties of Phase II Alloys

Alloy	Temperature (°C)	Temperature (°F)	Stress (MPa)	Stress (ksi)	Time to Failure (hours)	LMP	Elongation at Failure (%)
IT-A	538	1000	414	60	644.5#	-	-
IT-A	649	1200	380	55	115.4	24.17	2.8*
IT-A	760	1400	311	45	8.2	24.95	11.6*
IT-B	538	1000	414	60	764.1#	-	-
IT-B	649	1200	380	55	126.9	24.24	6.5
IT-B	760	1400	311	45	46.9	26.36	22.0
IT-C	538	1000	414	60	623.5#	-	-
IT-C	649	1200	380	55	40.3	23.41	16.9
IT-C	760	1400	311	45	16.7	25.52	53.9
IT-C	760	1400	104	15	143.7	27.26	74.3

* = Specimen failed at thermocouple attachment.

= Specimen unloaded prior to failure.

LMP = $T(12.5 + \log t) \times 10^{-3}$ where T is in °R.

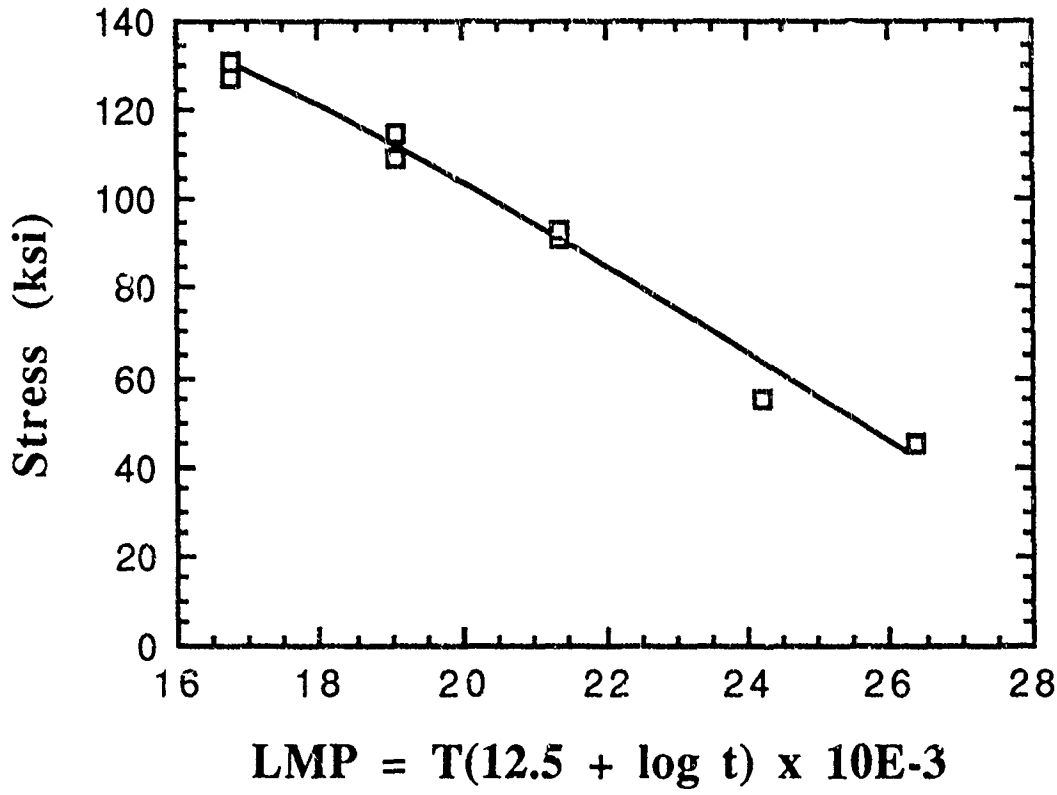


Figure 3-76 Larson-Miller curve for the rupture life of Ti-24.5Al-8Nb-2Mo-2Ta (IT-B) determined from test results over the temperature range of 540 to 760°C (1000 to 1400°F). The LMP value is calculated with temperature on the Rankine scale.

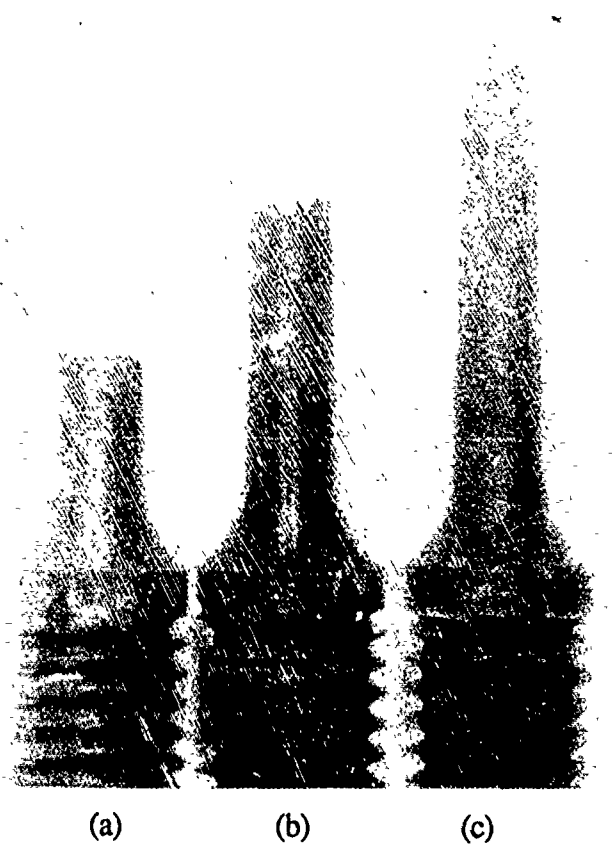


Figure 3-77 Stress/rupture specimens of (a) Ti-24.5Al-6Nb-2Mo-2Ta-2V (IT-A), (b) Ti-24.5Al-8Nb-2Mo-2Ta (IT-B), and (c) Ti-23.5Al-2Nb-2Mo-2Ta-2Cr (IT-C) tested in air at 760°C (1400°F) and an initial stress of 310 MPa (45 ksi).

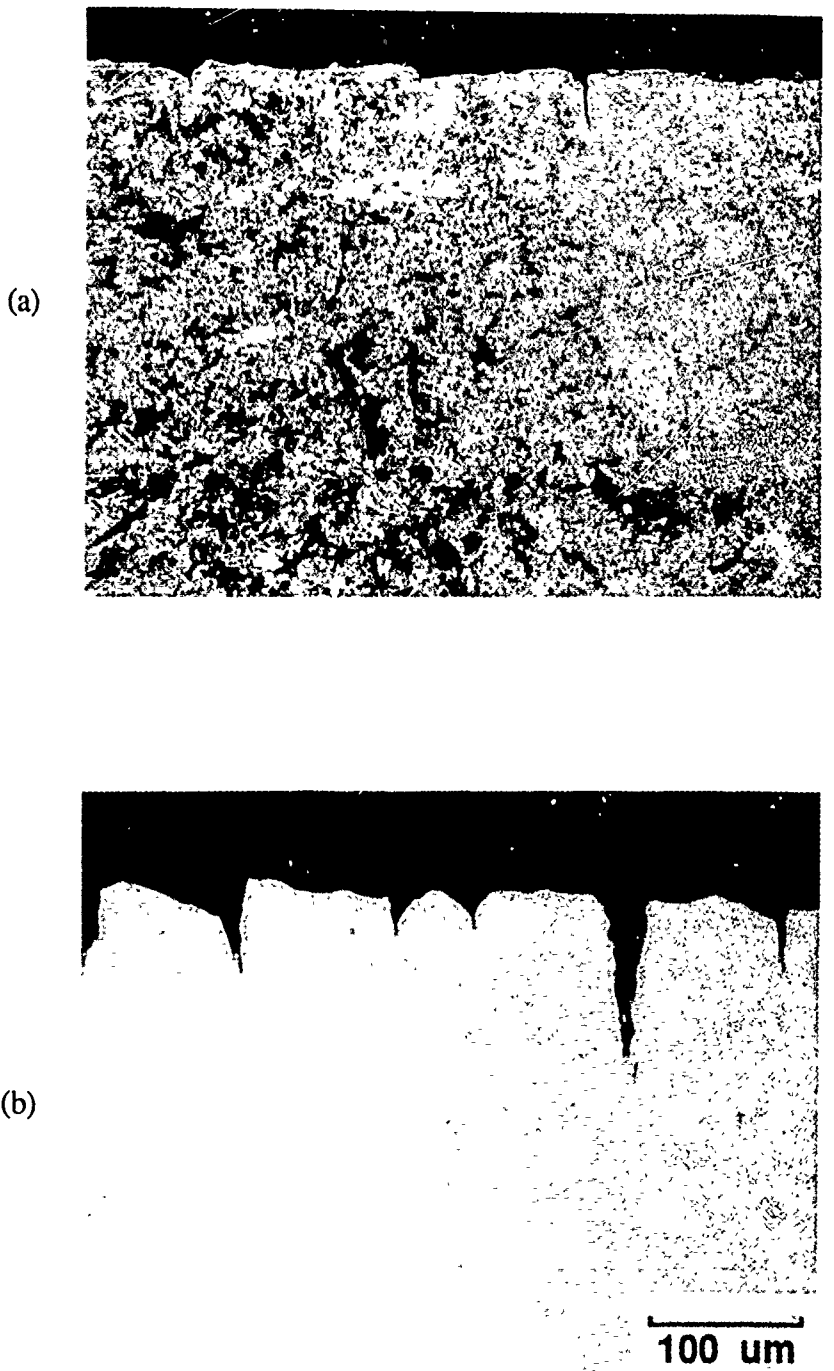


Figure 3-78 Surface cracking of Ti-24.5Al-8Nb-2Mo-2Ta (IT-B) stress/rupture specimens tested at (a) 650°C (1200°F) for 127 hours and (b) 760°C (1400°F) for 47 hours.

Table 3-37 Fracture Toughness Data for Phase II Alloys

Alloy	Temperature (°C)	Temperature (°F)	K_Q (MPa \sqrt{m})	K_Q (ksi \sqrt{in})	No. of Invalids	K_{EE} (MPa \sqrt{m})	K_{EE} (ksi \sqrt{in})
IT-A	24	75	15.7	14.3	3	18.2	16.5
IT-A	24	75	14.7	13.4	3	18.2	16.5
IT-A	204	400	19.7	17.9	3	22.0	20.0
IT-A	427	800	33.0	30.0	5	41.7	37.9
IT-A	649	1200	19.5	17.7	4	34.2	31.1
IT-A	760	1400	14.5	13.2	4	26.5	24.1
IT-B	24	75	15.8	14.4	4	17.2	15.6
IT-B	24	75	14.4	13.1	3	16.0	14.5
IT-B	204	400	20.5	18.6	3	22.6	20.5
IT-B	427	800	36.7	33.4	5	51.8	47.1
IT-B	427	800	38.1	34.6	4	49.2	44.7
IT-B	649	1200	21.1	19.2	4	44.2	40.2
IT-B	760	1400	18.7	17.0	6	34.2	31.1
IT-C	24	75	15.6	14.2	3	19.7	17.9
IT-C	24	75	16.8	15.3	3	20.6	18.7
IT-C	204	400	16.9	15.4	3	21.2	19.3
IT-C	427	800	19.1	17.4	5	29.5	26.8
IT-C	649	1200	23.0	20.9	4	42.4	38.5
IT-C	649	1200	25.1	22.8	4	46.1	41.9
IT-C	760	1400	21.1	19.2	6	50.9	46.3

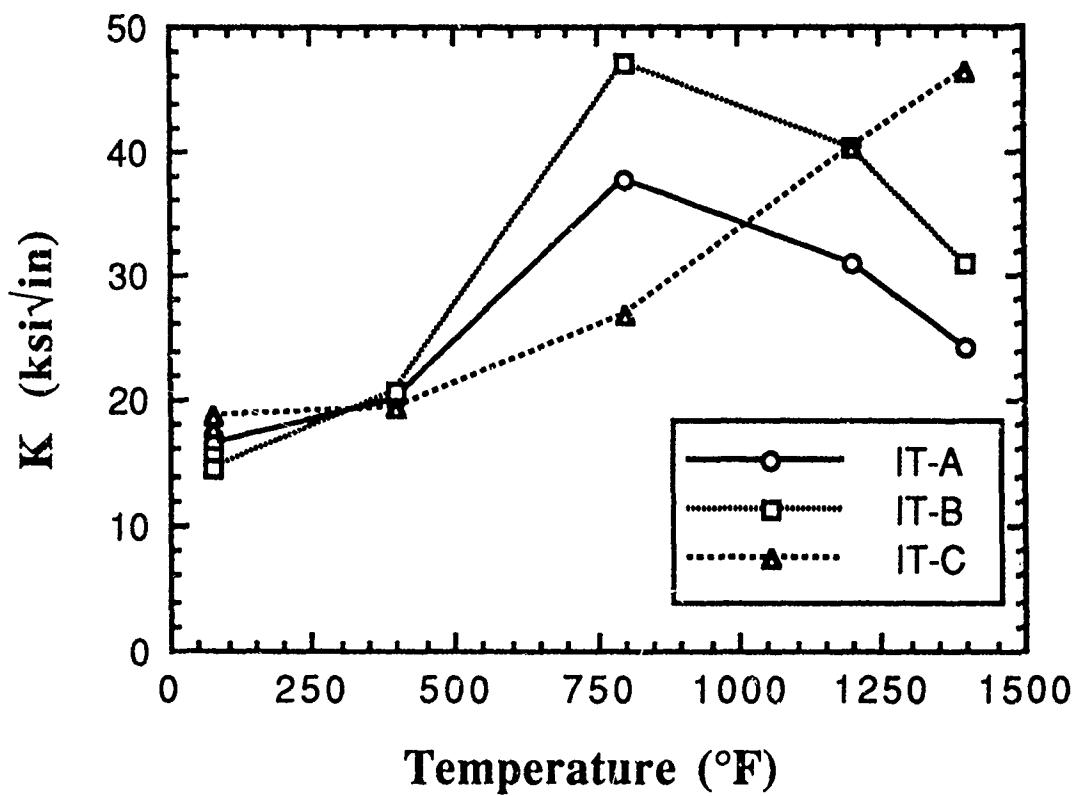


Figure 3-79 Equivalent energy fracture toughness of Phase II alloys plotted as a function of test temperature.

tensile strength both increase with increasing test temperature across the entire range of temperatures which were tested. Fracture toughness was not evaluated after the 100 hour thermal exposure at 705°C (1300°F), and it is not known if the decreasing fracture toughness values of Ti-24.5Al-6Nb-2Mo-2Ta-2V (IT-A) and Ti-24.5Al-8Nb-2Mo-2Ta (IT-B) at temperatures above 427°C (800°F) were effected by microstructural instability.

LCF testing of the Phase II alloys was conducted over the temperature range of room temperature to 760°C (1400°F). The LCF specimens were 11.4 cm (4.5 in) long with a 1.9 cm (0.75 in) gage length and 0.51 cm (0.20 in) gage diameter. Testing was conducted in strain control with an 'A' ratio of 1.0. For elevated temperature testing, induction heating was used. This caused some difficulty since the button head region was kept at low temperatures where the material was shown to be sensitive to notch weakening. After several specimens of the alloy with a low Nb level, Ti-23.5Al-2Nb-2Mo-2Ta-2Cr (IT-C), failed at the button head, the specimen configuration and gripping technique were modified. The button heads were removed and subsequent tests were conducted by gripping the specimen along the shoulder region with hydraulic grips.

The LCF test results are tabulated in Tables 3-38 and 3-39 and the data for each individual alloy are plotted in Figures 3-80 and 3-81. For each of the three Phase II alloys, fatigue life was highest at 427°C (800°F). The 205°C (400°F) fatigue properties were also quite high but fewer tests were run. As a result, it was not clear what the high-strain, short-life fatigue properties of these alloys would be at 205°C (400°F). The room temperature fatigue properties of the Phase II alloys were relatively similar to the 205°C (400°F) and 427°C (800°F) properties at the 10⁷ endurance limit; however, for room temperature tests there was little difference between the strain range for short-life testing and that for the 10⁷ endurance limit. A similar situation was found to be true for 650°C (1200°F) testing where small incremental changes in strain range significantly effected fatigue life. When test temperatures were increased to 760°C (1400°F), a substantial drop in fatigue life was evident for each of the Phase II alloys.

Fractographic analysis was also carried out on all of the Phase II LCF test specimens, and in some cases, plateau electropolish and etch techniques were used to more carefully identify microstructural features associated with the fatigue initiation sites. Most frequently, large microstructural features such as prior beta grain boundaries were not found to be common fatigue initiation sites as has been found for other alloy / microstructural conditions including beta solution treated Ti-24Al-11Nb. Fatigue initiation was generally localized to very small regions where it was difficult to discern the exact microstructural feature involved, but in some cases, fatigue initiation could be traced to primary alpha-2 grains. The processing techniques which were employed in this program to achieve microstructural refinement were clearly effective in altering the source of fatigue initiation and improving the overall fatigue performance of the alloys.

Examples of fatigue initiation sites characterized by the electropolish and etch technique are shown in Figures 3-82 and 3-83. The test specimen BX25 which was tested at 205°C (400°F) and a strain range of 1.0 percent is shown in Figure 3-82. In this case, fatigue initiation was traced to a prior beta grain boundary which intersects the surface of the specimen. Specimen BX27 which was tested at 650°C (1200°F) and a strain range of 1.0 percent is shown in Figure 3-83. In this case, it appears that the test environment influenced fatigue initiation which was located within a prior beta grain. The fracture surface of specimen B5 which was tested at 427°C (800°F) and a strain range of 1.5 percent is shown in Figure 3-84. Although it is clear that the initiation site on specimen B5 is located at the surface, it is difficult to establish a relationship between fatigue initiation and microstructure for this specimen.

Table 3-38 LCF Results from Phase II Testing

Alloy	Specimen No.	Temperature (°C)	Temperature (°F)	Strain Range (%)	Cycles to Failure
IT-A	A15	24	75	0.80	119665(a)
IT-A	A14	24	75	0.90	6779
IT-A	A12	205	400	0.90	104027
IT-A	A11	205	400	1.00	23882
IT-A	A6	427	800	0.90	123531(a)
IT-A	A4	427	800	0.90	(b)
IT-A	A1	427	800	1.00	39027
IT-A	A5	427	800	1.50	2094
IT-A	A3	649	1200	0.80	1083
IT-A	A10	649	1200	0.80	12060(c)
IT-A	A16	649	1200	0.90	884
IT-A	A13	649	1200	0.90	42369
IT-A	A2	649	1200	1.00	1122
IT-A	A9	760	1400	0.60	100663(a)
IT-A	A8	760	1400	0.80	14988
IT-B	B6	24	75	0.90	36162
IT-B	BX30	24	75	0.90	52547
IT-B	BX31	24	75	1.00	5936(c)
IT-B	BX28	205	400	0.90	122256(a)
IT-B	BX25	205	400	1.00	25867
IT-B	B4	427	800	0.90	126920(a)
IT-B	B1	427	800	1.00	51926(d)
IT-B	BX22	427	800	1.00	110866(a)
IT-B	B5	427	800	1.50	2254
IT-B	B3	649	1200	0.80	102988(a)
IT-B	BX23	649	1200	0.90	127201(e)
IT-B	B2	649	1200	1.00	1386
IT-B	BX27	649	1200	1.00	5997
IT-B	BX29	760	1400	0.60	8939(f)
IT-B	BX26	760	1400	0.70	928
IT-B	BX24	760	1400	0.90	395(g)

(a) = Specimen unloaded prior to failure.

(b) = Failed at button head on loading, see text.

(c) = Specimen failed at button head.

(d) = Specimen failed at extensometer.

(e) = Internal initiation

(f) = Specimen failed at Ta inclusion.

(g) = Specimen failed at W inclusion.

Table 3-39 LCF Results from Phase II Testing of Alloy IT-C

Alloy	Specimen No.	Temperature (°C)	Temperature (°F)	Strain Range (%)	Cycles to Failure
IT-C	C47	24	75	0.80	130156(a)
IT-C	C38	24	75	0.90	11938
IT-C	C43	205	400	0.90	41229
IT-C	C46	205	400	1.00	14119
IT-C	C41	427	800	1.00	42261
IT-C	C34	427	800	1.00	(b)
IT-C	C42	427	800	1.20	4371
IT-C	C40	649	1200	0.90	67950
IT-C	C35	649	1200	0.90	(b)
IT-C	C39	649	1200	1.00	2752
IT-C	C37	760	1400	0.60	28286(g)
IT-C	C36	760	1400	0.80	1470

(a) = Specimen unloaded prior to failure

(b) = Failed at button head on loading, see text.

(g) = Specimen failed at W inclusion

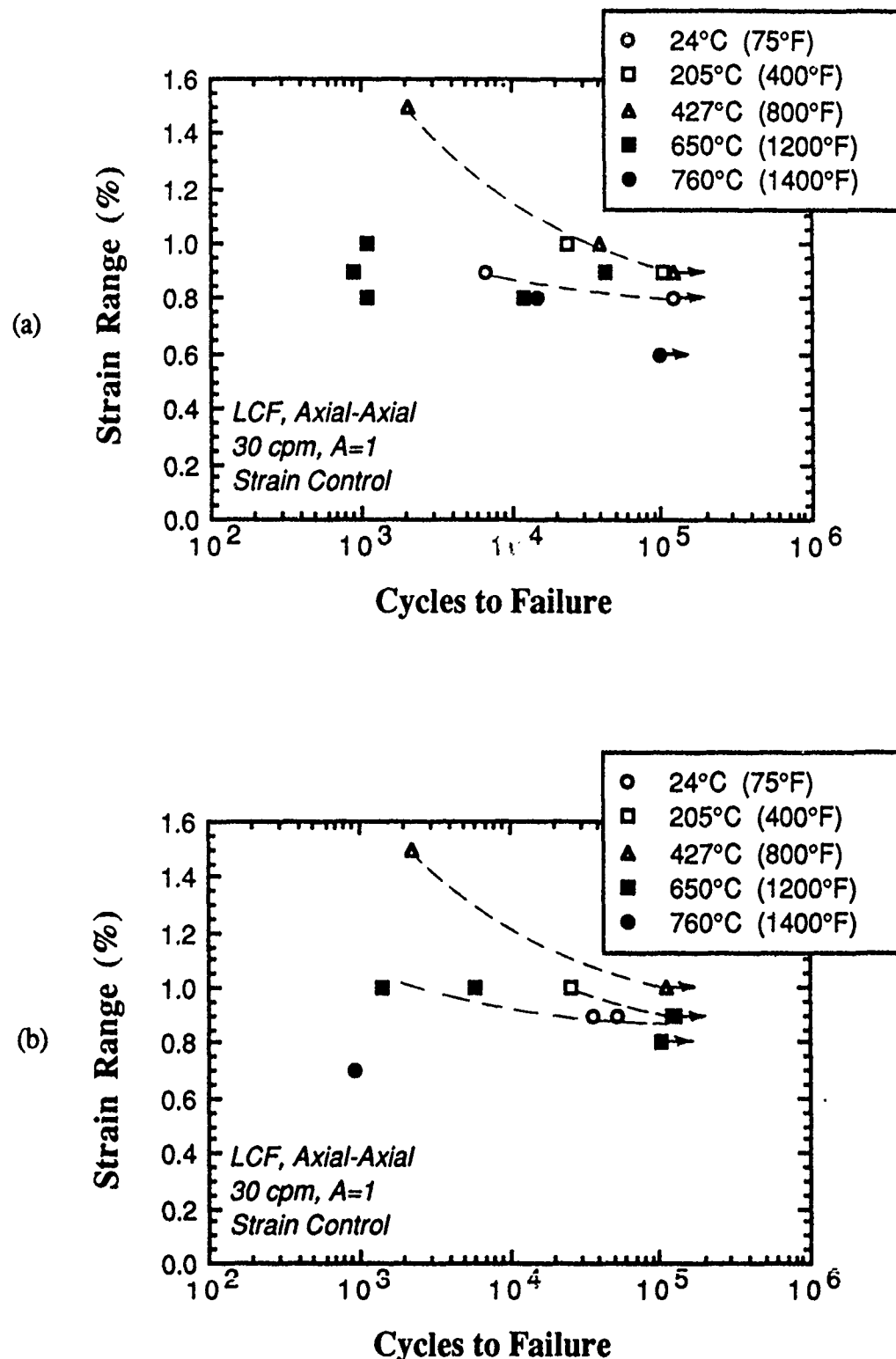


Figure 3-80 LCF results for (a) Ti-24.5Al-6Nb-2Mo-2Ta-2V (TT-A) and (b) Ti-24.5Al-8Nb-2Mo-2Ta (TT-B).

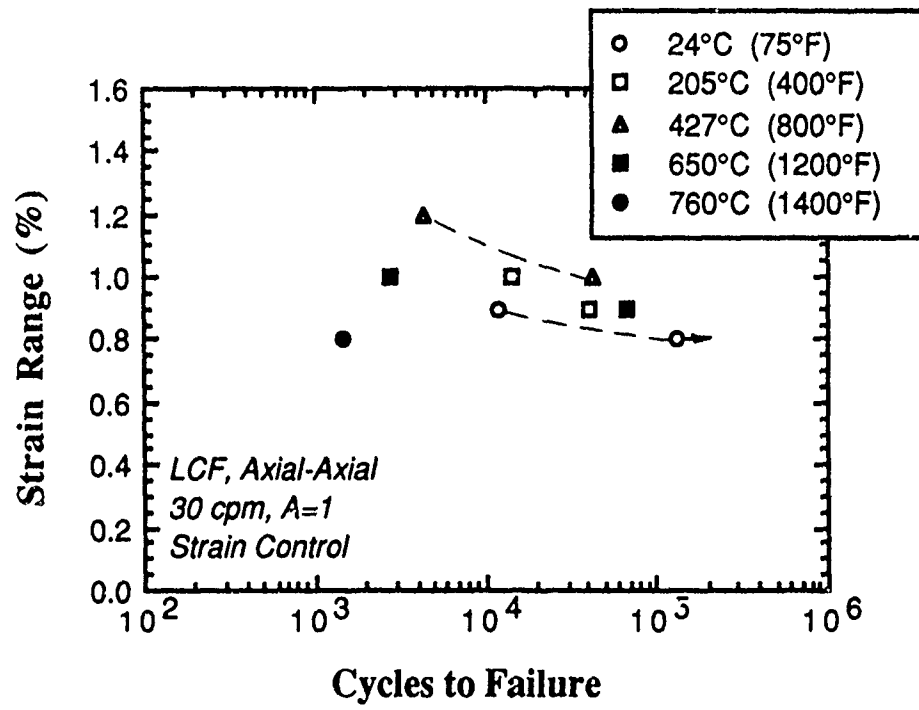


Figure 3-81 LCF results for the alloy Ti-23.5Al-2Nb-2Mo-2Ta-2Cr (IT-C).

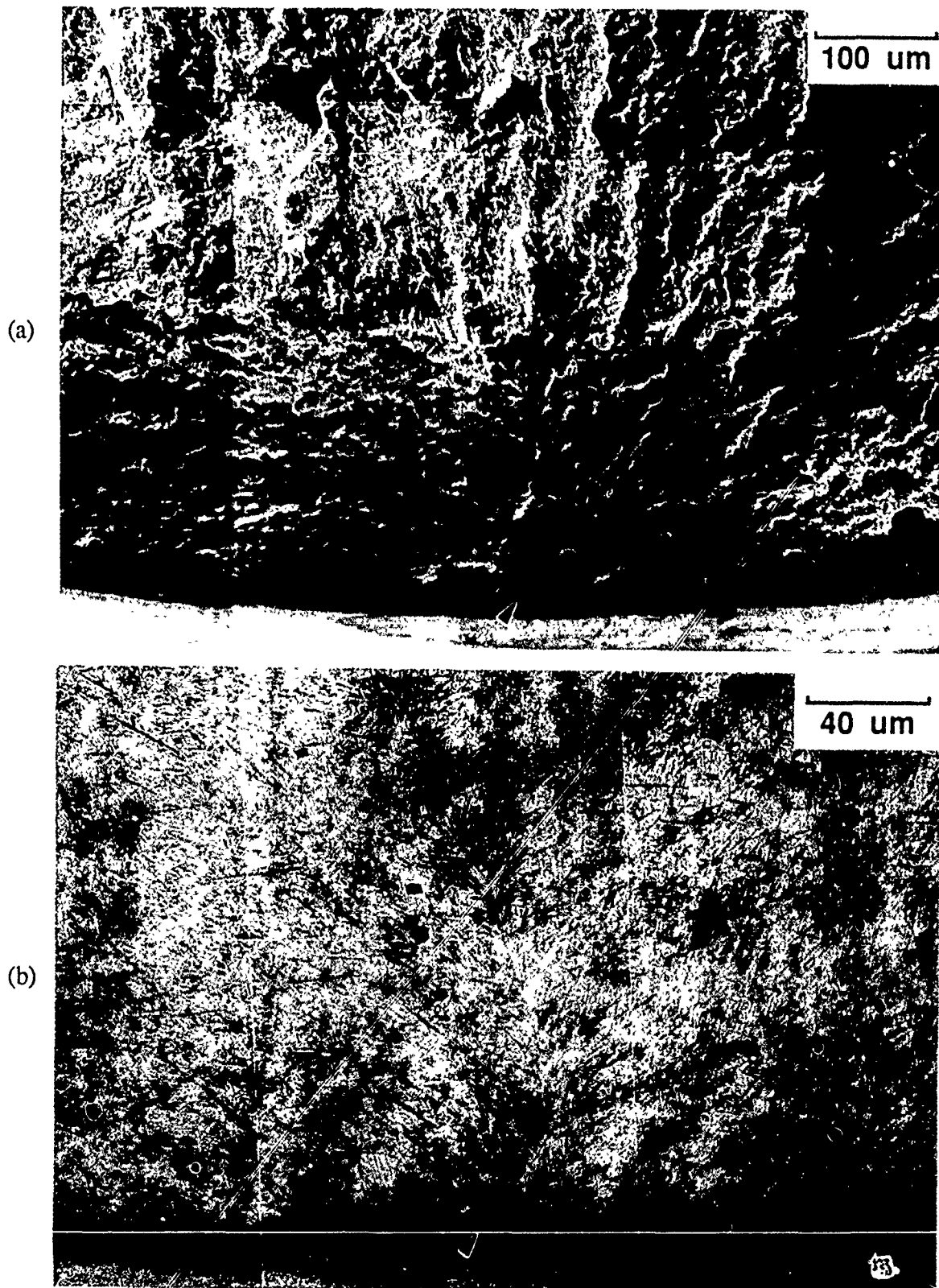


Figure 3-82 SEM micrographs of specimen BX25 showing (a) fracture initiation site and (b) microstructure immediately below the initiation site when revealed by plateau electropolish and etch techniques.

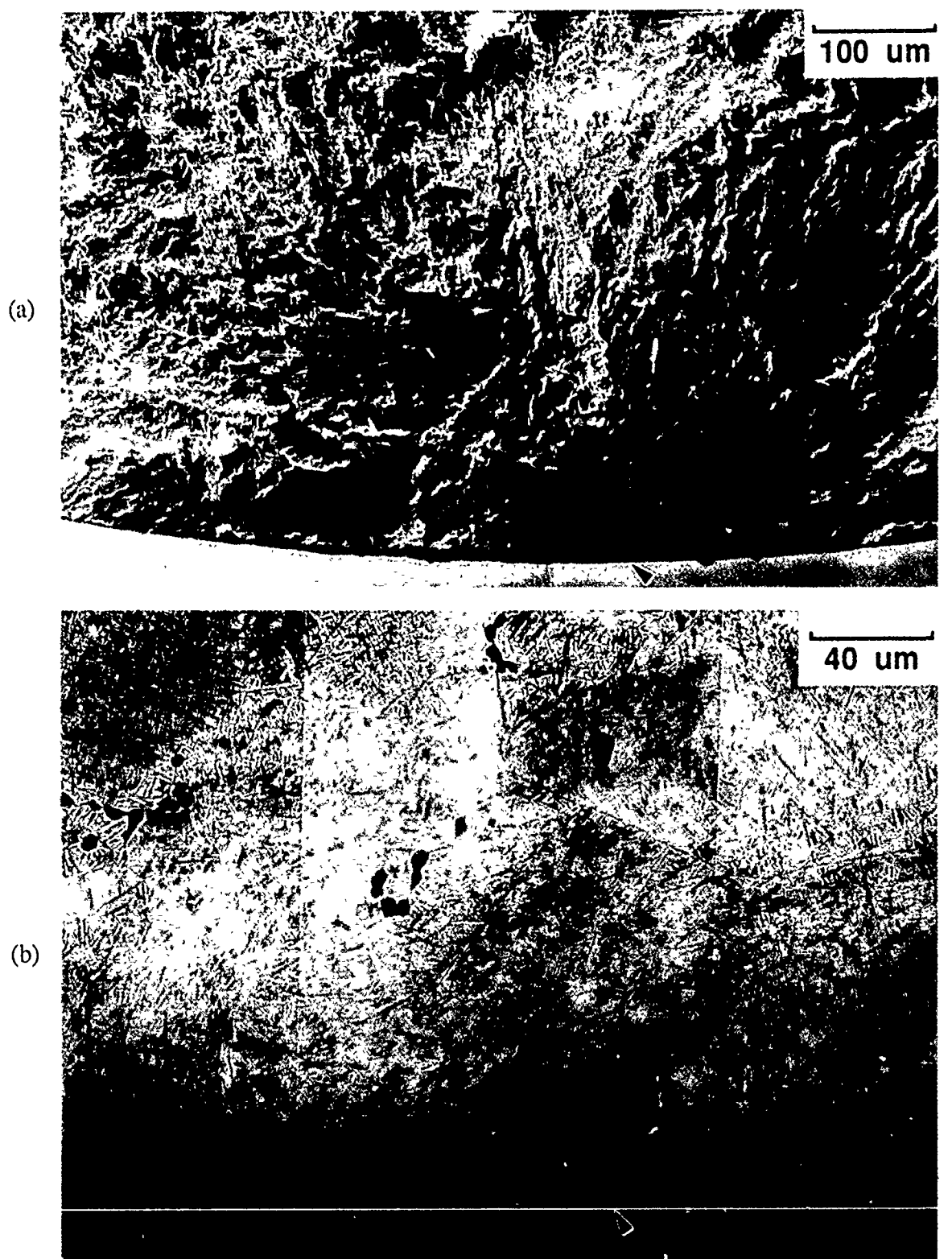


Figure 3-83 SEM micrographs of specimen BX27 showing (a) fracture initiation site and (b) microstructure immediately below the initiation site when revealed by plateau electropolish and etch techniques.

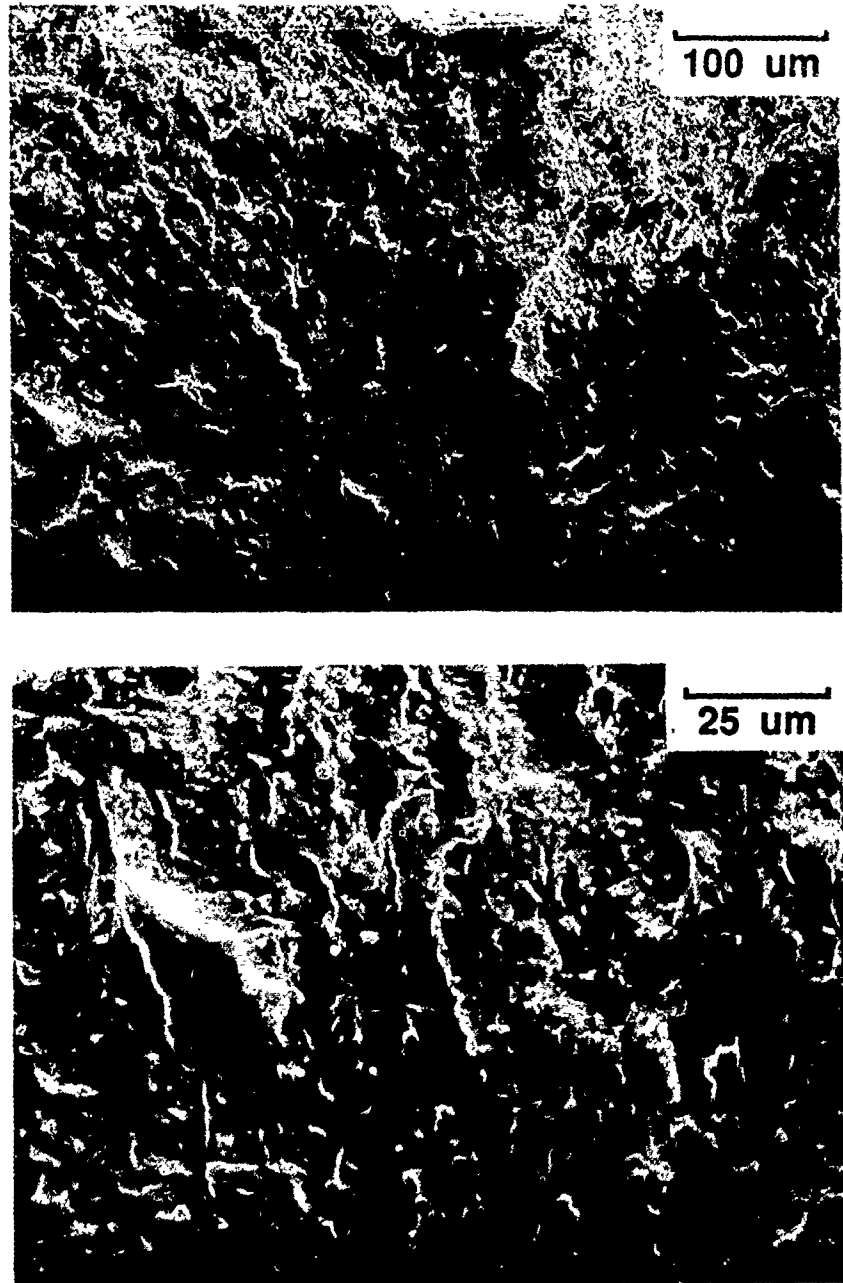


Figure 3-84 SEM micrographs of specimen B5 showing fracture initiation site after testing at 427°C (800°F) and a strain range of 1.5 percent.

Phase II - Summary

In Phase II of the program, three new alloys were selected for a larger evaluation of mechanical properties. The alpha-2 plus beta compositions Ti-24.5Al-6Nb-2Mo-2Ta-2V (IT-A), Ti-24.5Al-8Nb-2Mo-2Ta (IT-B) and Ti-23.5Al-2Nb-2Mo-2Ta-2Cr (IT-C) were selected. The Al levels of these alloys were reduced slightly from the Task 4 alloys in order to obtain a better balance between creep resistance and room temperature fracture toughness and ductility. The beta stabilizing additions were selected for their effects on strength, ductility, fracture toughness and microstructural control.

Each of the Phase II alloys was alpha-2 plus beta processed to employ the benefits of microstructural refinement on fracture toughness and ductility as identified in Phase I, Task 2. Processing studies indicated that induction melting and direct extrusion yielded a very inhomogenous microstructure while VAR followed by beta forging and alpha-2 plus beta extrusion yielded a more homogeneous product.

The creep resistance, rupture life, tensile strength and LCF properties of the Phase II alloys were encouraging while fracture toughness, tensile ductility and notched tensile strength are of concern. In addition, the properties of the alloys Ti-24.5Al-8Nb-2Mo-2Ta (IT-B) and Ti-23.5Al-2Nb-2Mo-2Ta-2Cr (IT-C) were degraded with thermal exposure, and each of the alloys exhibited secondary cracking at higher strain levels during elevated temperature testing. While many of the design properties of the Phase II alloys show significant pay-off in terms of weight savings and temperature capability, it has not yet been established whether the tensile ductility and fracture toughness are sufficient.

4.0 Conclusions

The objective of this program was to study the basic mechanisms which contribute to the toughness of alloys based on the compound Ti₃Al and use this knowledge to develop new families of alloys whose balance of properties would be appropriate for aircraft engine applications. This objective was approached by evaluating the effects of alloying additions and microstructure on mechanical properties while simultaneously analyzing the deformation behavior of each individual alloy. Alloys with a good balance of creep resistance, tensile strength and low cycle fatigue resistance have been identified along with separate alloys which demonstrate high fracture toughness. Those alloys which have a fracture toughness above 33 MPa \sqrt{m} (30 ksi \sqrt{in}) do not have a balance of engineering properties superior to conventional Ti alloys such as Ti-6242. Although much has been learned about the variables which influence fracture toughness, uncertainty remains with regard to the application of alloys which demonstrate relatively low fracture toughness (ie <20 ksi \sqrt{in}) and notch sensitivity.

TEM analysis revealed significant new information about the deformation behavior of alpha-2 titanium aluminide alloys. Although no alloying element was found to have a distinct influence on the mobility of c+a/2 dislocations at low strain levels, specific relationships between temperature and deformation behavior were identified. The density of c+a/2 dislocations was not increased over the temperature range of room temperature to 500°C (932°F) for alpha-2 and alpha-2 plus beta alloys when tested to 2.0 percent plastic strain. In the alpha-2 plus beta alloys, the density of c+a/2 dislocations actually decreased with increasing test temperature while accommodation was achieved in the beta phase as the test temperature reached 500°C (932°F). Temperature was also found to have a significant influence on deformation behavior during creep testing. Dynamic recovery was found to occur in the beta phase of the Phase II alloys at a creep test temperature of 760°C (1400°F) while the beta phase of the 540 and 650°C (1000 and 1200°F) specimens remained heavily deformed and often contained a fine precipitation of alpha-2 particles.

Much knowledge about general alloying effects on the balance of mechanical properties has been generated. When Al is added in excess of 25 atom percent, fracture toughness and ductility are diminished. When the Al level is much less than 24 atom percent, creep resistance is significantly reduced. As a result, the Al level of 24.5 atom percent was chosen for Phase II of this program. A similar rationale can be used to select the level of Mo. Increasing Mo benefits creep resistance, tensile strength and fatigue life but Mo levels much above 2 atom percent can degrade fracture toughness and ductility. When considering the effects of Al and Mo, a disconcerting fact becomes evident:

- there is an inverse relationship between fracture toughness and creep resistance for the alpha-2 titanium aluminide alloys studied in this program.

Some flexibility exists for the total level of beta stabilizing addition. At levels of much less than about 12 atom percent total beta stabilizing addition, the single or near single phase alpha-2 titanium aluminide alloys show limited strength, ductility and toughness. When the total level of beta stabilizing addition is increased to 14 atom percent, rupture life is reduced. For certain applications, the higher levels of beta stabilizing addition may not present a problem. In addition to Mo, other beta stabilizing additions such as Ta and V can be substituted for Nb. However, although both Ta and V can improve the strength of alpha-2 titanium aluminide alloys, it is not clear that these additions are beneficial. While Ta increases cost and promotes difficulty in melting practices, V can degrade environmental resistance (although this was not studied in this particular program) and neither increases toughness or ductility. In addition, the reduction in density for the V for Nb substitution is of little significance.

The other alloying elements which were studied in this program, Ga, Sn, Zr, Cr and Er, offered no clear benefit to the balance of mechanical properties. The alloys which contained the Al substitutes Ga and Sn were particularly brittle. The alloying elements Cr and Zr had no significant adverse effects; however, no clear benefit could be associated with these elements and Zr is noted for poor environmental resistance when added to Ti alloys. The rapidly solidified alloys which contained Er were disappointing but it is clear that the major difficulty with these alloys is associated with processing problems.

Microstructure was shown to have significant effects on mechanical properties in Phase I of the program. For some properties, such as ductility, a wider range of test results were achieved for microstructural variations of a single alloy than for the entire range of compositions when microstructure was held at a near constant. In this situation, refined microstructures produced by alpha-2 plus beta processing and heat-treatment were shown to have considerably higher room temperature ductility than alloys which were beta solution treated. In general, these refined microstructures possess higher fracture toughness as well. However, the fracture toughness of Ti-25Al-5Nb-1Mo (IT-5) was higher for the beta solution treated condition when coarse colonies of alpha-2 platelets were present.

This program has been instrumental in the effort at GEAE to develop an improved understanding of the alpha-2 titanium aluminide alloy system. The conclusion of this contract effort coincides with the end of our overall alloy 'screening' program at GEAE on what we consider second generation alpha-2 titanium aluminide alloys. The second generation alloys are those which are based on the Ti-Al-Nb system with additions of the common beta stabilizing elements Mo, Ta and V. It is our belief that, as a result of this and other programs, the 'general' effects of second generation alloying are well understood and that only a detailed analysis of specific alloys can lead to an increased understanding and modest improvement of second generation alloys. While the main emphasis of this program was placed on the interpretation of alloying effects, it was clearly shown that microstructure has a significant effect on mechanical properties. A thorough analysis of the influence of processing and microstructure on the mechanical properties of second generation alpha-2 titanium aluminide alloys in the Air Force contract, "Microstructure / Processing Effects on Properties of Titanium Aluminides" (F33615-89-C-5615), is appropriate.

Second generation alloys such as Ti-24.5Al-8Nb-2Mo-2Ta (IT-B), are certain to be evaluated in more detail for application specific properties. Although the fracture toughness of such alloys is not high, their promising creep resistance warrants careful evaluation by design and inclusion in future demonstration programs.

5.0 References

1. H.A. Lipsitt, "Titanium Aluminides - An Overview", *High Temperature Ordered Intermetallic Alloys*, C.C. Koch et al, eds., Pittsburgh, PA, The Materials Research Society, 1985, p. 351.
2. J.P. McAndrew and C.R. Simcoe, "Investigation of the Ti-Al-Cb System as a Source of Alloys for use at 1200° - 1800°F", WADD Technical Report 60-99, 1960.
3. S.M.L. Sastry and H.A. Lipsitt, "Ordering Transformations and Mechanical Properties of Ti_3Al and Ti_3Al-Nb Alloys", *Metallurgical Transactions*, 8A, Oct. 1977, p. 1543.
4. M.J. Blackburn, D.L. Ruckle and C.E. Bevan, "Research to Conduct an Exploratory Experimental and Analytical Investigation of Alloys", Technical Report AFML-TR-78-18, 1978.
5. P.L. Martin, H.A. Lipsitt, N.T. Nuhfer and J.C. Williams, "The Effects of Alloying on the Microstructure and Properties of Ti_3Al and $TiAl$ ", *Titanium '80*, vol. 2, p. 1245.
6. C.G. Rhodes, unpublished research, Rockwell Science Center, 1985.
7. B.J. Marquardt and G.E. Wasielewski, "Alloying Element Effect on the Beta Transus Temperature of Alpha-2 Titanium Aluminide Alloys", TMS Fall Meeting, Cincinnati, OH, 1987.
8. M.J. Marcinkowski, "Theory and Direct Observation of Antiphase Boundaries and Dislocations in Superlattices", *Electron Microscopy and Strength of Materials*, eds. G. Thomas and J. Washburn, Interscience, 1963, p. 427.
9. N.E. Paton, R.G. Baggerly and J.C. Williams, "Deformation and Solid Solution Strengthening of Titanium-Aluminum Single Crystals", AFOSR Final Report, Contract No. F44620-72-C-0043, 1976.
10. B.J. Marquardt and G.K. Scarr, unpublished research, GE Aircraft Engines, 1986.
11. S.A. Court, J.P.A. Lofvander, P. Kurath and H.L. Fraser, "The Plastic Deformation of Polycrystalline Ti_3Al Deformed at Room Temperature, 300°C and 650°C", *Sixth International Conference on Titanium*, eds. P Lacombe, R. Tricot and G. Beranger, vol. 2, p. 949.
12. S.A. Court, M.H. Loretto and H.L. Fraser, "Dislocations in As-cast and Deformed Samples of Ti_3Al and $Ti-25Al-4Nb$ ", *Scripta Met.*, vol. 21, 1987, p. 997.
13. A.P. Woodfield, J. White and M.H. Loretto, "The Nature of Faulted Defects in Ti Alloys", *Scripta Met.*, vol. 19, 1985, p. 33.
14. M. Thomas, A. Vassel and P. Veyssiere, "c Slip in Ti_3Al ", *Philosophical Magazine A*, vol. 59, No. 5, 1989, p. 1013.
15. J.P.A. Lofvander, S.A. Court, M.H. Loretto and H.L. Fraser, "Mobility of c Dislocations in Ti_3Al ", *Philos. Mag. Lett.* 60, (3), 1989, p. 111 - 116.

16. M.J. Blackburn and M.P. Smith, "Research to Conduct an Exploratory Experimental and Analytical Investigation of Alloys", Technical Report AFWAL-TR-80-4175, 1980.
17. S.J. Gittis and D.A. Koss, "On the Macroscopic Flow Behavior of the Phases Present in Ti-24Al-11Nb", *High Temperature Ordered Intermetallic Alloys - III*, C.T. Liu, A.I. Taub, N.S. Stoloff and C.C. Koch eds., Pittsburgh, PA, The Materials Research Society, 1989, p. 323.
18. J.C. Williams and M.J. Blackburn, "The Structure, Mechanical Properties and Deformation Behavior of Ti-Al and Ti-Al-X Alloys", *Ordered Alloys - Structural Applications and Physical Metallurgy*, Claitors Publishing Division, Baton Rouge, 1970.
19. D.A. Wagner, "Manufacturing Technology for Advanced Propulsion Materials, Phase III-Non-Fracture-Critical Titanium Aluminides", Interim Report No. 4, 1 August 1987 through 29 February 1988, AF Contract F33615-85-C-5014.
20. B.J. Marquardt, unpublished research, GE Aircraft Engines, 1986.
21. C.H. Ward and J.C. Williams, "Tensile Behavior of Ti-25Al-10Nb-3V-1Mo as a Function of Temperature", TMS Fall Meeting, Indianapolis, IN, 1989.
22. S.J. Balsone, "The Effect of Elevated Temperature Exposure on the Tensile and Creep Properties of Ti-24Al-11Nb", *Oxidation of High Temperature Intermetallics*, J. Doychak and T. Grobstein eds., TMS-AIME, 1988, p. 219-234.
23. ASTM E992, "Practice for Determining a Fracture Toughness of Steels using Equivalent Energy Methodology".